

---

*Extratropical Cyclones and their influence on  
Greenland Ice Sheet surface mass balance  
and dynamics*

Luca Maffezzoni

---

A thesis submitted in partial fulfilment of the requirements of Liverpool John Moores  
University for the degree of Doctor of Philosophy.

March 2022

## List of Contents

---

|   |           |
|---|-----------|
| <b>Abstract</b> .....   | <b>13</b> |
| <b>Author's Declaration</b> .....   | <b>14</b> |
| <b>Acknowledgements</b> .....   | <b>15</b> |
| <b>1. Introduction</b> .....  | <b>17</b> |
| 1.1. Background .....   | 17        |
| 1.2. Thesis Aims and Originality .....  | 19        |
| 1.2.1. AIM 1: Relevance and Originality .....   | 19        |
| 1.2.2. AIM 2: Relevance and Originality .....   | 20        |
| 1.3 Summary of Chapters .....   | 21        |
| <b>2. Greenland Ice Sheet Mass Balance, Hydrology, Dynamics and Climatic Forcing</b><br>..... | <b>23</b> |
| 2.1. Introduction.....  | 23        |
| 2.2. Mass balance .....   | 27        |
| 2.2.1. What is Mass Balance? .....  | 27        |
| 2.2.2 Surface Mass Balance.....   | 27        |
| 2.2.3. Ice Motion and Terminating Environment of Glaciers .....                               | 30        |
| 2.2.3.1. Ice Discharge .....  | 32        |
| 2.2.4. Past, Present and Future of the GrIS Mass Balance .....                                | 33        |
| 2.2.4.1. Mass Balance Calculation Methods.....  | 33        |
| 2.2.4.2. Past and Present GrIS Mass Balance.....  | 34        |
| 2.2.4.3. Future GrIS Mass Balance.....  | 36        |
| 2.3. Atmosphere-GrIS Interactions .....   | 38        |
| 2.3.1. Introduction .....   | 38        |
| 2.3.2. Jet-Streams and Large-Scale Atmospheric Circulations.....                              | 39        |
| 2.3.2.1 Dynamic Anticyclones .....  | 41        |
| 2.3.2.2 Extratropical Cyclones .....  | 43        |
| 2.3.3. Climatic Indices .....   | 47        |
| 2.3.3.1. Description of the NAO and GB Indices .....  | 47        |
| 2.3.3.2. Recent Behaviour of the NAOI and GBI .....   | 49        |

## List of Contents

|           |  |           |
|-----------|--|-----------|
| 2.4.      | Hydrology, Dynamics and GrIS Mass Balance .....                                  | 50        |
| 2.4.1.    | Introduction .....   | 50        |
| 2.4.2.    | Surface Meltwater Routing and Englacial Environment.....                         | 51        |
| 2.4.3.    | Subglacial Water Flow and Dynamics.....  | 53        |
| 2.4.4.    | Fjord Circulation.....   | 55        |
| 2.5.      | Extratropical Cyclones and Future GrIS Precipitation .....                       | 56        |
| 2.5.1.    | Extratropical Cyclone Characteristics .....                                      | 56        |
| 2.5.2.    | Extratropical Cyclone trends in the Greenlandic Region .....                     | 57        |
| 2.5.3.    | Future Storm Tracks, Cyclones and GrIS Precipitation .....                       | 57        |
| 2.6.      | Research priorities.....   | 58        |
| <b>3.</b> | <b><i>Regional Climate Model and Extratropical Cyclones.....</i></b>             | <b>60</b> |
| 3.1.      | Introduction.....  | 60        |
| 3.2.      | Data Sources.....  | 60        |
| 3.2.1.    | The MAR .....  | 60        |
| 3.2.2.    | Extratropical Cyclone Dataset .....  | 61        |
| 3.3.      | Methodology .....  | 62        |
| 3.3.1.    | The MAR and SMB/SEB .....  | 62        |
| 3.3.2.    | Cyclones Filtering and Tracking.....   | 64        |
| 3.4.      | Results .....  | 65        |
| 3.4.1.    | The MAR and SMB/SEB Temporal Variability .....                                   | 65        |
| 3.4.2.    | The MAR and Spatial SMB Variability.....   | 68        |
| 3.4.3.    | Cyclonicity in the Greenlandic Region.....                                       | 72        |
| 3.4.3.1.  | Spatial Distribution in Different Seasons and Monthly Frequencies .....          | 72        |
| 3.5.      | Discussion and Conclusion.....   | 74        |
| <b>4.</b> | <b><i>The Impact of Extratropical Cyclones on the GrIS SEB and SMB .....</i></b> | <b>77</b> |
| 4.1.      | Introduction.....  | 77        |
| 4.1.1.    | Synoptic Circulation Types and SMB .....   | 79        |
| 4.1.2.    | Synoptic Circulation Types and SEB .....   | 80        |
| 4.2.      | Data and Methods .....   | 83        |
| 4.2.1.    | Data Sources .....   | 83        |
| 4.2.2.    | Methodology .....  | 83        |

## List of Contents

|           |  |            |
|-----------|--|------------|
| 4.3.      | Results .....  | 85         |
| 4.3.1.    | Winter .....   | 85         |
| 4.3.2.    | Summer .....   | 90         |
| 4.4.      | Discussion .....   | 97         |
| 4.5.      | Conclusion .....   | 102        |
| <b>5.</b> | <b><i>Late Summer/Early Autumn Cyclonic Rainfall and Ice Flow of the GrIS.....</i></b> | <b>104</b> |
| 5.1.      | Introduction.....  | 104        |
| 5.2.      | Data and Methods.....  | 106        |
| 5.2.1.    | Data Sources .....   | 106        |
| 5.2.2.    | Methodology .....  | 109        |
| 5.2.3.    | Study Sites .....  | 114        |
| 5.3.      | Results .....  | 123        |
| 5.3.1.    | General Meteorological Analysis .....  | 123        |
| 5.3.2.    | Magnitude of the Cyclonic Events and Energy Balance.....                               | 127        |
| 5.3.3.    | Cyclonic Events and Ice Dynamics at Sites A, B, C, D and E .....                       | 132        |
| 5.3.3.1.  | Timing of ice velocity data .....  | 132        |
| 5.3.3.2.  | Ice Velocity Analysis .....  | 134        |
| 5.3.3.3.  | Site A, 2015 .....   | 139        |
| 5.3.3.4.  | Site B, 2015.....  | 141        |
| 5.3.3.5.  | Site C, 2015.....  | 146        |
| 5.3.3.6.  | Site D, 2015 .....   | 152        |
| 5.3.3.7.  | Site E, 2013.....  | 155        |
| 5.3.3.8.  | Site E, 2012.....  | 161        |
| 5.3.3.9.  | Summary of ice velocity and runoff around the cyclone's events                         | 166        |
| 5.4.      | Discussion.....  | 166        |
| 5.4.1.    | Land Terminating Glaciers .....  | 166        |
| 5.4.2.    | Marine Terminating Glaciers .....  | 168        |
| 5.4.3.    | Rainfall Trend and self-regulation in the ablation zone .....                          | 169        |
| 5.5.      | Conclusion .....   | 173        |
| <b>6.</b> | <b><i>Synthesis and Discussion .....</i></b>   | <b>174</b> |
| 6.1.      | Introduction.....  | 174        |
| 6.2.      | Summary of the Research and Limitations .....  | 174        |
| 6.2.1.    | Aim 1: Extratropical Cyclones and their Impact on the GrIS.....                        | 174        |

List of Contents

|  |            |
|--|------------|
| SMB and SEB .....  | 174        |
| 6.2.2 Aim 2: Cyclones and their Impact on GrIS Ice Motion.....       | 179        |
| 6.3. Prospective for Future Research.....                            | 184        |
| 6.3.1 Impact of Extratropical Cyclones on the GrIS SMB and SEB ..... | 184        |
| 6.3.2 Impact of Cyclonic Rainfall on the GrIS Ice Motion .....       | 187        |
| 6.4. Concluding Remarks .....  | 188        |
| <b>References Cited .....</b>  | <b>191</b> |
| <b>Appendix A.....</b>   | <b>215</b> |
| <b>Appendix B.....</b>   | <b>216</b> |
| <b>Appendix C .....</b>  | <b>220</b> |
| <b>Appendix D.....</b>   | <b>222</b> |
| <b>Appendix E .....</b>  | <b>226</b> |
| <b>Appendix F .....</b>  | <b>234</b> |

List of Figures

---

**Figure 2.1** Greenland Digital Elevation Model (DEM)..... 23

**Figure 2.2** Principal oceans, seas and bays surrounding Greenland..... 24

**Figure 2.3.** Average temperature at .995 sigma level in winter (a) and summer (b) and ice cover from NSIDC (Walsh et al., 2015) during the climatological period 1986-2015..... 26

**Figure 3.1.** The MAR Greenland domain with ice sheet mask..... 63

**Figure 3.2.** (a) Annual values of the Surface Mass Balance (SMB) integrated over the entire GrIS during a glaciological years and average summer albedo ..... 67

**Figure 3.3.** Modelled 1958-1990 average melt (a) and 1991-2015 minus 1958-1990 difference (b) ..... 68

**Figure 3.4.** Modelled 1958-1990 average runoff (a) and 1991-2015 minus 1958-1990 difference (b) ..... 69

**Figure 3.5.** Modelled 1958-1990 average temperature (a) and 1991-2015 minus 1958-1990 difference (b)..... 70

**Figure 3.6.** Modelled 1958-1990 average refreezing (a) and 1991-2015 minus 1958-1990 difference (b)..... 70

**Figure 3.7.** Modelled 1958-1990 albedo (a) and 1991-2015 minus 1958-1990 difference (b) ..... 71

**Figure 3.8.** Modelled 1958-1990 average SMB (a) and 1991-2015 minus 1958-1990 difference (b) ..... 71

**Figure 3.9.** Number of cyclonic days for winter season over the entire Greenland domain during the period 1958-2016..... 72

**Figure 3.10.** Same as Fig 3.9 but for spring..... 72

**Figure 3.11.** Same as Fig 3.9 but for summer ..... 73

**Figure 3.12.** Same as Fig 3.9 but for autumn ..... 73

**Figure 3.13.** Percentage of cyclonic days during the twelve months for the period 1958-2016..... 74

List of Figures

**Figure 4.1.** Map of the Greenland divided into the six main drainage basins ..... 85

**Figure 4.2.** Standardized anomalies of SMB and SEB variables averaged over the entire GrIS in winter for the 20 % most intense cyclones during the period 1958-2016 ..... 86

**Figure 4.3.** Spatial representation of the standardized anomalies over the entire GrIS of ME (a), LWD (b), LWU (c) and SHF (d) in winter ..... 87

**Figure 4.4.** Same as Fig 4.3 but for QQZ (a) and TTZ (b). ..... 88

**Figure 4.5.** Same as Fig 4.2 but calculated by including 40 % and 60 % of the most intense cyclones during the period 1958-2016 in winter. .... 88

**Figure 4.6.** Same as Fig 4.2 but calculated for each of the six drainage basins of Fig 4.1. .... 89

**Figure 4.7.** Standardized anomalies of SMB and SEB variables averaged over the entire GrIS in summer for the 20 % most intense cyclones during the period 1958-2016 ..... 90

**Figure 4.8.** Same as Fig 4.7 but only for the ablation zone. .... 91

**Figure 4.9.** Spatial representation of the standardized anomalies over the entire GrIS of AL (a), LWD (b), ME (c) and SHF(d) in summe ..... 92

**Figure 4.10.** Same as Fig 4.9 but for SWD (a) and TTZ (b). .... 93

**Figure 4.11.** Same as Fig 4.7 but calculated by including 40 % and 60 % of the most intense cyclones during the period 1958-2016 in summer. .... 93

**Figure 4.12.** Same as Fig 4.11 but only for the ablation zone. .... 94

**Figure 4.13.** Same as Fig 4.7 but calculated for each of the six drainage basins of Fig 4.1. .... 94

**Figure 4.14.** Same as Fig 4.7 but calculated for each of the six drainage basins of Fig 4.1. .... 95

**Figure 4.15.** Same as Fig 4.13 but only for the ablation zone. .... 96

**Figure 4.16.** Same as Fig 4.14 but only for the ablation zone. .... 97

**Figure 4.17.** Same as Fig 4.9 but for cloud cover in winter and summer. .... 98

List of Figures

**Figure 5.1.** Greenland divided into 260 drainage basins grouped in 7 regions ..... 111

**Figure 5.2.** Structure of the GIS process utilised to extract the average ice velocities and errors associated along the glacier’s flowlines, developed with the use of QGIS and GDAL software libraries..... 113

**Figure 5.3.** Geographical location of the study sites. .... 115

**Figure 5.4.** Site A and surrounding area of the GrIS..... 116

**Figure 5.5.** Same as Fig 5.4 but for the B site. .... 117

**Figure 5.6.** Same as Fig 5.4 but for the C site..... 118

**Figure 5.7.** Same as Fig 5.4 but for the D site. .... 119

**Figure 5.8.** Same as Fig 5.4 but for the E site ..... 120

**Figure 5.9.** 500 mb Geopotential Height (m) Composite Mean from NCEP-NCARv1 reanalysis..... 123

**Figure 5.10.** TTZ Anomaly Composite Mean extracted from the MAR..... 124

**Figure 5.11.** Same as Fig 5.10 but for the mean cloud cover. .... 125

**Figure 5.12.** Same as Fig 5.10 but for the mean daily rainfall ..... 126

**Figure 5.13.** Daily surface energy budget below the ELA..... 129

**Figure 5.14.** Same as Fig 5.13 but for site E..... 131

**Figure 5.15.** Top: Average ice velocity along flowline A1 during image pair periods for which ice velocity data were available. Red dotted line represents the multi-year ice velocity. Bottom: Daily meltwater, rainfall, runoff over the entire basins where runoff occurred and daily temperature below the ELA. Timing of the cyclonic event is shaded in grey in Top and Bottom subplots. .... 140

**Figure 5.16.** Ice velocities along flowline A1 during selected image pairs periods. .... 141

**Figure 5.17.** Same as Fig 5.15 but for site B, flowlines B1 and B2..... 144

**Figure 5.18.** Same as Fig 5.15 but for site B, flowlines B3 and B4..... 145

List of Figures

**Figure 5.19.** Same as Fig 5.16 along flowlines B1, B2, B3 and B4. Here, two image pairs cover the cyclonic period and are shaded in grey in the legend. .... 146

**Figure 5.20.** Same as Fig 5.15 but for site C, flowlines C1 and C2. .... 148

**Figure 5.21.** Same as Fig 5.15 but for site C, flowlines C3 and C4. .... 149

**Figure 5.22.** Same as Fig 5.16 along flowlines C1, C2, C3 and C4..... 151

**Figure 5.23.** Same as Fig 5.15 but for site D, flowlines D1 and D2..... 153

**Figure 5.24.** Same as Fig 5.16 along flowlines D1, D2..... 155

**Figure 5.25.** Same as Fig 5.15 but for the cyclonic event 2013, site E. Flowlines E1, E2..... 157

**Figure 5.26.** Same as Fig 5.15 but for the cyclonic event 2013, site E. Flowlines E3, E4, E5. .... 158

**Figure 5.27.** Same as Fig 5.16 but for cyclonic event 2013. Flowlines E1, E2, E3, E4 and E5. .... 160

**Figure 5.28.** Same as Fig 5.15 but for the cyclonic event 2012, site E. Flowlines E1, E2..... 162

**Figure 5.29.** Same as Fig 5.15 but for the cyclonic event 2012, site E. Flowlines E3, E4, E5. .... 163

**Figure 5.30.** Same as Fig 5.16 but for the cyclonic event 2012. Flowlines E1, E2, E3, E4 and E5..... 165

**Figure 5.31.** Rainfall fraction compared to the total precipitation between 15<sup>th</sup> August-15<sup>th</sup> October at each site below the ELA, calculated every five years and covering the climatological reference period 1986-2015 along with the trend their equation and statistical significance. .... 171

**Figure 5.32.** Ice velocities along flowline C1 and C2 during selected image pairs periods. .... 172

## List of Tables

---

|  |     |
|--|-----|
| <b>Table 3.1.</b> Contiguous Greenland ice sheet (GrIS) averages and trends of SMB and climatic components. ....   | 66  |
| <b>Table 5.1</b> Description of the datasets from which the ice velocity data of specific study sites were extracted.....  | 109 |
| <b>Table 5.2</b> Summary of the study sites and glaciers along with names and lengths of the flowlines. ....   | 122 |
| <b>Table 5.3.</b> Total rainfall/meltwater/runoff during the cyclonic period 2015 and comparison with the 1986-2015 climatic average of the same period ...  | 128 |
| <b>Table 5.4.</b> Same as Table 5.3 but for site E.....  | 130 |
| <b>Table 5.5.</b> Summary table of the velocity image pairs utilised in this study at specific sites. For each site the cyclonic period analysed is highlighted.....                                   | 133 |
| <b>Table 5.6.</b> Summary of ice velocity change along the flowlines of marine terminating glaciers around the cyclonic periods .....  | 135 |
| <b>Table 5.7.</b> For marine terminating glaciers, the percentage of total cyclone period covered and percentage of cyclones days in the satellite data period which cover the event are provided..... | 136 |
| <b>Table 5.8.</b> Same as Table 5.6 but for land terminating glaciers.....   | 137 |
| <b>Table 5.9.</b> Same as Table 5.7 but for land terminating glaciers.....   | 138 |



### Glossary of Main Acronyms used in the Text

---

|                                |   |
|--------------------------------|---|
| <b><i>AL</i></b>               | Albedo  |
| <b><i>D</i></b>                | Ice Discharge                                 |
| <b><i>ELA</i></b>              | Equilibrium Line Altitude                     |
| <b><i>GrIS</i></b>             | Greenland Ice Sheet                           |
| <b><i>Gt</i></b>               | Gigatonne                                     |
| <b><i>LHF</i></b>              | Latent Heat Flux                              |
| <b><i>LWD</i></b>              | Long-Wave Downward                            |
| <b><i>LW<sub>net</sub></i></b> | Long-Wave Net Radiation                       |
| <b><i>LWU</i></b>              | Long-Wave Upward                              |
| <b><i>MAR</i></b>              | Modèle Atmosphérique Régional                 |
| <b><i>MB</i></b>               | Mass Balance                                  |
| <b><i>ME</i></b>               | Melt  |
| <b><i>NCEP</i></b>             | National Centres for Environmental Protection |
| <b><i>NCAR</i></b>             | National Center for Atmospheric Research      |
| <b><i>QQZ</i></b>              | Specific Humidity (2 meters above surface)    |
| <b><i>RA</i></b>               | Rainfall                                      |
| <b><i>RCM</i></b>              | Regional Climate Model                        |
| <b><i>RCP</i></b>              | Representative Concentration Pathway          |
| <b><i>RF</i></b>               | Refreezing                                    |
| <b><i>R<sub>net</sub></i></b>  | Total Net Radiation                           |
| <b><i>RU</i></b>               | Runoff  |
| <b><i>SEB</i></b>              | Surface Energy Balance                        |
| <b><i>SF</i></b>               | Snowfall                                      |
| <b><i>SHF</i></b>              | Sensible Heat Flux                            |
| <b><i>SLR</i></b>              | Sea Level Rise                                |
| <b><i>SMB</i></b>              | Surface Mass Balance                          |
| <b><i>SWD</i></b>              | Short-Wave Downward                           |
| <b><i>SW<sub>net</sub></i></b> | Short-Wave Net Radiation                      |
| <b><i>TTZ</i></b>              | Temperature (2 meters above surface)          |

## **Abstract**

---

The Greenland Ice Sheet (GrIS) stores enough freshwater to raise global sea level by more than 7 m, so its response to climate variability is of considerable societal significance. Extratropical cyclones impact its surface mass budget (SMB) via both solid and liquid precipitation but their impacts on surface energy balance (SEB) are less known. Moreover, the ability of cyclonic rainfall to reach and perturb the ice-bed interface influencing ice dynamics, remains an open question. The thesis helps fill these knowledge gaps by 1) exploring the net effect of extratropical cyclones on the GrIS surface mass balance; and 2) investigating how they can influence ice dynamics through their input of meltwater and rainfall to the subglacial hydrological system.

The first aim was addressed by calculating mean meteorological and surface mass/energy balance terms during periods when the GrIS was under the influence of extratropical cyclones. This was achieved using a 58-year integration of the Model Atmospherique Regional (MAR) along with a cyclone dataset covering the Northern Hemisphere for the same period. The results indicated that extratropical cyclones have a net positive effect on GrIS mass balance in summer, lowering air temperatures and increasing albedo (due to snowfall) that suppress the meltwater production in the ablation region. During winter, the analysis reveals abundant snowfall leading again to a positive impact on GrIS mass balance.

The MAR outputs and the cyclone dataset were also used to identify cyclonic rainfall events over the western flank of the GrIS during late summer/early autumn; the period where their occurrence could have the biggest impact on ice dynamics. A GIS procedure was applied to data from the GoLIVE and MEaSURES Selected Glacier satellite ice velocity datasets to extract ice motion of the glaciers during the melt season and around the cyclonic period. The major finding here was an acceleration along both marine and land terminating glaciers in response to extratropical cyclone passage, forced by subglacial hydrological changes resulting from inputs of rainfall and meltwater. The thesis therefore concludes that extratropical cyclones have a positive impact on the net surface mass balance in the current climate, but that their passage during autumn may already enhance dynamic thinning.

## **Author's Declaration**

---

I declare that no portion of the work referred to in the thesis has been submitted in support of an application for another degree or qualification of this or any other university or other institute of learning.

## **Acknowledgements**

---

Special Thanks must be addressed to the Ph.D supervisors Laura and Tom for their precious guidance, both scientific and human. Without them, the greatest adventure of my life in Liverpool could not have come true. They are people of great emotional intelligence and humanity, who have spent many efforts to give me important scientific feedback throughout the work and precious support during the writing thesis.

A sincerely thank to my family, and especially my parents and my grandma for their financial support and for accepting my departure outside the national borders, away from home.

A special thanks to Anna and Alessandro for their mental support during the last two years characterized by the pandemic. They always believed in me and always encouraged me to finish my PhD even in difficult times.

Finally, I would like to thank Luca Maffezzoni. Despite great difficulties, Luca managed to push himself beyond his limits and achieve this goal. A dream born from his childhood, that of wanting to explore the science of climatology and glaciers carrying out work related to this discipline. A goal in which only he has always firmly believed, without never give up, even in adverse moments and which has now come true and he hope it can continue in the future with new projects



# **1. Introduction**

## **1.1. Background**

Approximately 85 % of Greenland is permanently covered in ice. After Antarctica, the Greenland ice sheet (GrIS) is the Earth's second largest ice sheet with an area of about 1.7 million km<sup>2</sup>, a volume of 2.85 million km<sup>3</sup> (Tedesco et al., 2015) with a maximum thickness of 3,375 m in the central north-eastern region (Bamber et al., 2013). Being the largest body of fresh water in the Northern Hemisphere the GrIS, if it melted entirely, it would represent a potential sea level rise (SLR) over 7 meters (Bamber et al., 2001; Van den Broeke et al., 2008; Griggs et al., 2012). The IPCC WGI sixth Assessment Report in 2021 (Masson-Delmotte et al., 2021) estimated a GrIS mass loss of 4890 Gt between 1992 and 2020 with a sevenfold increase from 34 Gigatons per year between 1992 and 2001 to 247 Gigatons per year between 2012 and 2016. It contributed to SLR by 13.5 mm reaching the highest contribution in the last decade (Slater et al., 2021) becoming the second contributor after thermal expansion (Hanna et al., 2020; Hugonnet et al., 2021). Under the lower emission scenario Shared Socioeconomic Pathways (SSP1)-2.6 and higher emission scenario (SSP5)-8.5, the GrIS will likely contribute to SLR for centuries and lead to a SLR between 100 and 130 mm by 2100. In terms of societal and economic impact, the SLR contribution will lead to an increase of coastal floods, storm surge and erosion with an expected damage under the RCP 8.5 scenario up to US\$1,600 billion by 2050 (Abadie et al., 2020) considering the 136 major coastal cities.

During the last sixty decades the temperature in the Arctic (and hence Greenland) has increased at a rate twice as fast as the rest of the planet due to sea ice reduction. This phenomenon is known as Arctic amplification (Meleshko et al., 2016) and is predicted to continue in a global warming scenario. Arctic amplification has led to an increase in the GrIS mass loss via ice discharge which includes ice calving and melting across the grounding line (the point at which a glacier starts to float) and snow/ice meltwater runoff, with the latter dominating during the last twenty years (King et al., 2020; Mankoff et al., 2020). Regarding future estimates of meltwater, a study of Hofer et al. (2019) demonstrate how the main source of intra-climatic model

## Introduction

disagreement relies on the parameterization of clouds water phase and related downward long-wave radiation. A more recent multi-model comparison (Goelzer et al., 2020) show how the higher inter-model spread in future projection occurs in the high ablation zone. This is due to difficulties in modelling the altitude of snow-rain fraction related to uncertainties with Greenland temperature projections (Fettweis et al., 2013a) which has implication in term of temperature and density of the snow or ice at the surface (Niwano et al., 2021).

Another challenge is determining ice loss driven by accelerated flow, known as dynamic thinning, and the resulting contribution of this to future SLR (Pritchard et al., 2009; Goelzer et al., 2020). Water at the surface reaching the bed is the primary driver at GrIS margins that feed this mechanism. It comes from meltwater production at the surface and from episodes of rainfall on the GrIS which are predicted to become more frequent and intense in the future, affecting ever greater altitudes (Oltmanns et al., 2019; Niwano et al., 2021). While recent literature has emerged regarding the impact on GrIS ice motion at the margins driven by an increase in meltwater, the impact of cyclonic rainfall episodes remains unexplored.

Both solid and liquid precipitation along with clouds and moisture, whose impact on the GrIS remain a future challenge to address, are mainly delivered over Greenland by weather phenomena called extratropical cyclones. Their frequency over Greenland along with air moisture fraction in the polar region of the GrIS have increased over the recent past and will likely increase in the future, due extratropical cyclones' poleward shift driven by global warming (Yin, 2005; Zappa et al., 2013). For this reason, the aim of this thesis is to expand the knowledge regarding the impact of the extratropical cyclones on the GrIS. Understanding the role they play on the GrIS mass balance in the recent past is crucial for producing more accurate projections of the contribution of the GrIS to SLR over the next 100-200 years which include the influence of these weather phenomena.

## **1.2. Thesis Aims and Originality**

The thesis is divided into two main aims:

- AIM 1: To study the direct impact of extratropical cyclones on surface energy and mass balance of the GrIS using a regional climate model and a cyclone dataset covering the entire Northern Hemisphere. The results will allow identification of the most important parameters involved in energy and mass fluxes over the GrIS under cyclonic weather conditions, inform our understanding of the impact of cyclones during their passage over different portions of the GrIS and enable better estimation of the contribution of the GrIS to SLR.
- AIM 2: To expand the knowledge and understanding of the dynamic response of the GrIS to water input related to episodes of cyclonic rainfall and related meltwater production along the west margin of the GrIS. This will help with predictions of dynamic changes in this region where these episodes are expected to increase at a higher rate than elsewhere on the GrIS (Tedesco & Fettweis, 2012; Goelzer et al., 2020).

### **1.2.1. AIM 1: Relevance and Originality**

In the recent past, research was primarily focused on studying the cyclone tracks around Greenland and related cyclonic activity, in order to explain the accumulation variability over the GrIS, since extratropical cyclones are the major weather type producing precipitation over Greenland. A number of studies tried to link large-scale atmospheric circulation patterns described by climatic indices to cyclonic precipitation over different region of the GrIS. The links between these indices and cyclonic precipitation over Greenland appear weak and limited to the time period selected. A recent study shows how most of the interannual variability of accumulation over the GrIS can be linked and explained by the variability and frequency of cyclones affecting Greenland (Chen et al., 2016). Another recent study underlined the indirect key role of extratropical cyclones in delivering warm air masses on the GrIS, and then enhancing melting (McLeod & Mote, 2016).

All these studies, increased the understanding of the link between cyclonic activity and precipitation (Chen et al., 1997; Schuenemann et al., 2009), and also the indirect impact of cyclones on the GrIS meltwater production , via the movement of warm air masses over Greenland (McLeod & Mote, 2015, 2016). However, there isn't a clear quantitative picture regarding their impact on different areas of the GrIS in terms of components of the radiation budget and so which parameters research needs to focus on in order to improve future projections for the GrIS surface mass balance. This work aims to address this gap and represents the first study which provides a qualitative and quantitative description of the direct impact of cyclones on precipitation and surface energy components along with their spatial variability over the GrIS. The work uses a cyclone dataset provided by the National Snow and Ice Data Centre (NSIDC) which covers the period 1958-2016 and gives the central position of cyclones and tracks their displacement with a resolution of 2.5°. This cyclone dataset has been utilised by many studies in order to obtain a clear understanding of cyclone frequency and intensity in the Northern Hemisphere, however, it has never been used to study cyclonic activity over the entire GrIS. This is due to limits in the algorithms used for detecting and tracking the cyclones over the central high region of the GrIS. Here, the reduction of pressures to sea level is often interpreted by the algorithm as spurious quasi-stationary cyclones over the central Greenland. In this work, thanks to the development of filtering algorithms, it was possible to overcome this obstacle. This allowed for the first time, along with the use of a regional climate model to study and analyse spatial variability of glaciological and climatic components of the GrIS surface under the influence of cyclones.

### **1.2.2. AIM 2: Relevance and Originality**

During the last twenty years, due an increase of atmospheric temperature, the amount of surface meltwater of the GrIS has increased considerably during the summer season (Van den Broeke et al., 2016). This has led to an increase in the magnitude and frequency of surface meltwater pulses that reach the base of the GrIS. These can perturb the ice-bed interface, influencing ice motion (see Chapter 2, section 2.4.3). However, the impact on the GrIS ice motion of an increasing amount

of surface water reaching the bed, remain unknown. Much research has focused on the relation between summer meltwater production and ice motion in the ablation zone but little attention has been paid to the impact of cyclonic rainfall events which are predicted to increase in magnitude and frequency (Oltmanns et al., 2019; Niwano et al., 2021). In fact, in a global warming scenario, periods of rainfall over the GrIS will be increasingly frequent, with solid precipitation being replaced at ever higher altitudes by liquid precipitation (Schuenemann & Cassano, 2010; Mottram et al., 2017).

Only a recent pioneering study (Doyle et al., 2015) highlighted for the first time the ability of a late-summer cyclonic event to trigger an acceleration of ice motion of a land-terminating region of the west GrIS due to high pulses of meltwater and rain reaching the bed from the surface. Despite the originality of the work, it only provides in-situ observations of a single cyclone event over one land terminating portion of the GrIS and so is limited in terms of assessing the dynamics response at a larger scale. The work in this thesis aims to provide more information in this area by studying the impact of three cyclonic rainfall events on different regions of the GrIS characterized by land and marine terminating glaciers. To achieve this aim, a method based on the analysis of a variety of remote sensing ice velocity products, a GrIS digital elevation model (DEM) and outputs of a regional climate model was developed. The methodology allowed a more extensive study on this topic than the in-situ study of Doyle et al. (2015) and provides the potential for further study of the phenomena as new ice velocity data from remote sensing techniques become available.

### **1.3 Summary of Chapters**

Chapter 2 presents the geographical, glaciological, climatological and meteorological background material and literature regarding the GrIS and cyclones. Firstly, the GrIS morphology is described along with its geographical position and the climate that characterizes its interior and margins. Secondly, the physical processes involved in the mass accumulation and loss of the GrIS along with their past, present and future estimates and related calculation methods are described. Thirdly, there is a focus on

## Introduction

the atmosphere, the anticyclonic and cyclonic weather types, their climatology and behaviour in the Greenlandic region and their interaction with the GrIS. Finally, the role of surface meltwater reaching the bed and fjords in regulating ice motion and interaction between extratropical cyclones and the GrIS is presented.

Chapter 3 presents the temporal and spatial trends and variability of the key meteorological and glaciological outputs of the regional climate model utilised. It then goes onto presenting the cyclone dataset, the filtering process applied and a climatology of cyclones in the Greenlandic domain for each season. The work performed in this section is then used in the studies presented in Chapter 4 and 5.

Chapter 4 presents the datasets and methodology developed to investigate the impact of extratropical cyclones on the GrIS in terms of surface mass and energy balance. The results discussed are focused on the overall impact of cyclones over the entire GrIS, the ablation zone and specific selected major drainage basins.

Chapter 5 describes the datasets utilised and methodology applied to analyse the impact of three cyclonic episodes of rainfall in late summer/early autumn on ice motion of glaciers located along the west margins of the GrIS. The results are discussed along with meteorological and glaciological framework of each glacier during the entire ablation season.

Chapter 6 presents the synthesis and main conclusions of the thesis along with a discussion regarding the limitations of this study and potential future research.

---

## 2. *Greenland Ice Sheet Mass Balance, Hydrology, Dynamics and Climatic Forcing*

---

### 2.1. Introduction

The GrIS is characterised by numerous drainage basins consisting of many glaciers that flow from the higher altitudes in the interior to the lower margins towards the edge. In terms of topography, the GrIS descends steeply from its central-eastern part (the ice divide) to the oceans, with a more gently sloping gradient on the west than elsewhere (Toyokuni et al., 2018) (Figure 2.1).

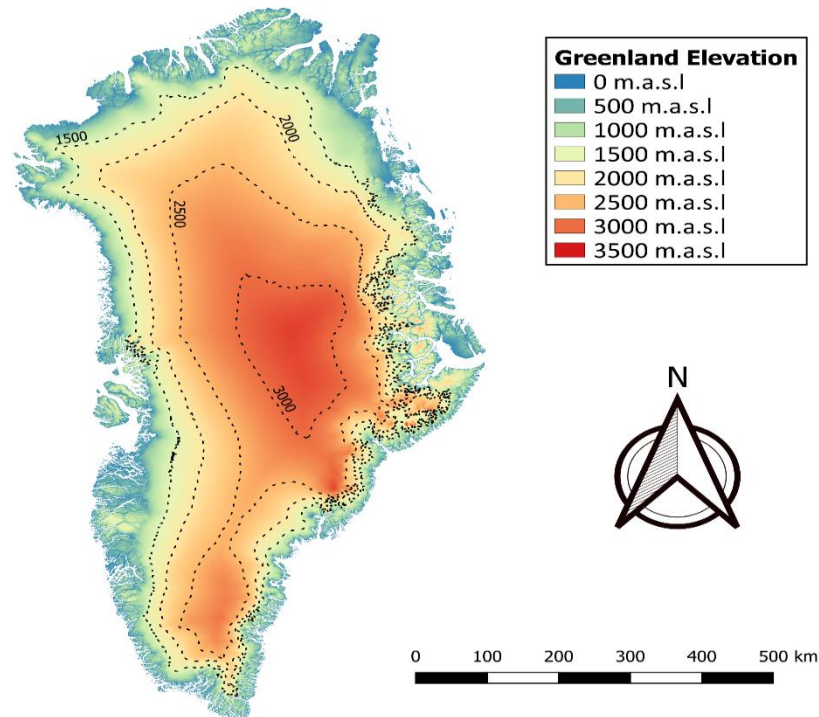


**Figure 2.1** Greenland Digital Elevation Model (DEM) from Howat et al. (2014). Spatial resolution of 90x90 m.

Greenland lies between the Arctic Ocean to the north where sea ice is permanent and the Atlantic Ocean to the south. It is enclosed by Irminger and Greenland Seas on the east and Baffin Bay on the west (Figure 2.2) where an ice belt is present from early winter until late spring. An exception is the Labrador Sea which surrounds Greenland in the south-west where sea ice is absent all year round.



**Figure 2.2** Principal oceans, seas and bays surrounding Greenland

The GrIS has substantial differences in Surface Air Temperature (SAT) between coastal and interior regions and also between northern and southern portion due to varying latitude, presence or absence of sea ice and different origin of air masses (Cappelen et al., 2014). In winter, the difference between mean temperature on the northern coast and the southern coast can be greater than 30°C (Cappelen et al., 2014) with temperature along the coast normally ranging from -23°C to 0°C (Hanna et al., 2012) (Figure 2.3). During the warm season the difference reduces and mean temperature is above zero almost everywhere on the coast (Hanna et al., 2012).

Often, melting occurs in the lower elevation regions of the Ice Sheet during summer from May until September (Stendel, 2019). Conversely, the altitude and high albedo in the central part, impede the air temperature from rising above 0°C even in summer, resulting in values that can reach -60°C during winter (Cappelen et al., 2014). Clear skies favour low temperatures due to radiative cooling of the ice surface at higher altitudes, with consequent temperature inversion. This produces katabatic winds, where the cold and dense air masses, accumulated at the surface of the higher elevation areas of the ice sheet, move because of gravity from interior towards the margin of the GrIS (Cappelen et al., 2014). Finally, winds coming from intense cyclonic

activity in the North Atlantic and Baffin Bay usually affect the southern and western part of Greenland, with a northern shift during summer (Cappelen et al., 2014).

The central north-eastern area is the driest region of Greenland, with annual average precipitation value around  $130 \text{ mm yr}^{-1}$ . Conversely, the highest precipitation amounts are found in the southern part, especially along the coast, reaching a value of  $2000 \text{ mm yr}^{-1}$  in the extreme south-east (Ohmura, 1999; Hanna et al., 2006; Berdahl et al., 2018). Overall, Bromwich et al. (1998) found an annual mean precipitation over the entire GrIS of  $358 \text{ mm yr}^{-1}$ , which is an average value of different reanalysis and time periods considered, ranging from 1958 to 1996. Despite Global Warming, this average value of precipitation has not undergone significant changes (Van den Broeke et al., 2016).

The sea currents around Greenland are the result of the interaction between the surface winds and the North Atlantic branch of the thermohaline circulation driven by the variation in density of the water masses due to different temperature and salinity (Rahmstorf, 2003). As a result of the Coriolis force and the temperature gradient between the Equator and the North Pole, the south-western warm current of the North Atlantic Ocean flows superficially until it reaches the Norwegian/Greenland Sea and Arctic Ocean (Buckley & Marshall, 2016). At these latitudes the current cools and due to its greater salinity than the surrounding water it sinks in the Arctic Ocean and in the seas north-east of Greenland. Here, the deep polar water flows like a cold, icy current southward along the south-east coast of Greenland reaching the west coast and Baffin Bay or moving southward into the Atlantic Ocean (Cappelen et al., 2014).

As indicated by the last IPCC AR6 WG1 a decline of this circulation is very likely in all SSP scenarios, with a moderate to high rate of Greenland melting that could weaken this circulation in the North Atlantic and partially dampen the effect of global warming at these high latitudes in the next two centuries (Bakker et al., 2016). Conversely, as argued by a recent work (Lenaerts et al., 2015) the future slowdown is dominated by warming of the surface oceans with enhanced GrIS freshwater forcing playing a minor role. Overall, this flow of currents is part of the Atlantic Meridional Overturning Circulation (AMOC) which affects the entire Atlantic Ocean.

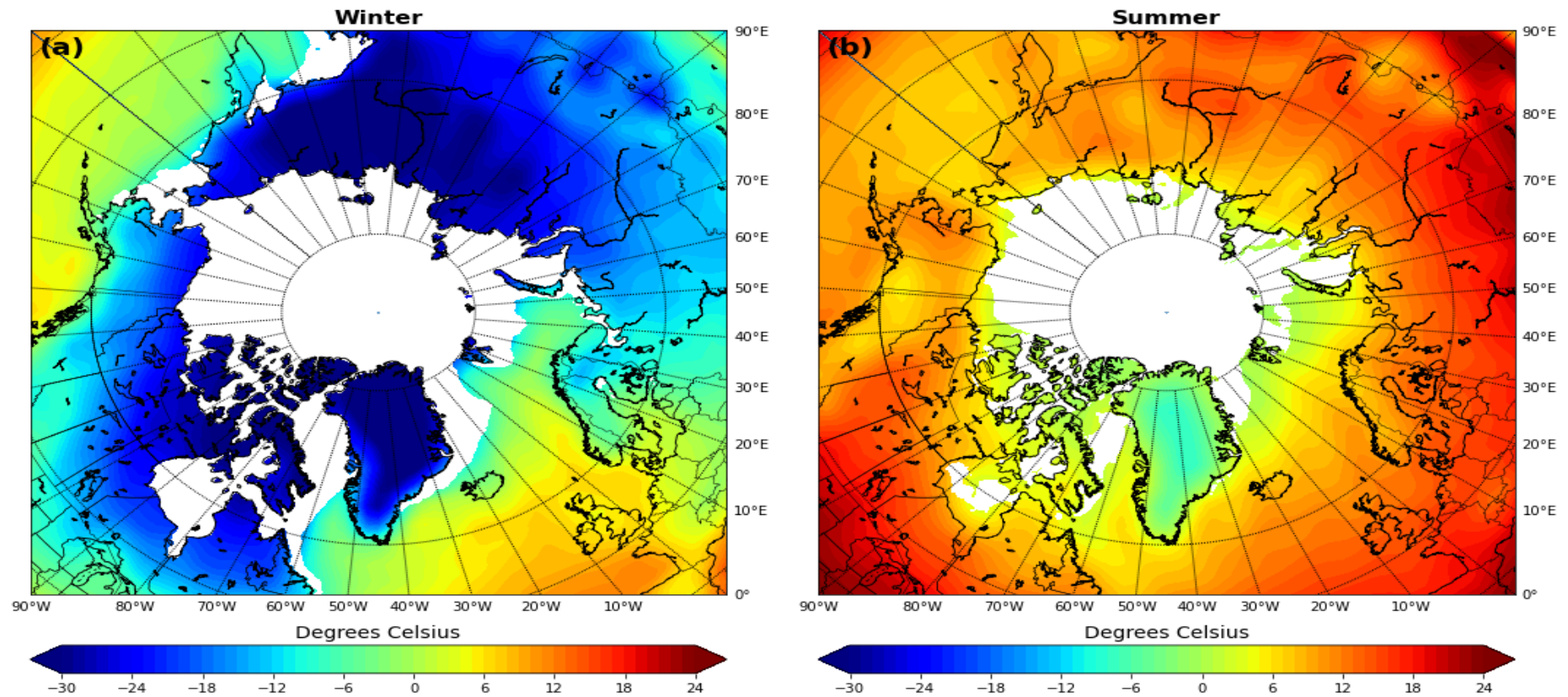


**Figure 2.3.** Average temperature at .995 sigma level in winter (a) and summer (b) from NCEP-NCAR 1 reanalysis (Kalnay et al., 1996) and ice cover from NSIDC (Walsh et al., 2015) during the climatological period 1986-2015. Only ice concentration above 50 % is shown.

## 2.2. Mass balance

### 2.2.1. What is Mass Balance?

The mass balance of a glacier or an ice sheet is simply the gain and loss of snow and ice from the glacier system during a glaciological year (running from 1st October in one year to 30th September of the following year for the GrIS). Ice sheet mass balance ( $MB$ ) expressed in  $Gtons\ yr^{-1}$  is controlled by the difference between mass gain or loss at the surface via surface mass balance ( $SMB$ ) and mass lost from solid ice discharge ( $D$ ) where it terminates into the sea, integrated over a glaciological year (Cuffey & Paterson, 2010; Chen et al., 2016; Van den Broeke et al., 2017)

$$MB = SMB - D \quad (1.1)$$

Considering the total mass balance, the  $SMB$  indicates only the contribution on the surface of the GrIS, excluding mass lost via icebergs and melt where glaciers meet the seawater.

### 2.2.2 Surface Mass Balance

To reconstruct the surface ice sheet mass change during a glaciological year it is of fundamental importance to break down and understand the physical processes that govern this system. The  $SMB$  is the balance between accumulation and ablation (i.e. snow/ice input versus output) consisting in the sum of all sources and losses of mass from the surface to the firn/ice/snow interface (Cuffey & Paterson, 2010; Van den Broeke et al., 2016; Van den Broeke et al., 2017):

$$SMB = P - SU - ER - RU \quad (1.2)$$

Where  $P$  is total precipitation (both solid as snow and liquid),  $SU$  is the total sublimation,  $ER$  is erosion of surface snow by wind, and  $RU$  is runoff of water outgoing from the ice sheet. The area with a positive  $SMB$  during a glaciological year is the accumulation zone whereas the area with a negative  $SMB$  is called the ablation zone. These two zones are separated by the equilibrium line altitude (ELA) where

$SMB = 0$  (Van den Broeke et al., 2016). Subsequently to calculate the runoff balance we have to break down all the components involved in the liquid water balance as follow (Van den Broeke et al., 2016; Van den Broeke et al., 2017):

$$RU = RA + CO + ME - RT - RF \quad (1.3)$$

Where  $RA$  is rainfall,  $CO$  is condensation vapour at the surface,  $ME$  is the meltwater production and  $RT$  and  $RF$  are, respectively, the retention and refreezing of liquid water in the firn or snow.  $CO$  and  $ME$  are related to Surface Energy Balance (SEB) that summarises the contribution of all energy fluxes towards and away from the ice sheet.

Meltwater is the primary source for loss of ice/snow via runoff and results when the surface energy balance (SEB) is positive (directed to surface) and the surface is at  $0^{\circ}\text{C}$ . The meltwater energy is the result of the SEB factors that can be summarized (Van den Broeke et al., 2017):

$$M = SW_{in} + SW_{out} + LW_{in} + LW_{out} + SHF + LHF + G_f \quad (1.4)$$

$$M = SW_{net} + LW_{net} + SHF + LHF + G_f \quad (1.5)$$

Where  $M$  is usable energy for melt,  $SW_{net}$  and  $LW_{net}$  are net shortwave (solar shortwave ingoing  $SW_{in}$  minus reflected  $SW_{out}$ ) and net longwave (long wave ingoing  $LW_{in}$  minus outgoing  $LW_{out}$  from the atmosphere/snow/ice) radiation fluxes. Sensible heat fluxes ( $SHF$ ) and latent heat fluxes ( $LHF$ ) are determined by the difference between surface and air temperature and humidity at 2 metres above the surface along with winds, atmospheric turbulence, surface roughness. Finally,  $G_f$  representing the heat flux from the ground.

Seven years of radiation observation at the surface of the GrIS, covering the period September 2003 - August 2010, was carried out by van den Broeke et al. (2011) with the use of three Automatic Weather Stations (AWS) located in the ablation zone of the west Greenland at 6 (S5), 38 (S6) and 88 (S9) km from the ice sheet margin at elevation of 490, 1020 and 1520 m.a.s.l. The most important source for ice melting at all 3 sites was the positive  $SW_{net}$ . This depends on solar radiation scattering and

absorption in the clear atmosphere, scattering and absorption due to clouds and multiple scattering between surface and clouds along with surface reflection (albedo) (Van den Broeke et al., 2008). The thinner atmosphere, along with a decrease relative humidity owing to lower temperatures that limit the atmospheric moisture content (van den Broeke et al., 2011) transmits more  $SW_{in}$  radiation at higher altitude. Conversely, in the lower ablation zone, the relative dark glacier ice exposed throughout summer and caused by the early (late) melt season due to a higher temperature, leads to low albedo values, permitting higher peaks in  $SW_{in}$  absorption.

Based on work of van den Broeke et al. (2011),  $SW_{net}$ , is maximum between June and July reaching a peak of  $120 \text{ W/m}^2$  over the low ablation region and  $80 \text{ W/m}^2$  at the equilibrium line at S9 in the west Greenland (Van den Broeke et al., 2008). The second source of energy comes from  $SHF$  whose magnitude and sign are determined, as mentioned before, by a number of factors including difference between surface and air temperature, surface roughness, winds and atmospheric turbulence. In the lower ablation zone, it can reach a value of  $70 \text{ W/m}^2$  in summer due to a higher air temperature carried by warm air coming from tundra (Van den Broeke et al., 2009). Conversely, at higher altitudes, the highest values are registered in late winter due to radiative cooling of the snow at the surface (Van den Broeke et al., 2009). At the annual scale,  $LHF$  is almost always slightly negative (favouring sublimation) and it can be just above zero (favouring deposition) during summer, where relative humidity of the air at ice sheet margins can be higher than at the surface. Finally,  $LW_{net}$  is always negative in the ablation zone in western region of the ice sheet during all seasons. This is due to values of  $LW_{out}$  emitted by snow/ice that are almost always greater than  $LW_{in}$  coming from clouds and moisture in the lower atmosphere. As shown by Van den Broeke et al. (2008), at all sites it reaches a negative peak of  $-50 \text{ W/m}^2$  in late spring due to snow heating in contrast with cold and dry air masses above the surface.

Overall, considering all the energy fluxes from and towards the ice surface, in the lower ablation zone the melt season usually starts at the end of April whereas May marks the start of the melt season in the middle to higher ablation zone. As pointed out by van den Broeke et al. (2011) the average seasonal cycle of melt as well

as inter-annual melt variability is mainly driven by absorption of shortwave radiation; an exception is the lower ablation zone, where the turbulent fluxes of sensible and latent heat contribute significantly to the melt energy.

### **2.2.3. Ice Motion and Terminating Environment of Glaciers**

Glaciers ice motion is a result of a number of factors including valley geometry (steepness), glacier geometry (thickness) and properties (temperature, density), bedrock condition, subglacial hydrology and terminal environment (land, sea, sea ice) (Cuffey & Paterson, 2010). It plays a crucial role in GrIS mass balance, especially at its margins where marginal ice flow can drag inland ice downstream and lead to ice thinning both via dynamic thinning and exposure of the ice to higher temperatures and greater ablation towards lower elevations and ice discharge (Davison et al., 2019).

Ice moves with a shear stress parallel to the surface due to gravity under the thrust of its own weight. It is controlled by the slope and hampered by basal drag and lateral drag of surfaces of the valley through friction. Glacier flow is the result of three different processes that can act individually or simultaneously as follows: 1) ice deformation, 2) basal sliding at the bed-ice interface due to the presence of meltwater and 3) soft bed subglacial deformation (Cuffey & Paterson, 2010).

In glaciers without or with negligible meltwater at the base, ice movement is mainly due to ice or bed deformation. The permanent ice deformation occurs as a result of strain in response to stress and in a substance such as ice can take two forms, creep and fracture (Placidi et al., 2006). The two main factors that govern these mechanisms are respectively the structure of an ice crystal and movement/interactions of different ice crystals in polycrystalline aggregate of ice. Generally, fractures occur when a glacier cannot creep fast enough under the stress applied and crevasses are the most evident result of this process of permanent ice deformation. Focusing on the glacier's bed, deformation occurs due to the fact that it is often not characterised by hard impermeable bedrock but by unconsolidated, unsorted or poorly sorted subglacial sediments ranging from boulders to clay known as till, the deformation of which can result in ice motion (Cuffey & Paterson, 2010).

For glaciers with large volumes of meltwater under pressure at the ice-bed interface it represents the primary factor affecting the velocity of the ice flow (Nienow et al., 2017). In Greenland the most important source of liquid water is the meltwater produced at the surface during the melt season and this can penetrate into the GrIS reaching the bed through the hydrological system (see information on supraglacial and englacial hydrological system in section 2.4.2). If the meltwater in the subglacial environment is under pressure at the ice-bed interface, it facilitates decoupling and enhanced ice flow through a mechanism called basal sliding (Bartholomew et al., 2012; Nienow et al., 2017). This mechanism as well as being controlled by the amount of meltwater reaching glacier bed, is also regulated by subglacial drainage structure (Fountain & Walder, 1998; Chu, 2013; Nienow et al., 2017). See section 2.4.3 for further detail on subglacial drainage.

Apart from the water in the subglacial drainage system, the terminus environment of the glacier also plays a fundamental role in ice motion. Glaciers can terminate on land (land terminating) or into the sea (marine terminating). They have different characteristics due to their terminating environment which contribute to their ice flow regime and mass balance (Cuffey & Paterson, 2010).

Land terminating glaciers are laterally bounded by valley walls and their mass balance depends on climate and ice motion towards lower and warmer margins of the GrIS, with some dry or lacustrine ice calving at the terminus (Diolaiuti et al., 2004; Trüssel et al., 2013). They gain mass in the accumulation zone and lose mass in the lower elevation ablation zone due to sublimation and runoff of surface meltwater. On average, their ice flow is lower if compared to tidewater glaciers, because the terrestrial terminating environment exerts greater friction at the bed than a marine environment (Cuffey & Paterson, 2010). In addition to lateral moraines, they are characterized by frontal moraines of lodgement till (unsorted glacial sediment) resulting from glacial soil erosion during the advance of the glacier and this often leads to the development of a periglacial lake into which the glacier meltwater flows (Cuffey & Paterson, 2010). Overall, the velocity of the GrIS peripheral land terminating glaciers is mainly determined by the amount of meltwater that reaches the glacier bed which varies depending on the season. A speed up during summer

due to a large amount of water reaching the subglacial drainage system favouring basal sliding, is followed by a slowdown during winter months, where the presence of meltwater is negligible (Davison et al., 2019).

Marine terminating glaciers are surrounded and constricted by valley walls that end in a fjord, where they discharge icebergs to the sea or ocean under the process of calving. The resulting fronts can be totally grounded on the sea floor, or seen as a floating extension, which can be an ice tongue or ice shelf. For marine terminating glaciers, the position of the conversion of grounded to floating ice is denoted as the grounding line (Haeberli & Whiteman, 2015). In addition to the meltwater reaching the bed, ice motion of the terminal part of tidewater glaciers is governed by the interaction of their termini with sea currents/sea temperature, sea ice concentration and bathymetry of the fjords through a mechanism explained in detail in section 2.4.4.

#### **2.2.3.1. Ice Discharge**

Ice discharge is one of the most important factors affecting mass balance of an ice sheet. It represents between a third and a half of ice loss from the GrIS (Benn et al., 2017). This is governed by the submarine melting and breakaway of icebergs (ice calving or dynamic ice loss) at the terminal region of valley glaciers which terminate in fjords (Enderlin et al., 2014) and are sometimes characterised by a floating ice tongue extending far away from the grounding line (Joughin et al., 2012; Benn et al., 2017). These processes together are commonly known as frontal ablation (Truffer & Motyka, 2016) and are quantified by calculating ice discharge through a glacier's cross section (Rignot & Kanagaratnam, 2006; Mouginot et al., 2019; King et al., 2020). Ice calving and submarine melting are influenced by many factors such as geometric characteristics of the fjords which influence the water circulation along with its interaction with surface meltwater runoff at the base of the glacier reaching the tongue (Chu, 2013). Due to the uniqueness of each individual fjord and difficulties in modelling ice discharge, behaviour of these tidewater glaciers is not fully understood and is difficult to predict (Benn et al., 2017).

## **2.2.4. Past, Present and Future of the GrIS Mass Balance**

### **2.2.4.1. Mass Balance Calculation Methods**

The most common method to calculate mass balance is the Mass Budget Method (MBM) (Mohajerani, 2019). However, during the last few decades, due to an increase of satellite technologies, new methods such as gravimetry and radar and laser altimetry were used to assess the mass balance of the GrIS. Each method has distinct advantages and disadvantages as detailed below.

The GRACE (Gravity Recovery and Climate Experiment) dual-satellite mission has surveyed the Earth's time-variable gravity field (IPCC, 2013). If applied to the Greenland region, gravity observation, once corrected and deconvolved, provide a direct estimate of the ice-mass change. However the methodology has two main limitations which are; 1) the brevity of the time series and 2) the coarse resolution with a spatial footprint  $\sim 200\text{km}$  (Van den Broeke et al., 2016).

Radar and laser altimetry data from satellites and aircraft cover a longer temporal range, starting from mid-1980s. Both techniques measure surface-elevation changes which must be converted to mass change. As with the gravity methodology, these two techniques are also affected by some drawbacks. Snow density and wetness play a key role on the penetration of radar signal into the snow pack and especially in the firn, affecting the measurements and introducing uncertainties (IPCC, 2013). Moreover, this technique is not suitable for study along the steep coastal margins of the GrIS where the signal appears weak and inconsistent due to the large footprint of the radar altimeter. Conversely, laser altimeter estimates are not affected by this problem, since the rapidly changing terrain in steep slope areas is better resolved by its smaller footprint. It has been used from aircraft for many years, until the launch of NASA's ICESat satellite in 2003 which has provided for the first time, data with footprint around 17 metres. Limits of this technique are being sensitive to cloud cover and records must be intercalibrated and spatially interpolated due to large ground track separation before obtaining satisfying results (Van den Broeke et al., 2016). Finally, both radar and laser altimeters measure the

change in elevation which can be converted to volume change and then used to calculate mass change and this generates another source of additional uncertainties.

Gravity and altimetry methods do not allow partitioning of mass loss into SMB and ice discharge. If this is required, the MBM can be used. The surface mass balance is calculated from regional climate models (Hanna et al., 2011; Box, 2013; Fettweis et al., 2017; Mottram et al., 2017) coupled with a snow module able to reproduce mass and energy exchanges on the surface of the ice sheet. Subsequently the dynamic mass loss, breakaway of icebergs (ice calving) and submarine melting (Box & Colgan, 2013), at the terminal regions of tidewater glaciers, are quantified and subtracted from the surface mass balance in order to obtain the net mass balance. The method adopted to calculate ice discharge is based on calculation of ice flux across a gate which is normally located at the grounding line of each glacier into the fjord. The main parameters involved in calculation of this flux across the gates are ice density along with ice velocity and thickness derived from satellite data (IPCC, 2013).

Although the MBM allows resolution of each component of mass balance, as the mass change represents a relatively small difference between three large source and sink terms, it is very sensitive to uncertainties in these. This is especially true for surface mass fluxes such as snowfall and meltwater runoff; because these cannot be accurately measured from space, they must be interpolated from scarce in situ measurements and/or simulated using dedicated regional climate models, which introduces potentially large uncertainties (Vernon et al., 2013).

#### **2.2.4.2. Past and Present GrIS Mass Balance**

Because of limited spatial coverage of ice cores and observations (Van den Broeke et al., 2017) much work has focused on MBM method, using the regional climate models to model energy and mass fluxes in order to obtain the surface mass balance (Hanna et al., 2011; Box, 2013; Fettweis et al., 2017; Mottram et al., 2017). However, because of uncertainties and divergences due to few in situ observations and discordant reanalysis, it's not possible to accurately depict the evolution of surface mass balance prior to 1950, although raw but concordant estimates have been obtained (Van den Broeke et al., 2017).

Prior to 1960 the annual surface mass balance remained positive through time with values between  $500 \text{ Gt yr}^{-1}$  and  $400 \text{ Gt yr}^{-1}$  although the values are approximated. In this period a slight decline is detected between 1920 and 1940 and around 1960 due to an important increase in surface temperature over the Greenland area (Box, 2013), associated with higher values in runoff and decrease in precipitation. From 1960 to 1990 all models are in agreement, with a positive surface mass balance between  $400 \text{ Gt yr}^{-1}$  and  $450 \text{ Gt yr}^{-1}$ .

A strong increase in melt and runoff has been observed since mid-1990s, during JJA, associated with higher temperature and clear sky due to a persistent anticyclonic weather regime over Greenland (Fettweis et al., 2010; Belleflamme et al., 2012; Box et al., 2012; Overland et al., 2012; Fettweis et al., 2013b; Hanna et al., 2014; Chen et al., 2016; Tedesco & Fettweis, 2020) described in section 2.3.2.1. As a consequence, the GrIS, during the last two decades has experienced a general decrease in albedo and summer snowfall (Box et al., 2012; Tedesco & Fettweis, 2020) along with a series of surface meltwater runoff records, reaching a summer average around  $400 \text{ Gt yr}^{-1}$  with peaks of  $600 \text{ Gt yr}^{-1}$  in 2012 and 2019 and consequent SMB around zero (Ettema et al., 2009; Box, 2013; Fettweis et al., 2017; Mottram et al., 2017; Van den Broeke et al., 2017; Tedesco & Fettweis, 2020).

Recent studies (Enderlin et al., 2014; Van den Broeke et al., 2016; Van den Broeke et al., 2017) focused on GrIS confirm, after 40 years of relative stability, the rapid increase in ice discharge from a value around  $410 \text{ Gt yr}^{-1}$  to  $550 \text{ Gt yr}^{-1}$  between 2000 and 2020 (Mouginot et al., 2019; King et al., 2020). This increase of ice discharge during the last twenty years has been attributed to a period of rapid atmospheric and oceanic warming causing an acceleration and a widespread retreat of glaciers terminating into the fjords, especially along the south and western coast of the GrIS (Straneo et al., 2013; Catania et al., 2020; King et al., 2020). Here, a widespread and near synchronous glacier retreat suggests that tidewater glaciers are sensitive to both atmospheric and oceanic forcing through the factors mentioned in section 2.2.3 and which processes are detailed in section 2.4.4 (Straneo et al., 2013; Benn et al., 2017).

Combining surface mass balance and ice discharge, after 30 years (1960-1990) of slightly positive values, mass balance has experienced a decline in recent decades (Ettema et al., 2009; Box & Colgan, 2013; Fettweis et al., 2017; Mottram et al., 2017; Van den Broeke et al., 2017; Mouginot et al., 2019). Considering the period 1991-2015, 61 % of the increased mass loss can be attributed to decrease in SMB and the reminder to increase in ice discharge (Van den Broeke et al., 2017). Analysis of surface elevation and mass changes from Cryosat-2 and GRACE satellite confirm this decline, showing how the Greenland Ice Sheet had a net annual mass balance around  $-228 \text{ Gt yr}^{-1}$  during the period 2002-2010 (Sasgen et al., 2012) and  $-286 \text{ Gt yr}^{-1}$  for the period 2010-2018 (McMillan et al., 2016; Mouginot et al., 2019; King et al., 2020).

#### **2.2.4.3. Future GrIS Mass Balance**

In a global warming scenario, all the components which contribute to the GrIS mass loss are predicted to increase at a rate greater than precipitation due to increased temperatures in the Greenlandic region (Schuenemann & Cassano, 2010). Future projections of temperatures are obtained from global climate models (GCMs) forced in sixth Assessment report (AR) of the IPCC (Masson-Delmotte et al., 2021) by one set of scenarios called Shared Socioeconomic Pathways or SSPs. They are an update of the one set of scenarios used in the fifth AR of the IPCC call representative concentration pathways (RCP) of Greenhouse Gases (GHG) which describe different climate futures, depending on the volume of GHG emitted in the years to come and labelled in a possible range of radiative forcing values in the year 2100 that are respectively 2.6, 4.5, 6.0 and  $8.5 \text{ W m}^{-2}$ . The SSPs add to RCP scenarios socio-economic narratives, taking into account many parameters such as population growth, technological and economic growth, GDP and energy use. In increasing order of radiative forcing, they are respectively SSP1-1.9, SSP1-2.6, SSP2-4.5, SSP3-7.0 and SSP5-8.5 with the first (latter) predicting a global increase of temperature above pre-industrial level at the end of the century around  $1.5^\circ\text{C}$  ( $4.4^\circ\text{C}$ ).

A general agreement among the models forced by SSP5-8.5 shows a warming in 2080-2099 (relative to the 1980-1999) to be between  $3.3^\circ\text{C}$  and  $5.7^\circ\text{C}$  at global scale while between  $6.2^\circ\text{C}$  and  $15.2^\circ\text{C}$  in the Arctic due to Arctic Amplification

phenomenon. In this warmer climate, precipitation is projected to increase in all models over Greenland in a range between 14-24 % where liquid precipitation will increase slightly by more than solid precipitation (Masson-Delmotte et al., 2021). However, this slight increase in solid precipitation will not offset melt and runoff, for which a three-fold increase for the worst emission scenarios is predicted (Fettweis et al., 2012; Rae et al., 2012; Mottram et al., 2017). As projected by regional climate models, the surface mass balance trend is going to be consistently below zero around 2050, reaching the value between  $-200 \text{ Gt yr}^{-1}$  and  $250 \text{ Gt yr}^{-1}$  ( $-850 \text{ Gt yr}^{-1}$  and  $1200 \text{ Gt yr}^{-1}$ ) over 2080-2099 for the SSP1-2.6 (SSP5- 8.5 scenario) (Goelzer et al., 2020) with a consequent SLR of about  $6 \pm 4 \text{ cm}$  ( $13 \pm 4 \text{ cm}$ ).

Focusing attention on different GrIS regions, two studies conducted by Fettweis et al. (2012) and Goelzer et al. (2020) reveal that the northern and north-eastern drainage basins of the GrIS will be the regions most affected by increases in temperature during the next century. The authors suggest this might be the consequence of the local warming induced by the Arctic Sea ice cover reduction. However, due to its lower elevation and hence temperatures closer to the melting point, the south-west region is the area with the highest projected surface mass balance loss. The multi-model-average indicates a trend for the south-west region of around  $-40.59 \text{ Gt yr}^{-1} \text{ } ^\circ\text{C}^{-1}$  in RCP4.5 scenario and  $-68.27 \text{ Gt yr}^{-1} \text{ } ^\circ\text{C}^{-1}$  in RCP8.5 reaching a value of  $-250 \text{ Gt yr}^{-1}$  at the end of 21<sup>st</sup> century. This region is followed by the northern and south-eastern regions, where the maximum projected surface mass balance anomalies are respectively  $-200 \text{ Gt yr}^{-1}$  and  $-150 \text{ Gt yr}^{-1}$  for the RCP 8.5 scenario. Taking into account the negative trends of surface mass balances, the results obtained in these studies indicate a cumulative contribution to SLR by the end of this century of between 1 and 4 cm for the south-west basin, and up to 2 cm for northern basins, whereas the contribution of other regions of the ice sheet doesn't exceed 1 cm.

Along with future surface mass balance negative anomalies, ice discharge is likely to contribute to the GrIS decline and SLR. Although difficulties in modelling frontal ablation remain one of the main challenge in quantifying the future contribution of Greenland outlet glaciers to SLR much progress has been made

(Catania et al., 2020). In a recent study of Nick et al. (2013), a glacier flow model that includes a fully dynamic treatment of marine termini is used to simulate behaviour and ice discharge in the 21<sup>st</sup> and 22<sup>nd</sup> century, of four marine-terminating glaciers which collectively drain about 22 % of the entire GrIS under a mid-range (A1B) and extreme future warming (RCP 8.5) scenarios. The ice lost from these glaciers during a glaciological year, is within the range 30-47  $Gt\ yr^{-1}$  for the first century and 34-54  $Gt\ yr^{-1}$  for the second century under A1B scenario, with a two-fold increase under RCP 8.5 scenario and a consequent cumulative SLR ranging from 8.5 mm (18.6 mm) to 17.5 mm (49 mm) by 2100 (2200). Since the loss of ice of these four glaciers represent roughly a fifth of the total, the authors reach the conclusion that the predicted SLR from dynamics changes, considering the entire GrIS, lie in a range between 40-85 mm by 2100. These values are consistent with those obtained by Price et al. (2011) that estimates an upper bound of 45 mm by the end of 21<sup>st</sup> century due to ice calving.

Along with warmer oceans and reduction of Arctic Sea ice, a positive trend of ice calving and submarine melt in the next decades, can be attributed to a general increase in runoff (and subsequent increase of subglacial water at the grounding line) and its interaction with seawater as detailed in section 2.4.4. Despite recent improvements in monitoring and understanding the subglacial hydrology and interaction with ice calving and submarine meltwater in marine-terminating glaciers (Straneo et al., 2013), it is not possible to predict with certainty their future behaviour in response to climatic and oceanic forcing (Benn et al., 2017). Further efforts are necessary to enable a understanding of the physical processes that govern ice-ocean boundary layer, plume dynamics along with a development of detailed models with simple but robust calving laws (Straneo et al., 2013) and a good knowledge of fjords bathymetry to obtain a successful modelling of fjord circulation (Straneo et al., 2013; Benn et al., 2017).

## **2.3. Atmosphere-GrIS Interactions**

### **2.3.1. Introduction**

The mass balance of the GrIS is very sensitive to atmospheric forcing (Fettweis et al., 2013b), with Hanna et al. (2013, 2014) highlighting that the recent sharp decrease of the GrIS SMB can be primarily attributed to it, with the ocean playing a minor role. To help understand GrIS response to atmospheric forcing, much work has focussed on the relationship between climatic indices which describe the state of the atmosphere in or near the Greenlandic region and GrIS surface mass balance.

In the following sections, after a brief description of the global atmospheric circulation and its dynamics at mid/high latitudes, the anticyclonic and cyclonic circulation will be discussed because they exert an important influence on the GrIS SMB mass balance. Subsequently, the climatic significance and use of North Atlantic Oscillation Index (NAOI) and Greenland Blocking Index (GBI) will be discussed, along with their ability to describe the atmospheric circulation in the North Atlantic and the Greenlandic region.

### **2.3.2. Jet-Streams and Large-Scale Atmospheric Circulations**

Atmospheric and oceanic transport processes distribute energy around the earth from region with a surplus of radiation (low latitudes) towards regions with a deficit (high latitudes). Observations of the poleward heat transport of the earth indicate that the atmosphere is the primary transporting agent poleward of 30° (Trenberth & Caron, 2001). At 35° latitude, in which the peak total poleward transport in each hemisphere occurs, the atmospheric transport of energy accounts for 78 % of the total in the Northern Hemisphere and 92 % in the Southern Hemisphere (Czaja & Marshall, 2005).

The atmosphere's circulation is driven by solar energy, which heats the Earth's surface with variable intensity (decreasing from the Equator to higher latitudes), and the Earth's rotation. As a consequence of these two factors, air masses circulate to redistribute heat poleward via the Hadley, Polar and Ferrel cells in each hemisphere (Giuliaci et al., 2010). The Hadley cell is thermally direct, with its ascending branch marked by the intertropical convergence zone. The rising air reaches the upper limit of the troposphere and moves towards the tropical belt around 30° north and south. Here, owing to Coriolis force and the conservation of angular momentum, the winds

accelerate eastward, generating the Subtropical Jet Stream. Here they descend below the Subtropical Jet due to radiative cooling and upper-level convergence (Pauluis et al., 2010; Stachnik & Schumacher, 2011; Huang & McElroy, 2014). Conversely, in the Polar Cell, located between 90°N and 60°N, air subsides due to strong radiative cooling and diverges at lower levels (Pauluis et al., 2008).

The result of the interaction between warm air from the Hadley Cell, and cold air from the Polar Cell, is the third (passive) Ferrel Cell. Poleward winds in the Ferrel Cell are deflected east due to the Coriolis force. The Polar Front is the boundary between warm tropical air and the colder higher-latitude air. Here, the strong horizontal temperature gradient translates into a poleward pressure gradient which amplifies with height in the troposphere. The result is the Polar Front Jet Stream (Giuliaci et al., 2010). This is known as a narrow, high speed wind that generally flows from west to east at the top of the troposphere (Archer & Caldeira, 2008). This narrow band undergoes a latitudinal shift during the year. An increase (decrease) in solar irradiation in the Northern Hemisphere during summer (winter) favours a poleward (equatorial) shift of the Polar Front Jet Stream due to a weakening (strengthening) of the polar cell and strengthening (weakening) of the Hadley Cell.

The weather in the middle and high latitudes depends on the behaviour of the Polar Front Jet Stream (see section 2.3.2.1 and 2.3.2.2 for more information). For this reason, interest has grown regarding the behaviour of the Hadley cell and related Polar Front Jet under climate change. For example Hu et al. (2013) and Tao et al. (2015) used simulations of the Coupled Model Intercomparison Project Phase 5 (CMIP5) to conclude that the Hadley Cell expands increasingly poleward as radiative forcing increases. Consistent with this response, a poleward shift of the Polar Front Jet Stream (Pena-Ortiz et al., 2013) along with its weakening has been detected in recent decades as the global climate has warmed, although a recent study of Overland et al. (2012) detected a momentary equatorward movement of the Polar Front Jet Stream in early summer during the period 2007-2012.

During the last decades observational studies have indicated that near surface air temperature in the Arctic has increased twice as fast as the global mean rate (Masson-Delmotte et al., 2021). Since the Polar Front Jet is a thermal wind that arises

due to temperature contrast between cold polar air and warm tropical air, the stronger the temperature gradient is, the stronger the Polar Jet Front. Weakening of the gradient due to Arctic amplification should therefore be expected to result in slower westerlies, and hence reduce the speed at which Rossby waves propagate eastward. In turn this may increase the persistence of weather types which are tied to the circulation within the waves' ridges and troughs (Dunn-Sigouin & Son, 2013). For example, persistence of the upper-level ridges can lead to protracted heat and drought events in summer forced by subsidence in anticyclones (Dunn-Sigouin & Son, 2013; Barnes et al., 2014); persistence of troughs can lead to severe flooding triggered by extratropical cyclones (Mohr et al., 2019; Walsh et al., 2020). However, research to date has not detected any weakening of the Polar Front Jet Stream during the period 1979-2018 (Blackport & Screen, 2020b; Blackport & Screen, 2020a) albeit an increase of blocking events over the North Atlantic in the recent decades (Hanna et al., 2015; McLeod & Mote, 2016). Overall, experiments suggest that the response of the Polar Front Jet Stream to Arctic amplification is far from being robust, and its expected changes under continued warming remains poorly understood (Meleshko et al., 2016).

Summarizing, the meanders of the Polar Front Jet Stream modulate the weather in the middle and high latitudes, characterised by specific large scale atmospheric circulations with different characteristics. Anticyclonic flow represents the ridges while the cyclonic flow is experienced in the troughs of the Polar Front Jet Stream at upper levels. The positions of these circulation types play a key role in determining the type of weather phenomena at the lower-level of the atmosphere.

### **2.3.2.1 Dynamic Anticyclones**

Among the different atmospheric circulation regimes, dynamic anticyclones are one of the most important circulation types. They are called dynamic due to continuous movement of air masses related to general circulation of the atmosphere. It is possible to subdivide dynamic anticyclones into upper and lower-level types. Upper-level anticyclones diagnose regions of high pressure aloft, which are co-located with warm columns of air because the rate at which pressure drops with altitude is

inversely related to its temperature (Giuliaci et al., 2010). Conversely, lower-level anticyclones are formed below downstream of ridges, where due to flow deceleration, air masses converge at upper levels, driving divergence (high pressure) at the surface (Giuliaci et al., 2010).

From a meteorological point of view, lower-level anticyclones are large-scale circulations of subsiding, warm and dry winds rotating clockwise around a centre of high surface pressure in the North Hemisphere, due to the pressure gradient (directed radially outward) and the Coriolis Force (Giuliaci et al., 2010). Subsidence can bring surface pressure to around 1020 hPa and from which the adjective "dynamic" assigned to these anticyclones comes from (Brunt, 2011).

Semi-permanent anticyclones are found in the sub-tropics, corresponding to the location of the Hadley Cell's descending limb. Within anticyclones, winds are light and skies are usually relatively clear. In the Northern Hemisphere they advect tropical air masses on their western flank (Fettweis et al., 2010; Fettweis et al., 2013b; Hanna et al., 2014). The recent and future expansion of the Hadley cell and consequent shift of anticyclones towards higher latitudes implies a poleward expansion of the anticyclonic subtropical belt, with a consequent tropospheric warming and increasing risk of extreme heat and drought in the mid and high latitudes (Hu & Fu, 2007; Russo et al., 2014; Spinoni et al., 2018)

Focusing on the GrIS, the simultaneous increase in frequency of anticyclonic conditions in the summer associated with a steady decline in mass balance (Belleflamme et al., 2012; Box et al., 2012; Fettweis et al., 2013b; Hanna et al., 2014; Hanna et al., 2015; Tedesco & Fettweis, 2020) shows how anticyclones strongly impact an ice sheet SMB acting mainly on SEB through three different mechanisms: (1) By advecting warm air to enhance the temperature dependent heat fluxes; (2) increasing the downward (and net) shortwave flux; (3) suppressing snowfall events. At the same time, a higher frequency of summer anticyclonic conditions have driven a warming in oceanic temperature around Greenland, favouring an increase in ice calving and subglacial melt of tidewater glaciers through processes described in section 2.4.4 (Catania et al., 2020).

### **2.3.2.2 Extratropical Cyclones**

Extratropical cyclones are large scale weather patterns in which air masses rotate counterclockwise (in the Northern Hemisphere) around a strong centre of low pressure. They form as disturbances along the Polar Front Jet Stream which is the “river”, on which synoptic storms grow and propagate (Barnes & Screen, 2015). The strong temperature gradient across the Polar Front serves as a reservoir of potential energy that is converted into kinetic energy. They have a primary role in determining the local weather being the major weather system producing precipitation over the GrIS (Chen et al., 1997). Their approach is characterised by an advection of moist and relatively warm air while during their passage an overcast sky delivers precipitation and is accompanied by strong cold winds. (MacCabe et al., 2001; Bengtsson et al., 2005; Mesquita et al., 2008; Zappa et al., 2013; Chang et al., 2016; Rinke et al., 2017).

Extratropical cyclones develop around a centre of low pressure at the ground. To make the central low pressure to develop it is necessary that above it in the high troposphere, a divergence area of air masses is greater than the convergence of the air masses on the ground. In the upper troposphere the divergence occurs in response to winds accelerating towards ridge crests of the Polar Front Jet Stream driven by the interaction between centrifugal, gradient and Coriolis forces. Once the centre of low pressure at the ground is driven by the divergence at high altitude, the air masses with different origin (polar and tropical) and characteristic, start converging and moving from the bottom to the top of the atmosphere, in the centre of low pressure, due to Coriolis and Gradient force. Around the centre of low pressure, these air masses start moving counter-clockwise towards each other due to Coriolis and Gradient forces, generating two contact areas between them called cold and warm front (Giuliaci et al., 2010).

When a cyclone is developed, cold air starts replacing warm air along the cold front that rises and cools adiabatically, generating intense precipitation (Brunt, 2011). Similarly, along the warm front, the warm air slowly flows up over the cold air, where it condenses and produces precipitation. Since the warm front propagates much lower (11 to 33 miles per hour) than the cold front (Brunt, 2011) the difference in propagation speeds between the two fronts allows the cold front to overtake the

warm front, reaching the status of occluded front. Here, the entire warm air mass is above the cold one. This is the start of cyclone's decay and dissipation that occurs within 1-2 days (Brunt, 2011).

The mean radius of an extratropical cyclone may vary between 300-400 km over the continents, to more than 900 km over the oceans and during both, winter and summer, the radius of cyclones is larger over the oceans in comparison to the continents (Rudeva & Gulev, 2007). Storm size and intensity (maximum depth in its centre) are smaller in the warm season (Gulev et al., 2001; Rudeva & Gulev, 2007) due to the weakening of the meridional temperature gradient and slowing of the upper atmosphere winds. They are one of the main drivers that contribute to the meridional atmospheric heat and moisture transport from mid-latitudes into the Arctic where Greenland lies (Rinke et al., 2017; Akperov et al., 2018), especially in autumn, winter and spring (Sorteberg & Walsh, 2008). They have a strong influence on the sea-ice retreat in a warming climate because their passage enhances longwave downward radiation, and leads to the advection of warm air, increasing sea-ice melting or retarded sea-ice growth in autumn and winter (Boisvert et al., 2016; Kim et al., 2017; Polar\_Portal, 2021). In turn sea-ice changes can impact cyclones behaviour by modifying their frequency and intensity (Rinke et al., 2013). Recent studies have shown how a reduced extent of Arctic ice in winter favour a warmer boundary layer (Valkonen et al., 2021). This coincides with changes in moisture content and temperature gradient with a decrease of vertical stability of the atmosphere, with transport of moisture aloft due to stronger convection favouring high levels of baroclinicity and then extratropical cyclones development (Koyama et al., 2017).

Moisture delivered by the extratropical cyclones represent almost 70 % of the entire potential precipitable water over the Arctic region (Sorteberg & Walsh, 2008) where they are the only source of precipitation (liquid and solid). This fresh water in the Arctic influences the salinity of the oceans (Sorteberg & Walsh, 2008) and land snow cover. In this context, although cyclones exert the most important influence on snow accumulation over Greenland, the complex GrIS topography also affects the dynamics of passing extratropical cyclones (Chen et al., 1997).

Cyclones impinging on the GrIS from the west can be blocked by the elevation of the Ice Sheet and decay in Baffin Bay or move north-eastward through Nares Strait to the Arctic Ocean (Chen et al., 1997). Cyclones approaching Greenland from the southwest can be divided by the ice sheet with a parent cyclone moving towards north-west of Greenland into Baffin Bay, and a new cyclone that redevelops off the southeast coast of Greenland (Chen et al., 1997; Rogers et al., 2004). Finally, cyclones that approach Greenland from the south but do not interact directly with the ice sheet, usually intensify as they pass through the Icelandic Low (IL) (Chen et al., 1997). In general, because of the topography of the GrIS, the largest precipitation events occur when a passing cyclone generates winds that are orographically uplifted by the edges of the GrIS where air raises and water condenses, favouring precipitation (Schuenemann et al., 2009).

The interaction between cyclones and the GrIS permits division of the ice sheet into five different regions, each with different precipitation characteristics (Bender, 1984; Chen et al., 1997; Bromwich et al., 1998; Ohmura, 1999; Hanna et al., 2006; Schuenemann et al., 2009; Berdahl et al., 2018). The first region is the north coastal region located to the north of 80°N. This is with the driest region, with a mean annual precipitation (MAP) of around 16 cm yr<sup>-1</sup> (Chen et al., 1997). Here, precipitation is much greater in summer than in winter (Chen et al., 1997) driven by a northward shift of the Polar Front Jet Stream (Chen et al., 2016). The most intense precipitation occurs when a low pressure, located in close proximity of the northern, north-eastern part of the GrIS, converges and drives upslope flow in the north coastal region, causing orographic precipitation (Chen et al., 1997).

Subsequently, according to the precipitation characteristics, the central region is divided into three sub-regions, which are the central west coastal region, central interior and central east coastal region (Chen et al., 1997; Hanna et al., 2006; Schuenemann et al., 2009). The east region has a MAP of approximately 18 cm yr<sup>-1</sup> (Chen et al., 1997). This area receives the highest amount of precipitation during summer and autumn when cyclone tracks extending northward through the Greenland Sea are more frequent. The cyclonic flow associated with these patterns results in onshore flow over the east coast of the GrIS, leading to considerable

precipitation totals (Schuenemann et al., 2009). The west and central interior regions receive the greatest precipitation during summer when more frontal cyclones come from Baffin Bay free of sea ice which favours their development and maintenance. However, while the total amount of precipitation on MAP on the west coast is around  $30 \text{ cm yr}^{-1}$  due to orographic enhancement, the central interior receives only  $16.7 \text{ cm yr}^{-1}$  as air masses are dried out on their passage across the ice sheet (Chen et al., 1997).

Finally, the southern region mostly lies below  $68^\circ\text{N}$ . Heavy snowfall and rainfall here drive MAP to  $2 \text{ m yr}^{-1}$  in the south east coast and  $1 \text{ m yr}^{-1}$  on the south west coast (Bromwich et al., 1998; Ohmura, 1999; Hanna et al., 2006; Schuenemann et al., 2009; Berdahl et al., 2018). The most significant precipitation events in this area occur when an extratropical cyclone is located in the Labrador Sea. Here, close to the southwest coast of Greenland cyclonic flow drives moist air onshore from the North Atlantic. Upon reaching Greenland, air is steeply uplifted leading to strong orographic enhancement of precipitation (Schuenemann et al., 2009). This flow configuration typically results when a cyclone approaches Greenland from the south-west and splits into two systems with different trajectories, which then affect the southern region on both sides of the GrIS.

As emphasized by Chen et al. (1997) and Bromwich et al. (1998), changes in cyclone position south of Greenland could have a completely different impact on precipitation. In particular, during a displacement of weak low toward Labrador Sea, enhanced precipitation falls over south Greenland and especially in the south-east thanks to a development of lee cyclones near the coast (Rogers et al., 2004; Schuenemann et al., 2009). Conversely, if the centre of the IL is farther east (near Iceland), precipitation events do not affect the GrIS. (Berdahl et al., 2018)

In addition to precipitation, cyclones can have a direct effect on SEB, increasing the albedo in the event of snowfall (Noël et al., 2015) enhancing incident longwave radiation through increasing the emissivity and temperature of the atmosphere, with the latter also amplifying the turbulent heat fluxes (Van den Broeke et al., 2009). Indeed periods of high meltwater generation along the east coast of the

GrIS have been shown to be driven by enhanced extratropical cyclone frequency over this region of the ice sheet (McLeod & Mote, 2016).

Similarly, McLeod and Mote (2015) underlined the key role of precursor cyclones (slow moving cyclones originated upstream, or to the west, of a block's central meridional axis at or prior the peak of blocking intensity) for intensifying Extreme Greenland Blocking Episodes (periods of extremely high pressure) over Greenland. It has been observed that the 500 hPa heights associated with extreme GBEs accompanied by precursor cyclones are significantly greater over Greenland if compared to those lacking a precursor cyclone with higher level of meltwater production. This is due to greater advection of southerly warm air masses, that contribute to raising of latent and heat flux and shortwave radiation under clear sky, especially in the south and west of the GrIS.

Overall, it is clear that cyclonic and anticyclonic weather types exert a fundamental control on GrIS mass balance. For this reason, much recent research has assessed whether climatic indices can be used to establish the accumulation, precipitation and melting rate over the entire GrIS or part of it. In the next section, the two main indices used to represent circulation regimes over the North Atlantic Ocean and their link to the GrIS SMB and SEB are discussed.

### **2.3.3. Climatic Indices**

#### **2.3.3.1. Description of the NAO and GB Indices**

The North Atlantic Oscillation (NAO) is the dominant mode of atmospheric variability in the Atlantic Region (Appenzeller et al., 1998; Visbeck et al., 2001; Hurrell & Deser, 2010). It represents the “seesaw” of atmospheric surface pressure fluctuation between the Azores and Iceland (Hurrell et al., 2003; Hanna et al., 2015). It is defined as being in a positive (negative) mode when both the semi-permanent low pressure over Iceland and high pressure over Azores are simultaneously strong (weak) (Hurrell, 1995; Serreze et al., 1997; Hurrell et al., 2003).

A common approach to characterizing the NAO teleconnection pattern is through the North Atlantic Oscillation Index (NAOI) which is typically a normalized mean sea-level pressure (SLP) index between a southern station, generally located in

the Azores or Portugal, and a northern station in Iceland (Hurrell, 1995; Hurrell et al., 2003). Although the station-based NAO index has been widely applied, a disadvantage of this method comes from the static nature of the stations (Hurrell & Deser, 2010; Hanna et al., 2015). Thus, the NAOI can instead be calculated as the leading mode in the empirical orthogonal function (EOF) of SLP over the North Atlantic sector (Hurrell et al., 2003). This technique is suited better to capturing the spatial pattern of the NAO which in winter season accounts for approximately one-third of the total variance in SLP in the North Atlantic (Hurrell & Deser, 2010). The total variability explained by the NAO reaches a minimum during summer where the oscillation becomes weaker (Appenzeller et al., 1998; Visbeck et al., 2001; Knight et al., 2009; Hurrell & Deser, 2010).

During a positive NAO phase in wintertime, temperatures in the West Greenland region, tend to be below average and associated with dry conditions (Hurrell, 1995; Visbeck et al., 2001; Hurrell & Deser, 2010; Woollings et al., 2014). Conversely, during the negative NAO, temperatures tend to remain above average, with higher precipitation in the west and south-west part of the GrIS (Hurrell, 1995; Gulev et al., 2001; Visbeck et al., 2001; Hurrell & Deser, 2010; Woollings et al., 2014).

Although many studies argued possible mutual interaction between the atmosphere, ocean and sea-ice, due to heat exchange, that modulate NAO and sea surface temperature (SST)/ice extent in North Atlantic, significant uncertainty remains. Recent findings (Hurrell & Deser, 2010) show a positive (negative) correlation between winter positive phase of the NAO and the extent of the Labrador (Greenland) Sea ice. Another possible link regards the NAO phase and the temperature of North Atlantic which follows a quasi-periodicity cycle of 70 years called Atlantic Multidecadal Oscillation (AMO) characterised by a cold and warm phase and described by a normalised index. Indeed, Woollings et al. (2014) showed how the AMO index is slightly anticorrelated with NAOI, suggesting high frequency of negative (positive) NAO during the positive (negative) phase of AMO, due to the weakening (strengthening) of the Polar Front Jet Stream. In fact, a positive phase of the AMO indicates oceanic temperature above the average in the North Atlantic that by heating the air above can decrease the temperature gradient and the baroclinicity

in this area, favouring greater meridian exchanges due to a weakened Polar Front Jet Stream. As pointed out by Hurrell and Deser (2010) and Wanner et al. (2001) there is no preferred time scale of variability of the NAO where large changes can occur within seasonal, annual and multidecadal scale. In this context, on short time scale, NAO behaviour can be explained as a consequence of natural internal variability whereas interdecadal variability may be influenced by ocean and sea-ice processes (Wanner et al., 2001)

At a regional level, the NAO is strongly related to the incidence and intensity of blocking high pressure over Greenland, depicted by the GBI (Hanna et al., 2015). This index is related to the mean 500 hPa geopotential height for the 60-80°N, 20-80°W region (Hanna et al., 2016) and it clearly depicts the intensity of high pressure blocking across the entire Greenland region, called Greenland Blocking Events (GBE) (Hanna et al., 2016). Extreme GBEs are associated with highest values of the GBI (lowest values of the NAO) and generally correspond to high values of temperature during summer over the GrIS.

#### **2.3.3.2. Recent Behaviour of the NAOI and GBI**

Schneider et al. (2007) found an increase, during winter, in the number and intensity of cyclones southeast of the GrIS from 1957 to 2002, consistent with a high percentage of positive values of the NAO. However, Sodemann et al. (2008) identified a more long-range moisture transport over the GrIS during the NAO negative phase in winter leading to the advection of more moisture (potential for strong precipitation) from southerly locations. This result agrees with Bromwich et al. (1999) who found a strong negative correlation between NAO and precipitation in Greenland in winter ( $r = -0.75$ ) over the 1985-1996 period, with correlation even stronger in southern regions ( $r = -0.80$ ) when the accumulation is higher if the Icelandic Low is weak and displaced toward Labrador Sea. In the central-west region and south-west regions, a weak but persistent negative correlation has been detected between NAO and precipitation (Appenzeller et al., 1998; Bromwich et al., 1999; Rogers et al., 2004; Hutterli et al., 2005; Mosley-Thompson et al., 2005; Hanna et al., 2006; Chen et al., 2016). On the other hand, Berdahl et al. (2018) found no

correlation between precipitation in the south-east region and the NAO index while Hanna et al. (2006) found no significant statistical relation between winter NAO and precipitation over all Greenland for the longer 1958-2003 period. Thus, as identified by Chen et al. (2016) the impact of the NAO appears to be spatially and temporally limited and the relation is highly sensitive to the time period selected (Hanna et al., 2006).

Hanna (2003) found that air temperatures in southern Greenland were negatively correlated with the NAO, concluding that the transition to more positive NAO conditions could explain the cooling trend over the 1958-2001 period. The shift to more positive NAO conditions may therefore have dampened the impact of global warming on mass loss in the southern half of the GrIS during summer. Conversely, during the last two decades in summer, a simultaneous strong increase in temperatures, meltwater, runoff and ice discharge has been observed, along with a persistent positive phase of the GBI (Hanna et al., 2016; McLeod & Mote, 2016; McMillan et al., 2016) correlated with a negative NAO phase (Belleflamme et al., 2012; Box et al., 2012; Fettweis et al., 2013b; Hanna et al., 2014; Hanna et al., 2015).

Despite the negative (positive) trend of the summertime NAOI (GBI), during the last two decades, it remains difficult to conclude if this trend is due to internal variability or anthropogenic climate change. In fact, GCMs (Global Circulation Models) do not simulate their recent trends during the last twenty years and reveal a decrease (increase) trend of GBI (NAOI) (Belleflamme et al., 2012; McLeod & Mote, 2016; Delhasse et al., 2021).

## **2.4. Hydrology, Dynamics and GrIS Mass Balance**

### **2.4.1. Introduction**

Glaciers can be categorised into three main types, cold, polythermal and temperate, according to temperature and pressure within the ice. Cold glaciers are characterised by an ice-bed interface under the pressure melting point. Conversely, in temperate (or wet based) glaciers almost all the ice is at the pressure melting point apart from the surface layer, and large amount of meltwater is typical at the ice-bed interface.

Finally, polythermal glaciers are an intermediate type, with a complex thermal structure.

The interior of the GrIS is a typical example of cold base glacier. Conversely, the peripheral glaciers of the ice sheet can be considered into the wet-based category. Here the meltwater plays a key role both at the surface and the ice-bed interface, having a decisive impact on ice dynamics and flow. Before the 2000s, the importance of meltwater on the dynamics was ignored, since the GrIS was thought to be stable through time and the surface impermeable due to its thickness. However, as well as a sharp rise in surface melt due to an increase in water generation and runoff since 1990, a growing number of studies have increasingly underlined its key role on dynamics in this environment (Creys & Schoof, 2009; Werder et al., 2013; Nienow et al., 2017).

Representing a fundamental part of the GrIS system, is the production, routing and withdrawal of meltwater (Chu, 2013). The flow of meltwater involves movement over the surface of the ice sheet (supraglacial), within the ice sheet (englacial), and under the ice sheet (subglacial). Generally, a large amount of surface meltwater can reach the subglacial environment if the capacity of snow and firn layers to store it is limited. Water can flow into lakes, crevasses and englacial conduits (Fountain & Walder, 1998; Chu, 2013) through which it can reach the ice-bed interface influencing the ice motion. However, before explaining the mechanisms by which the surface meltwater influences the dynamics of the GrIS, it is of fundamental importance to describe all the elements involved in meltwater flow and storage since they determine the amount of surface water reaching the bed.

#### **2.4.2. Surface Meltwater Routing and Englacial Environment**

At the beginning of the melt season, during late spring, the surface meltwater percolates into the snow and firn and refreezes at depth. As the temperature increases during the warm season, firn becomes saturated with meltwater, forming “a slush zone” in the accumulation region where water can refreeze, whereas in the ablation zone, the snow melt results in the exposure of bare ice. Here, a system dominated by water percolation turns into a system dominated by meltwater that

starts flowing through a growing network of supraglacial streams which develops through thermal water erosion. During the warm season, it progresses towards a network of streams, punctuated by supraglacial ponding lakes in depression over impermeable ice. Here the water can drain into englacial and subglacial environment via crevasses and lakes or leave the GrIS at the margins.

Crevasses are one of the structures that can connect supraglacial and englacial environments. When a crevasse opens along the entire ice thickness, across a supraglacial stream or lake, it provides a pathway for surface water to drain into the ice sheet and reach the englacial environment. Here, if meltwater ponds within a crevasse to greater than approximately 92 % of crevasse depth, it can initiate hydrofracture due to the density difference between ice and water (Weertman, 1973). If meltwater continues to fill the crevasse as it propagates downwards, the crevasse can hydrofracture through a glacier's entire ice thickness (Colgan et al., 2016). Hydrofracture can result in a permanent connection between the supraglacial and subglacial hydrologic networks known as a moulin (narrow, tubular and vertical channels created by turbulence and frictional heat dissipation of the flowing water) (Chu, 2013; Nienow et al., 2017). Water can also drain into the GrIS through hydrofracture that opens beneath the lakes, although this mechanism is less common (Chu, 2013). Once water drains into hydrofractures, it feeds moulins that connect the supraglacial environment to subglacial network. These englacial channels can only exist if the tendency of the closure due to ice creep is balanced by frictional energy dissipated by water flow (Fountain & Walder, 1998). As underlined by Straneo et al. (2013), great volumes of meltwater from the surface during the summer season, can fill hydrofractures up to the point at which the ice becomes rheologically weakened. This causes the ice to shatter and deform under its own weight due to the slope, which can in turn can enhance ice flow towards lower and warmer altitudes, reducing the SMB of a glacier.

Once water, through hydrofractures, reaches the subglacial environment at the ice-bed interface, it plays a key role on the glacier's dynamics, favouring the acceleration of the ice flow downstream. It occurs especially in summer in the lower part of the ablation zone where surface meltwater along with hydrofractures are

abundant. Conversely, due to a combination of decreasing meltwater availability and a reduction in crevassing due to a reduced stress regime, the density of moulins decreases with elevation (Nienow et al., 2017).

### **2.4.3. Subglacial Water Flow and Dynamics**

The bed of the GrIS ablation and lower accumulation zones can be characterized by two different systems described as inefficient and efficient (Chu, 2013; Nienow et al., 2017). The first, also called a “distributed” system, is a sheet of water of more or less uniform thickness (Creys & Schoof, 2009) consisting of a small conduit connecting network that is not well developed and inefficient at draining large amounts of water. The second, called a “channelised” system, consisting of a network of a few main channels with high hydraulic efficiency, incised into the base of the ice bedrock or sediments and enlarged by the frictional heat dissipation of water (Werder et al., 2013).

As mentioned previously in section 2.4.1 in wet-based glaciers the most important factor influencing ice flow is the meltwater reaching ice-bed interface from englacial environment. Here, if under pressure, it facilitates decoupling and enhanced ice flow via basal sliding (Fountain & Walder, 1998; Bartholomew et al., 2012; Nienow et al., 2017). The magnitude of basal sliding acting on ice-bed interface, is strictly related to the effective pressure in the subglacial drainage system defined as the ice overburden pressure (ice creeping) minus water pressure (Cuffey & Paterson, 2010; Schoof, 2010). A lower effective pressure (overburden minus water pressure) due to an increase of water pressure weakens the ice-bed contact and permits faster sliding.

During the early melt season, an increase in ice flow is observed due to increase of water pressure at the ice-bed interface related to the inefficient “distributed” system. In this period of the year the first high meltwater inputs overwhelm the network of cavities with low hydraulic efficiency (Werder et al., 2013) causing a drop in effective pressure but increase in water pressure with consequent ice acceleration due to increased basal sliding (Fountain & Walder, 1998; Nienow et al., 2017). However, during seasonal progression, with the intensification of surface melting, inputs to the subglacial drainage system cause elements of the distributed

system to become unstable, resulting in the development of the “channelised” system (Fountain & Walder, 1998; Schoof, 2010). Once created, these conduits, having high potential drainage rate, can easily drain future meltwater inputs which tend to decrease as the melt season draws to close. This decrease generally causes a drop in subglacial water pressure with a consequent decrease in basal sliding and ice velocity (Chu, 2013). The existence of these efficient channels persists as long as the ice discharge is enough to offset the ice creep closure. Therefore, channel closure begins simultaneously with the decrease of the surface melt water inputs, in the late part of the melt season, with steadily decreasing of water pressure and ice motion in transition towards the winter season (Bartholomew et al., 2010; Andrews et al., 2014; Davison et al., 2019).

Starting from the 2000s studies underlined how the increase of meltwater produced at the surface during the last decades in summer is followed by a seasonal increase in ice flow. It has the potential to increase the rate of mass lost drawing ice to lower elevations where temperatures are warmer (Rignot & Kanagaratnam, 2006; Joughin et al., 2008; Schoof, 2010). However, despite strong melt seasons during the last decade, in land terminating glaciers, faster movement during the early melt season, due to higher meltwater pulses reaching the bed, is systematically offset by a subsequent slow down during the second half of the season or during winter (Sundal et al., 2011; Chu, 2013; Sole et al., 2013; Tedstone et al., 2013; Tedstone et al., 2015; Nienow et al., 2017), with an overall decrease in ice motion at annual scale.

Despite the progress made to better understand the processes linking surface meltwater, subdrainage system and ice motion, uncertainties still remain. Although the increase in summer meltwater has led to a slowdown of the ablation zone of glaciers that terminate on land, it is not clear if, in a warming scenario, the cold season will shorten to the point of not being able to counterbalance the summer ice speed up (Davison et al., 2019). Furthermore, higher temperatures, will lead to the formation of meltwater, lakes and hydrofractures at ever higher altitudes. This will likely result in an ever greater influx of water into the subglacial drainage system of this part of the GrIS, where the impact is still somewhat unknown, but an increasing annual speed up related to more meltwater production in the recent years has been

found (Davison et al., 2019). Thus, the migration to higher altitudes of the annual decrease in ice motion observed in the ablation zone due to high summer meltwater production is the subject of debate and controversy.

The increase of surface meltwater discharge at the base of the glacier where it terminates into fjords, also plays a key role in the recent speed up of different marine terminating glaciers. Glacier interactions with sea currents and the resulting impacts on ice discharge and submarine melting as mentioned in section 2.2.5.2 are key processes (Holland et al., 2008; Jenkins, 2011; Seale et al., 2011; Joughin et al., 2012; Straneo et al., 2013; Slater et al., 2016; King et al., 2020) which are discussed further in the next section.

#### **2.4.4. Fjord Circulation**

While basal lubrication from enhanced meltwater input is the dominant mechanism for increased velocities on wet land terminating glaciers, interaction with the ocean, sea ice and bathymetry of the fjord play a primary role for marine terminating glaciers (Chu, 2013; Benn et al., 2017). The fjord shape influences the ocean currents that along with surface water temperature controls the existence of sea ice and ice mélange at the edge of tidewater glaciers. In fact, dense sea ice and ice mélange are able to reduce the speed of the ice calving rate and so can modify the advance/retreat of the glacier and glacier velocity (Straneo et al., 2013). The fjord bathymetry and shape also influence the water layering and streams regulating the water flow close to the grounding line and underneath the ice floating tongue (Joughin et al., 2012; Straneo et al., 2013). Finally, through shallow regions called “pinning points” or overdeepened basins the fjord bathymetry can encourage a steady state or a rapid retreat of the glacier (Benn et al., 2017). This is the primary reason why glaciers with termini in the same fjord can show an asynchronous behaviour (Bartholomäus et al., 2016; Motyka et al., 2017).

Recent work has identified links between subglacial hydrology and fjord interaction as mentioned in section 2.2.5.2 about marine-terminating glaciers. The emergence of subglacial water at the grounding lines of tidewater glaciers perturbs water stratification, drawing warm ocean water at depth along fjords to calving

fronts, resulting in transfer of heat from ocean to ice and increasing the potential break-up and submarine melt of the glacier terminus (Joughin et al., 2012; Benn et al., 2017; Nienow et al., 2017; Cowton et al., 2018; Slater et al., 2018).

By observations and modelling, Slater et al. (2018) show how the glacial meltwater at the front of a tidewater glacier in west Greenland, occupy only a small percentage of the ice-ocean contact zone. However, they are sufficient enough to cause a vigorous circulation of the fjord along the entire glacier calving front. They favour the rapid inflow of warmer water towards the calving front which, thanks to its temperature and kinetic energy, causes an increase in frontal ablation (Slater et al., 2018), melting and undercutting the base of the glacier tongue. In many cases this mechanism changes the geometry of the glacier' front, reducing the surface of the glacier in contact with the bottom of the fjord and causing an increase in speed of the glacier itself towards the sea due to a decreased resistance of the tongue to flow (Benn et al., 2017; Catania et al., 2020).

## **2.5. Extratropical Cyclones and Future GrIS Precipitation**

### **2.5.1. Extratropical Cyclone Characteristics**

Cyclonicity is heavily influenced by the Polar Front Jet Stream, which exhibits strong seasonality. In winter, regions with the highest density of cyclones tracks are North Atlantic and Pacific Oceans, where the occurrence of the storms is up to 2.5 times higher than over continents where their passage is more frequent in summer with a frequency from 1.5 to 4 times higher than the oceanic counterpart (Gulev et al., 2001; Simmonds & Keay, 2001; Rudeva & Gulev, 2007). Focusing on size and intensity, cyclone radii and intensity over the oceans are generally higher than those over the continents for both winter and summer. During the cold season, most cyclogenesis events occur over Pacific Ocean, subtropical north America coast, North Atlantic Ocean and Barents Sea (Nielsen & Randall, 1991; Gulev et al., 2001). Conversely, in summer a decrease in summer cyclogenesis is observed in these regions while an increase is detected over continental areas (Rudeva & Gulev, 2007). Finally, Cyclolysis occurs most frequently in the Gulf of Alaska, north-eastern Canada, eastern

Mediterranean Sea and central Russia (Hoskins & Hodges, 2002; Bengtsson et al., 2005) as well in the Barents Sea and Arctic Ocean (Sorteberg & Walsh, 2008).

### **2.5.2. Extratropical Cyclone trends in the Greenlandic Region**

Although comparison between studies is limited by different time spans and cyclone detection/tracking algorithms (Raible et al., 2007), many studies identify an increase in the number of storms at high latitudes, including the Greenlandic region (Gulev et al., 2001; Wang et al., 2006; Ulbrich et al., 2009; Sepp & Jaagus, 2011; Koyama et al., 2017; Valkonen et al., 2021). However, opposing behaviour between winter and summer has been observed, with an increase in cyclones' intensity and their deepening in the cold season, and a decrease in the warm season (Gulev et al., 2001; Chang et al., 2016). Despite these changes, the peak of cyclonic activity still remains along the North Atlantic track, where the Greenland Sea and the Icelandic Low remain the main areas of cyclogenesis (Serreze, 1995; Akperov et al., 2018).

For the Greenlandic region in particular, an increase in cyclone frequency and intensity from mid-1900s both in winter and summer has been observed (Zhang et al., 2004; Sepp & Jaagus, 2011; Akperov & Mokhov, 2013). Furthermore, Akperov et al. (2018) found evidence for an increase (decrease) in the frequency of deep cyclones in winter (summer) using an 11-member climate model ensemble and reanalysis data although a general increase in precipitation and rainfall/snow fraction detected in both season during the last forty years (Rinke et al., 2017; McCrystall et al., 2021).

### **2.5.3. Future Storm Tracks, Cyclones and GrIS Precipitation**

Ensembles of coupled climatic models show a general polar shift of storm tracks in 21<sup>st</sup> century, accompanied with a shift and upward expansion of baroclinic regions, associated with the change in thermal structure of troposphere (Yin, 2005; Harvey et al., 2013; Lehmann et al., 2014; Koyama et al., 2017; Valkonen et al., 2021). As underlined by Chang et al. (2016), the reasons of this shift can be found in the reduction of temperature gradient at the bottom of the troposphere due to Arctic Amplification and subtropics warming in the upper troposphere.

Focusing attention on the region which includes Greenland, North Atlantic and Europe, Zappa et al. (2013), concluded that simulations from stage 5 of the Climate Model Intercomparison Project (CMIP5) indicate an increase in the number of cyclones and their intensity in terms of wind and precipitation around Greenland under climate warming in summer, trading off against reduced frequency and wind cyclonic intensity elsewhere. However, these results conflict with the recent persistence of blocking events over Greenland in summer (Hanna et al., 2016; Tedesco & Fettweis, 2020). Conversely, during the cold season, the response is characterized by an increase (decline) of storms and wind intensity over north Greenland, British Isles and central Europe (elsewhere). As in summer, the amount of precipitation associated with cyclones is expected to increase in response to the increased atmospheric moisture content in a global warming scenario (Schneider et al., 2010; McCrystall et al., 2021).

Hence, despite differences amongst models, the consensus is a general polar shift of storm tracks (Harvey et al., 2013; Zappa et al., 2013; Lehmann et al., 2014), associated with an increase in precipitation intensity that follows from expectations of the response of the hydrological cycle to climate change (McCrystall et al., 2021; Valkonen et al., 2021). However, this change will be dominated more by a broad increase in precipitable water, rather than a change in the regional atmospheric circulation patterns as underlined by Mottram et al. (2017) with a RCM.

## **2.6. Research priorities**

During the recent past studies have focused on extratropical cyclones and their positive effect on the surface mass balance through increasing snowfall over the GrIS. There is theoretical knowledge regarding which factors of extratropical cyclones influence the surface mass balance and energy fluxes. However, their overall impact over the entire or different regions of the GrIS during different seasons has not yet been studied and this is a serious gap regarding projections of future GrIS extent. In this context, the aim of this work is to bridge this gap, trying to understand how extratropical cyclones influence each factor involved in the surface energy balance and surface mass balance. This will be crucial to improve future estimates of the GrIS

and its contribution to SLR determining whether extratropical cyclones despite mass gain via snowfall, may contribute to mass losses from the GrIS in a future warming scenario.

Apart from cyclones' impact on GrIS surface, a future increase in cyclone-induced rainfall during late summer/early autumn over the GrIS is projected under climate warming and already detected in the recent past (Niwano et al., 2021). These large pulses of fresh water could have the ability to perturb the subglacial drainage system of the GrIS, further enhancing the ice motion towards warmer, lower altitudes, favouring dynamic thinning and hence mass loss into the ocean. The consequences of these events on GrIS dynamic are still poorly understood. In this context this work will investigate this further, contributing to a more complete understanding of this mechanism, which can be exacerbated in a warming climate

The principal aim of this thesis is to understand the net effect of extratropical cyclones on the GrIS by addressing different processes: extratropical cyclones and SEB; extratropical cyclones and solid precipitation (and therefore, combined, SMB); the impact of late summer/early autumn cyclonic rainfall on GrIS ice motion. Briefly, a roadmap of how these different aspects will be addressed in the thesis:

- In Chapter 3 the cyclone dataset and a regional climate model output will be shown. They will be useful for the interpretation of results in Chapter 4 and as a guide to the choices made in chapter 5 regarding which portion of the GrIS under the influence of cyclonic rainfalls episodes should be studied.
- In Chapter 4 a workflow composed of several algorithms will be applied on the regional climate model and cyclone dataset with the aim to detect the impact of extratropical cyclones on surface energy and mass fluxes of the GrIS
- In Chapter 5, by the use of the regional climate model, will be identified episodes of late summer/early autumn cyclonic rainfall and their spatial footprint. Ice velocity of drainage basins affected by cyclonic rainfall for which there is sufficient summer coverage of satellite data will be extracted through geomatic tools. The outputs of the regional climate model and reanalysis will enable the interpretation of ice motion during both the summer season and cyclonic events.

## ***3. Regional Climate Model and Extratropical Cyclones***

---

### **3.1. Introduction**

The aim of this chapter is to introduce to the main tool and dataset utilised in this work that are respectively:

- The MAR (Modele Atmospherique Regional)
- The extratropical cyclone dataset

They are pivotal instruments to address the two key questions of this work described in chapter four and five that are respectively:

- 1) What is the direct impact of extratropical cyclones on the GrIS SMB and SEB?
- 2) How do rainfall events (caused by extratropical cyclones) influence the ice flow of the GrIS during late summer/early autumn?

In the first part of this chapter, the MAR outputs are outlined, which illustrate variations of the GrIS SMB and SEB through space and time. Second, the cyclone dataset is presented, describing the algorithm used to detect and track this weather phenomenon and generate this dataset. The necessary processes of cleaning and filtering the dataset to delete spurious systems over the GrIS is also addressed. Finally, an overview of the distribution and frequency of cyclones in different seasons around Greenland in the last six decades is presented.

### **3.2. Data Sources**

#### **3.2.1. The MAR**

The outputs employed here for the period 1958-2016 come from the coupled atmosphere-snow MAR version 3.9 (Fettweis et al., 2017) with a resolution of 20 km which comprises a 3D atmospheric model coupled to the 1-D thermodynamic Surface Vegetation Atmosphere Transfer scheme (SISVAT: Soil Ice Snow Vegetation Atmosphere Transfer (Fettweis, 2007)). The atmosphere is simulated with a

mesoscale primitive equation model based on hydrostatic and thermodynamic equations (Gallée & Schayes, 1994; Gallée, 1995). Starting from the version 3.5.2 the GrIS bed topography and ice mask of Bamber et al. (2013) are used.

The snow-ice part of SISVAT, based on the CEN (Centre d'Etudes de la Neige) snow model CROCUS (Brun et al., 1992), is a one-dimensional multi-layered energy balance model that determines the exchanges between the sea ice, the ice sheet surface, the snow-covered tundra and the atmosphere (Gallée et al., 2001; Reijmer et al., 2012). In order to represent the evolution of the snowpack as a dynamic system and capture the surface and subsurface processes (which have a direct impact on energy absorption), the snow-ice model has been improved by adding the snow metamorphism and snow albedo laws of the CEN (Brun et al., 1992). Furthermore, a dynamic module of snow metamorphism which simulates albedo-meltwater feedback has been added.

The MAR used here is forced every six hours at its atmospheric lateral boundaries (temperature, humidity, wind and pressure) at each vertical MAR level by the NCEP/NCARv1 reanalysis dataset for the period 1958-2016 (Kalnay et al., 1996). The sea ice cover (SIC) and sea surface temperature (SST) are provided by the same reanalysis. They have a horizontal resolution of 2.5° (around 250 km at the Equator) with 17 different pressure levels starting from the ground/sea surface to the top of the troposphere. The NCEP and NCAR reanalysis use a frozen state of the art global data assimilation in order to reduce the chance of spurious non-stationarity.

### **3.2.2. Extratropical Cyclone Dataset**

For the same period as MAR output (1958-2016), extratropical cyclones were extracted from the record compiled by Serreze (2016) at the National Snow and Ice Data Centre (NSIDC). An automatic detection algorithm along with a tracking algorithm (Serreze et al., 1997) was used to identify and trace extratropical cyclones at six-hourly resolution across the Northern Hemisphere. They were applied on the sea level pressure (SLP) fields of NCEP/NCAR reanalysis. The MAR is forced by the same reanalysis dataset thus ensuring consistency between the forcing data used to produce the cyclone and MAR datasets.

The detection algorithm is based on a series of search patterns, able to test if a grid-point SLP value within a  $3 \times 3$  grid is at least 1 hPa higher than the central point. This procedure is repeated up to three grid points away from the central point with a maximum diameter detection of 1750 km. In order to track the cyclones during their entire life, (also determining its surface level pressure tendency, SLPT), a tracking algorithm is necessary. Serreze (1995) developed a tracking system based on a simple “nearest neighbour” analysis which starts from the first timestep ( $t_i$ ), allocating a unique number to every cyclone identified by the detection algorithm, and then continues into the next timestep ( $t_{i+1}$ ). If a system at  $t_{i+1}$  falls within the  $3 \times 3$  grid around a cyclone at  $t_i$ , this is taken as a continuation of the cyclone at  $t_i$  and the same number is given. The minimum distance from all untracked systems at  $t_{i+1}$  is calculated with respect to the remaining numbered system at  $t_i$ . Then, if the distance of the centre of a cyclone at  $t_{i+1}$  is less than 1400 km from a cyclone centre identified at  $t_i$ , and the SLPT is less than 40 hPa, the ID number for the  $t_i$  cyclone is carried over to the corresponding cyclone at  $t_{i+1}$ . At this point, all cyclones not paired from  $t_i$ , are considered to have filled (cyclolysis), whereas cyclones unpaired at  $t_{i+1}$  are considered new cyclones (cyclogenesis). The 1400 km threshold is based on manual analysis carried out by the authors before the development of the algorithm, while the 40 hPa SLPT avoid the potential error of pairing a very deep cyclone in chart  $t_i$  with a new, weak cyclone at  $t_{i+1}$ .

### **3.3. Methodology**

#### **3.3.1. The MAR and SMB/SEB**

Following the methodology described below we are trying to answer two main questions useful for interpreting the results and guiding the study in the following chapters:

- Have a clear picture of the temporal and spatial behaviour of the GrIS surface energy and mass balance during the period 1958-2016.

- Have a clear picture of the spatial behaviour and monthly to seasonal frequency of the extratropical cyclones around Greenland during the period 1958-2016.

The SMB components of the GrIS were resampled to glaciological years over the contiguous GrIS ice mask of the MAR; grid cells with over 50 % of ice cover were considered as glaciated (Figure 3.1).

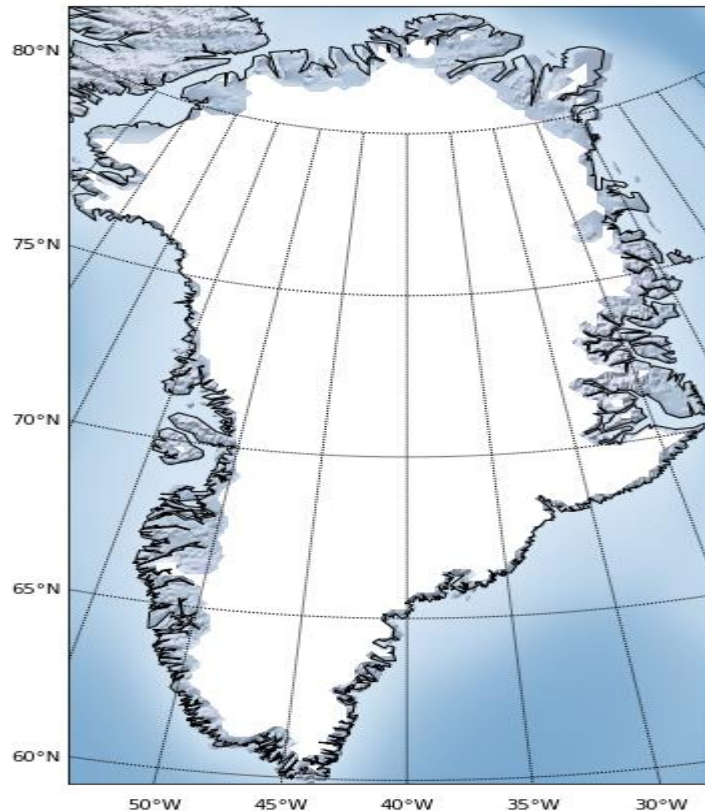


**Figure 3.1.** The MAR Greenland domain with ice sheet mask (white).

The SMB behaviour was explored by analysing the temporal variability of the GrIS precipitation (P), melting (ME), runoff (RU), rainfall (RA) refreezing (RF), albedo (AL), longwave downward (LWD), air humidity (QQZ), temperature (TTZ), sublimation (SU) and wind erosion (ER) during the period 1958-2016. Temporal trends during the periods 1958-1990 and 1991-2016 were analysed using the Wald test linear regressions, a statistical method able to say if the trend of the dependent variable is statistical significant or not (Gourieroux et al., 1982). We divide the data into these two periods because the MB has undergone a decrease after 1991 and where 60% of mass loss is attributable to SMB (Van den Broeke et al., 2016).

To study spatial variability of the SMB components and air temperature, mean average values during 1958-1990 over the entire GrIS were computed and differenced from the 1991-2016 period. The aim was to detect which regions of the GrIS were more affected by this change. To detect areas where the difference in means between the two periods was statistically significant, a student's t-test was applied to each pixel (with p-value of 0.05).

### 3.3.2. Cyclones Filtering and Tracking

Serreze and Barrett (2008) suggest that several screening steps are necessary in the cyclone dataset to remove spurious features that appear from the reduction of surface pressure to sea level over high and complex topography such as the Greenland interior. Therefore, following these suggestions, cyclones that lasted less than 24 hours (4 time-steps), or cyclones that remain stationary over the GrIS for all their entire lifetime were discarded. To limit the analysis to robust systems, cyclones that do not deepen at least 2hPa during their lifetime were also eliminated. After this screening and filtering process, a high frequency of spurious systems emerged, especially during the warm season, over the interior part of the GrIS. Therefore, another screening step was applied to discard cyclones spending their entire life over the GrIS interior.

Cyclones located between 102°W-24°E longitude and 54°-90°N latitude were selected for the analysis, providing their spatial distribution over and around Greenland. This region spans longitudinally from the Hudson Bay to the Norwegian Sea and latitudinally from the Arctic Ocean to the North-Atlantic. The spatial behaviour of cyclones in different seasons was assessed by calculating the mean number of cyclonic days per season ( $N_s$ ) for each grid cell of a 3° regular grid over the entire domain, defined:

$$N_s = \frac{P}{Y \times 4} \quad 3.1$$

Where  $P$  is the number of cyclone' events (number of 6-hourly charts) during the period 1958-2016 and  $Y$  is the number of years in 1958-2016 interval (59).

Subsequently, the number of monthly relative frequencies ( $Nm$ ) of cyclonic days were calculating during the 59 years period according to:

$$Nm = \frac{N \times 100}{D \times Y} \quad 3.2$$

Where  $N$  is the number of days featuring at least one six-hourly SLP field chart with a cyclone within 750 km from the GrIS, and  $D$  is the number of the days of the month. Note that the threshold of 750 km was chosen because this is the upper limit of the typical size of cyclones which include most of cyclones affecting Greenland and therefore, can have a direct impact on GrIS (Rudeva & Gulev, 2007) within this distance.

### **3.4. Results**

#### **3.4.1. The MAR and SMB/SEB Temporal Variability**

Table 3.1 lists the averages and trends over the climatic period 1958–1990, during which the mass of the GrIS remained approximately in equilibrium, and the recent imbalance period 1991–2016. During the period spanning from 1958 to 1991 the SMB (Figure 3.2a) and ice discharge  $D$  (Mouginot et al., 2019; King et al., 2020) remained around  $+ 400 \text{ Gt yr}^{-1}$  -  $400 \text{ Gt yr}^{-1}$  with a consequent mass balance close to zero. After the middle-90s, an increase in ice discharge and an overall decrease in SMB of around 4 % per year, also driven by reduced albedo, led the GrIS to have a persistent negative annual MB.

To explain the trend of the SMB and its recent decline, we assessed the temporal behaviour of its main components (Figure 3.2b). Total annual precipitation ( $P$ ) varied between 600 and 800  $\text{Gt yr}^{-1}$  without having a significant trend over the full period. Even though no change in total precipitation on the GrIS is evident, the RA increased over the last 25 years. During the period 1958-1990, 4.7 % or 34  $\text{Gt yr}^{-1}$  (Table 3.1) of the modelled precipitation fell as rain while for the next period 1991-2016 it increased to 5.6 % (40  $\text{Gt yr}^{-1}$ ) although this trend results statistically insignificant ( $p > 0.05$ ).

Total SU had very low values if compared to other components, just between  $-7 \text{ Gt yr}^{-1}$  and  $13 \text{ Gt yr}^{-1}$  and no significant ( $p < 0.05$ ) trend is detected (reported in Appendix A) while wind erosion (ER) was around zero (not shown). ME and RU vary between 400 to  $600 \text{ Gt yr}^{-1}$  and 200 to  $400 \text{ Gt yr}^{-1}$  during the period 1958-1990 without a significant trend. Subsequently, they increased substantially during the period 1991-2016, with a positive trend around 4 % per year, reaching values up to  $1100 \text{ Gt yr}^{-1}$  for ME and  $700 \text{ Gt yr}^{-1}$  for RU in 2012. However, a simultaneous but modest increase in refreezing (RF) of melt and rainfall has limited the mass loss. This underlines the importance of firn in holding water that would be lost via RU in a warmer climate, although a percentage reduction from 42 % to 38 % in the total annual refreezed ME is observed during the last 20 years.

Overall, all the SMB components analysed demonstrate large inter-annual variability although their increase is clear since the mid-1990s. In this context it is worth underlining how the recent increase of ME and RA is consistent with the increase of TTZ and QQZ (Figure 3.2c) which in turn enhanced the downward flux of longwave radiation (LWD) (Figure 3.2d).

**Table 3.1.** Contiguous Greenland ice sheet (GrIS) averages (1961–1990 and 1991–2015,  $\text{Gt yr}^{-1}$  with standard deviation) and trends (1961–1990 and 1991–2015,  $\text{Gt yr}^{-2}$  with standard error) of SMB and climatic components.

| <b><i>SMB and climatic components</i></b> | <b><i>Average (1958-1990)</i></b> | <b><i>Trend (1958-1990)</i></b> | <b><i>Average (1991-2016)</i></b> | <b><i>Trend (1991-2016)</i></b> |
|---|-----------------------------------|---------------------------------|-----------------------------------|---------------------------------|
| <b>SMB</b>                                | $405 \pm 103$                     | $-1.46 \pm 2.02$                | $311 \pm 137$                     | $-11.98 \pm 2.81$               |
| <b>P</b>                                  | $710 \pm 68$                      | $-1.19 \pm 1.33$                | $721 \pm 61$                      | $0.12 \pm 1.72$                 |
| <b>RA</b>                                 | $34 \pm 8$                        | $0.06 \pm 0.16$                 | $40 \pm 10$                       | $0.51 \pm 0.21$                 |
| <b>SU</b>                                 | $4.15 \pm 4.73$                   | $0.22 \pm 0.08$                 | $4.29 \pm 4.12$                   | $-0.18 \pm 0.11$                |
| <b>ME</b>                                 | $466 \pm 75$                      | $0.11 \pm 1.50$                 | $601 \pm 165$                     | $15.22 \pm 3.31$                |
| <b>RU</b>                                 | $299 \pm 62$                      | $0.06 \pm 1.23$                 | $405 \pm 126$                     | $12.29 \pm 2.42$                |
| <b>RF</b>                                 | $199 \pm 20$                      | $0.10 \pm 0.40$                 | $233 \pm 47$                      | $3.50 \pm 1.10$                 |
| <b>AL</b>                                 | $0.79 \pm 0.00$                   | $0.00 \pm 0.00$                 | $0.78 \pm 0.01$                   | $0.001 \pm 0.01$                |
| <b>TTZ</b>                                | $-7.86 \pm 0.52$                  | $0.02 \pm 0.01$                 | $-7.15 \pm 1.03$                  | $0.10 \pm 0.01$                 |
| <b>QQZ</b>                                | $2.29 \pm 0.08$                   | $0.00 \pm 0.00$                 | $2.39 \pm 0.16$                   | $0.01 \pm 0.01$                 |
| <b>LWD</b>                                | $223 \pm 3$                       | $0.17 \pm 0.05$                 | $225 \pm 4$                       | $0.32 \pm 0.10$                 |

Regional Climate Model and Extratropical Cyclones

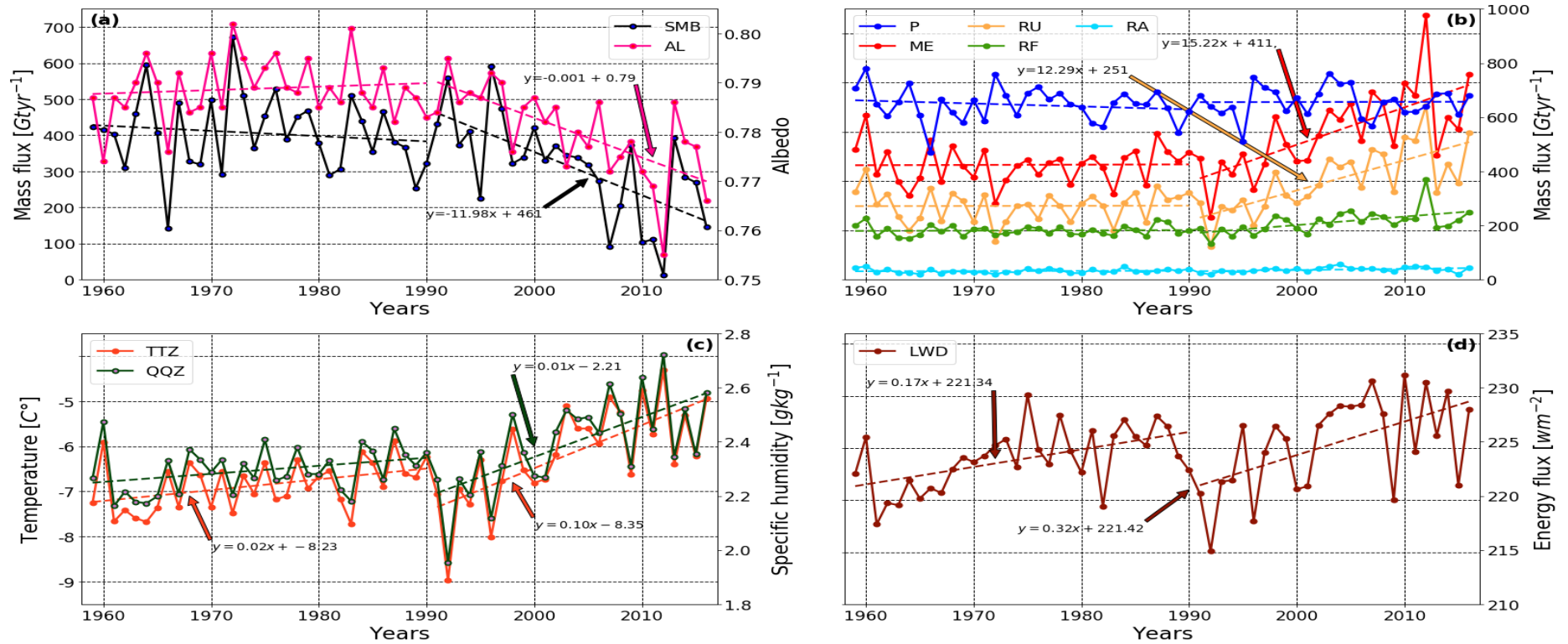


**Figure 3.2.** (a) Annual values of the Surface Mass Balance (SMB) integrated over the entire GrIS during a glaciological years and average summer albedo (AL). (b) Same as for SMB but for total precipitation (P), melt (ME), runoff (RU), Refreezing (RF) and rainfall (RA). (c) Summer values of temperature (TTZ) and specific humidity (QQZ) at 2 meters above the surface and the longwave downward (d) (LWD). Dashed lines indicate linear trends for the periods 1958-1990 and 1991-2016. Regression lines values are indicated only for those statistically significant.

### 3.4.2. The MAR and Spatial SMB Variability

Figure 3.3a shows the mean ME for the period 1958-1990. The highest melt rates are experienced in the south-west/west regions due to lower altitude and consequent higher temperature (Figure 3.5a) and reduced albedo (Figure 3.7a). The second highest melt rates are reached in the eastern region (up to  $\sim 2000 \text{ Kg m}^{-2}\text{yr}^{-1}$ ) especially near the coast. Overall, ME increases with decreasing latitude, underlining how the southern region is more affected by warm air if compared to northern region. Figure 3.3b shows how the mean annual ME has increased over a large part of the GrIS during the period 1991-2016 if compared to the period 1958-1990 and especially along the

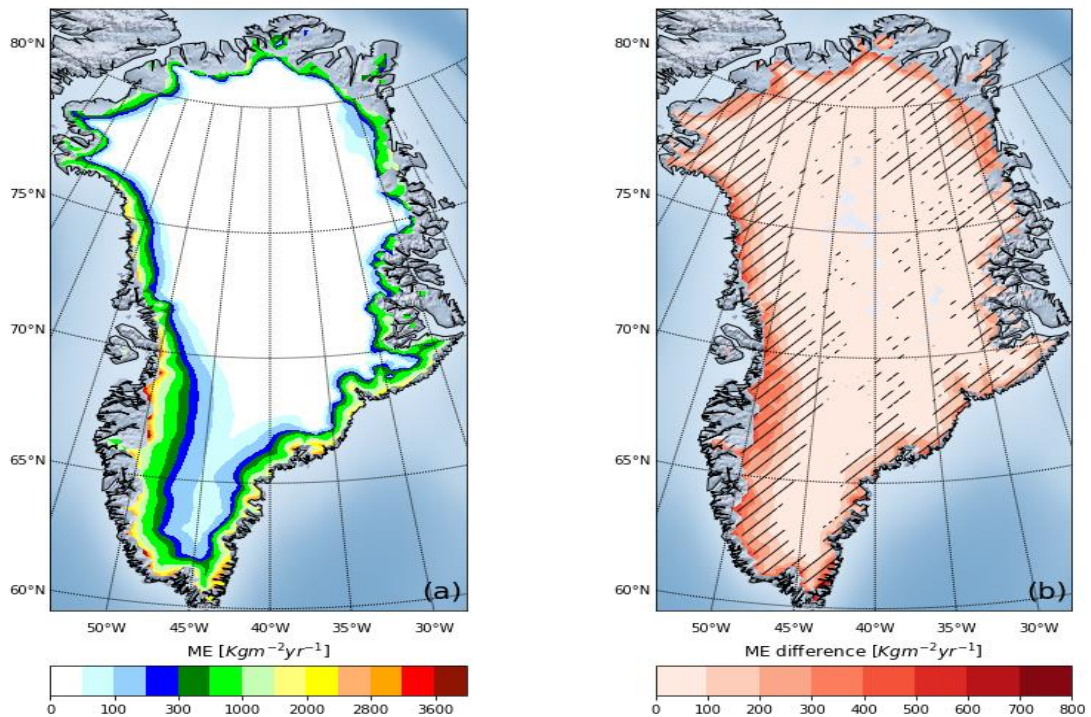


**Figure 3.3.** Modelled 1958-1990 average melt (a) and 1991-2015 minus 1958-1990 difference (b). Hatched areas indicate differences that are significant at the 95 % level.

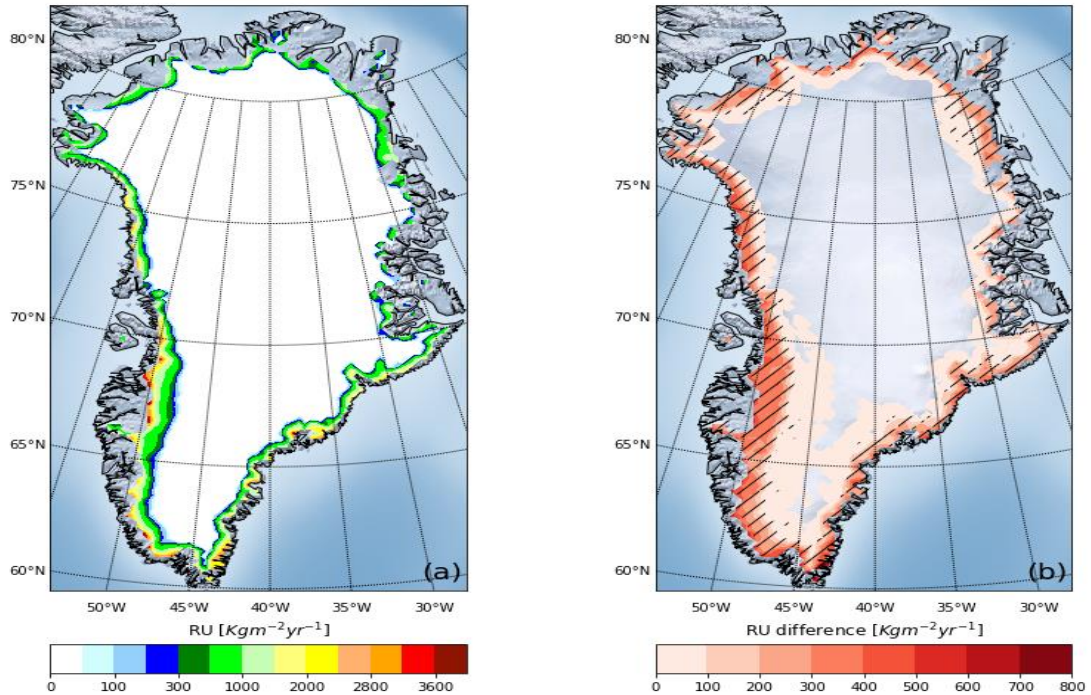


**Figure 3.4.** Modelled 1958-1990 average runoff (a) and 1991-2015 minus 1958-1990 difference (b). Hatched areas indicate differences that are significant at the 95 % level.

borders and the south-western flank, reaching a value here of  $+ 600 \text{ Kg m}^{-2}\text{yr}^{-2}$ . This increase is a consequence of increased temperature over the entire GrIS (Figure 3.5b) and decreased AL (Figure 3.7b) in the ablation zone (Figure 3.8a) during the last few decades. Pronounced increase of RU (Figure 3.4b), if compared to the period before 1990 (Figure 3.4a), can be observed in the ablation zone and it was fed by ME not dampened by RF in the firn, which is already saturated (Figure 3.6a). Conversely, a recent increase in refreezing of ME in the lower and upper accumulation zone (Figure 3.6b) into the firn, avoid high rates of RU in this area. Overall, the widespread increase in temperature over the entire GrIS (Figure 3.5b) seems to drive opposite effects between the ablation and accumulation zones: lowering the AL and SMB in the former, whilst enhancing them in the accumulation zone (Figure 3.7b and Figure 3.8b) due to increases in snowfall.

Regional Climate Model and Extratropical Cyclones

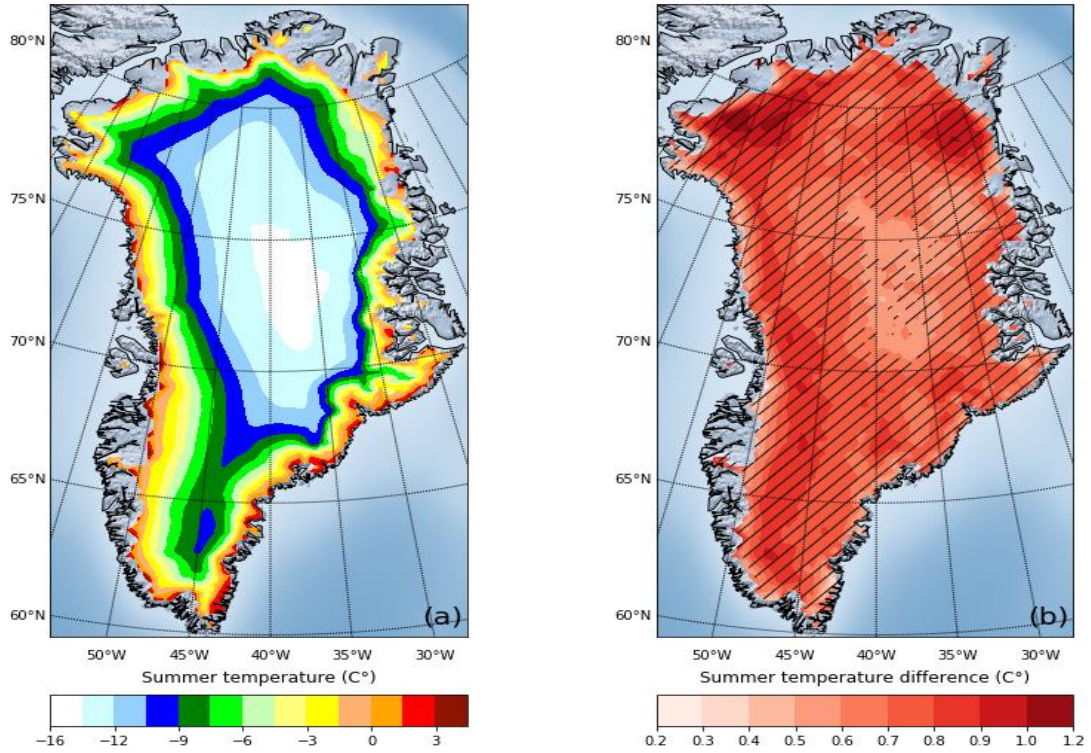


**Figure 3.5.** Modelled 1958-1990 average temperature (a) and 1991-2015 minus 1958-1990 difference (b). Hatched areas indicate differences that are significant at the 95 % level.

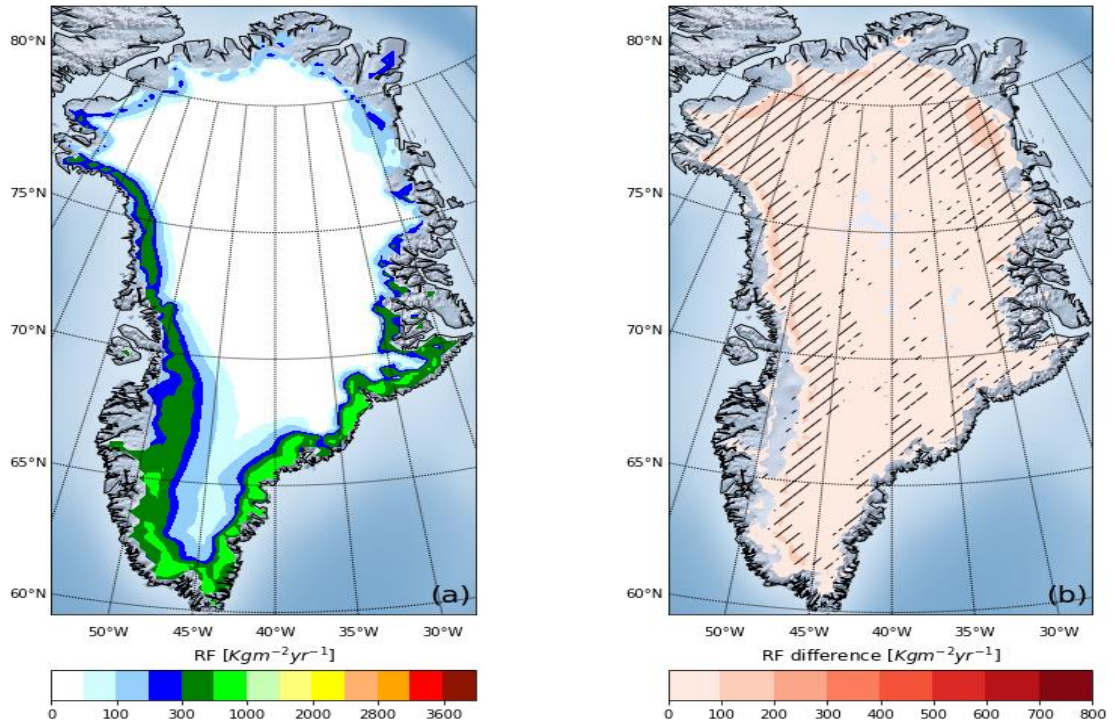


**Figure 3.6.** Modelled 1958-1990 average refreezing (a) and 1991-2015 minus 1958-1990 difference (b). Hatched areas indicate differences that are significant at the 95 % level.

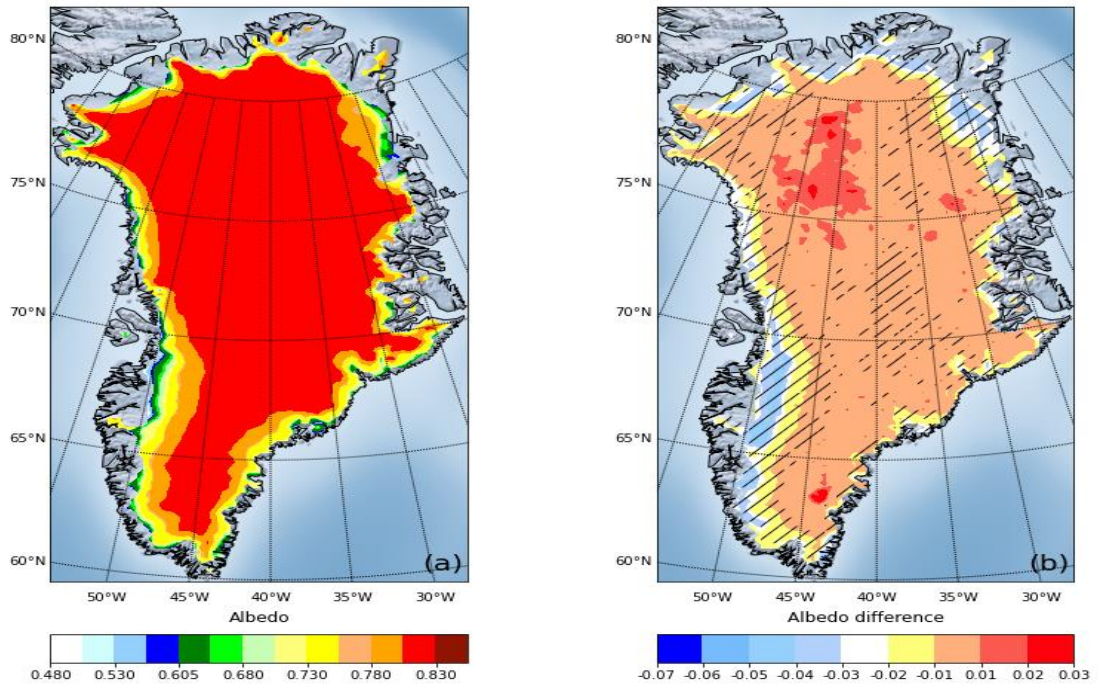


**Figure 3.7.** Modelled 1958-1990 albedo (a) and 1991-2015 minus 1958-1990 difference (b). Hatched areas indicate differences that are significant at the 95 % level.

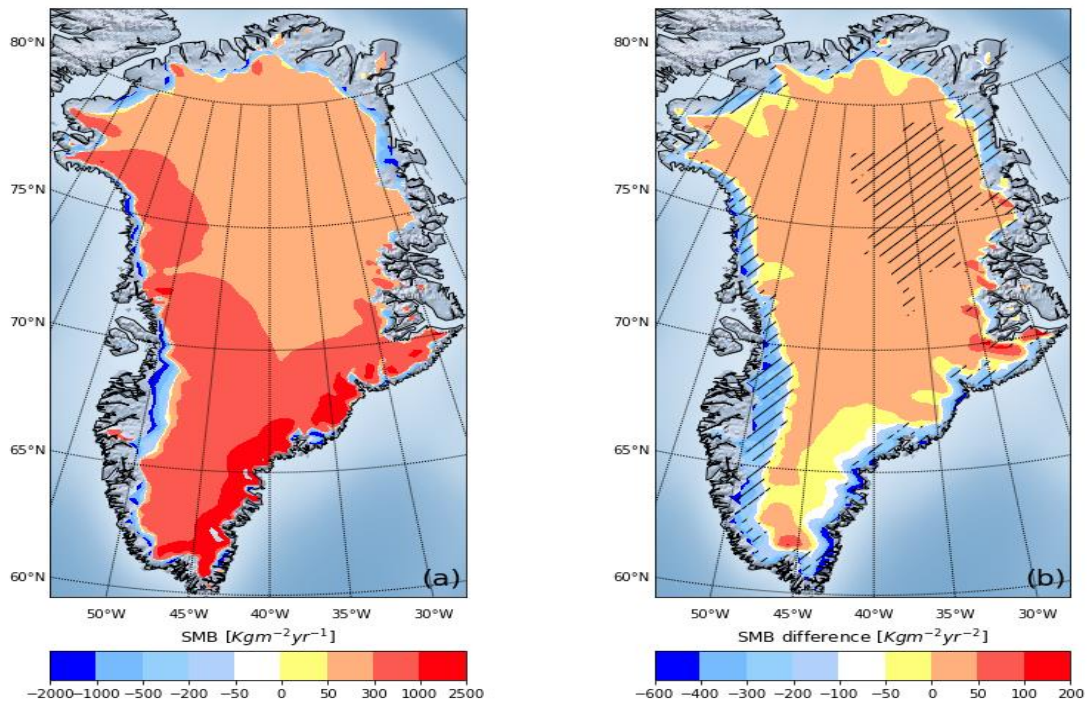


**Figure 3.8.** Modelled 1958-1990 average SMB (a) and 1991-2015 minus 1958-1990 difference (b). Hatched areas indicate differences that are significant at the 95 % level.

### 3.4.3. Cyclonicity in the Greenlandic Region

#### 3.4.3.1. Spatial Distribution in Different Seasons and Monthly Frequencies

In winter (Figure 3.9) and spring (Figure 3.10), the peak of cyclonic activity is located off the east coast of southern Greenland. It is in line with previous studies (Serreze, 1995; Serreze et al., 1997) where this region is identified as the region where the Icelandic Low (IL) stationed semi permanently.

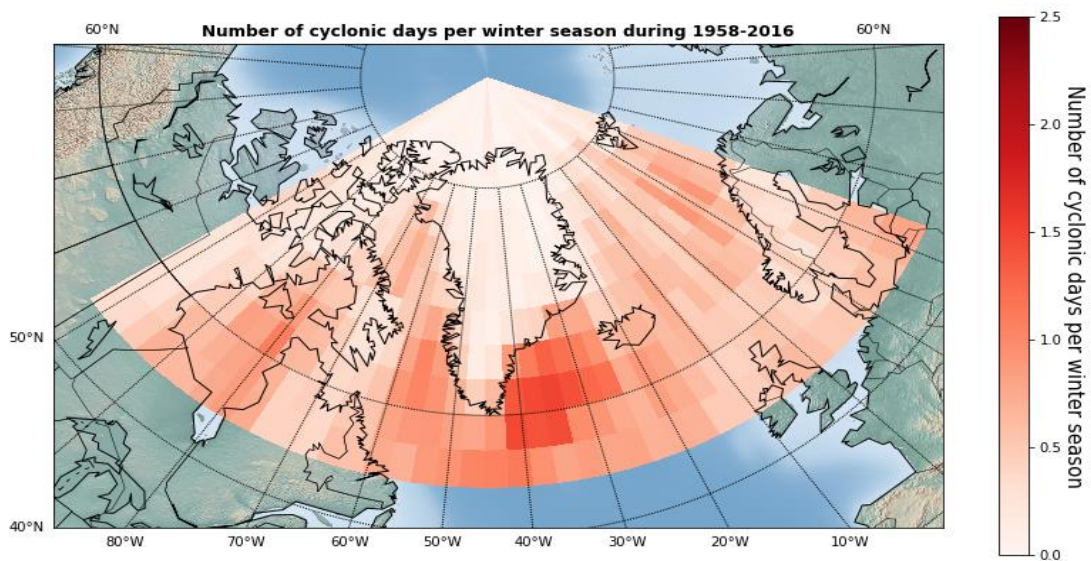


**Figure 3.9.** Number of cyclonic days for each grid box of 3X3 degrees obtained from Eq. 3.1 for winter season over the entire Greenland domain during the period 1958-2016.

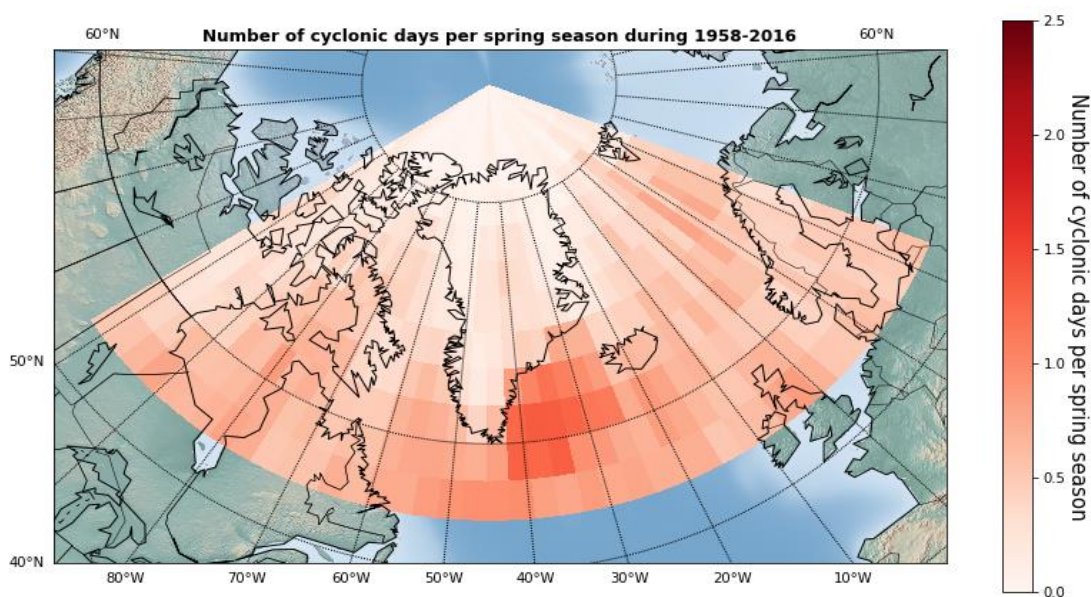


**Figure 3.10.** Same as Fig 3.9 but for spring

In autumn (Figure 3.12), although the IL persists, another peak in cyclonic activity is located in the south-west, over Hudson Bay and extending north-eastward into Baffin Bay. Finally, in summer (Figure 3.11), a weakened IL and a more homogeneous distribution of cyclones around all Greenland is observed. Overall, it can be observed that the number of cyclonic days decreases with latitude over Greenland, reaching approximately zero in the most northerly part of the domain.

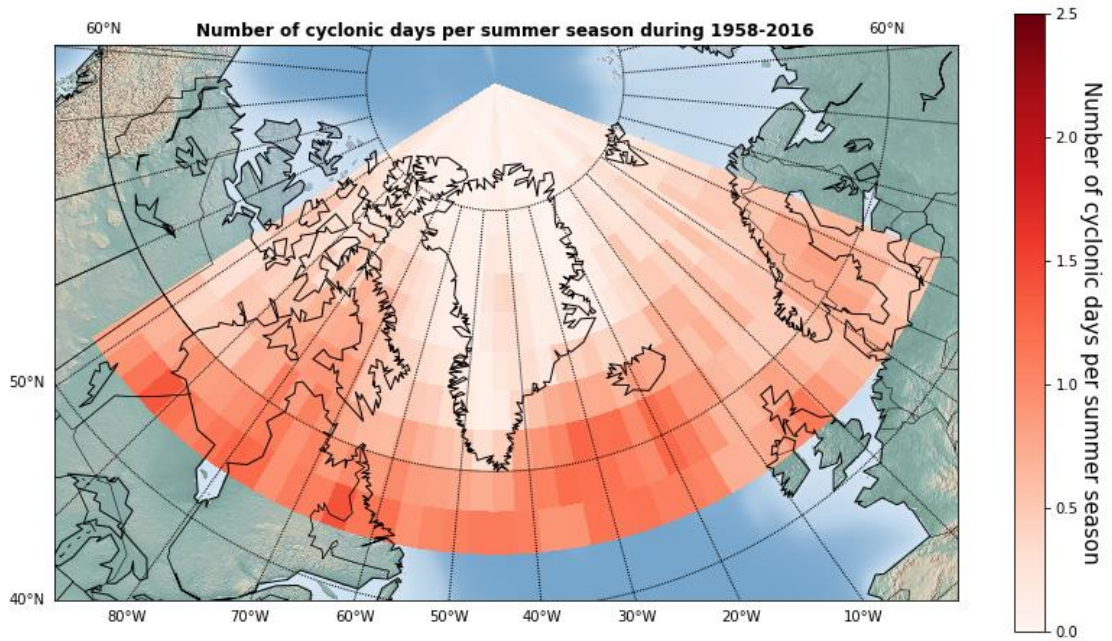


Figure 3.11. Same as Fig 3.9 but for summer

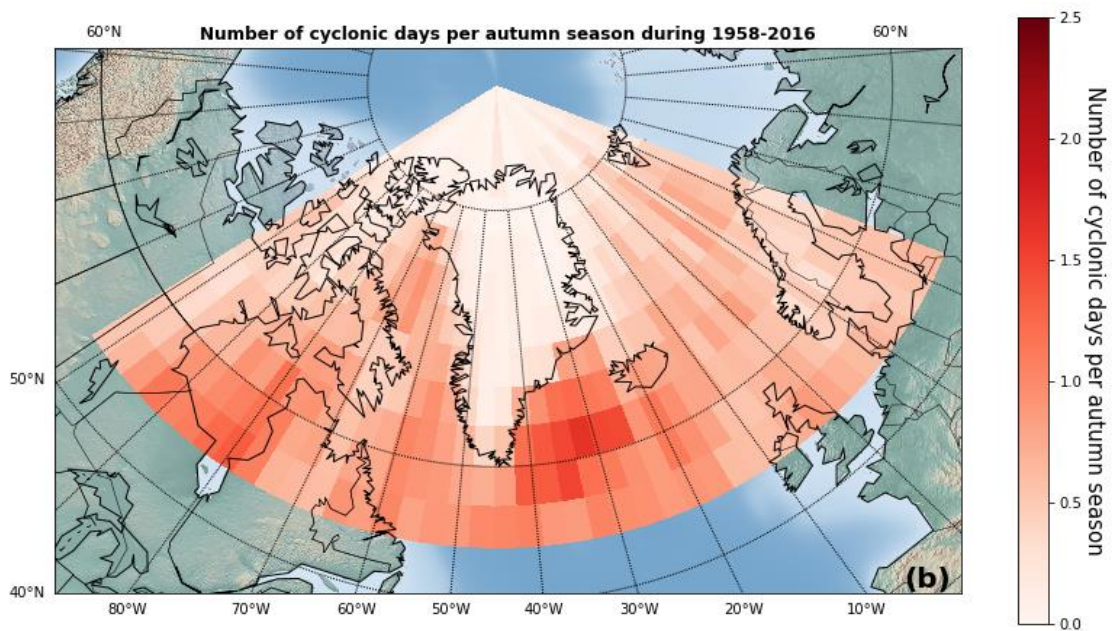
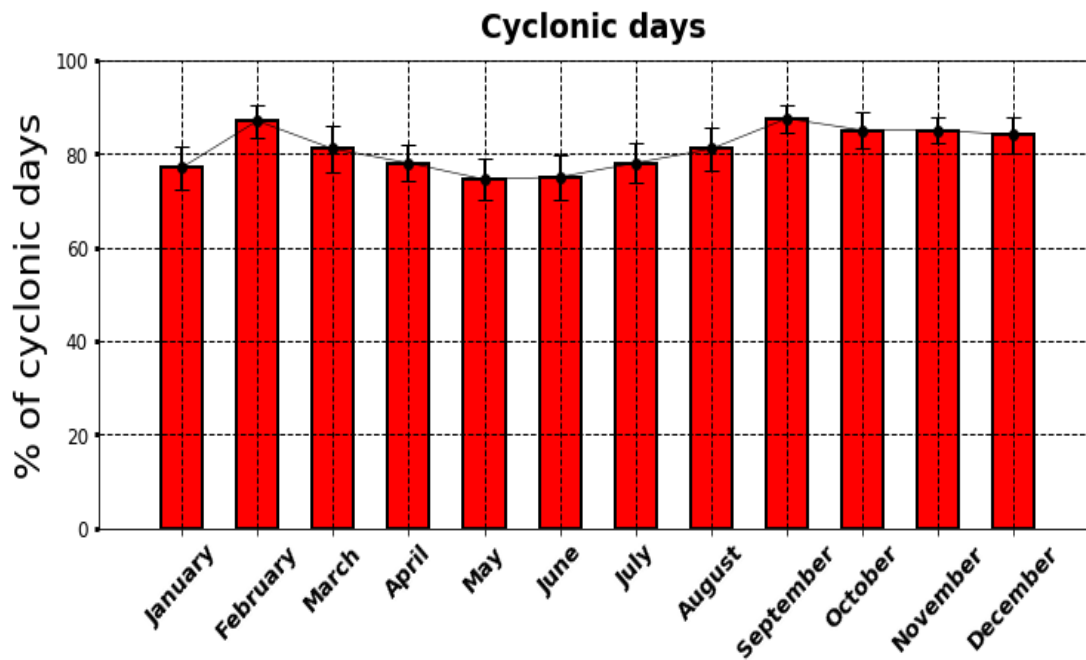


Figure 3.12. Same as Fig 3.9 but for autumn

Figure 3.13 shows the relative frequency of cyclonic days (days with at least a 6-hourly cyclone chart within a distance of 750 km from the Ice Sheet) during the 12 months, covering the period 1958-2016. The peak is observed both in September and February while the lower values occur between March and August. During the entire autumn a highest percentage of cyclonic days is consistent with the timing of the peak of meridional exchanges of polar and subtropical air masses in this region (Giuliaci et al., 2010).



**Figure 3.13.** Percentage of cyclonic days during the twelve months for the period 1958-2016. Black whiskers indicate the standard deviation.

### 3.5. Discussion and Conclusion

The inter-annual variability of all the SMB components is due to the primary role of tropospheric circulations (Fettweis et al., 2013b; Hanna et al., 2014; Hanna et al., 2016; McLeod & Mote, 2016) that varies every year. However, the GrIS surface mass balance time series shows a significant decrease since the mid of 1990s (Fettweis et al., 2017). This is due to an abrupt increase of meltwater runoff not counterbalanced by an increase in precipitation, which instead remained approximately constant during the period 1958-2016 (Van den Broeke et al., 2016). The persistent low values of surface mass balance during the last decade were accompanied by an increase in

temperature, humidity and consequent long-wave downward over the entire GrIS (Hanna et al., 2012; Hofer et al., 2019). However, it is worth underlining how this negative surface mass balance trend was mainly due to a significant loss of mass concentrated at lower elevations on the GrIS and especially in the south-western part where temperatures hover near the melting point throughout the ablation season. Here the mass loss was not counterbalanced by the modest increases in snowfall over the interior of the ice sheet (Box et al., 2013). In this context, the firn appears to dampen the meltwater runoff due to an increasing amount of refreezing during the last twenty years. However, especially in the south-west region of the GrIS, the capacity of the firn to buffer runoff is compromised by larger amounts of meltwater if compared to the past, which enhances the firn compaction with a reduction of pore spaces that are not able to store further meltwater (Cuffey & Paterson, 2010).

The decrease of albedo and surface mass balance and increase in melt especially in the ablation zone, is consistent with the more frequent episodes of summertime high pressure since the end of the 1990s (Fettweis et al., 2010; Belleflamme et al., 2012; Box et al., 2012; Overland et al., 2012; Fettweis et al., 2013b; Hanna et al., 2014; Chen et al., 2016; Tedesco & Fettweis, 2020). Summer high pressure favours the advection of warm air over the GrIS especially along its western flank that with clear skies increases the amount of sensible heat fluxes and shortwave downward, reducing albedo and enhancing melt. In turn, the enhanced melt favours snow grain metamorphism, which further reduces the albedo, feeding the albedo-melt feedback (Box et al., 2012). Conversely, at higher altitudes of the GrIS the impact of anticyclonic warm advections remains limited, since here the sensible heat fluxes and short-wave downward play a minor role. However, some exceptional summer warm advection in the last decade, have led to episodes of meltwater production and rainfall up to the Summit (Bennartz et al., 2013; Tedesco & Fettweis, 2020; Xu et al., 2022), leaving open the question if in a warmer scenario the central part of the GrIS will hold under repeated warm advections of this magnitude.

Focusing on the spatial distribution of extratropical cyclones, in section 3.4.3 a peak in frequency between Iceland and south-eastern Greenland in the area of the Icelandic Low during autumn winter and spring is shown, while in all the seasons the

number of cyclonic days generally decreases with increasing latitude. These results explain why the highest precipitation totals are observed in the southern region during winter, reaching a peak above  $2000 \text{ Kg m}^{-2}\text{yr}^{-1}$  in the south-east (Schuenemann et al., 2009), followed by a gradual decrease to the north where the lowest precipitation totals are encountered. Precipitation here is concentrated in summer, reflecting the northward shift of the polar jet stream and attendant cyclonicity (Chen et al., 1997; Archer & Caldeira, 2008; Schuenemann et al., 2009). In the interior of the GrIS, cyclones are almost absent due to the blocking effect that the extreme elevation of the ice sheet has on cyclones trajectories (Chen et al., 1997).

The outcomes obtained in this chapter, in addition to introducing the data sets used, play a key role in the analyses of chapters 4 and 5:

1. The analysis in Chapter 4 regarding the impact of extratropical cyclones will be evaluated for the GrIS and its respective drainage basins and the ablation zone which results in this chapter indicates as a key region for future SMB estimates.
2. The frequency of the cyclones in the Greenlandic region obtained here will be used to help interpret the results in Chapter 4 regarding the impact of these weather systems on different regions of the GrIS.
3. The assessment of the impact of cyclonic rainfall on ice velocity in Chapter 5 will be focused on the west/south-west coast of the GrIS. This is because results in this chapter have revealed this region as the one where temperatures hover near the melting point throughout the ablation season. This should imply a higher frequency of cyclonic rainfall events here than elsewhere on the GrIS with a tendency to rise sharply in the future.

## *4. The Impact of Extratropical Cyclones on the GrIS SEB and SMB*

---

### **4.1. Introduction**

The GrIS SMB has been becoming less positive since the start of the 1990s and the reason is mainly to be found in the change of the weather circulation. This is the main driver related to SMB of the GrIS, such shown by model-based study of Box et al. (2004) where about the 90 % of the SMB variability is due to changes in annual precipitation and summer air temperature which drives high rates of surface melt. These two factors, in the GrIS region, are linked to the two main different migratory weather types: cyclones and anticyclones. Their movement and displacement are responsible of meridional moisture and heat exchanges (Wallace et al., 1988; Sorteberg & Walsh, 2008) which play a key role in governing the climate of the GrIS by directly determining the daily weather conditions. High frequency of periods of high pressure in summer drive more negative values of the GrIS SMB due to high temperatures and humidity. Conversely, extratropical cyclones are a source of solid precipitation, and this, should imply a net positive effect on the GrIS SMB but through which SEB and precipitation pathways remains a key question.

Many investigation have attempted to find links between climatic indices such as the NAO and GBI and large-scale atmospheric circulation patterns, and to explain and predict precipitation and melting at GrIS surface and the SMB behaviour (Appenzeller et al., 1998; Bromwich et al., 1999; Rogers et al., 2004; Hutterli et al., 2005; Belleflamme et al., 2012; Fettweis et al., 2013b; Hanna et al., 2014; Hanna et al., 2015; Hanna et al., 2016). The link between NAO and cyclonic precipitation is spatially or temporally limited, while the relation between GBI and summer temperature (and melt) appears robust. This led to a flourishing literature regarding the anticyclones' impact on the GrIS SMB and their link with the GBI (Hanna et al., 2016; McLeod & Mote, 2016; McMillan et al., 2016), but less attention has been paid to the cyclonic counterpart. An exception to this was a study of (Chen et al., 2016)

who demonstrated the key role of extratropical cyclones in driving the inter-annual variance of the SMB through their control on snow accumulation patterns. Apart from this study, during the recent few decades, attention was primarily focused on assessing the spatial behaviour of cyclonic activity around Greenland and related solid and liquid precipitation over different regions of the GrIS (MacCabe et al., 2001; Schuenemann et al., 2009; Ulbrich et al., 2009; Schuenemann & Cassano, 2010; Chang et al., 2016).

Some studies have shown the indirect impact of precursor cyclones in directing warm air masses on the GrIS (McLeod & Mote, 2015, 2016; Oltmanns et al., 2019) and then enhancing melting. However, apart from these controls, cyclones should also be expected to directly modulate the GrIS radiation budget via cloud cover and the influx of air masses of different nature (cold and dry and warm and moist)(Mote, 1997; Van den Broeke et al., 2008), although their overall impact on the GrIS remains unexplored. It is therefore critical to increase understanding of the impact that extratropical cyclones have on the GrIS SEB and SMB factors for two main reasons:

1. The cyclonic activity in a future warming scenario is predicted to increase with medium confidence while precipitation with high confidence in the Greenlandic region, (Schuenemann & Cassano, 2010; Zappa et al., 2013; Masson-Delmotte et al., 2021)
2. They are a source of clouds, which impact in climatic conditions characterised by air masses of different properties carried by cyclones is still unexplored and which optical depth modelling is the greatest uncertainty regarding the future GrIS meltwater production (Hofer et al., 2019).

Based on these needs, the aim of this study is to improve our understanding of the influence of extratropical cyclones on the GrIS SMB and SEB. The remainder of this chapter is organised as follows:

- Sections 4.11 and 4.12 provide a literature review regarding the synoptic circulation types such as cyclones and anticyclones and link with glaciers/ice sheets SMB and SEB.
- Section 4.2 provides an explanation of data sets and methodology.

- Section 4.3 provides the results regarding the impact of extratropical cyclones on the GrIS SMB and SEB.
- Section 4.4 and 4.5 provide a discussion and conclusion of this work.

#### **4.1.1. Synoptic Circulation Types and SMB**

One goal since the 1960s was to link the glacier behaviour to the recurrence and frequency of specific atmospheric circulation types such as cyclones and anticyclones. This attempt was motivated by the fact of finding simple atmospheric indices able to link the advance or retreat of glaciers to weather variability. To reach this aim some methods were applied to circulation fields such as geopotential height fields, or other meteorological variables, in order to reduce a wealth of multivariate climate data into specific synoptic patterns which exhibit homogeneous characteristics. In this direction, the first attempt to link variation in front position for a couple of alpine glaciers, to the recurrence of cyclonic and anticyclonic weather type using the deviation from average height of 500 mb, was the work of Hoinkes (1968). It was followed by other work using surface level pressure (SLP) and 500 geopotential height maps to link SMB variability with flow regimes or air masses (Fitzharris et al., 1992; Fitzharris et al., 1997; Pohjola & Rogers, 1997).

Other authors (Yarnal, 1984; Mote, 1997; Fealy & Sweeney, 2007; Cullen et al., 2019), by performing cluster analysis on component scores of a principal component analysis of daily 700 mb or 500 mb, extracted synoptic type with cyclonic, anticyclonic curvature or zonal flow. Subsequently, by the use of a multiple regression analysis, they showed how the large amount of variance in glaciers mass balance could be explained using the frequency of these types as predictors. Compared to the previous ones, this methodology has made it possible to consider how different arrangement of the baric figures (spatial displacement of air pressure) has a different meteorological impact on glaciers. This has improved the predictability of glacier behaviour as a function of the large atmospheric centres of action. In this direction, using a classification based on the origin and direction of air masses, a study on glaciers in the Southern Alps by Cullen et al. (2019) tried to link winter snowfall (accumulation) and summer ablation to the large-scale atmospheric circulation. Their

findings, in line with previous work, summarize a general trend of high melt rates during warm anticyclonic advections as opposed to low melt rates and high accumulation rates during cyclonic conditions.

Focusing on Greenland, satellite passive microwave sensors were utilised by Mote (1997) to assess the spatial range of melting on the GrIS and its relationship with atmospheric flow at the 700 mb level. They concluded that the greatest melt extents were driven by western movement of the trough axis from its climatological mean position in Northern America, with a consequent warm southerly geostrophic flow across Greenland. Conversely, the lowest mean melt extent was due to a lowering in geopotential height ranging from Baffin Bay to Iceland, along with a rise in geopotential heights in the north-eastern part of Canada that produced anomalous cold north-westerly flow over the GrIS.

#### **4.1.2. Synoptic Circulation Types and SEB**

Further studies were carried out in order to investigate not only the relationship between synoptic weather types and glacier mass balance but also their different impact on the SEB and the role played by the clouds. They are presented in this section and represent a crucial literature, useful for interpreting the results of this work. In fact, these studies were performed on glaciers located in maritime and continental climate which reflect the opposite climatic condition of the GrIS margins and its interior which in turn can have different impact on glaciers SEB.

The weather type classification approach, discussed in the previous section, was also utilised to study how different weather circulations can modulate the radiation budget of a glacier. The fundamental assumption of the synoptic climatological approach is that distinct synoptic-scale patterns are associated with high ablation rates, whereas others are associated with reduced melt depending on their ability or not to drive the ice ablation via energy exchange at the ice-atmosphere interface. In this physical process, clouds should also be expected to play a key role in SEB although only a few studies are available, and it is therefore critical to increase understanding of the impact of clouds on glaciers' SEB.

Using the aforementioned technique, Hannah and McGregor (1997) did not find a significant difference between melt rates of a glacier in the Pyrenees across some weather types, although the partitioning of the energy balance components was different. In this direction, a more recent study of Matthews et al. (2015) didn't find a correlation between NAOI and melt rate of Icelandic glaciers. However, thanks to their SEB study approach, they demonstrated how this correlation remains hidden because of the counteracting effects of the NAO on energy fluxes dependent and independent by temperature. These two studies underlined the importance of examining the synoptic controls of the individual SEB components with a particular focus on clouds, temperature and atmospheric water content.

Another study aimed at quantifying the impact of different weather types on SEB partitioning of an alpine glacier located at mid-latitude in a continental area in Colorado during the summer season, was done by Cline (1997). Overall, the highest melt rates driven by sensible heat flux along with net radiation were identified during the anticyclonic pattern. Conversely, the cyclonic pattern was the only one regime where meltwater energy was below zero. This can be explained by cold air which reduces the sensible and latent heat fluxes along with a negative net radiation driven by clouds which decreased the short-wave downward not counterbalanced by the increase in long-wave downward.

The results obtained by Cline (1997) are in line with two more recent works. The first was the study of Braun et al. (2001) which demonstrated how surface energy fluxes during the anticyclonic regime in summer were associated with high glacier meltwater production. Conversely, during the cyclonic counterpart, it remained near or below zero. The second was the study of Chen et al. (2018), which analysed the impact of clouds on SEB on a continental glacier, and showed how the long-wave downwards increasing due to cloud cover was not enough to counterbalance the decrease of short-wave downward.

Two more studies (Conway & Cullen, 2016; Cullen & Conway, 2017) revealed the impact of clouds on the SEB of a maritime glacier in the southern alps of New Zealand by the use of an automatic weather station located in the ablation area. In line with Chen et al. (2018) also for this maritime glacier, the authors identified the

short-wave downward as the primary source of energy for glacier melt but contrary to the continental glaciers, Conway and Cullen (2016) found a more conspicuous weakening of short-wave downward by the atmosphere (23 %) and clouds (31 %) due to higher humidity in this region located near the marine environment. This study underlined how the meltwater energy during cloudy or clear sky is almost equal during the entire year. In fact, during the summer, warmer and more humid air masses associated with cloudy skies, cause a reduction of short-wave downward counterbalanced by high values of sensible and latent heat flux along with long-wave downward. Hence, unlike the continental glacier studied by Cline (1997) and Chen et al. (2018) here the short-wave downward is less important and can be counterbalanced by other energy fluxes.

At the end of their study, Cullen and Conway (2017) compared the SEB behaviour of their maritime alpine glacier with a transect in the west coast of Greenland (Van den Broeke et al., 2008; Van den Broeke et al., 2009; van den Broeke et al., 2011). The atmospheric transmission of solar radiation is less than observed in the west margins of the GrIS where short-wave downward plays a more important role. However, at both locations, the clouds have a positive effect on long-wave net, increasing the total net radiation, although the reduction of short-wave downward. Finally, turbulent fluxes are directed towards the surface apart for latent heat flux in Greenland due to a predominance of sublimation over deposition (van den Broeke et al., 2011). Overall, the SEB partitioning in the ablation zone in the west coast of Greenland is similar to the SEB of maritime glaciers and acquires characteristics of continental glaciers as the accumulation zone in the interior of the Ice Sheet is approached.

Overall, from the forementioned literature, a cyclonic regime is associated with cold air masses which reduces meltwater production. However, clouds have a positive impact on the GrIS SEB at marine margins, heating the snowpack, reducing refreezing and hence enhancing runoff (Van Tricht et al., 2016). Thus, it is clear, how the impact of cyclones on the GrIS SEB, that carry air masses with different moisture and temperature that interact with each other, generating clouds and precipitation over different regions of the GrIS with different climatic regimes, remains an open

question. Moreover, their positioning and their trajectories can make portions of GrIS fall more under the influence of one air masse than another, with completely different impact in terms of energy and mass balance. Accordingly, this chapter focusses on summer and winter to address the following questions:

1. How do cyclones impact the SMB (and SEB) of the GrIS during the ablation season?
2. Despite winter solid precipitation, can cyclones, in a projected warming scenario, contribute to future GrIS winter decline at the margins where average temperatures are higher and normally close to or above zero?

## 4.2. Data and Methods

### 4.2.1. Data Sources

To examine the impact of extratropical cyclones on the GrIS, the MAR along with the cyclone dataset presented in section 3.2.1 and 3.2.2 are employed for the entire period 1958-2016. To study the SEB and SMB components of the GrIS surface, only pixels of the MAR where the ice cover is more or equal to 50 % are considered to be glaciated. As mentioned in the methods' section of Chapter three, before using the cyclones' dataset, screening was necessary to remove spurious systems. From the NCEP/NCARv1 reanalysis, wind values around cyclone's centre were also extracted to compute cyclone intensity (see Section 4.2.2, below).

### 4.2.2. Methodology

For each cyclone, an Accumulated Cyclone Energy (ACE) index was calculated during its life as the sum of the maximum wind speed at each time step (every 6 hours for the cyclone dataset). To obtain the latter, for each pixel, up to three grid points away from the cyclone's centre, Eq 4.1 was applied to the horizontal  $U_z$  and Vertical  $V_z$  wind at 500 hPa extracted from the reanalysis, and the highest among  $Max$  values was taken for each time step:

$$Max = \sqrt{U_z^2 + V_z^2} \quad 4.1$$

The geopotential height of 500 hPa was chosen for five reasons: (1) the low pressure' centre moves roughly with the speed of the 500 hPa wind above it (Giuliaci et al., 2010); (2) to avoid any possible interference with the GrIS surface; (3) because it is the geopotential height at which cyclonic vorticity is normally calculated due its strong correlation with the GrIS SMB and SEB quantity (Tedesco & Fettweis, 2020); 4) due to its usage in estimating the GBI (Hanna et al., 2013; Hanna et al., 2016) 5) 500 hPa height well depicts the behaviour of the Polar Frontal Jet Stream (Giuliaci et al., 2010). Subsequently, the 20 %, 40 % and 60 % of the most intense cyclones were extracted. This enabled a sensitivity analysis to see if the strength of cyclones affects our conclusions regarding their impact on the GrIS SEB and SMB components.

Regarding the second source of data from the MAR, values of the output of each pixel of each day of the year between 1958-2016 and each variable  $X$  were converted into standardized anomalies  $Z$  (Eq 4.2). The average  $\mu$  and standard deviation  $\sigma$  of each pixel during that day were calculated using the values of that day of the year during the entire period 1958-2016.

$$Z = \frac{X - \mu}{\sigma} \quad 4.2$$

In this study the standardized anomalies were preferred to the real values. This permitted to compare/merge the results of different areas of the GrIS with parameter values of different magnitudes which would have made comparisons difficult.

Subsequently, an algorithm was applied to compute the standardised anomaly of each SMB and SEB variable during cyclonic days. Briefly, the algorithm, extracted the average value of a pixel coming from each daily values when a cyclone was within a distance of 750 km that pixel. This procedure was repeated for all pixels covering the GrIS in order to obtain a clear picture of the spatial distribution of the impact of extratropical cyclones for each variable. The average z-score of each variable over the entire Ice Sheet was then calculated both in winter and summer and also over the ablation region in the latter. Furthermore, by applying Rignot's drainage basins subdivision mask (Figure 4.1) to each map, it was possible to detect, quantify

and compare the spatial variability of cyclones' impact on different drainage basins. Note that, in order to assess the sensitivity of the results to cyclone intensity, the analysis was repeated with the 20 %, 40 % and 60 % of most intense cyclones

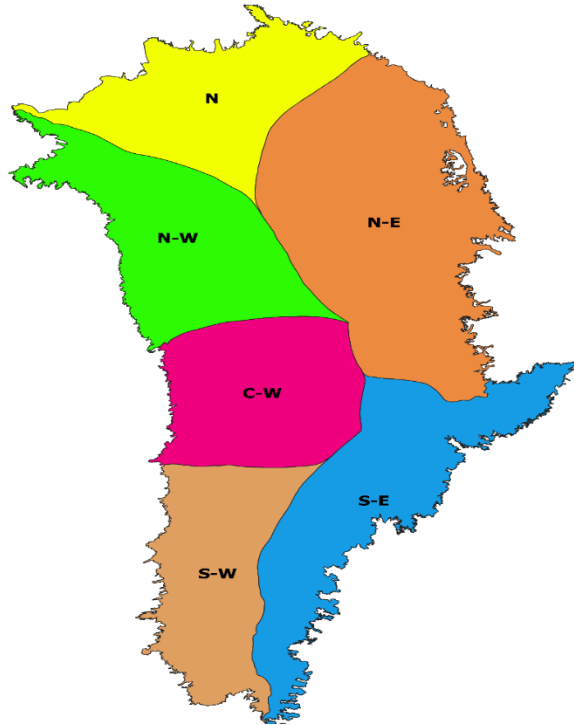


**Figure 4.1.** Map of the Greenland divided into the six main drainage basins produced by E. Rignot and J. Mouginit and used during the ice sheet mass balance inter-comparison exercise (IMBIE) 2016.

## 4.3. Results

### 4.3.1. Winter

The impact, of the 20 % most intense extratropical cyclones (an average of 10 cyclones per winter season) over the entire GrIS on SMB and SEB variables is provided in Figure 4.2. A significant increase of QQZ and TTZ occurs during their passage in conjunction with a positive anomaly of both components of  $LW_{net}$  that are respectively LWD and LWU. Conversely a significant decrease in the SHF is observed. A positive impact is detected on both SMB and SF and a clear surface pressure (SP) negative deviation indicates a cyclonic regime. Overall, no significant deviation from zero is observed for ME, LHF, RA and sublimation (SU) or vertical and horizontal wind UUZ, VVZ.

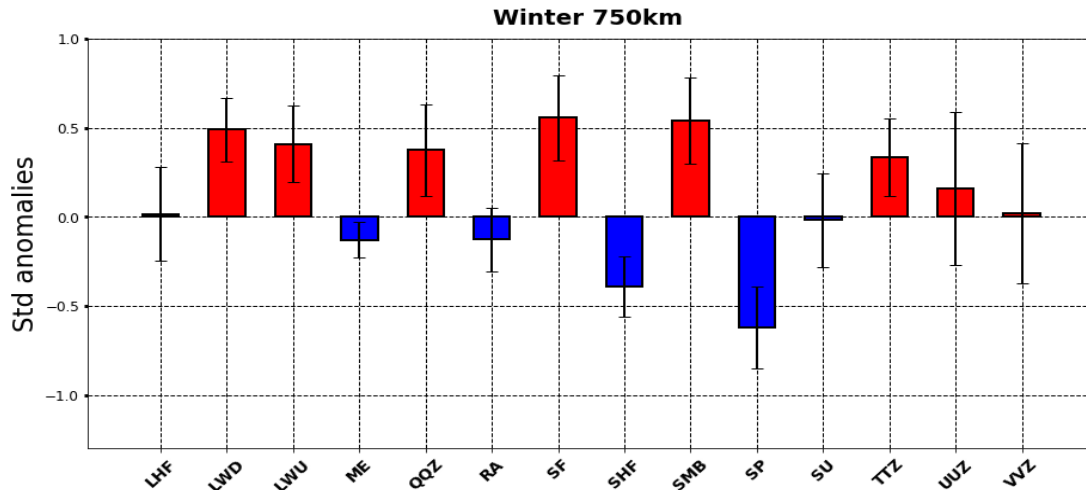


**Figure 4.2.** Standardized anomalies of SMB and SEB variables averaged over the entire GrIS in winter. The average represents the mean value of the MAR pixels where ice cover is more or equal to 50 %. The value of each pixel is calculated by averaging all values in the form of standardized anomaly obtained whenever a cyclone of the 20 % most intense during the period 1958-2016 was within 750 km from that pixel in winter. Vertical bars indicate the standard deviation of the standardized anomalies.

Figure 4.3 and Figure 4.4 indicate the spatial behaviour of the variables, that show the deviation from the average calculated for the 20 % most intense cyclones apart from SF and SP; the results for the 40 % and 60 % most intense cyclones are reported in Appendix B. Figure 4.3b, Figure 4.3c, Figure 4.4a and Figure 4.4b illustrate a similar spatial distribution of LWD, LWU, QQZ and TTZ, with the highest values located in the north and north-west of the Ice Sheet, whereas the lowest values are confined in the south-eastern region. Figure 4.3a shows a slight increase of ME in the ablation region, whereas there is a general negative anomaly of SHF with a decreasing intensity from north to south, apart for a positive narrow strip going from the north-eastern margins to centre of the GrIS (Figure 4.3d). Figure 4.5 shows the comparison of the standardized anomaly of each variable calculated over the entire GrIS considering the 20 %, 40 % and 60 % of the most intense cyclones. Overall, as cyclones of lesser intensity are considered in the sample, a decrease of the magnitude of all variables that significantly deviate from zero, can be observed (apart from TTZ, which remains stable).

Figure 4.6 illustrates the values calculated over each drainage basin considering the 20 % of the most intense cyclones. The S-W and S-E regions have lower values for most of the variables, while N-W, N-E and N are the regions with the highest values. Conversely, the negative anomaly of SHF decreases homogeneously from N-W to N analysing the drainage basins in an anticlockwise direction. Following the same direction, anomaly of surface pressure (SP) increases, although its fall in the N.

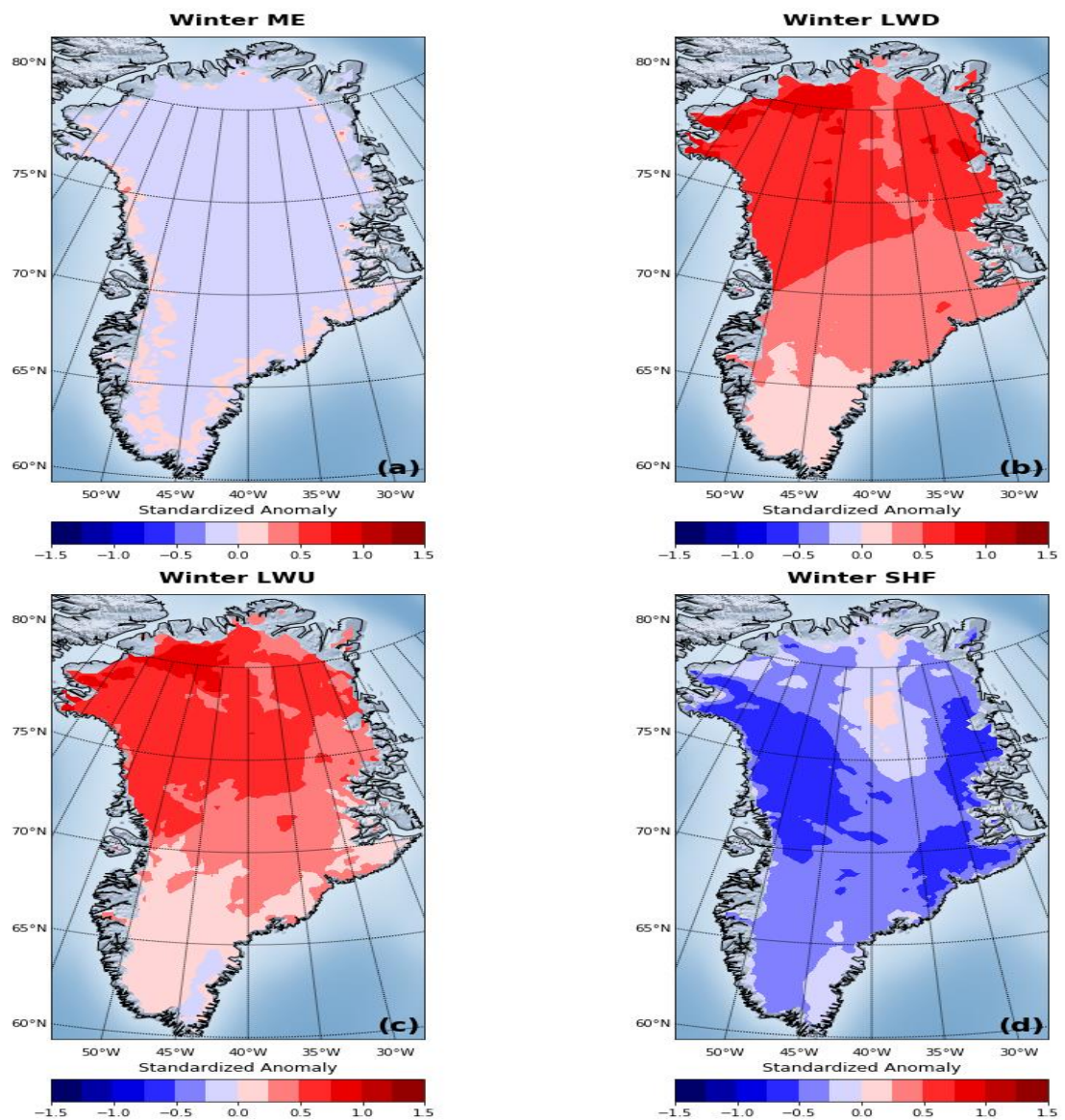


**Figure 4.3.** Spatial representation of the standardized anomalies over the entire GrIS of ME (a), LWD (b), LWU (c) and SHF (d). Value of each pixel is calculated by averaging all values in the form of standardized anomaly obtained whenever a cyclone of the 20 % most intense during the period 1958-2016 was within 750 km from that pixel in winter.

The Impact of Extratropical Cyclones on the GrIS SEB and SMB

Winds show opposite behaviour during the passage of cyclones in the west and east portions of the GrIS with an increase in magnitude in the former and a decrease (albeit not significant) in the latter. Finally, LHF and sublimation (SU) do not show significant positive or negative deviations from the average. Overall, including an increasing number of cyclones of lower intensity (40 % and 60 % of the most intense), the magnitude of the anomalies of all the variables decreases at all the drainage basins (reported in the Appendix C), following the behaviour detected previously.

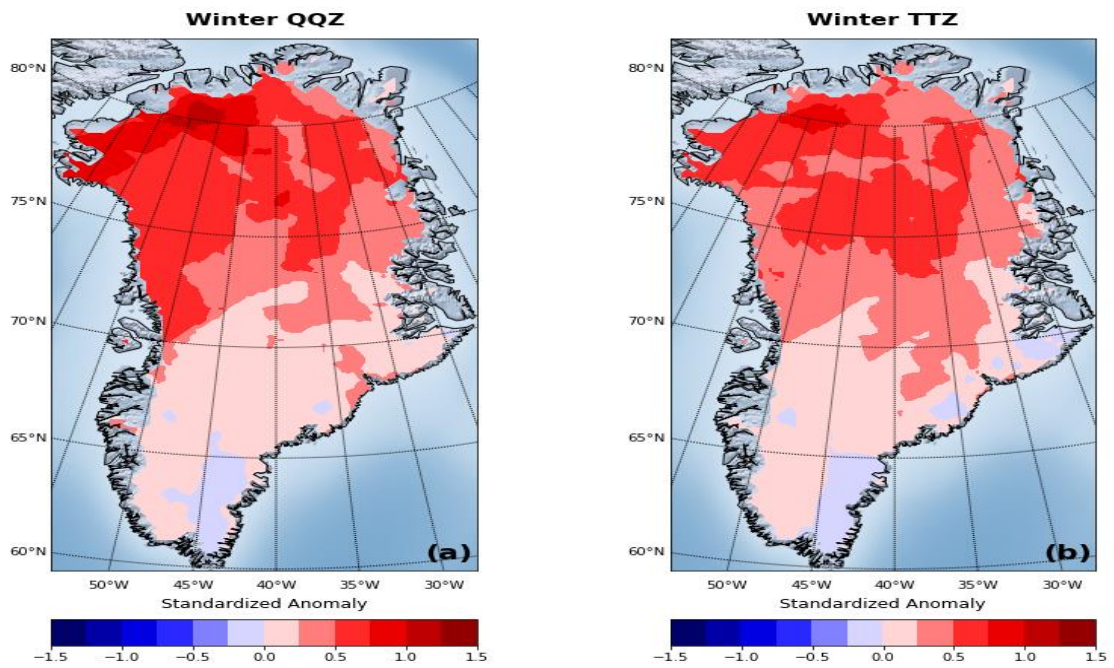


Figure 4.4. Same as Fig 4.4 but for QQZ (a) and TTZ (b).

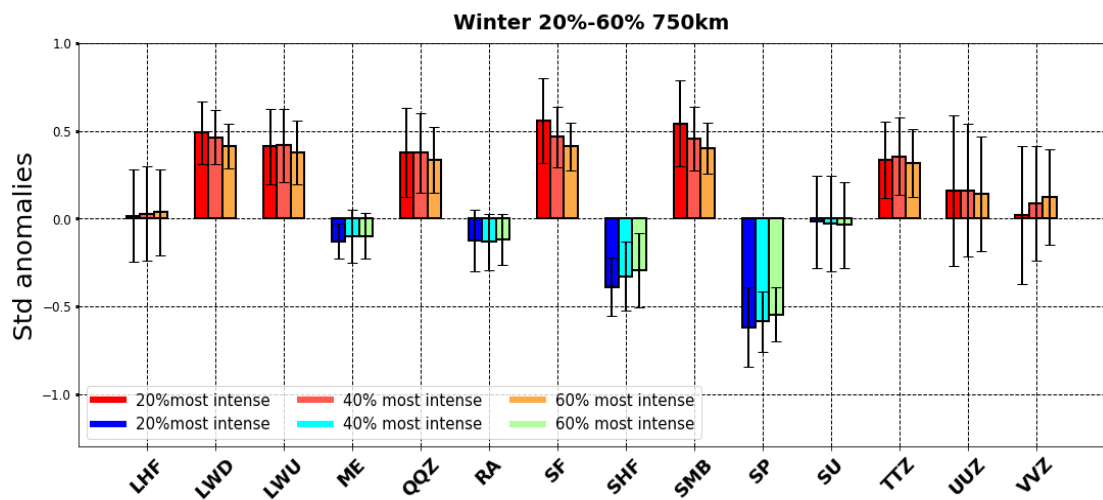
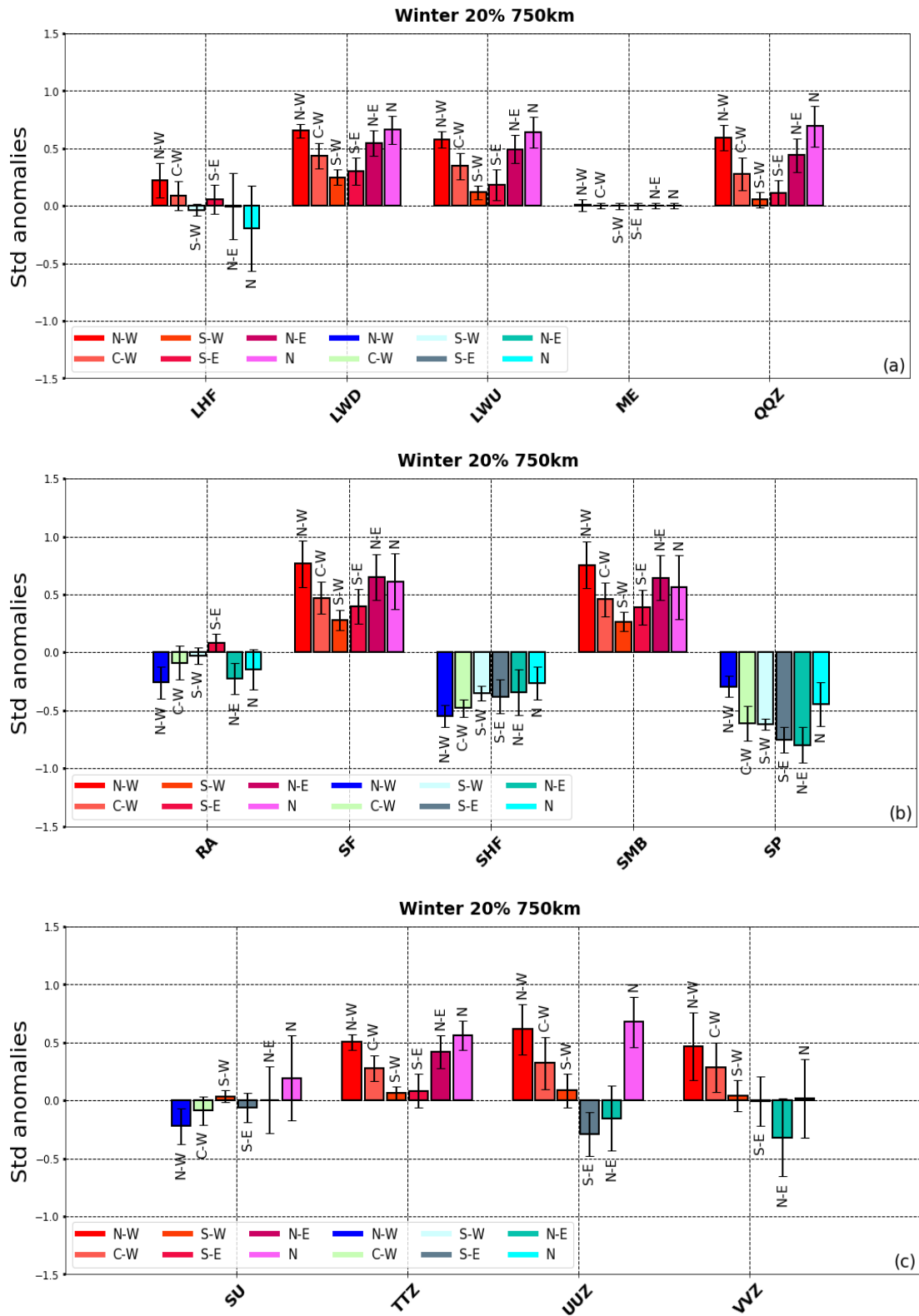


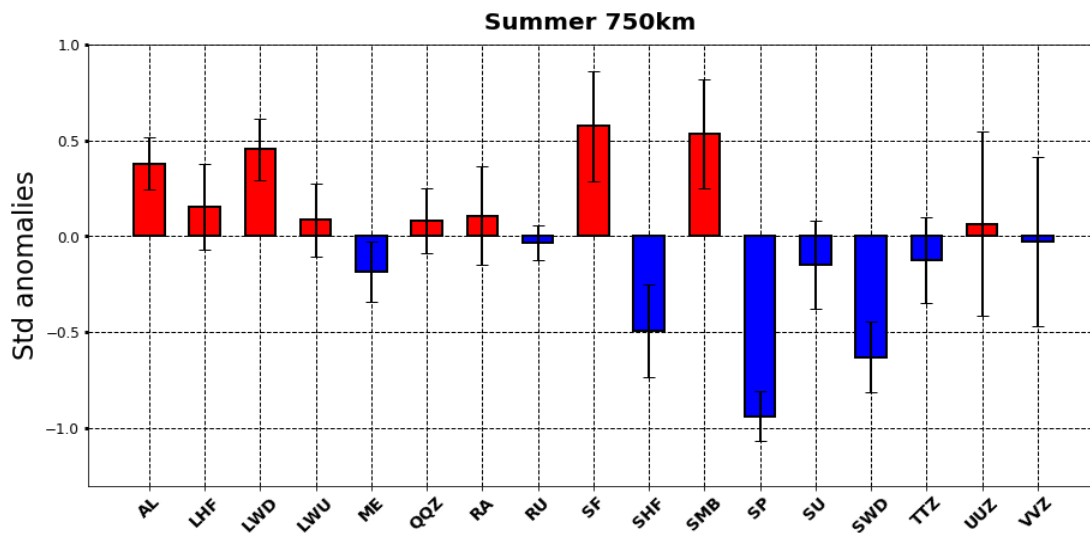
Figure 4.5. Same as Fig 4.2 but calculated by including 40 % and 60 % of the most intense cyclones during the period 1958-2016 in winter.



**Figure 4.6.** Same as Fig 4.2 but calculated for each of the six drainage basins of Fig 4.1.

### 4.3.2. Summer

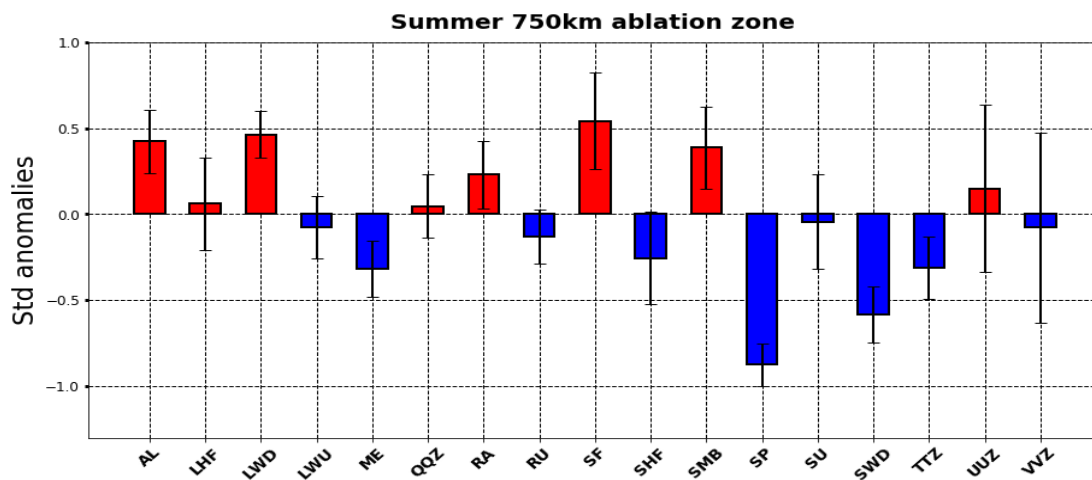
The impact of extratropical cyclones on the entire GrIS SMB and SEB variables is provided in Figure 4.7 for the 20 % most intense cyclones (an average of 9 cyclones per summer season). Overall, their passage has a positive effect on the SMB, via SF and increased AL. As in winter, LWD increases, but it is not counterbalanced by LWU which remains around zero. Negative anomalies of ME, SHF and SWD are observed. Overall, anomalies of LHF, LWU, QQZ, RA, RU, sublimation (SU) and TTZ have values not significantly different from zero while a clear negative surface pressure (SP) deviation, indicates a cyclonic context. Focusing only on the ablation zone (Figure 4.8) the deviation value of the SHF it is still negative, although less pronounced. Lower (higher) and statistically significant values of TTZ along with ME (RA and AL) are observed while slightly lower values of SMB and SF are detected.



**Figure 4.7.** Standardized anomalies of SMB and SEB variables averaged over the entire GrIS in summer. The average represents the mean value of the MAR pixels where ice cover is more or equal to 50 %. Value of each pixel is calculated by averaging all values in the form of standardized anomaly obtained whenever a cyclone of the 20 % most intense during the period 1958-2016 was within 750 km from that pixel

In order to explore spatial variability in the impact of extratropical cyclones on the GrIS SMB and SEB, the main parameters are plotted on a pixel-by-pixel basis for the most intense 20 % of systems in Figure 4.9 and Figure 4.10 (results for the 40 % and 60 % most intense cyclones are reported in Appendix D). Over the entire Ice

Sheet, during summer, the passage of cyclones is associated with a general increase of AL and LWD, along with a decrease of SHF and SWD. However, it is worth underlining the north-eastern area of the GrIS where the SHF become positive and other variables aforementioned are close to zero or become of an opposite sign if compared to the rest of the GrIS. Furthermore, the reduction of the negative value of SHF already found previously in the ablation zone is confirmed by Figure 4.9d, where positive values can be observed along the GrIS margins. Finally, TTZ and ME show a similar behaviour with an increase in the high accumulation zone and a decrease in low accumulation zone and ablation zone.



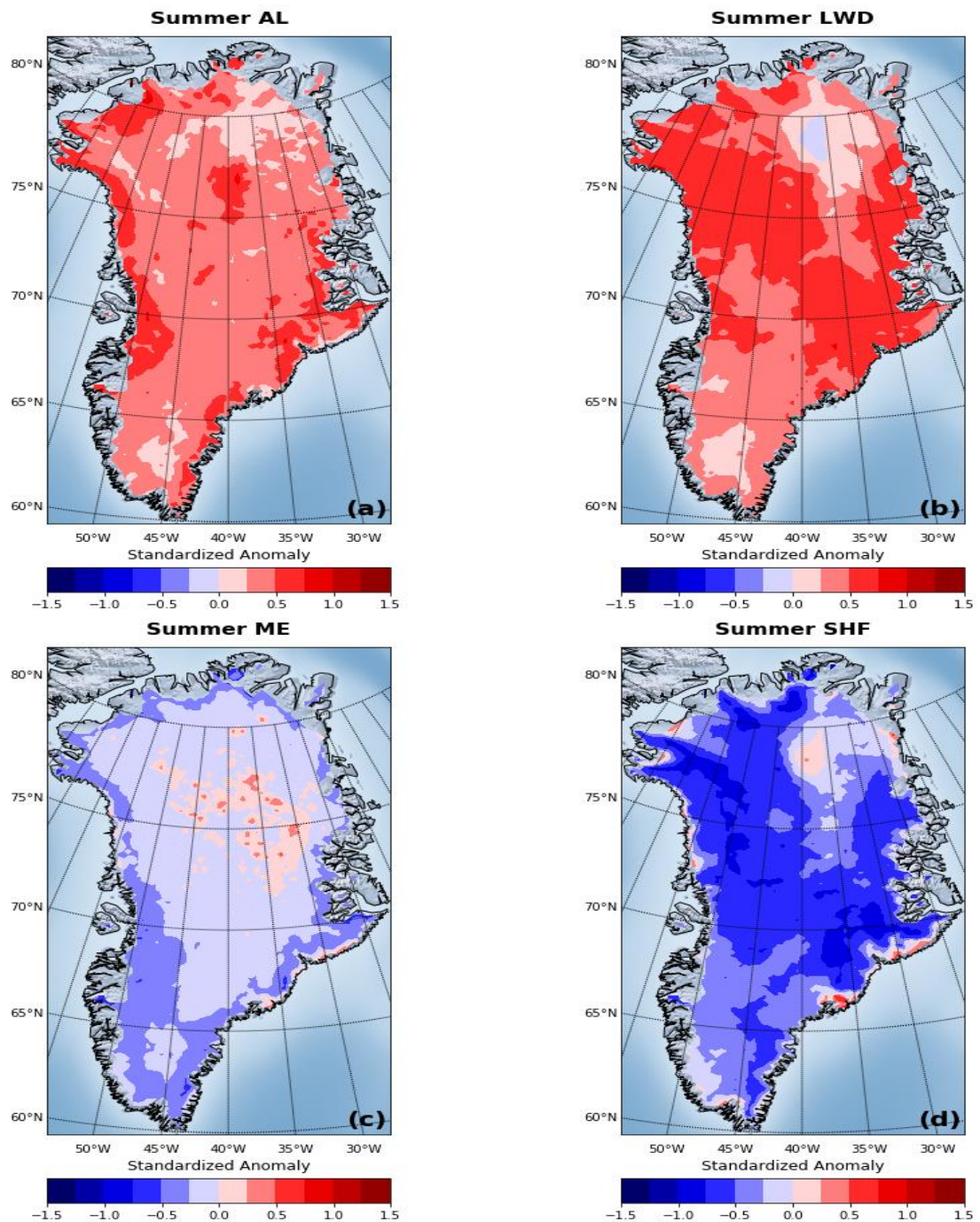
**Figure 4.8.** Same as Fig 4.7 but only for the ablation zone.

Figure 4.11 and Figure 4.12 show the standardized anomaly for each variable considering the 20 %, 40 % and 60 % of the most intense cyclones over the entire ice sheet and ablation zone. As for winter, a decrease in magnitude of all values can be observed as of the intensity of cyclones is reduced.

Figure 4.13 and Figure 4.14 illustrate the values calculated over each drainage basin, considering the 20 % of the most intense cyclones. Unlike in winter, during summer the anomaly values of many variables don't present a clear behaviour across the basins. SMB, SF, LWD and SWD are an exception where values are particularly high in the N-W and low in the S-W. It is important to note that the anomalies of many variables are often not very pronounced in this latter basin if compared to the others as detected in winter. Conversely, the lowest negative value of ME is detected in this basin. The basins located in the North and West are affected by an increase in

## The Impact of Extratropical Cyclones on the GrIS SEB and SMB

south-westerly winds while winds from north-east most affect the south-eastern drainage basins.



**Figure 4.9.** Spatial representation of the standardized anomalies over the entire GrIS of AL (a), LWD (b), ME (c) and SHF(d). Value of each pixel is calculated by averaging all values in the form of standardized anomaly obtained whenever a cyclone of the 20 % most intense during the period 1958-2016 was within 750 km from that pixel in summer.

The Impact of Extratropical Cyclones on the GrIS SEB and SMB

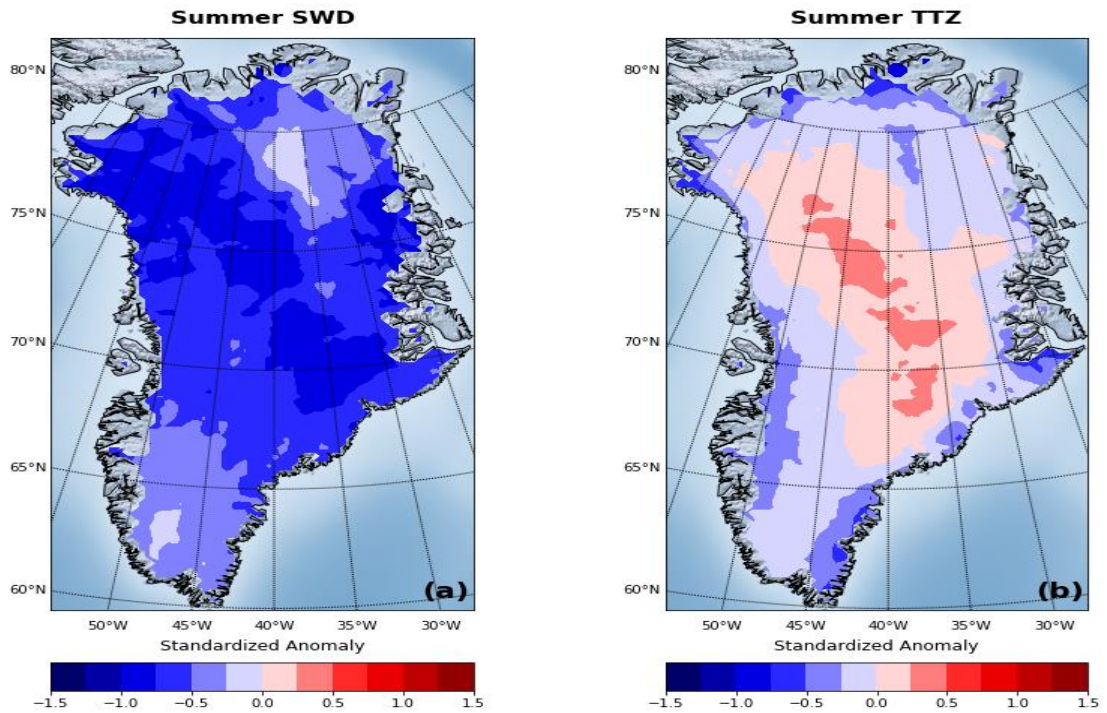


Figure 4.10. Same as Fig 4.9 but for SWD (a) and TTZ (b).

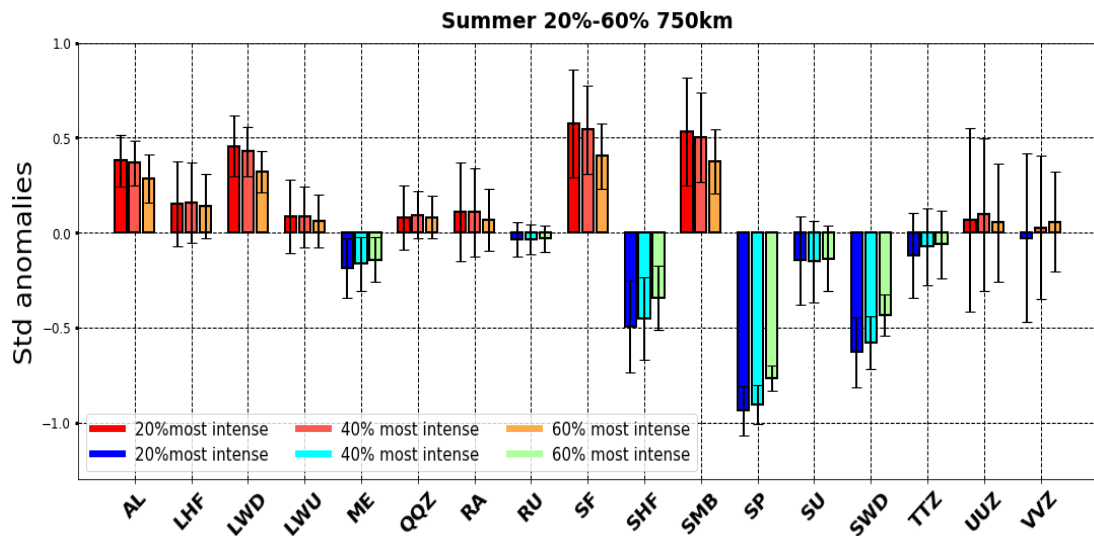


Figure 4.11. Same as Fig 4.7 but calculated by including 40 % and 60 % of the most intense cyclones during the period 1958-2016 in summer.

The same procedure was applied, but only for the ablation zone (Figure 4.15 and Figure 4.16). Unlike the whole basins, the decrease of ME, RU and TTZ is more pronounced with RU and TTZ statistically significant below the average. A less positive SMB and SF is observed if compared to values over the entire GrIS whereas, an increase in AL is detected and positive values of RA become statistically significant over most of the basins. Overall, including an increasing number of cyclones of lower

The Impact of Extratropical Cyclones on the GrIS SEB and SMB

intensity (40 % and 60 % of the most intense), a reduced magnitude of the anomalies across all drainage basins and their ablation zone is observed (reported in Appendix E).

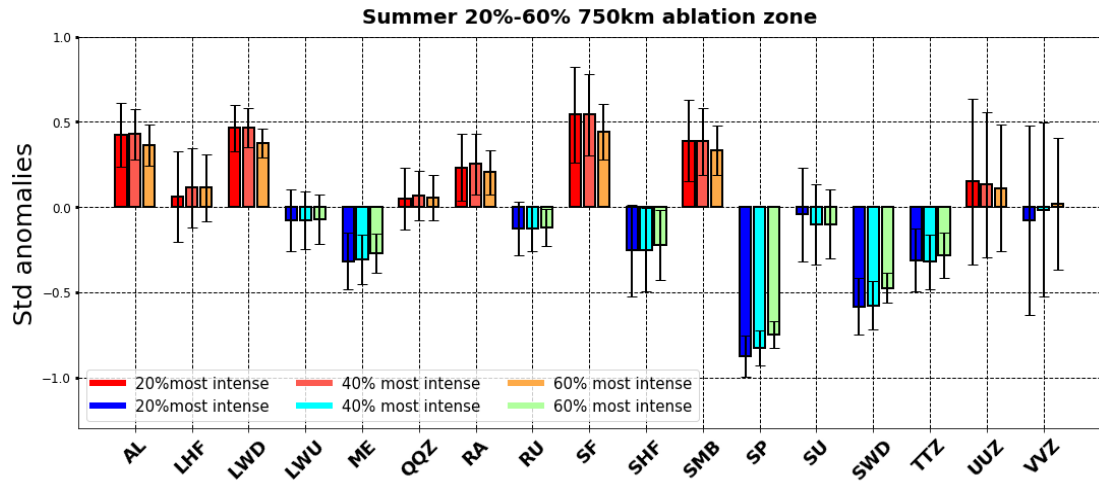


Figure 4.12. Same as Fig 4.11 but only for the ablation zone.

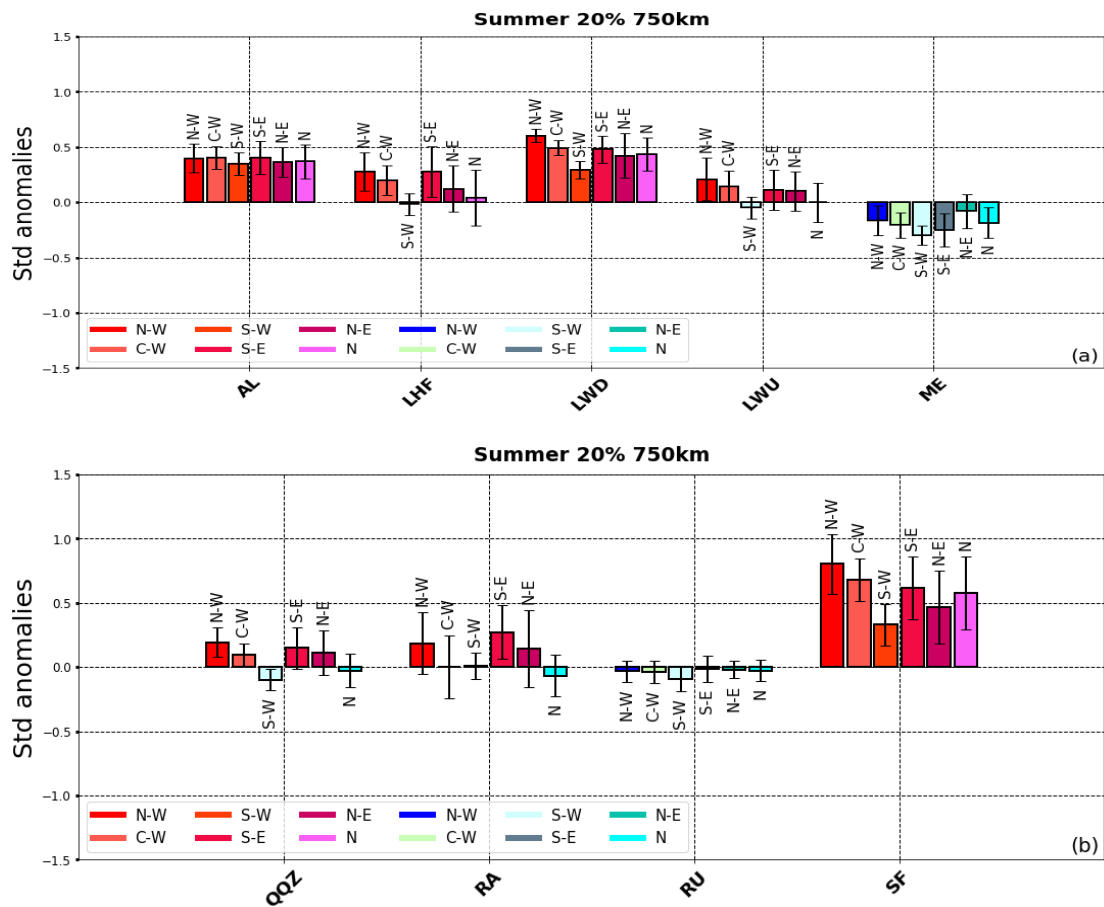
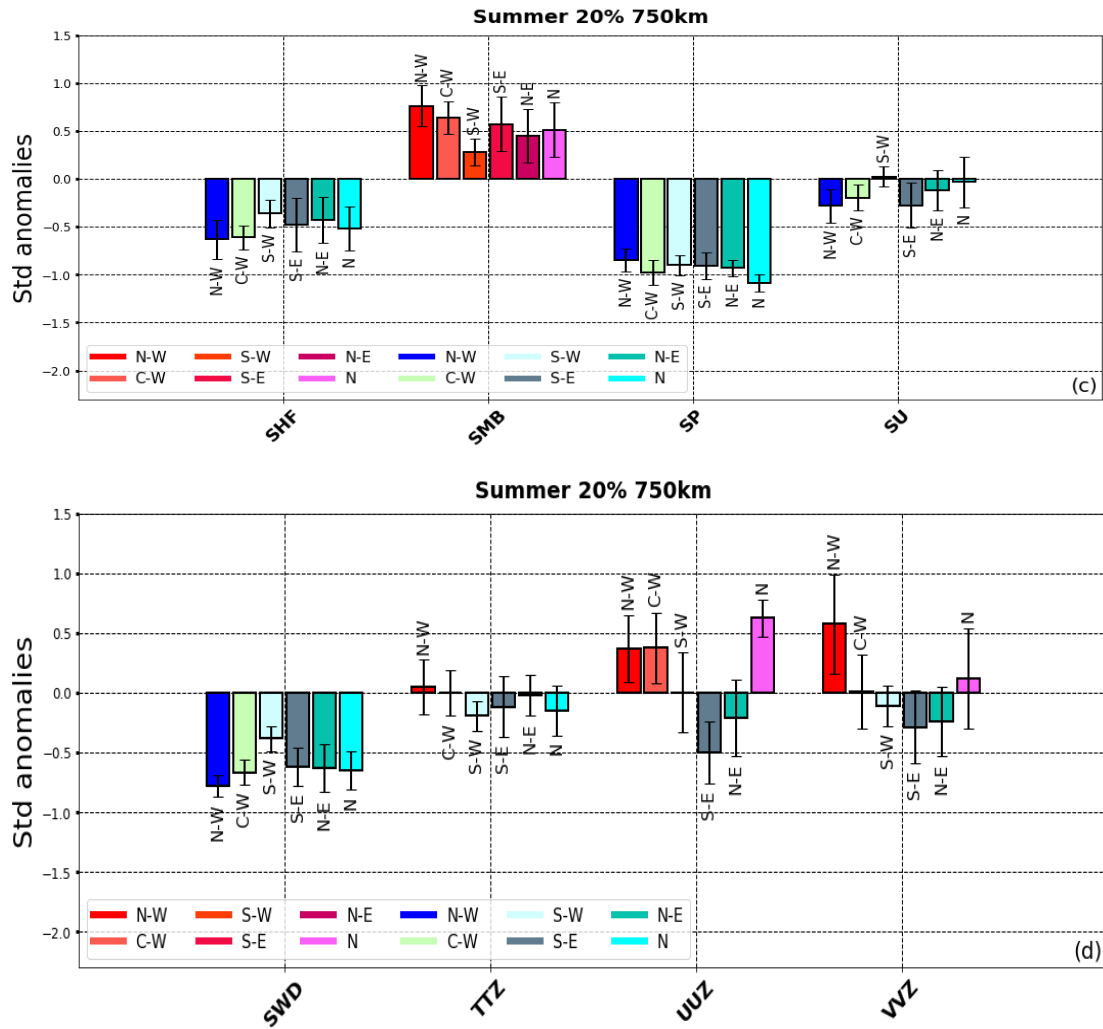


Figure 4.13. Same as Fig 4.7 but calculated for each of the six drainage basins of Fig 4.1.



**Figure 4.14.** Same as Fig 4.7 but calculated for each of the six drainage basins of Fig 4.1.

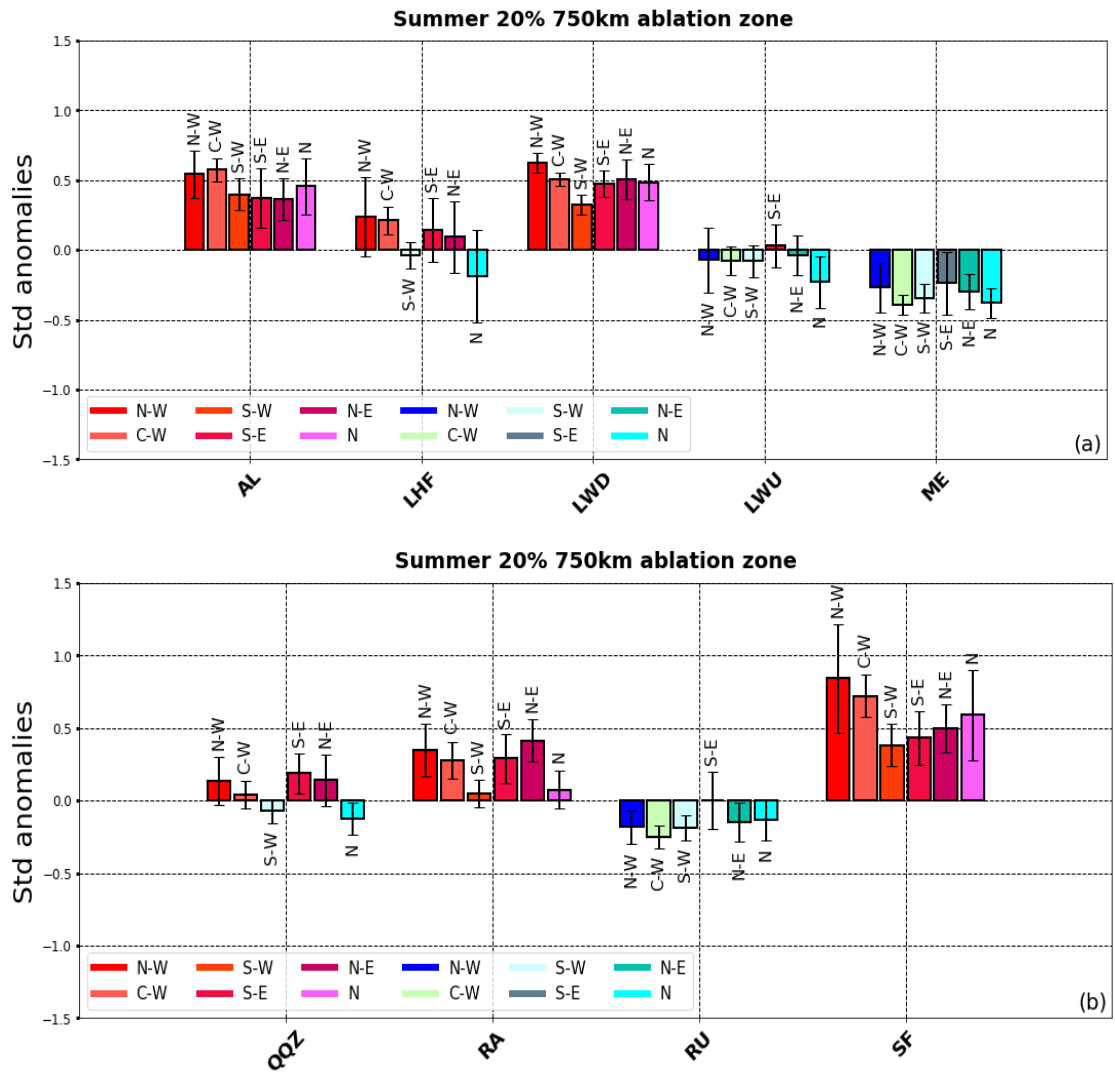


Figure 4.15. Same as Fig 4.13 but only for the ablation zone.

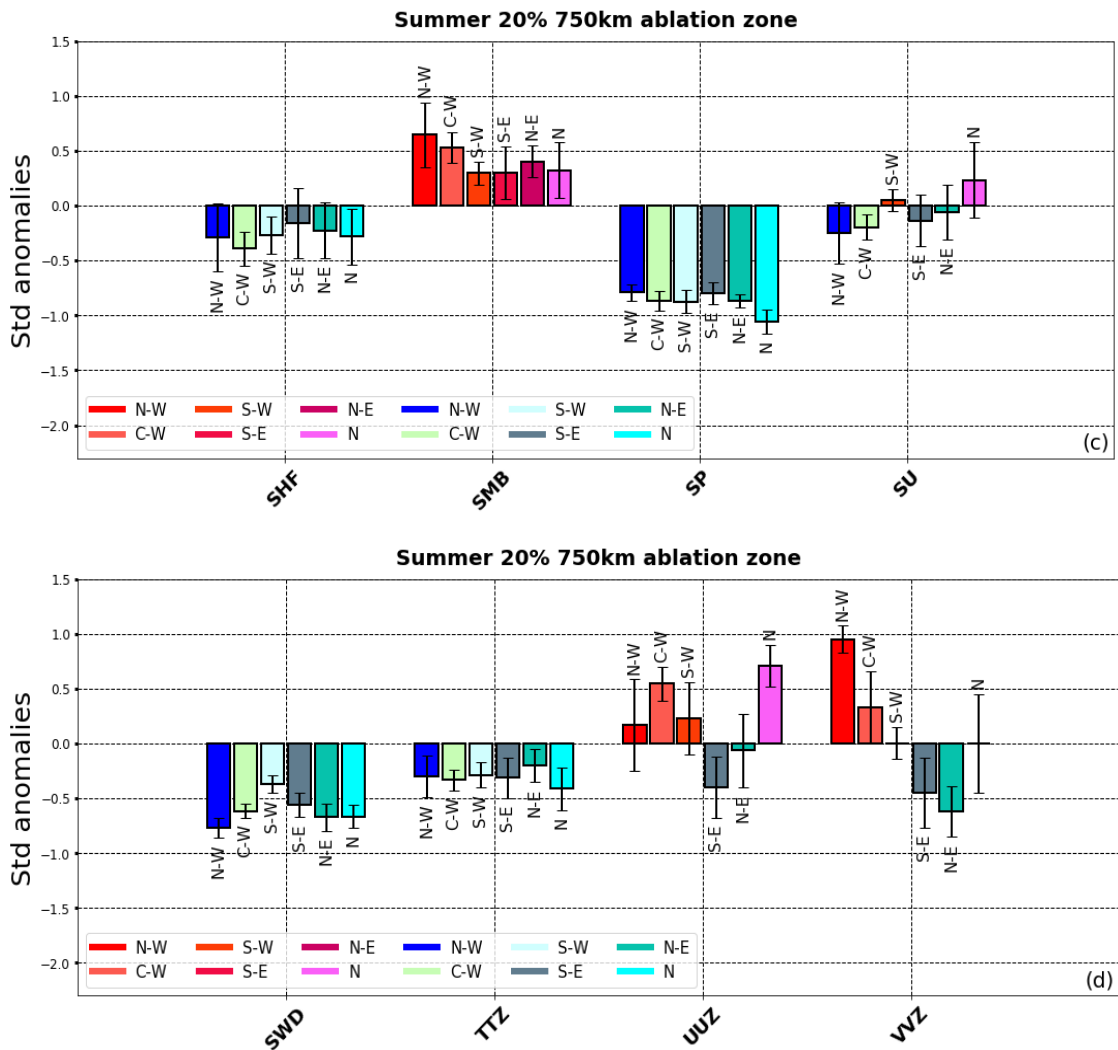
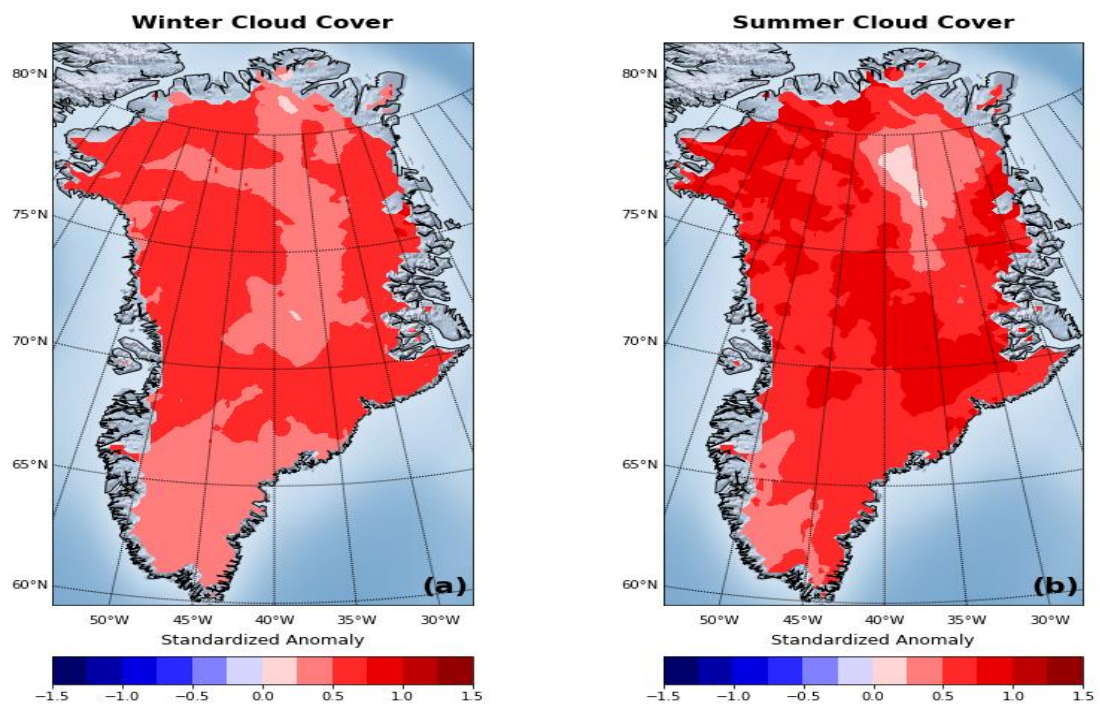


Figure 4.16. Same as Fig 4.14 but only for the ablation zone.

#### 4.4. Discussion

In this study, positive temperature anomalies were detected in winter over almost the entire GrIS during the passage of extratropical cyclones. This leads to the conclusion that the inflow of warmer than average air carried by cyclones had a greater influence than the colder counterpart characterised by polar air. The southerly winds not only carried heat, but also moisture over the ice sheet, resulting in increased relative humidity and cloud cover (Figure 4.17) (results for the 40 % and 60 % of the most intense cyclones are reported in Appendix F). They favoured overcast sky, increasing the long-wave downward and solid precipitation which via the latent heat release contributed to temperature rise and a positive surface mass

balance. This is in line with the study of Van den Broeke et al. (2008) who showed over the GrIS the relation between long-wave downward magnitude and sky emissivity which in turn is in function of air moisture and temperature. High sky emissivity and temperatures favoured an increase in the long-wave upward radiation detected over the entire GrIS which is a direct measure of its surface temperature. A pronounced decrease of sensible heat flux was detected, mainly due to a lower temperature difference between the air and the surface which is heated by long-wave downward and perturbed by a more sustained ventilation. However, despite its decrease, it remained positive (heat directed towards the surface) due to the thermal inversion which caused the surface and the lower air layers, in clear sky conditions and weak ventilation, to cool more than those above (Van den Broeke et al., 2009). Overall, despite the decrease in sensible heat flux, the positive temperature anomaly and increase of long-wave downward played a fundamental role in favouring meltwater production at the margins where average temperatures are higher and normally close to or above zero (Cappelen et al., 2014).



**Figure 4.17.** Same as Fig 4.9 but for cloud cover in winter and summer.

Despite the large positive anomalies of long-wave downward, long-wave upward, specific humidity and temperature, if calculated over the entire GrIS, important

differences emerge analysing their spatial behaviour over different drainage basins. In winter, the major anomalies were found in the area that includes all northern Greenland and especially the north-west with a decrease moving towards the south-east until encountering values of opposite sign. This is likely for two reasons. The first is the low frequency of cyclonic conditions in the North (see Section 3.4.3) (Serreze, 1995; Chen et al., 1997; Serreze et al., 1997) which makes the standardized anomalies of variables during the passage of cyclones more pronounced. The second relies in the fact that cyclones approaching the GrIS from west or south-west are blocked in their eastward flow due to the height of its central area (Chen et al., 1997). Here, they are forced to stop into Baffin Bay, where they decay or move up to the Arctic Ocean (Serreze, 1995). Thus, during a cyclonic event with the centre located in this area, the west and north-west regions experience warm and moist air advection from the south instead of the influx of cold air masses from the north.

Conversely, the south-east was influenced by a frequent passage of cyclones (see section 3.4.3) that with their movement from the Labrador Sea/ North Atlantic Ocean towards a region between the Greenland strait and south of Iceland, led the advection over the GrIS of polar air masses instead of the warm subtropical ones. This made the anomalies in this region, and generally in the southern part of the GrIS minor or of the opposite sign if compared to the rest of the GrIS.

Finally, it is important to highlight the slightly positive anomalies of the sensible heat flux in a strip extending from the edges to the centre of the GrIS in its north-western part. This may be due to an increase in descending winds (Foehn) coming from the higher areas of the GrIS and driven by the cyclonic circulation located over the Baffin Bay. The adiabatic compression of this dry wind would be consistent with the reduction in cloud cover (Figure 4.17), with a decrease in the long-wave downward and an increase in temperature which heats the surface and increases the sensible heat flux.

In summer, the cyclonic passage led to an increase in the long-wave downward and a decrease in the short-wave downward, both consistent with an increase in cloud cover (Figure 4.17b). Clouds can also cause snowfall over the GrIS, further reducing the net shortwave radiation due to the higher albedo, especially in

the ablation zone where the absorbed solar energy is the dominant factor governing surface melt variability (Box et al., 2012). Along with snow, at the GrIS margins, cyclones can lead to rainfall that can go beyond the ablation zone (Davison et al., 2019). However, observing the spatial behaviour of the temperature, it is clear its increase in the highest central part of the GrIS and decrease elsewhere, especially in the ablation zone. Thus, cyclones in summer were associated with colder air masses that together with a strong decrease in incident short-wave radiation had the capacity to lower the temperature during their passage in the ablation zone, diminishing meltwater production.

Conversely, in the high accumulation zone, the solar radiation has less influence due to high albedo. Here, the increase of the long-wave downward radiation together with the latent heat release, due to condensation of rising air masses on the GrIS, counterbalanced the loss of short-wave downward. This favoured a modest increase in temperature and melt in this area. Overall, the sensible heat flux was negative over almost the entire GrIS due to a lower temperature difference between the surface and the air above caused by the advection of cooler air. Even in summer, the positive anomaly of sensible heat flux in the north-eastern area, is likely due to the warm and dry descending winds coming from the south-west. This hypothesis is confirmed by a simultaneous decrease of long-wave downward and increase short-wave downwards in this area due to lower cloud cover (Figure 4.17b), that could be related to lower values of humidity.

Unlike in winter, the frequency of cyclones in summer appears more uniform over the whole of the GrIS (see section 3.4.3) and this is due to a synchronous north-shift of the storm tracks and a weakening of the Icelandic Low (Cappelen et al., 2001). The spatial distribution of the summer variables anomalies confirms this behaviour by showing only a less pronounced gradient along the north-south direction.

Overall, this work underlines the cyclones' positive contribute on GrIS SMB both in winter and summer. A constant presence of cyclonic regime during the cold season guarantees high level of solid precipitation whereas, in summer, the event of snowfall and cold air can dampen the meltwater runoff and increase albedo in the ablation zone. For these reasons, their decrease in frequency along with an

intensification of strong anticyclonic events over Greenland during the last two decades in summer (Chen et al., 2016) have led to a long dry periods with high temperatures and clear sky, enhancing a positive surface energy balance and consequent widespread surface GrIS melting (Fettweis et al., 2010; Fettweis et al., 2013b).

As shown by the sensitivity analysis, a decrease of cyclone intensity is related to reduction in the anomaly magnitude for each variable. What appears evident is how cyclones with lower central pressure (associated with stronger winds and precipitation) have a greater impact in reducing melt in summer and increasing the surface mass balance in both seasons. This allows us to conclude that changes to the intensity of extratropical cyclones (in addition to changes in frequency) may should be considered in future projections of the GrIS SMB.

Indeed, future projections indicate an increase in frequency and intensity during summer, and a slight decrease in intensity in winter; increases in precipitation are anticipated under cyclones for both season (Zappa et al., 2013). However, in a global warming scenario, the state-of-the-art global climate models (McCrystall et al., 2021), predict over Greenland a replacement of rainfall at the expense of snowfall at the GrIS margins at higher altitudes favoured by higher temperature. In this direction, a recent study carried out by Oltmanns et al. (2019), confirms that this trend is already underway, with an increase in frequency and magnitude of melt events and rainfall, triggered by cyclonic-induced warm advections during the last decades. These findings along with our results, should imply a future decrease in Greenland mass gain within a single cyclonic event, especially in ablation zone where temperatures are around the freezing point both in winter and summer. Here, rainfall will be more frequent and extended at the expenses of solid precipitation, and the ability in dampening meltwater production in summer will be reduced due to higher temperature. However, some doubts remain regarding the future magnitude of this process, driven by the uncertainties related to cloud modelling, which impact on SEB is more important in terms of SMB than the uncertainties in future temperature estimation (Hofer et al., 2019).

## 4.5. Conclusion

The aim of this chapter was to investigate the direct impact of extratropical cyclones on each component of the SEB and SMB of the GrIS. The analysis enabled identification of which variables are most affected by the passage of cyclones. This investigation was pursued by the use of a cyclone dataset covering the entire northern hemisphere obtained from the study of NCEP-NCAR reanalysis and the MAR forced by the same reanalysis for the entire period 1958-2016. The impact of extratropical cyclones on each SEB variables and SMB, over the entire GrIS was established. A general positive impact of cyclones on the SMB was detected especially via snowfall (which enhances albedo in summer and hence reduces melt energy). In winter, they enhance the radiative forcing, increasing the temperature but not enough to produce enough meltwater at the margins to counterbalance the solid precipitation. In summer, their passage reduced the short-wave downwards over the entire GrIS and temperature along the margins, in the ablation zone, decreasing the meltwater production. Conversely, air masses associated with their passage over the highest interior of the GrIS increased the temperature and energy balance directed towards the surface, increasing melting. A sensitivity analysis showed an overall decrease in intensity of almost all variables as the magnitude of the cyclones decreases.

Despite their positive contribute to the GrIS SMB, as previously underlined, future projections suggest an increase in cyclone-induced meltwater episodes, along with upslope shift of the limit between rain and snowfall. This may increase episodes of large pulses of water capable of reaching the bed of the GrIS at ever higher altitudes, perturbing the subglacial drainage system. In turn, this could have an impact on the mass balance of the GrIS by affecting the ice motion of its glaciers, although still unknown. In this context, the aim of the next chapter, will be to expand the knowledge in this direction and try to fill this gap, by studying the impact of different cyclonic events over different sites of the GrIS which include both land and marine terminating glaciers. This will allow us to establish more clearly if this

The Impact of Extratropical Cyclones on the GrIS SEB and SMB

mechanism is frequent and must be considered in future studies concerning the decline of the GrIS driven by cyclonic rainfall.

## *5. Late Summer/Early Autumn Cyclonic Rainfall and Ice Flow of the GrIS*

---

### **5.1. Introduction**

During the past two decades, many studies have been done to understand the ice motion response of the GrIS land margins to increases in meltwater runoff during the summer period (Sole et al., 2013; Tedstone et al., 2013; Tedstone et al., 2015; Mottram et al., 2017; Cowton et al., 2018; Williams et al., 2020). The most important factor influencing seasonal to interannual ice flow of land terminating glaciers of the GrIS is the dynamic response of the subglacial drainage system to variability in surface meltwater (see section 2.4.3)(Zwally et al., 2002; Bartholomew et al., 2010; Schoof, 2010; Bartholomew et al., 2011; Colgan et al., 2011; Hoffman et al., 2011; Bartholomew et al., 2012; Andrews et al., 2014; Hoffman & Price, 2014). A general increase of ice motion is observed during the early melt season due to the first intense meltwater pulses which overwhelm the subglacial drainage system (Creys & Schoof, 2009; Schoof, 2010; Werder et al., 2013; Andrews et al., 2014; Davison et al., 2019). However, due to the development of an efficient drainage capacity, a decrease of ice motion during the rest of the season is observed, that can intermittently increase only through meltwater pulses larger than those earlier in the melt season (Iken et al., 1986; Schoof, 2010; Bartholomew et al., 2011; Cowton et al., 2013).

Research over the last decade suggests that strong meltwater production in some land-terminating glaciers initiates faster movement during the early melt season, which is systematically offset by a subsequent slower-down resulting in an overall decrease in ice motion at an annual scale (Sundal et al., 2011; Sole et al., 2013; Tedstone et al., 2013; Nienow et al., 2017). It is suggested that this “self-regulation” mechanism may reduce the dynamic thinning of glaciers in a future warmer climate (Davison et al., 2019; Oltmanns et al., 2019).

Conversely, Davison et al. (2019) and Doyle et al. (2014) highlight that self-regulation at higher altitudes on the GrIS has not been detected and an ice velocity

increase is observed during warmer summers at these locations. It is not clear if self-regulation will migrate further inland in a warming climate scenario. However, as argued by Davison et al. (2019) in the future, the presence of glacial melt lakes and their drainage will likely take place at ever higher altitudes as summer with high melt rate are expected to be the usual situation at the end of this century. These will allow an expansion of the connection systems between the surface and the bed, with a probable ice velocity increase in a warmer climate.

Another factor which has the potential to produce large surface water input to the bed is demonstrated by the pioneering study of Doyle et al. (2015). They showed how an intense period of cyclonic rainfall resulted in a sudden acceleration, interrupting the decrease of ice motion due to self-regulation mechanism in the ablation zone of two land-terminating glaciers in West Greenland. This large input of surface water to the bed was able to overwhelm the subglacial drainage system during the key period of late summer/early autumn when it was in transition to an inefficient drainage mode. This work showed, for the first time, the potential impact of cyclonic rainfall on ice motion although it only provides information on one event at a particular location and time of year and to what extent this can be generalised remains undetermined. To understand the potential impact of cyclonic rainfall events on the annual velocity and hence on dynamic thinning of the GrIS, which influence the SLR, more events need to be studied to fully determine the spatial and temporal effects of these events. In addition, studies considering marine terminating environments should be analysed as, unlike land terminating glaciers, marine terminating glaciers show a recent overall increase in annual velocity (Howat et al., 2007; Benn et al., 2017; Van den Broeke et al., 2017).

Generally, the frequency, amplitude and duration of cyclonic rainfall events have increased in the recent past (Oltmanns et al., 2019; Niwano et al., 2021) and are predicted to further increase in a future warming scenario (Schuenemann & Cassano, 2010; Doyle et al., 2015; Oltmanns et al., 2019). Thus, understanding their impact on the GrIS and how this might change in the future is a key area for prediction of SLR driven by the GrIS dynamic thinning.

In order to help address this gap in the research, expand the knowledge on this topic and consolidate the results obtained by Doyle et al. (2015), this chapter focuses on analyses of the impact on ice velocity of multiple cyclonic rainfall events on both land and marine terminating glaciers in the ablation zone in the west/south-west regions of the GrIS. This area was chosen as it is one of the low elevation areas of the GrIS where the increase in altitude from the margins is more gentle than elsewhere (Howat et al., 2014) and this, together with low latitude of this region, makes this portion of the GrIS the warmest (Rae et al., 2012). It was the most sensitive to increases in temperature in the recent past, present and future (Tedesco & Fettweis, 2012), and therefore also to events of rainfall (Niwano et al., 2021). The period of late summer/early autumn was chosen for this study as this is seen as a crucial period during which surface melt is beginning to decrease and the drainage system would normally be slowly closing down towards an inefficient system.

## **5.2. Data and Methods**

### **5.2.1. Data Sources**

The amount of cyclonic rainfall affecting the GrIS margin along with all relevant meteorological and glaciological parameters were extracted from the MAR (presented in section 3.2.1 and 3.2.2). Data from NCEP/NCARv1 reanalysis (Kalnay et al., 1996) were utilised to show their meteorological framework in terms of geopotential heights over the entire Greenlandic region. The three ice velocity datasets utilised were the product of two different projects. The first dataset, comes from the Global Land Ice Velocity Extraction (GoLIVE) project, version 1 (Scambos et al., 2016) (hereafter GoLIVE). The second project is the Making Earth System Data Records for Use in Research Environments (MEaSUREs) which includes the second and third datasets, available through the National Snow & Ice Data Centre (NSIDC) portal and are respectively 1) the MEaSUREs Greenland Ice Velocity: Selected Glacier Site Velocity Maps from InSAR, Version 3 (Joughin et al., 2020) (hereafter MEaSUREs selected glaciers) and 2) MEaSUREs Multi-year Greenland Ice Sheet Velocity Mosaic, Version 1 (Joughin et al., 2016) (hereafter MEaSUREs multi-year). These satellite data

products are explained below and summarised by a summary table at the end of this section (Table 5.1).

Ice velocity data in the first dataset GoLIVE were obtained from a technique called feature tracking, applied to optical panchromatic image pairs of 16 days from Landsat 8 satellite (Scambos et al., 2016). These data were provided with a resolution of 300 m and velocity are reported in  $m d^{-1}$  with an accuracy varying from  $0.02 m d^{-1}$  to  $1 m d^{-1}$ . The principle behind the feature tracking is the image matching which consists of identifying the same point in two satellite images taken at different times (Rosenau et al., 2015). If between image 1 and image 2 the point has moved, for example due to glacial flow, its coordinates will be different in the two images. The match between each image pair is generated by an image correlation algorithm applied on each pixel of both images. The algorithm compares each pixel of a feature within a variable size search box of the first image with a range of possible matching features in the second image. The best match is determined by the algorithm and horizontal displacement is calculated. Error estimates are provided with the data and include the statistical uncertainty of the correlation algorithm to accurately capture pixel offset and a value for geolocation errors between the two images.

The second dataset of MEaSURES selected glaciers, were derived using a combination of conventional Interferometric Synthetic Aperture Radar (InSAR) and speckle tracking techniques applied to image pairs of 11, 22 and 33 days, measured on an 11-day repeat cycle of the German Aerospace Center's (DLR) twin satellites TerraSAR-X / TanDEM-X (TSX/TDX). They are provided at a resolution of 100 m and velocity reported in  $m yr^{-1}$  with an accuracy from few to dozens  $m yr^{-1}$ . In regions where it was not possible to extract ice velocity, data were calculated through interpolation of data from surrounding areas. Error estimates are provided for all non-interpolated data. These include the statistical uncertainty associated with the InSAR and speckle tracking techniques (Joughin, 2002).

The conventional InSAR technique is based on the use of pairs of radar images where the microwave signal emitted from the satellite is "reflected" from the Earth's surface and captured by the satellite sensor. Given a pair of radar images of the same area collected during different days, this technique is able to produce interferogram

from the difference in phase of the return radar signals of the two images, which contain information regarding the displacement of the surface (Rao, 2011). This information can be extracted with a process of measuring the number of these phases called interferometric phase unwrapping (Rao, 2011). However, in many high accumulation areas or fast-moving glaciers ( $100 \text{ m yr}^{-1}$ ) phase unwrapping is not possible and often fails (Joughin, 2002). Errors are also provided and include the statistical uncertainty associated with the phase.

Where InSAR fails, it is possible to apply an alternate technique called “speckle tracking”. This technique follows the same procedure as feature tracking but instead of the algorithm correlation matching and tracking each pixel covering a specific feature in the two images, it uses recognition and correlation of the displacement of speckles or “granular interferences” due to specific irregularities on the surface (Joughin et al., 2018b). Although this technique can provide ice velocity data in many cases where InSAR is not able, the resolution is coarse and accuracy is lower and linked to the size of the chosen pixel’ search box size (Joughin, 2002). Furthermore, its use between images with large temporal separation is limited due to excessive displacements of the surface or other sources of decorrelation (Joughin, 2002). Errors provided, rely on speckle tracking error inherent to the SAR data.

The last ice velocity dataset MEaSUREs multi-year contains a multi-year ice-sheet-wide velocity mosaic for Greenland calculated over the period 1995-2015 (Joughin et al., 2016). The data were provided with a spatial resolution of 250 m, and ice velocity in each pixel is reported in  $\text{m yr}^{-1}$ . Ice velocity represents an error weighted average of all the available source data at each point and calculated through the three different techniques: InSAR and speckle tracking applied to SAR images and feature tracking applied on optical images (Joughin, 2002; Scambos et al., 2016). This averaging process means that at any given point, the velocity estimate could come from one or multiple image pairs depending on the available data. Error estimates are provided for each pixel and represent the average of all errors associated with the data and techniques used to produce the velocity at each pixel. Errors values can span from less than  $1 \text{ m yr}^{-1}$  up to 3% of calculated ice velocity depending on technique utilised and ice flow velocity analysed. Holes in the final

mosaic have been filled via interpolation and no errors values are provided with these.

**Table 5.1** Description of the datasets from which the ice velocity data of specific study sites were extracted.

| Dataset                              | Satellites   | Techniques   | Temporal coverage             | Spatial resolution | Temporal resolution |
|--------------------------------------|--|--|-------------------------------|--------------------|---------------------|
| MEaSURES Selected Glaciers Version 3 | TerraSAR-X<br>TanDEM-X<br>(TSX/TDX)                                  | InSAR phases / speckle tracking                    | June 2008 to present          | 100 m              | 11 or 22 days       |
| GoLIVE, version 1                    | LANDSAT-8  | Feature tracking                                   | May 2013 to April 2017        | 300 m              | 16 days             |
| MEaSURES Multi-year Version 1        | ALOS, ERS-1<br>ERS-2<br>LANDSAT-8<br>RADARSAT-1<br>RADARSAT-2<br>TSX | InSAR phases / speckle tracking / feature tracking | December 1995 to October 2015 | 250 m              | Not applicable      |

### 5.2.2. Methodology

The first step was to identify the cyclonic rainfall events during late summer/early autumn affecting the west and south-west regions of the GrIS (Figure 5.1). For the period covered by ice velocity datasets, all the episodes of cyclonic rainfall, regardless of their magnitude, were extracted and examined. A subset of these cyclones were then selected when these coincided with ice velocity data which met three crucial requirements: 1) temporal coverage of either the entire ablation season until the cyclonic event, or at least two months before the cyclonic event, were available 2) one or more image pairs partially or entirely cover the cyclonic rainfall event 3) have less than 50% of missing data across the study area. The first requirement was crucial since changes in ice velocity throughout the ablation season reflect the seasonal evolution of the subglacial drainage system in response to surface meltwater pulses reaching the bed (Schoof, 2010; Bartholomew et al., 2012; Chu, 2013; Nienow et al., 2017). This allows better interpretation of the ice velocity change during the cyclonic

event which is also influenced by the pre-event subglacial conditions driven by the interaction between the meltwater runoff reaching the bed during the summer season and response of the subglacial hydrological system. The second requirement was pivotal since the aim of this work was to study the ice velocity change during the cyclonic events and compare it with the surrounding periods and entire ablation season. A limitation of this study lies in the fact that it has not always been possible to find image pairs that include the entire cyclonic period. Therefore, cyclonic periods partially covered in one or two image pairs were also examined. Finally, the third requirement was necessary, since ice velocity data with large areas of missing points would have made comparison of ice velocity extracted from two different images in the ablation zone, where most of the work is focused, difficult or impossible. Since the overlap period between satellite images and MAR output cover the time span between 2008 and 2016, only three cyclonic events were selected for this work that met the forementioned criteria: 10<sup>th</sup>-14<sup>th</sup> September 2012, 5<sup>th</sup>-11<sup>th</sup> September 2013 and 28<sup>th</sup> August-6<sup>th</sup> September 2015.

Once the cyclonic events to be studied were identified, their weather synoptic framework was described. This was done to highlight the meteorological spatial footprint of the cyclonic events at sites studied with respect to the entire GrIS, through the study of key meteorological parameters. The mean composite geopotential heights at 500 mb were calculated during the events over Greenland and surrounding area along with the average position of the cyclone's centre. Cloud cover and total rainfall were calculated over the entire GrIS from the MAR which has a dedicated cloud scheme validated with in situ measurement especially developed to depict Arctic cloud characteristics and related precipitation (Hofer et al., 2017). The mean TTZ was also calculated as anomaly with respect to the 1986-2015 climatological average which represents the most recent climatological period that comprises all data utilised in this study.

The daily mean rainfall, meltwater production and runoff were calculated from the MAR during the entire melt season (May-September) and cyclonic events over the drainage basins of the glaciers involved in this study, obtained from Mougnot and Rignot (2019)(Fig 5.1). Rainfall and meltwater were calculated only

over the portion of the drainage basins where runoff occurs and hence can perturb the subglacial drainage system, influencing ice velocity via basal sliding (Sundal et al., 2011; Sole et al., 2013; Tedstone et al., 2013; Doyle et al., 2015). To explain variations of these parameters, the mean TTZ were calculated below the most recent climatological ELA (1986-2015) in the same drainage basins along with the highest elevation reached by melt during the cyclonic event. They were compared to the climatological mean 1986-2015 in order to show the exceptionality of these events and which of these parameters was the primary contributor to total runoff. Finally, the principal SEB components (LWnet, SWnet, SHF and LHF) were calculated below the ELA of the drainage basins of glaciers involved in this study during and around the event, to identify the unusualness of each energy flux and its potential contribution to meltwater production.

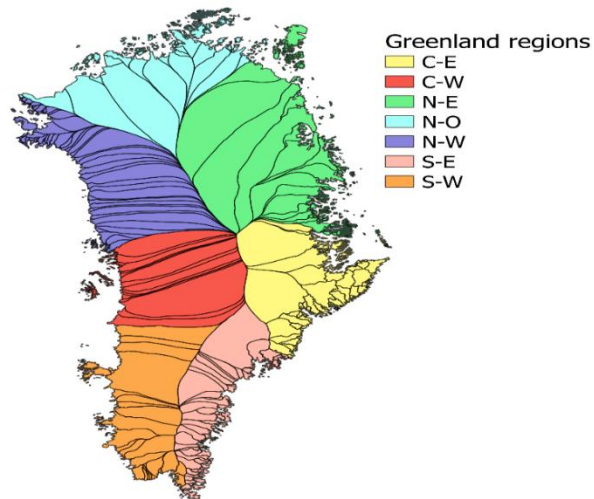


**Figure 5.1.** Greenland divided into 260 drainage basins grouped in 7 regions from raw data of Mouginot and Rignot (2019). This study is focused on sites of drainage basins located into west (red) and south-west (orange) regions.

The MEaSURES selected glaciers and MEaSURES multi-year velocity datasets were resampled through bilinear interpolation to the same coarser resolution of 300 m as the GoLIVE dataset to simplify processing and comparisons. Ice velocities of glaciers during the melt seasons and cyclonic events were calculated along their main vector flowlines because they represent their main motion trajectories (Strigaro et al., 2016; Zhang et al., 2020). In the literature central flowlines are often utilised to

determine the change of glacier length and retreat (Leclercq et al., 2012; Nuth et al., 2013), estimate the glacier ice volume (Li et al., 2012; Linsbauer et al., 2012), develop one-dimensional glacier models (Oerlemans, 1997; Strigaro et al., 2016) or describe the velocity dynamics of the glacier (Sundal et al., 2011; Heid & Kääb, 2012; Melkonian et al., 2014) as in this work. The precision calculation of these vectors requires a dataset that presents an average of coherent, robust and multi-year glacier velocity data that limit temporary and seasonal surface velocity variability (Zhang et al., 2020). The MEaSURES multi-year velocity dataset chosen for this study meets these requirements and a procedure to extract them was developed in QGIS as follows.

The MEaSURES multi-year velocity dataset were run through the *r.flow* algorithm (an algorithm that computes flowlines, flowpath lengths, and flow accumulation from an elevation map) (Mitasova et al., 1996) of GRASS-GIS (GRASS\_Development\_Team, 2020). The output of this algorithm for each glacier is an ensemble of segments of different length representing the direction of the main speed gradients interrupted by zone with reverse direction of the flow due to the irregular surface velocity. To overcome this problem and extract the main flowline paths, the *r.flow* results were superimposed onto a recent DEM of the GrIS covering the period 2009-2015 (Howat et al., 2017). The DEM values allowed merging of the main segments produced by the algorithm from the top to the bottom of each glacier and delineation of their principal flowlines.

Once the main flowlines of each glacier were extracted, they were utilised as input data in an algorithm developed using the QGIS and GDAL software libraries. It required as input the flowlines of one or more glaciers of a site, superimposed on an ice velocity image of the same site. As output, it returned the average velocity calculated along the flowlines on a buffer area which comprises all the pixels within a distance of 500 m from the flowlines (Figure 5.2). This procedure was repeated for all ice velocity images used in the study and all their associated error images. This permitted to obtain a single value of velocity and associated error along each flowline for ice velocity data covering each specific time period.

A more complex GIS algorithm was developed to detect the spatial variability of ice motion and data gaps along the flowlines for the ice velocity data covering the cyclonic event and surrounding periods. Briefly, the algorithm, from the bottom to the top of the flowline, obtained the average value of ice velocity extending two pixels in both directions perpendicular to the pixel intersected by the flowline. This guarantees better result if compared to the acquisition of the individual values of each pixel intersected by the flowline, which can be affected by a significant error.

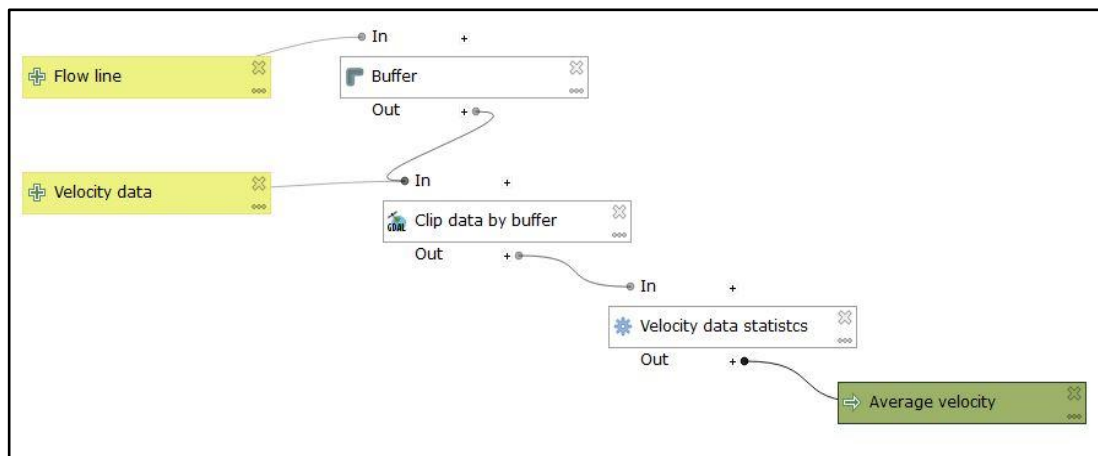


**Figure 5.2.** Structure of the GIS process utilised to extract the average ice velocities and errors associated along the glacier’s flowlines, developed with the use of QGIS and GDAL software libraries. It requires as input a flowline and ice velocity data of the same glacier and returns as output the average velocity along the flowline and associated error (not shown).

To investigate whether the number of glaciers out of the total which underwent an acceleration during cyclonic events is statistically significant or not, they were compared with the binomial distribution of observing the  $r$  acceleration due to chance alone. Eq 5.1 of probability mass function to calculate the binomial distribution was applied:

$$\frac{n!}{(n-r)!*r!} * p^r (1 - p)^{n-r} \quad 5.1$$

$n$  = number of trials

$r$  = number of successes (acceleration)

$p$  = probability of a success (acceleration) = 1/2

$1 - p$  = probability of a failure (deceleration) = 1/2

The binomial distribution p-value was also calculated to provide an indication of the statistical significance of the acceleration.

Finally, analysis of the rainfall fraction compared to total precipitation in the ablation zone of the drainage basin of each site was done during the key period that goes from the 15<sup>th</sup> August to 15<sup>th</sup> of October of each year from 1986 to 2015. This period was chosen for two reasons. Firstly, it covers all the cyclonic periods in this study. Secondly, from our preliminary analysis of the cyclonic events to be studied, it emerged that this is the period where it is most likely that cyclonic rainfall events will produce enough surface water to be able to perturb the subglacial drainage system of the GrIS which in this stage is in transition towards a winter mode. The results were calculated and shown during the six five-years windows that cover the reference period 1986-2015 used as climatological reference in this work. This analysis was done to elucidate if there has been an increase over time in the liquid fraction of precipitation during the key period of late summer/early autumn examined in this study.

### 5.2.3. Study Sites

Ice velocity data utilised in this study covers specific sites shown in Figure 5.3. Sites A, B, D and E covers portions of the GrIS within the ablation zone while site C includes a portion beyond the GrIS ELA up to 2000 m.a.s.l. For each site, the ice velocity obtained from the MEASUREs multi-year dataset ( $> 50 \text{ m yr}^{-1}$ ) are shown for the glaciers and the surrounding areas, and the flowlines of each glacier are also displayed. The reason behind filtering out ice velocity less than  $50 \text{ m yr}^{-1}$  is to remove possible spurious points where errors in the data are likely higher relative to the velocity value (Joughin et al., 2018a).

Sites A and B in the south-west region and C and D in the west region are studied in relation to a cyclonic event that occurred in 2015. The southernmost site is site A (Figure 5.4) and includes a single marine terminating glacier called Sermiligarssuk. The flowline extracted, stretches from the glacier calving front towards the interior up to an altitude of 1470 m.a.s.l. The average ice velocity along the flowline is  $475 \text{ m yr}^{-1}$ . Along the flowline, the ice velocity of  $850 \text{ m yr}^{-1}$  at the

front gradually decreases towards the interior reaching a value of  $400 \text{ m yr}^{-1}$  between the 10<sup>th</sup> and 15<sup>th</sup> km. An increase in ice velocity of  $+250 \text{ m yr}^{-1}$  is detected between the 15<sup>th</sup> and 20<sup>th</sup> km is followed by a gradual decrease till the end of the flowline where the lowest values are observed. This site experiences some of the highest air temperatures in Greenland (Cappelen et al., 2014) and this part of the coast receives considerable precipitation throughout the year, often in the form of rain during the summer and sometimes even during periods of cyclonic warm advections during winter (Schuenemann et al., 2009; Cappelen et al., 2014). The water in the fjords comes from the mix between the cold current along the east coast and the Gulf Stream. Its relatively high temperature makes this coastal area ice-free all year round (McDonagh et al., 2009; Rennermalm et al., 2009).

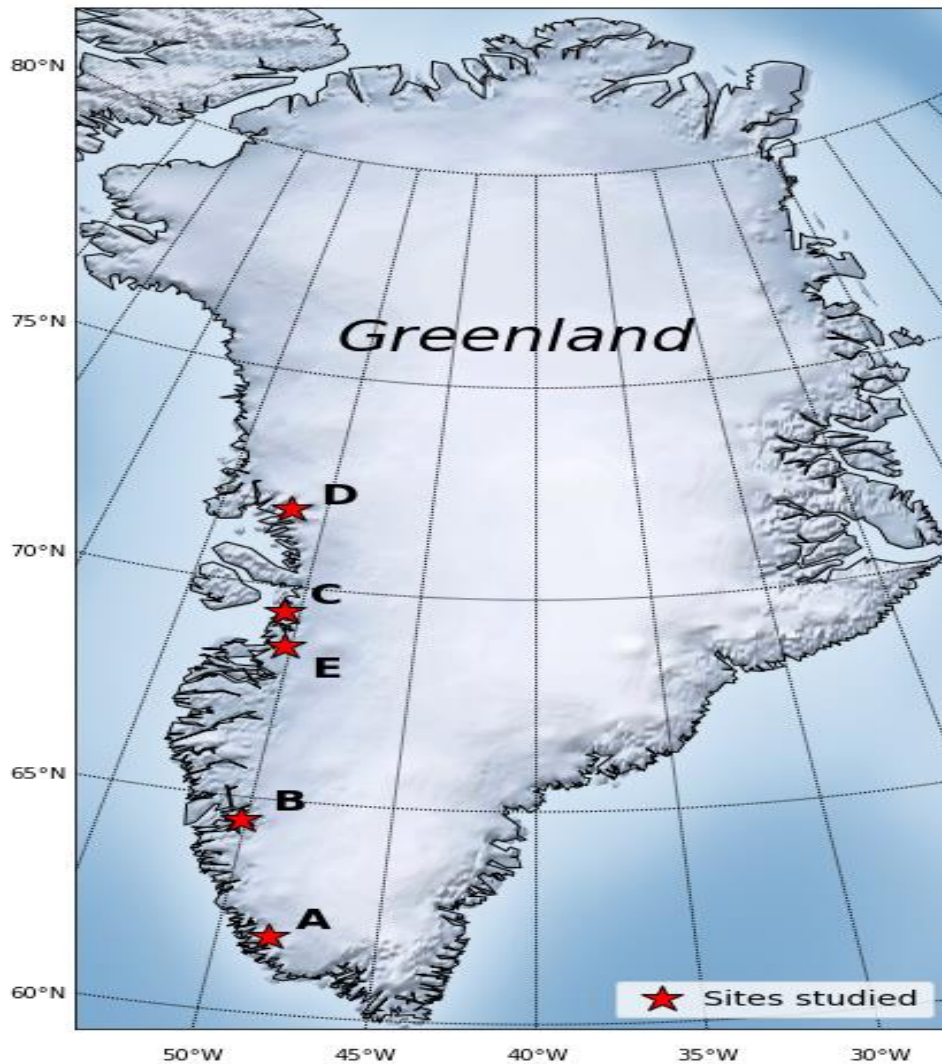
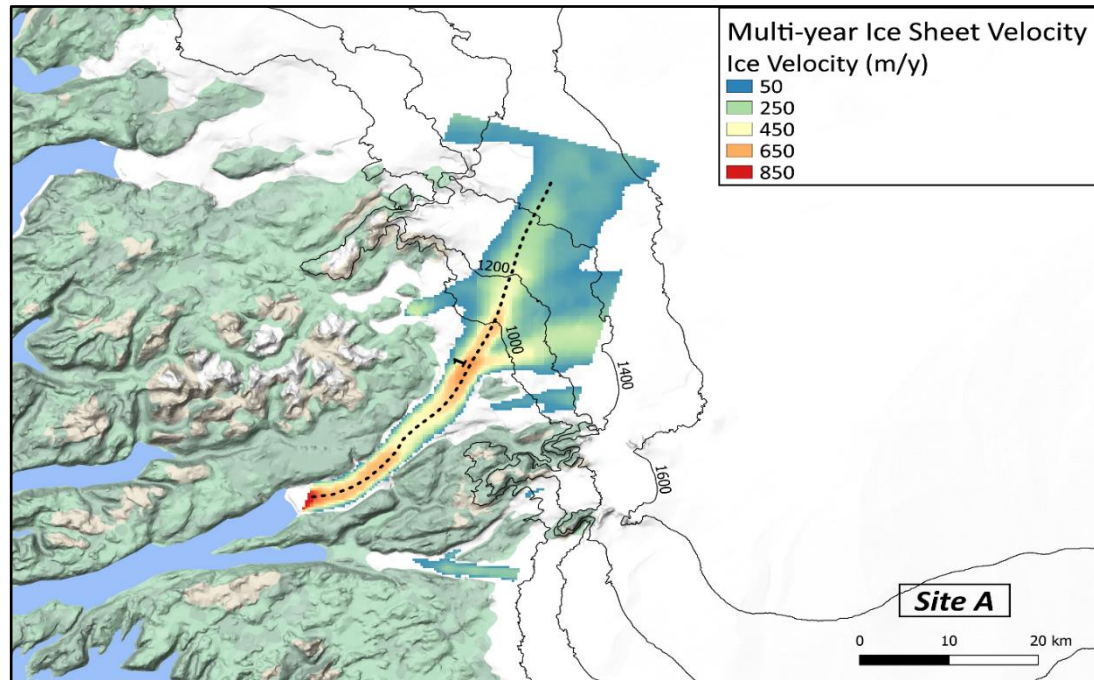


Figure 5.3. Geographical location of the study sites.



**Figure 5.4.** Site A and surrounding area of the GrIS. In the main figure MEaSUREs Multi-year Ice Sheet velocity data covering the period 1995-2015 (Joughin, 2018) is shown. Flowline extracted is the black dotted line indicated by number one. Ice surface contours (pale grey lines) are from Howat et al, 2014. White denotes ice covered area. Ice velocity less than  $50 \text{ m yr}^{-1}$  are filtered out. Gray, green and light brown shading denote land areas whereas light blue shading coastal and fjords water.

The second site B, (Figure 5.5) consists of two marine and one land terminating glaciers. The first marine glacier is called Akugdlerussup and is represented by flowline number 1. The second marine glacier is Kangiata Nunata which is divided into two main trunks indicated by the flowlines 2 and 3. The land terminating glacier called Kangaussarssup is described by the flowline number 4. The fastest flowing glacier is Kangiata Nunata with an average speed along flowline 2 of  $1276 \text{ m yr}^{-1}$  and flowline 3 of  $1622 \text{ m yr}^{-1}$ . Near the calving front, the velocity is around  $4000 \text{ m yr}^{-1}$  but this gradually reduces to values around  $100 \text{ m yr}^{-1}$  in the uppermost part of the flowlines located between 1200 and 1400 m.a.s.l. Akudlerussup glacier has an average velocity of  $593 \text{ m yr}^{-1}$ , with the highest values around  $1150 \text{ m yr}^{-1}$  near the calving front and the lowest values around  $100 \text{ m yr}^{-1}$  in the uppermost part of the flowline located between 1000 and 1200 m.a.s.l. The last, in terms of ice velocity, is Kangaussarssup glacier with an average value around  $123 \text{ m yr}^{-1}$ , which is fairly

uniform along its entire path from the GrIS margins up to 1250 m.a.s.l. As with site A, this site is located in one of the warmest areas of Greenland (Rae et al., 2012), although it receives less precipitation (Cappelen et al., 2014). A recent study conducted at this site showed that the general ice loss that occurred between 1985 and 2014 contributed more than 0.1 mm to SLR. The major contributors to this loss were due the two tidewaters glaciers whose calving fronts have retreated many kilometres (Motyka et al., 2017).

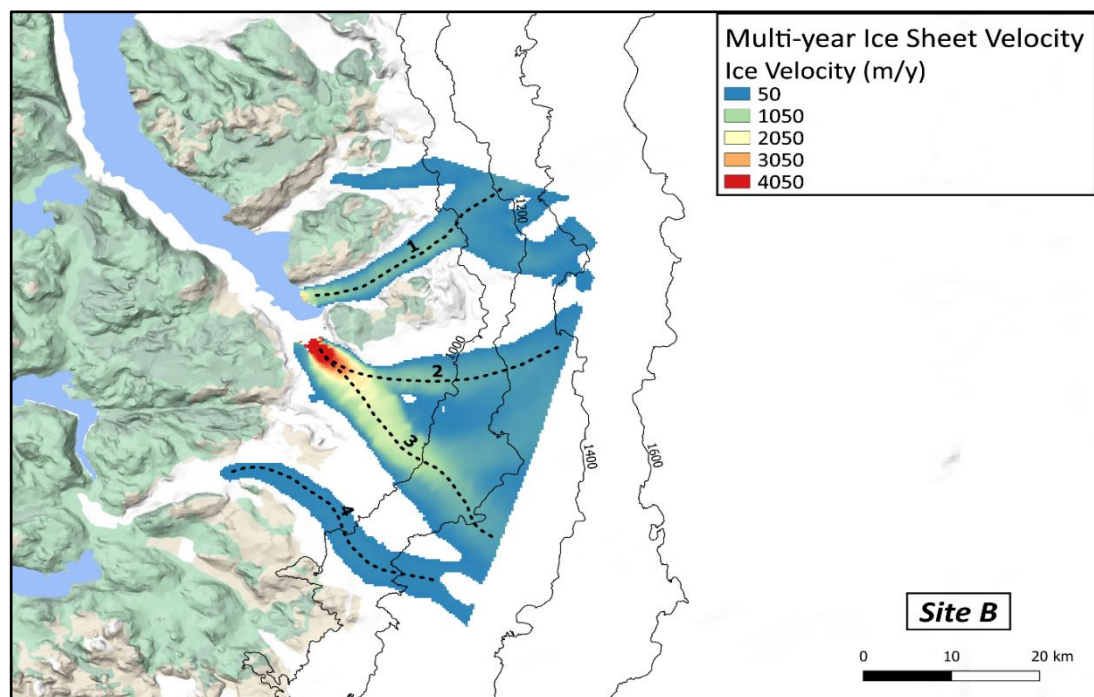


**Figure 5.5.** Same as Fig 5.4 but for the B site.

In the west region, the second site encountered when going from south to north is site C (Figure 5.6). This site is characterised by four marine-terminating glaciers that are respectively Kujatdleq (flowline 1), Equip Sermia (2), Avangnardleq (3) and Jakobshavn Isbrae glacier (4). Kujatdleq and Equip Sermia have an average ice velocity of  $269 \text{ m yr}^{-1}$  and  $120 \text{ m yr}^{-1}$ , with the highest values around  $1400 \text{ m yr}^{-1}$  near the front and lowest around  $100 \text{ m yr}^{-1}$  in the uppermost part of the flowlines located between 1800 and 2000 m.a.s.l. The Avangnardleq glacier has an average ice velocity of  $121 \text{ m yr}^{-1}$  with no significant trend in velocity between the front and the upper elevation end of the flowline located at 1900 m.a.s.l.

Jakobshavn Isbrae glacier show has far higher than the other three with an average value  $1735 \text{ m yr}^{-1}$  and the highest values around  $5000 \text{ m yr}^{-1}$  near the front reducing to values around  $500 \text{ m yr}^{-1}$  in the uppermost part of the flowline at an altitude of 1950 m.a.s.l. The most recent and comprehensive study of this glacier (Khan et al., 2020) estimates a total mass loss of  $1518 \pm 189 \text{ Gt}$  over the period 1880-2012, a third of which was lost in the last 40 years, and a tongue retreat of the order of tens of kilometres since 1900. Approximately 90 % of the value of the mass loss of the Jakobshavn is related to dynamic causes (Khan et al., 2020). This highlights the importance of understanding the future glaciers dynamic response to climatic and oceanic changes, and this work seeks to increase the knowledge in this area.

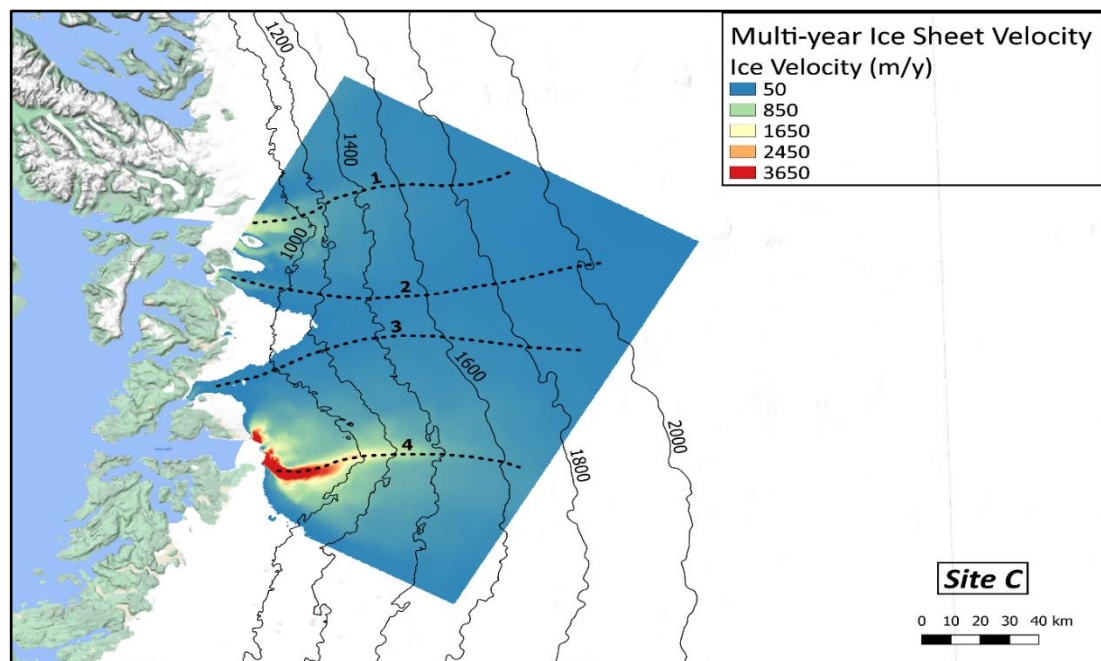


**Figure 5.6.** Same as Fig 5.4 but for the C site.

The second site studied in the west region is site D (Figure 5.7) consisting of two marine terminating glaciers, Rink (the northernmost) and Kangerdlugssup glacier with an average ice velocity of  $2731 \text{ m yr}^{-1}$  and  $1130 \text{ m yr}^{-1}$  are respectively the Rink and. Although they terminate in two adjacent fjords, in the first 12 km from the margins, the velocity of the Rink glacier remained near a value of  $3600 \text{ m yr}^{-1}$  while the velocity of Kangerdlugssup glacier ranges from  $1800 \text{ m yr}^{-1}$  to  $1000 \text{ m yr}^{-1}$ . From 12 km to the upper to the upper end of flowlines located around 700 m.a.s.l, the velocity decreases to a value around  $1800 \text{ m yr}^{-1}$  for the Rink glacier and a value

around  $900 \text{ m yr}^{-1}$  for the Kangerdlugssup glacier. These different ice velocity behaviours are confirmed by a recent study (Bartholomaus et al., 2016) which highlights how Rink glacier front flow is more influenced by the position of the calving front than the Kangerdlussup, where the evolution of subglacial drainage system plays a major role (Howat et al., 2010). This fact leads to the conclusion that local factors such as fjord geometry, bathymetry and circulation play a primary role in governing ice velocity at the front of these two glaciers affected by the same atmospheric and oceanic forcing due to their proximity.

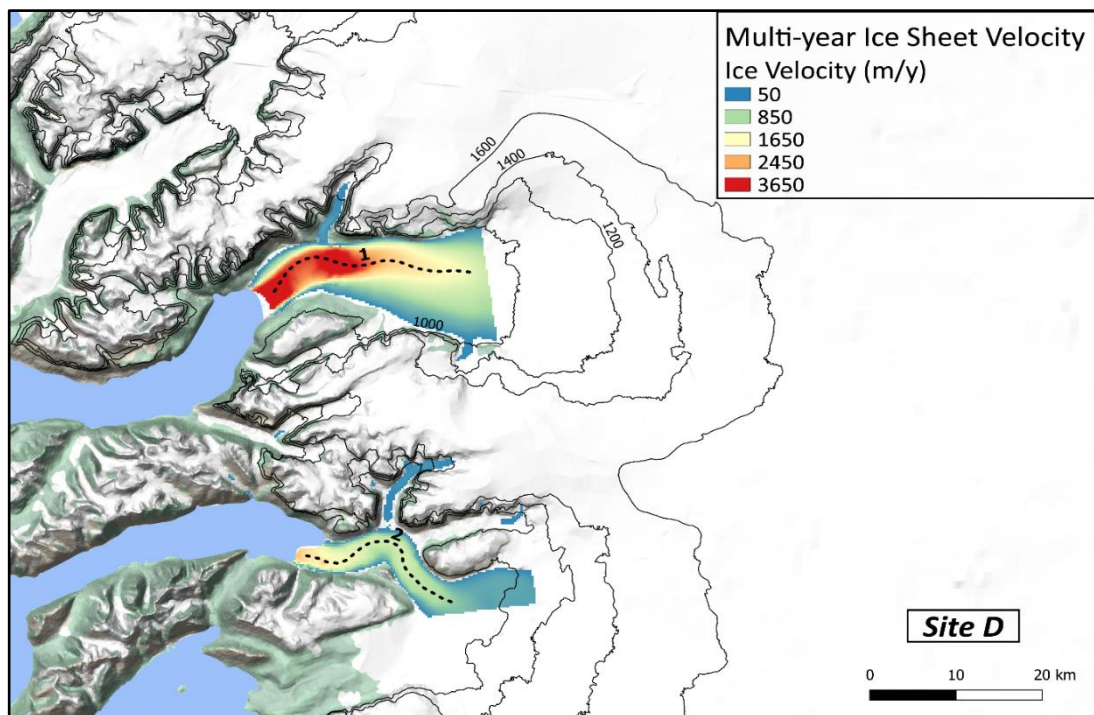


**Figure 5.7.** Same as Fig 5.4 but for the D site.

Site E (Figure 5.8), located in the west region, is studied with respect to cyclonic events which occurred in 2012 and 2013. The area examined ranges from elevations of 0 m.a.s.l. to around 850 m.a.s.l. The site is characterized by two marine-terminating glaciers located in the northernmost part which are respectively Alangordliup (Fig 5.8 flowline 1) and Sarqardliup (Fig 5.8 flowline 2) and two land-terminating glaciers, Quingap and Iliuliaik. Quingap is divided into two glacial tongues from which the respective flowlines depart (Fig 5.8 flowlines 3 and 4) while the second is called Iliuliaik through which the fifth flowline runs (Fig 5.8 flowline 5). Alangordliup and Sarqardliup, terminating in adjacent fjords, have different average

ice velocities along the flowlines of  $88 \text{ m yr}^{-1}$  and  $160 \text{ m yr}^{-1}$  respectively. The difference in these values is related to velocity in the first 20 km from the front, with Alangordliup around  $250 \text{ m yr}^{-1}$  and Sarqardliup less than  $70 \text{ m yr}^{-1}$ . The average velocities along the flowlines of the two land terminating glaciers are respectively  $82 \text{ m yr}^{-1}$  and  $73 \text{ m yr}^{-1}$  for the Quingap glacier and  $95 \text{ m yr}^{-1}$  for the Iliuliak glacier. Worth noting how, along these two glaciers, the flowlines cross areas of the GrIS characterised by an alternation of acceleration and deceleration. This is consistent with the literature (Catania et al., 2020) which underlines how, along the flowlines of land terminating glaciers in the ablation zone, there are no particular velocity trends but rather an alternation of areas with higher and lower ice velocity or vice-versa.

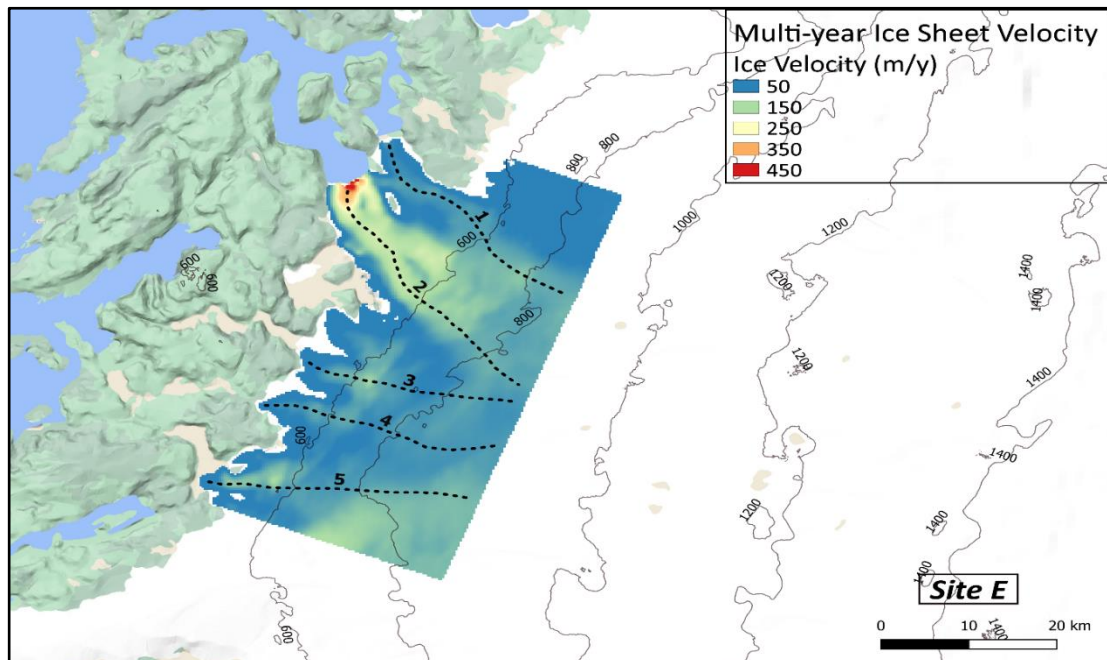


**Figure 5.8.** Same as Fig 5.4 but for the E site

The ice velocity in the ablation zone of the glaciers at site E were the subject of two recent studies of Tedstone et al. (2015) and Williams et al. (2020). In the first study, apart from the calving fronts, most of the area was subjected to an average decrease of annual ice motion during the period 2007-2014 compared with 1985-1994 despite a 50 % increase of surface meltwater production. In the second study which considers the land terminating margins of the site, the same deceleration was found between the period 2003-2012 and 1992-2003. Conversely, an overall acceleration related to a reduction of meltwater production, if compared with the

previous period, was detected for the period 2017-2019 in marginal land areas. The authors hypothesise that while at the margins of marine terminating glaciers the velocity is linked to the processes operating between ice and fjord sea water interface, in the rest of the site, different volumes of meltwater in the subglacial drainage system favours different ice dynamics response at the annual scale.

All the information regarding the sites involved in this study are summarised in Table 5.2. It includes the study sites for each cyclonic event, their geographical location, the glaciers included along with their terminal environment, name, length and flowline average ice velocity from MEaSURES multi-year.

**Table 5.2** Summary of the study sites and glaciers along with names and lengths of the flowlines.

| Site | Central Lat; Lon | GrIS region | Glacier name    | Terminating environment | Flowline name | Flowline length (km) | MEaSURES multi-year velocity ( $m\ yr^{-1}$ ) | Cyclonic event                |
|------|------------------|-------------|-----------------|-------------------------|---------------|----------------------|---|-------------------------------|
| A    | 61.7N;<br>48.1W  | S-W         | Sermiligarssuk  | Marine                  | A1            | 51.5                 | 475   | 28 August-6 September<br>2015 |
| B    | 64.2N;<br>49.4W  | S-W         | Akugdlerssup    | Marine                  | B1            | 26.1                 | 593   |                               |
|      |                  |             | Kangiata Nunata | Marine                  | B2            | 29.4                 | 1276  |                               |
|      |                  |             |                 |                         | B3            | 31.7                 | 1622  |                               |
|      |                  |             | Kangaussarssup  | Land                    | B4            | 29.7                 | 123   |                               |
| C    | 69.7N;<br>49.5W  | W           | Kujatdleq       | Marine                  | C1            | 85.7                 | 269   | 28 August-2 September<br>2015 |
|      |                  |             | Equip           | Marine                  | C2            | 123.9                | 120   |                               |
|      |                  |             | Avangnardleq    | Marine                  | C3            | 130.7                | 121   |                               |
|      |                  |             | Jakobshavn      | Marine                  | C4            | 84.6                 | 1735  |                               |
| D    | 71.6N;<br>51.1W  | W           | Rink            | Marine                  | D1            | 25.6                 | 2731  |                               |
|      |                  |             | Kangerdlugssup  | Marine                  | D2            | 21.9                 | 1130  |                               |
| E    | 68.6N;<br>50.2W  | W           | Alangordliup    | Marine                  | E1            | 28.1                 | 88  | 5-11 September<br>2013        |
|      |                  |             | Sarqardliup     | Marine                  | E2            | 33.8                 | 160   |                               |
|      |                  |             | Quingap         | Land                    | E3            | 23.2                 | 82  | 10-14 September<br>2012;      |
|      |                  |             |                 |                         | E4            | 26.9                 | 73  |                               |
|      |                  |             | Iliuliaik       | Land                    | E5            | 29.1                 | 95  |                               |

### 5.3. Results

#### 5.3.1. General Meteorological Analysis

Cyclonic activity during each event is well depicted by the composite mean of geopotential height at 500 mb over the western part of the Greenlandic region (Figure 5.9). Since site C and D were affected by the cyclonic event of 2015 for four

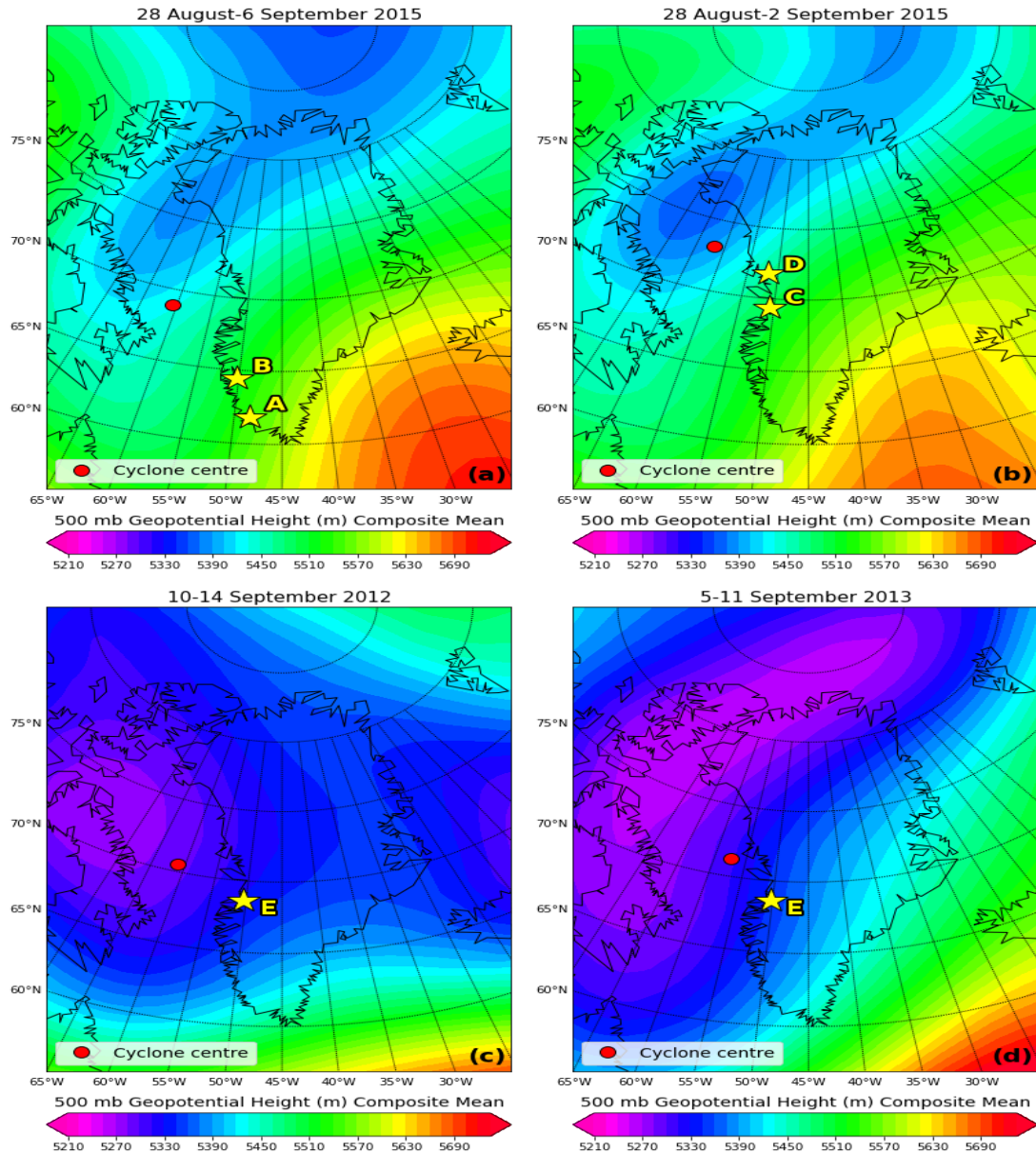


**Figure 5.9.** 500 mb Geopotential Height (m) Composite Mean from NCEP-NCARv1 reanalysis (Kalnay et al., 1996) during the period 28 August-6 September 2015 (a), 28 August-2 September 2015 (b), 10-14 September 2012 (c) and 5-11 September 2013 (d). Red dots indicate the average positions of the cyclones while yellow stars the study site locations for that event.

days less than site A and B, the meteorological analysis of this sub-period is shown.

The centres of the low pressures are located along Baffin Bay and with high pressures in the south-east of Greenland generate a cyclonic curvature which affects the south-west and west of the GrIS. The magnitude of the warm south-westerly advection over the GrIS can be seen in Figure 5.10 where the temperature anomaly reaches 4 C° (above the 1986-2015 climatological mean at the study sites).

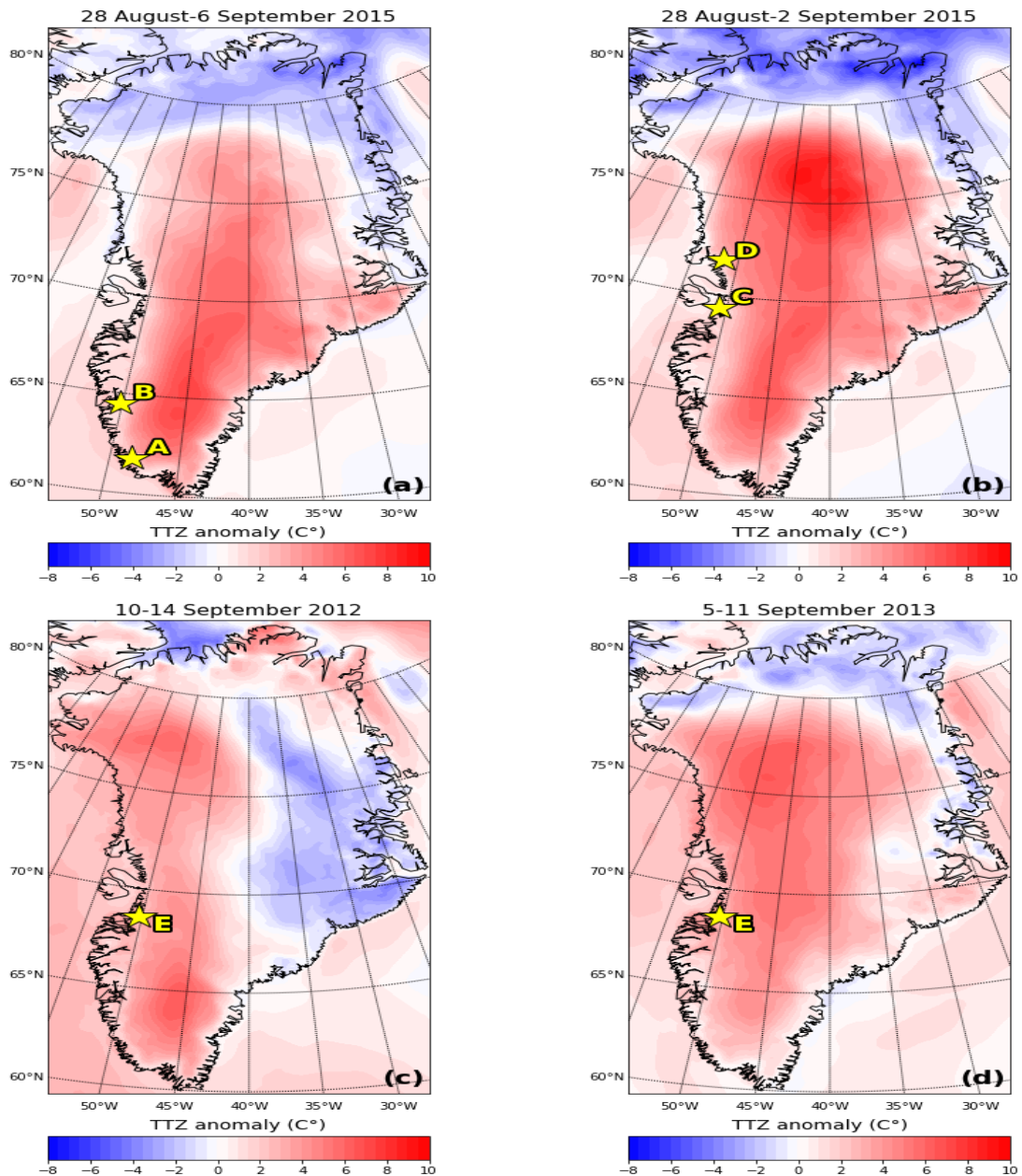


**Figure 5.10.** TTZ Anomaly Composite Mean extracted from the MAR during the period 28 August-6 September 2015 (a), 28 August-2 September 2015 (b), 10-14 September 2012 (c) and 5-11 September 2013 (d) compared to the climatological mean 1986-2015.

These air masses are characterised by extensive cloud cover (Figure 5.11) and high rainfall rate, which is especially heavy along the south-west/west margins where the study sites are located (Figure 5.12).

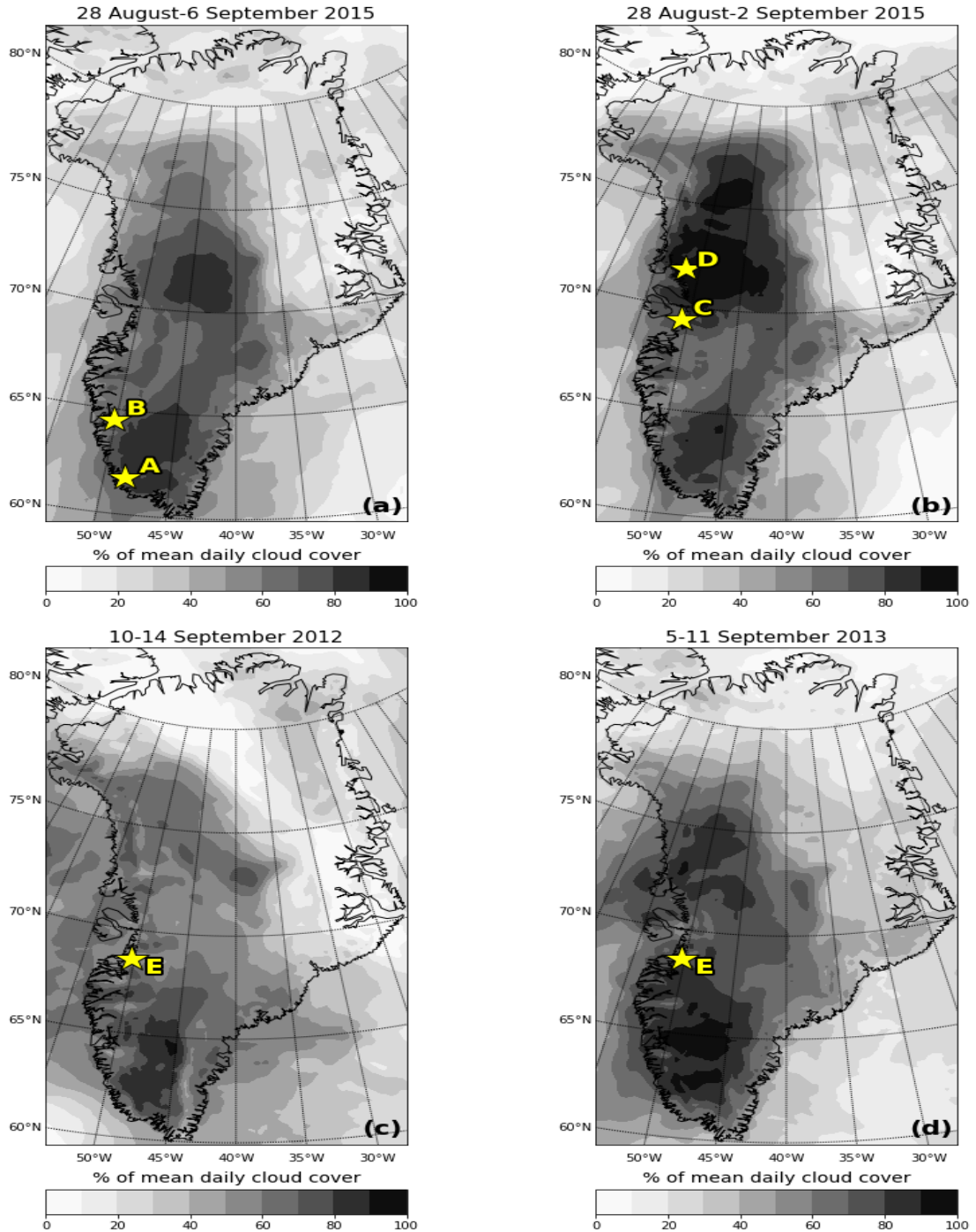
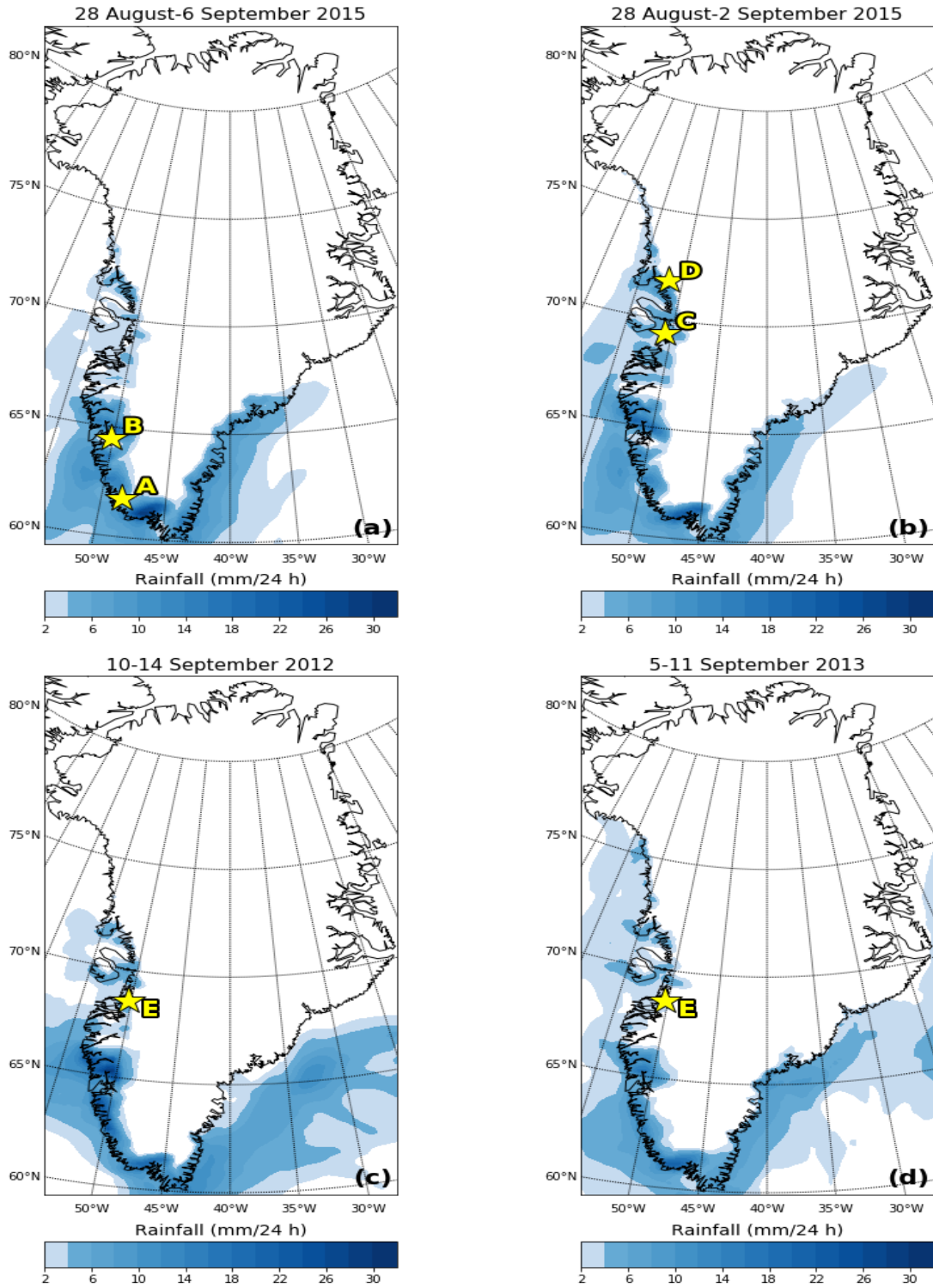


Figure 5.11. Same as Fig 5.10 but for the mean cloud cover.

Late Summer/Early Autumn Cyclonic Rainfall and Ice flow of the GRS



**Figure 5.12.** Same as Fig 5.10 but for the mean daily rainfall during the cyclonic period considered.

### **5.3.2. Magnitude of the Cyclonic Events and Energy Balance**

At site A the total value of meltwater plus rainfall during the cyclonic period was 125 mm. w.e. (Table 5.3). Rain contributed 20 % to this total, whereas meltwater 80 %. Rainfall and meltwater during the cyclonic period represented an amplification of +170 % and + 194 % which fed a +114 % in runoff if compared to values of the climatological mean 1986-2015, reaching a value of 81.13 mm. The exceptional nature of this cyclonic period was confirmed by even higher values for rain and meltwater reached at the site B which fed a runoff of 99.35 mm, higher in absolute value if compared to site A but representing a +79 % anomaly from the mean. Worth noting that the elevation where meltwater was produced during the event reached 2600 m.a.s.l at both sites while at site C and D up to elevations of 2100-2200 m.a.s.l.

The absolute values of rain and meltwater at site C and D was much lower to that detected at site A and B, but with percentage values both far higher than the climatological mean. The values of rainfall and meltwater fed a runoff of 35.26 mm at site C which represented a positive anomaly from the mean of +38 %. Conversely at site D, a value of 4.82 mm in runoff, was -42 % of the average value expected in this period of the year. At site E, meltwater production reached up to 300 m above the ELA and contributed more than 80 % to the total water available for runoff (Table 5.4) in both cyclonic events, although the highest positive deviation from the climatic mean was given by rain. Low absolute values of rainfall and meltwater (but much higher than the climatological mean) fed a runoff of 11.25 mm in 2012 and 15.44 mm in 2013 representing a deviation from the climatological mean of +30 % and 0 %

The positive values across all sites of rainfall and meltwater during the cyclonic periods were sustained by a positive SEB (Figure 5.13 and Figure 5.14) mainly driven by less negative net long-wave radiation due to higher values of downward long-wave radiation from clouds and positive values of turbulent heat fluxes. The highest values of latent and sensible heat flux along with long-wave net around zero, coincided with peaks of rain and meltwater production shown in the images of the next section. They were associated with the advection of moist warm air over the sites as confirmed by the meteorological analysis in section 5.3.1.

**Table 5.3.** Total rainfall/meltwater/runoff during the cyclonic period 2015 and comparison with the 1986-2015 climatic average of the same period for Site A (top left), B (top right), C (bottom left), D (bottom right):

| <b>Site A</b>                          | <b>mm</b> | <b>%</b> |
|--|-----------|----------|
| Total rainfall                         | 25.09     | 20 %     |
| Total meltwater                        | 99.84     | 80 %     |
| Total runoff                           | 81.13     |          |
| % of rainfall compared to climatology  | +170 %    |          |
| % of meltwater compared to climatology | +194 %    |          |
| % of runoff compared to climatology    | +114 %    |          |

| <b>Site B</b>                          | <b>mm</b> | <b>%</b> |
|--|-----------|----------|
| Total rainfall                         | 52.09     | 35 %     |
| Total meltwater                        | 97.15     | 65 %     |
| Total runoff                           | 99.35     |          |
| % of rainfall compared to climatology  | +186 %    |          |
| % of meltwater compared to climatology | +220 %    |          |
| % of runoff compared to climatology    | +79 %     |          |

| <b>Site C</b>                          | <b>mm</b> | <b>%</b> |
|--|-----------|----------|
| Total rainfall                         | 13.49     | 24 %     |
| Total meltwater                        | 41.28     | 76 %     |
| Total runoff                           | 35.26     |          |
| % of rainfall compared to climatology  | +320 %    |          |
| % of meltwater compared to climatology | +81 %     |          |
| % of runoff compared to climatology    | +38 %     |          |

| <b>Site D</b>                          | <b>mm</b> | <b>%</b> |
|--|-----------|----------|
| Total rainfall                         | 5.04      | 27 %     |
| Total meltwater                        | 13.35     | 73 %     |
| Total runoff                           | 4.82      |          |
| % of rainfall compared to climatology  | +303 %    |          |
| % of meltwater compared to climatology | +117 %    |          |
| % of runoff compared to climatology    | -42 %     |          |

Late Summer/Early Autumn Cyclonic Rainfall and Ice flow of the GrIS

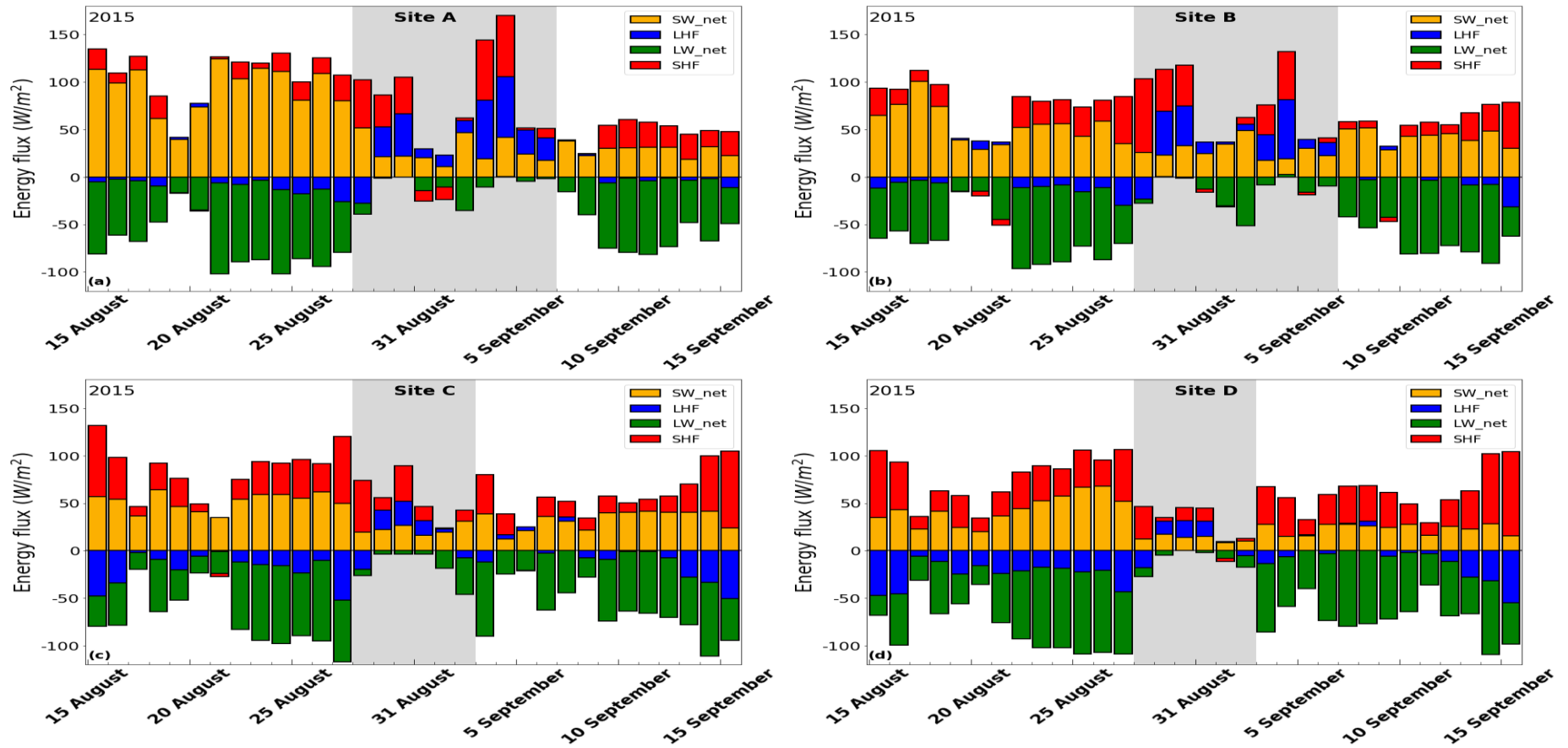


**Figure 5.13.** Daily surface energy budget below the ELA at site A (top right), B (top left), C (bottom left) and D (bottom right). The components in the legend are net short-wave (SWnet) and net long-wave (LWnet) radiation and the sensible (SHF) and latent (LHF) heat fluxes. These are defined as positive when they add heat to the surface.

**Table 5.4.** Total rainfall/meltwater/runoff during the cyclonic periods 2012 (left) and 2013 (right) and comparison with the 1986-2015 climatic average of the same period for site E.

| <b>Site E, 2012</b>                        | <b>mm</b> | <b>%</b> |
|--|-----------|----------|
| Total rainfall                             | 2.77      | 13 %     |
| Total meltwater                            | 17.69     | 87 %     |
| Total runoff                               | 11.25     |          |
| % of rainfall compared to climatology      | +394 %    |          |
| % of meltwater compared to the climatology | +154 %    |          |
| % of runoff compared to climatology        | +30 %     |          |

| <b>Site E, 2013</b>                        | <b>mm</b> | <b>%</b> |
|--|-----------|----------|
| Total rainfall                             | 5.05      | 15 %     |
| Total meltwater                            | 28.25     | 85 %     |
| Total runoff                               | 15.44     |          |
| % of rainfall compared to the climatology  | +195 %    |          |
| % of meltwater compared to the climatology | +114 %    |          |
| % of runoff compared to climatology        | +0 %      |          |

Late Summer/Early Autumn Cyclonic Rainfall and Ice flow of the GrIS

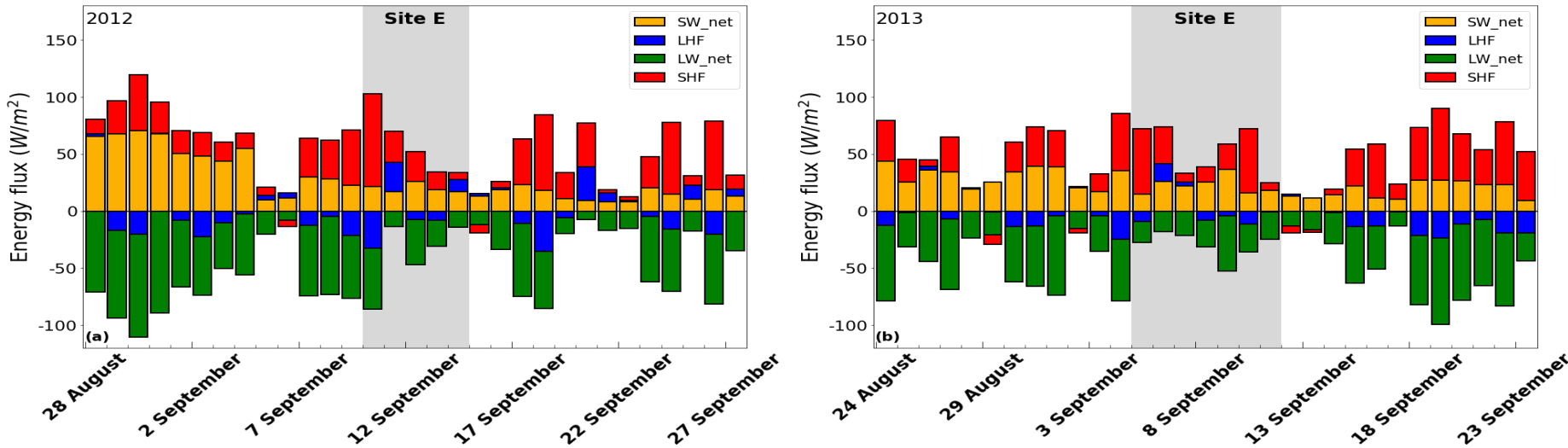


Figure 5.14. Same as Fig 5.13 but for site E, cyclonic events 2012 (a) and 2013 (b).

### **5.3.3. Cyclonic Events and Ice Dynamics at Sites A, B, C, D and E**

Given the large amount of image pairs used in this study, in the next section, their temporal coverage is summarised along with information they provide. Subsequently, ice dynamic at different sites around the cyclonic events and during the melt season is the describe along with the variations of glaciological and meteorological parameters.

#### **5.3.3.1. Timing of ice velocity data**

Table 5.5 includes all the dates of the image pairs utilised in this study in chronological order, with those which include the cyclonic periods in red bold. Ice velocity images covered a period that starts from May until the cyclonic event, apart from site A where data began in June. The temporal coverage of image pairs varies across sites and melt season depending on dataset used and repeat cycles of satellites involved.

Site A have no satellite image pair covering the month of May and a gap of three days in ice velocity data before the cyclonic event and the last two days of the cyclonic event are not covered by satellite data. Site B is the only one with two image pairs covering the cyclonic event although they include respectively nine previous days and three following days. Site C is the only one with two gaps in the ice velocity data covering the melt season between 28<sup>th</sup> May to 3<sup>rd</sup> June, and 20<sup>th</sup> to 28<sup>th</sup> June and a gap of seven days between 16<sup>th</sup> to 22<sup>nd</sup> August before the cyclonic event. It is worth noting how the ice velocity data before the cyclonic event at site C, covered a period going from 31<sup>st</sup> July to 15<sup>th</sup> August which is the earliest in the melt season of the entire study. Finally, at this site, the image pairs covering the cyclonic period also included five previous and five following days, being the single image pairs of the entire study with a total of ten non-cyclonic days in the ice velocity data during the event. Sites D and E (2013) were the only ones with velocity image pairs that covered the period before, during and after the event with no temporal gaps between them. Here, image pairs entirely cover the cyclonic event and also included the previous three days and the following two days at site D and the three previous days and the following day at site E (2013). At site E (2012), like site D and E (2013) the image pairs totally cover the cyclonic event but also included six previous days.

**Table 5.5.** Summary table of the velocity image pairs utilised in this study at specific sites. For each site the cyclonic period analysed is highlighted. Image pairs which totally or partially cover the cyclonic event are shown with red text and shaded in grey.

| Cyclonic event dates | 28 August-6 September 2015 |                       | 28 August-2 September 2015 |                       | 5-11 September 2013   | 10-14 September 2012  |
|----------------------|----------------------------|-----------------------|----------------------------|-----------------------|-----------------------|-----------------------|
|                      | Site A                     | Site B                | Site C                     | Site D                | Site E                | Site E                |
| Velocity data        | 3-18 June                  | 12-22 May             | 12-27 May                  | 7-17 May              | 4-14 May              | 17-27 May             |
|                      | 19 June-4 July             | 23 May-13 June        | 4-19 June                  | 18-28 May             | 15-25 May             | 28 May-7 June         |
|                      | 5-20 July                  | 14-24 June            | 29 June-14 July            | 29 May-30 June        | 26 May-5 June         | 8-18 June             |
|                      | 21 July-5 August           | 25 June-16 July       | 15-30 July                 | 01-11 July            | 6-16 June             | 19 June-10 July       |
|                      | 6 august-21 August         | 17-27 July            | 31 July-15 August          | 12-22 July            | 17-27 June            | 11-21 July            |
|                      | 25 August -4 September     | 28 July-7 August      | 23 August-7 September      | 23 July-2 August      | 28 June-8 July        | 22 July-1 August      |
|                      |                            | 8-18 August           | 8-23 September             | 3-13 August           | 9-30 July             | 2-12 August           |
|                      |                            | 19 August-29 August   |                            | 14-24 August          | 31 July-21 August     | 13-23 August          |
|                      |                            | 30 August-9 September |                            | 25 August-4 September | 22 August-1 September | 24 August-3 September |
|                      |                            |                       |                            | 5-15 September        | 2-12 September        | 4-14 September        |
|                      |                            |                       |                            |                       | 13-23 September       |                       |

### **5.3.3.2. Ice Velocity Analysis**

Table 5.6 and Table 5.8 show the percentage increase/decrease in ice velocity during the image pairs velocity period before, during and after (where data are available) the cyclonic event compared to the values of the preceding image pairs velocity period. Along with that, the percentage increase/decrease in mean daily runoff of image pair velocity period before (hereafter runoff 1) and during (hereafter runoff 4) the cyclonic event was calculated with respect to runoff in the preceding image pair velocity period. Doyle et al. (2015) stressed the importance of the temperature regime and runoff in the week before the cyclonic event, in contributing to ice acceleration and also included in the table are the percentage increase/decrease in mean daily runoff during the cyclonic days with respect to the week before (hereafter runoff 2) and the preceding satellite data period (hereafter runoff 3) for comparison to runoff 4. Finally, Table 5.7 and Table 5.9 provide the percentage of the total cyclone period covered and the percentage of cyclone days in the satellite data period which cover the event. The results are divided in the tables according to marine or terrestrial terminal environment of the glaciers. All the values in these tables will be utilised to describe ice velocity and change in runoff around the cyclonic events in the following sub-section of each site.

**Table 5.6.** Summary of ice velocity change along the flowlines of marine terminating glaciers around the cyclonic periods. For each period (Before, During and After the cyclonic event) the percentage of the increase/decrease of ice motion compared to the preceding image pair velocity period is provided. Values more than +5 % are highlighted in bold red and less than -5 % in bold blue. The percentage increase/decrease in mean daily runoff of image pair velocity period before (runoff 1) and during (runoff 4) the cyclonic event is calculated with respect to runoff in the preceding satellite data period. For comparison, the percentage increase/decrease in mean daily runoff during the event with respect to the week before (runoff 2) and in the preceding satellite data period (runoff 3) are shown. Positive values are highlighted in bold purple and negative values in bold brown.

| Terminating environment | Cyclonic event | Glacier        | Flow line | Before                      |            | *During                     |            |            |            | After                       |
|-------------------------|----------------|----------------|-----------|-----------------------------|------------|-----------------------------|------------|------------|------------|-----------------------------|
|                         |                |                |           | % of change in ice velocity | % Runoff 1 | % of change in ice velocity | % Runoff 2 | % Runoff 3 | % Runoff 4 | % of change in ice velocity |
| Marine                  | 2015           | Sermiligarssuk | A1        | - 5 %                       | - 28 %     | +29 %                       | +139 %     | +33 %      | -4 %       | No data                     |
|                         |                | Akugdlerssup   | B1        | +2%                         | - 34 %     | +12 %                       | +667 %     | +74 %      | +18 %      | No data                     |
|                         |                | Kangiata       | B2        | 0 %                         |            | +7 %                        |            |            |            |                             |
|                         |                | Nunata         | B3        | 0 %                         |            | +8 %                        |            |            |            |                             |
|                         |                | Kujatdleq      | C1        | +27 %                       | - 68 %     | -8 %                        | +198 %     | -28 %      | - 59 %     | -1 %                        |
|                         |                | Equip          | C2        | +41 %                       |            | -32 %                       |            |            |            | -5 %                        |
|                         |                | Avangnardleq   | C3        | +85 %                       |            | +2 %                        |            |            |            | -40 %                       |
|                         |                | Jakobshavn     | C4        | +8 %                        |            | +9 %                        |            |            |            | -12 %                       |
|                         |                | Rink           | D1        | +2 %                        | - 69 %     | +2%                         | +56 %      | - 16 %     | - 28 %     | +1 %                        |
|                         |                | Kangerdlugssup | D2        | +7 %                        |            | +7 %                        |            |            |            | -4 %                        |
|                         | 2013           | Alangordliup   | E1        | -26 %                       | - 95 %     | +72 %                       | +292 %     | +102 %     | +71 %      | -38 %                       |
|                         |                | Sarqardliup    | E2        | -9 %                        |            | +46 %                       |            |            |            | -33 %                       |
|                         | 2012           | Alangordliup   | E1        | -32 %                       | - 57 %     | +16 %                       | +43 %      | -64 %      | - 74 %     | No data                     |
|                         |                | Sarqardliup    | E2        | -26 %                       |            | +13 %                       |            |            |            |                             |

\* For site B both 19<sup>th</sup> -29<sup>th</sup> August and 30<sup>th</sup> August - 9<sup>th</sup> September periods are considered during the cyclonic event and results merged

**Table 5.7.** For each flowline of marine terminating glaciers, the percentage of total cyclone period covered and percentage of cyclones days in the satellite data period which cover the event are provided.

| Terminating environment | Cyclonic event | Glacier         | Flow line | *During  |  |
|-------------------------|----------------|-----------------|-----------|--|--|
|                         |                |                 |           | % of total cyclone period covered in satellite data period | % of cyclone days in the satellite data period |
| Marine                  | 2015           | Sermiligarssuk  | A1        | 80 %   | 73 %   |
|                         |                | Akugdlerussup   | B1        | 100 %  | 45 %   |
|                         |                | Kangiata Nunata | B2        |  |  |
|                         |                |                 | B3        |  |  |
|                         |                | Kujatdleq       | C1        | 100 %  | 37 %   |
|                         |                | Equip           | C2        |  |  |
|                         |                | Avangnardleq    | C3        |  |  |
|                         |                | Jakobshavn      | C4        |  |  |
|                         |                | Rink            | D1        | 100 %  | 55 %   |
|                         | Kangerdlugssup | D2              |           |  |  |
|                         | 2013           | Alangordliup    | E1        | 100 %  | 64 %   |
|                         |                | Sarqardliup     | E2        |  |  |
|                         | 2012           | Alangordliup    | E1        | 100 %  | 45 %   |
| Sarqardliup             |                | E2              |           |  |  |

\* For site B both 19<sup>th</sup> -29<sup>th</sup> August and 30<sup>th</sup> August - 9<sup>th</sup> September periods are considered during the cyclonic event and results merged

**Table 5.8.** Summary of ice velocity change along the flowlines of land terminating glaciers around the cyclonic periods. For each period (Before, During and After the cyclonic event) the percentage of the increase/decrease of ice motion compared to the preceding image pair velocity period is provided. Values more than +5 % are highlighted in bold red and less than -5 % in bold blue. The percentage increase/decrease in mean daily runoff of the satellite data period before (runoff 1) and during (runoff 4) the cyclonic event is calculated with respect to runoff in the preceding satellite data period. For comparison, the percentage increase/decrease in mean daily runoff during the event with respect to the week before (runoff 2) and the preceding satellite data period (runoff 3) are shown. Positive values are highlighted in bold purple and negative values in bold brown.

| Terminating environment | Cyclonic event | Glacier        | Flow line | Before                      |              | *During                     |               |               |              | After                       |
|-------------------------|----------------|----------------|-----------|-----------------------------|--------------|-----------------------------|---------------|---------------|--------------|-----------------------------|
|                         |                |                |           | % of change in ice velocity | % Runoff 1   | % of change in ice velocity | % Runoff 2    | % Runoff 3    | % Runoff 4   | % of change in ice velocity |
| Land                    | 2015           | Kangaussarssup | B4        | -5 %                        | <b>-34 %</b> | <b>+58 %</b>                | <b>+667 %</b> | <b>+74 %</b>  | <b>+18 %</b> | No data                     |
|                         | 2013           | Quingap        | E3        | <b>-33 %</b>                | <b>-95 %</b> | <b>+53 %</b>                | <b>+292 %</b> | <b>+102 %</b> | <b>+71 %</b> | <b>-28 %</b>                |
|                         |                |                | E4        | <b>-41 %</b>                |              | <b>+61 %</b>                |               |               |              | <b>-37 %</b>                |
|                         |                | Iliuliaik      | E5        | <b>-38 %</b>                |              | <b>+47 %</b>                |               |               |              | <b>-31 %</b>                |
|                         | 2012           | Quingap        | E3        | <b>-30 %</b>                | <b>-57 %</b> | <b>+13 %</b>                | <b>+43 %</b>  | <b>-64 %</b>  | <b>-74 %</b> | No data                     |
|                         |                |                | E4        | <b>-30 %</b>                |              | <b>+14 %</b>                |               |               |              |                             |
|                         |                | Iliuliaik      | E5        | <b>-30 %</b>                |              | <b>+8 %</b>                 |               |               |              |                             |

\* For site B both 19th -29th August and 30<sup>th</sup> August – 9<sup>th</sup> September periods are considered during the cyclonic event and results merged

**Table 5.9.** For each flowline of marine terminating glaciers, the percentage of total cyclone period covered and the percentage of cyclones days in the satellite data period which cover the event are provided.

| Terminating environment | Cyclonic event | Glacier        | Flow line | *During   |  |      |
|-------------------------|----------------|----------------|-----------|---|--|------|
|                         |                |                |           | % of total cyclone period covered in satellite period | % of cyclone days in the satellite data period |      |
| Land                    | 2015           | Kangaussarssup | B4        | 100 %   | 45 %   |      |
|                         | 2013           | Quingap        | E3        | 100 %   | 64 %   |      |
|                         |                |                | E4        |   |  |      |
|                         | 2012           | Quingap        | Iliuliaik | E5  | 100 %  | 45 % |
|                         |                |                | Iliuliaik | E3  |  |      |
|                         |                |                |           | E4  |  |      |
|                         |                |                | E5        |   |  |      |

\* For site B both 19th -29th August and 30<sup>th</sup> August – 9<sup>th</sup> September periods are considered during the cyclonic event and results merged

### 5.3.3.3. Site A, 2015

No ice velocity data were available during the month of May (Figure 5.15). During the first period available 3<sup>rd</sup> – 18<sup>th</sup> June the average ice velocity along A1 was around 100  $m yr^{-1}$  above the multi-year value which was 475  $m yr^{-1}$ . During this period the temperature was around 0 C° and melt onset was observed, although without runoff. In the subsequent period, from 19<sup>th</sup> June to 4<sup>th</sup> July, the average ice velocity of 752  $m yr^{-1}$  was reached; the highest among these data, in conjunction with temperature constantly above freezing, a gradual increase in meltwater production from 5 mm to 15 mm and runoff onset. A subsequent decrease in average ice velocity to 625  $m yr^{-1}$  was detected from the image pair covering the period 5<sup>th</sup> - 20<sup>th</sup> July. During the same period, however, there was a sustained gradual increase in runoff up to 8 mm fed by meltwater around 14 mm which was only interrupted by a momentary decrease between 12<sup>th</sup> to 14<sup>th</sup> July to around 5 mm. An image pair covering the period from 21<sup>st</sup> July to 5<sup>th</sup> August underlined a further gradual decline in ice velocity reaching the lowest average value of 520  $m yr^{-1}$ . This period was characterised by a rapid decline in runoff reaching daily values around 3 mm respectively on 3<sup>rd</sup> August followed by a gradual increase in meltwater to values up to 8 mm by 5<sup>th</sup> August. A further ice velocity decrease of -5 % was detectable in the subsequent image from 6<sup>th</sup> to 21<sup>st</sup> August with a -28 % change in runoff 1 (see Table 5.6). It was interrupted by a noteworthy velocity increase of +29 % (approximately + 120  $m yr^{-1}$ ) in the subsequent image pair during the period 25<sup>th</sup> August- 4<sup>th</sup> September which covered the 80 % of a cyclonic period and which represented 73 % of the days in the image pair (see Table 5.7). Here the increase in runoff 2 and runoff 3 (+139 % and +33 %) were opposite in value to runoff 4 (- 4 %). A cyclone event generated this period of strong runoff fed by meltwater and rain between 28<sup>th</sup> August and 6<sup>th</sup> September characterised by two peaks, interrupted by two days, 31<sup>st</sup> August and 1<sup>st</sup> September, where melt was around zero and no rain was detected. The first peak was on 30<sup>th</sup> August, and the second which was the highest, between 4<sup>th</sup> and 6<sup>th</sup> September where meltwater and rainfall reached the highest value of the entire season of around 26

Late Summer/Early Autumn Cyclonic Rainfall and Ice flow of the GrIS

mm and 6 mm respectively, which fed runoff with values near 10 mm comparable with the maximum values reached in July.

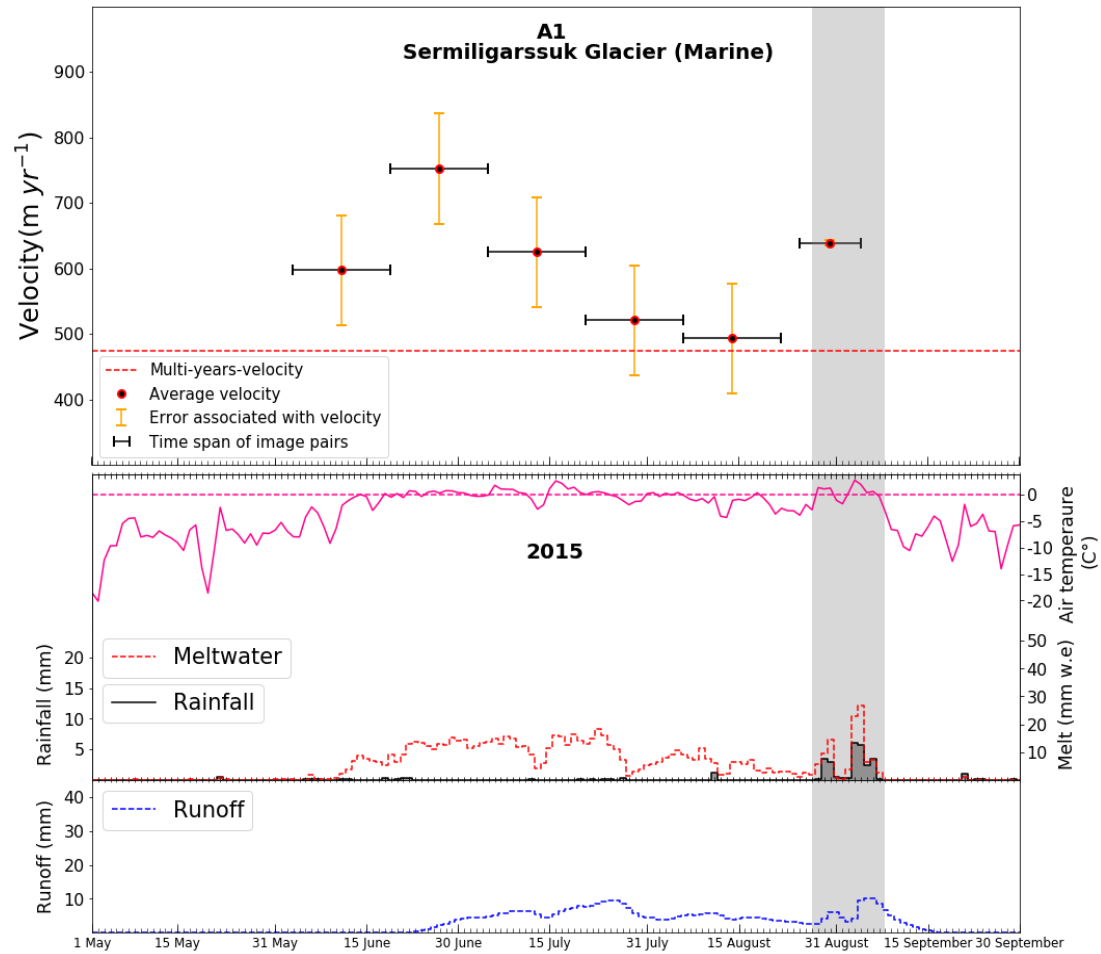


**Figure 5.15.** Top: Average ice velocity along flowline A1 during image pair periods for which ice velocity data were available. Red dotted line represents the multi-year ice velocity. Bottom: Daily meltwater, rainfall, runoff over the entire basins where runoff occurred and daily temperature below the ELA. Timing of the cyclonic event is shaded in grey in Top and Bottom subplots.

Velocities along the flowline of image pairs covering the cyclonic event and the preceding period are shown in Figure 5.16. Overall, ice velocity values covering the cyclonic period, remained well above ice velocity of the preceding period. However, considering the measurement errors, differences were particularly significant within the first 10 km from the calving front, with a gap up to  $150\ m\ yr^{-1}$  compared to a maximum ice velocity error of  $84\ m\ yr^{-1}$ . Velocities showed a general decreasing trend from a value around  $1000\ m\ yr^{-1}$  at the calving front to a value around  $120\ m\ yr^{-1}$  at 51 km from the calving front where data for the period 6<sup>th</sup>-21<sup>st</sup>

August ends. This linear decreasing trend in ice velocity was interrupted by a sharp decrease between 9 and 15 km from the calving front where values dropped by around  $400 \text{ m yr}^{-1}$  in 6 km and then increased again by  $200 \text{ m yr}^{-1}$  from 15 km to 25 km from the calving front.

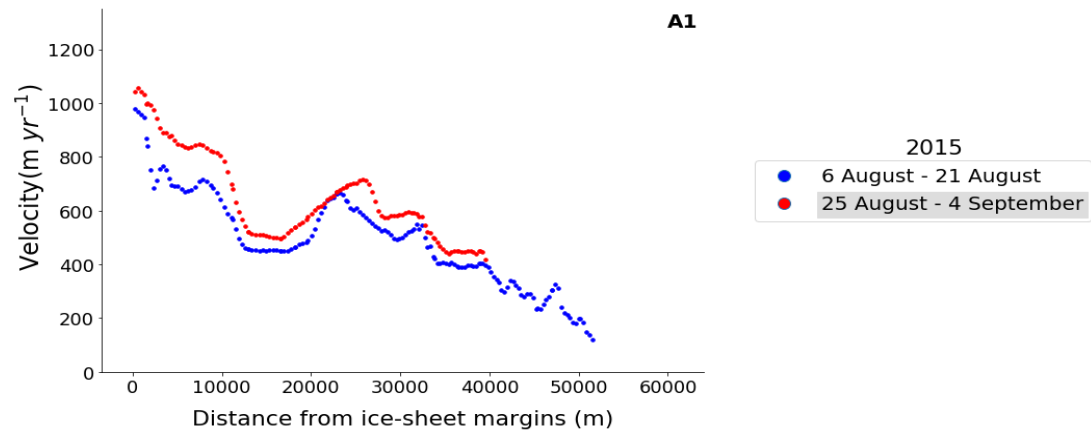


**Figure 5.16.** Ice velocities along flowline A1 during selected image pairs periods. Ice velocity of image pair which covers most of the cyclonic event is in red and shaded in grey in the legend.

#### 5.3.3.4. Site B, 2015

During May temperatures were below freezing with no significant production of meltwater and runoff (Figure 5.17, Figure 5.18). The first image pair available for this period covers eleven days from 12<sup>th</sup> to 22<sup>nd</sup> May. During this period the average ice velocities along flowline B1 and B4 were  $35 \text{ m yr}^{-1}$  and  $5 \text{ m yr}^{-1}$  above the MEASUREs multi-year values of  $593 \text{ m yr}^{-1}$  and  $123 \text{ m yr}^{-1}$ . Conversely the average ice velocity at B2 and B3 were  $164 \text{ m yr}^{-1}$  and  $164 \text{ m yr}^{-1}$  below the MEASUREs multi-year values of  $1276 \text{ m yr}^{-1}$  and  $1622 \text{ m yr}^{-1}$ . Overall, during this period, the average ice velocity values along B2, B3 and B4 were the lowest of the entire melt season. The subsequent image pair covered a period going from 23<sup>rd</sup> of May to 13<sup>th</sup> June, during which the melt onset started but without runoff. Here, there was an increase in ice velocity at all flowlines, more marked at B1 and B4. Along flowlines B1, B2 and B4 the average ice velocity from the image pair covering the period 14<sup>th</sup> to 24<sup>th</sup> June, reached the highest values recorder by this study of  $721 \text{ m yr}^{-1}$ ,  $1635 \text{ m yr}^{-1}$  and  $216 \text{ m yr}^{-1}$  while the second highest at B3 ( $1748 \text{ m yr}^{-1}$ ). This period

was characterised by a gradual increase in meltwater from 5 mm to 14 mm and runoff from 0 mm to 3 mm sustained by a temperature constantly above freezing. Along B3 the peak in average ice velocity of  $1766 \text{ m yr}^{-1}$  was reached in the subsequent image pair period between 25<sup>th</sup> June and 16<sup>th</sup> July but not at flowline B1, B2 and B4 where a decrease in velocity was observed. This period was characterised by an increase of meltwater and runoff with values around 16 mm and 9 mm between 1<sup>st</sup> – 10<sup>th</sup> July, followed by slight decrease for three days, and another increase characterised by some peaks in meltwater around 16 mm and a runoff value around 12 mm. The following image pair covered the period 17<sup>th</sup>-27<sup>th</sup> July where a value of meltwater around 18 mm was followed by a decrease to 4 mm, whereas runoff remained around 12 mm. During this period a general downward trend in ice velocity was observed at all flowlines, more sustained along B1, B2 and B3. During the period 28<sup>th</sup> July to 18<sup>th</sup> August a general decline in meltwater and runoff favoured by temperatures around or below the freezing point was interspersed by two small peaks. In the image pair covering this period 28<sup>th</sup> July to 7<sup>th</sup> August, an increase (decrease) of few tens of metres per year at B1 and B3 (B2 and B4) was observed. In the subsequent period between 8<sup>th</sup>- 18 August ice velocity decrease/increase along the flowlines, ranging from -5 % to +2 % was concurrent with a decrease in runoff of -34 % (see Table 5.6 and Table 5.8). The following two image pairs covered the period from 19<sup>th</sup> August to 9<sup>th</sup> September. They covered both a period of temperatures below freezing (accompanied by a decline in meltwater and runoff to lows not observed since early summer) and the cyclonic rainfall events and the three non-cyclonic days following this. The passage of a cyclone between 28<sup>th</sup> August - 6<sup>th</sup> September led to two close events of cyclonic rainfall accompanied by sustained production of meltwater, rainfall and runoff favoured by temperatures well above freezing, reaching daily values up to 23 mm, 19 mm and 12 mm; greater than or equal to the largest peaks observed during the entire melt season. Overall, during this period covered by two image pairs, an average acceleration of +12 %, +7 % and +8 % at B1, B2 and B3 was observed if compared to the preceding period, while at land terminating glacier B4 a larger increase of +58 % in ice velocity was detected (See Table 5.6 and Table 5.8). This increase in ice motion was accompanied by an increase of +667 %, +74 % and + 18 %

in runoff 2, 3 and 4 with the image pairs velocity period covering 100 % of the cyclone period which represents 45 % of the days in the two image pairs (see Table 5.7 and Table 5.9).

Ice velocity along the entire flowlines B2, B3 and B4 during the period 30<sup>th</sup> August-9<sup>th</sup> September remained along most of the path above the period 19<sup>th</sup> - 29<sup>th</sup> August which values, in turn, remained above the period 8<sup>th</sup> -18<sup>th</sup> August (Figure 5.19). B1 was an exception where ice velocity during the period 19<sup>th</sup> - 29<sup>th</sup> August remained above the other two periods. Along this flowline the highest velocity was within 2 km from the calving front with values around  $700 \text{ m yr}^{-1}$  in the pre-cyclone image period up to  $850 \text{ m yr}^{-1}$  in the subsequent two periods. From 2 km to 14 km from the calving front ice velocity varied between  $420 \text{ m yr}^{-1}$  for the earliest period and  $600 \text{ m yr}^{-1}$  for the others two. A peak around 15 km with values between  $600 \text{ m yr}^{-1}$  for pre cyclonic period and  $760 \text{ m yr}^{-1}$  for the first cyclone image period was followed by a gradual decrease to 20 km from the calving front, interrupted by slight velocity increase peaks of some tens of  $\text{m yr}^{-1}$  during each of the three periods. From 20 km to 23 km the velocity remained around  $300 \text{ m yr}^{-1}$  and then increased from this point to the end of the flowline by around  $100\text{-}150 \text{ m yr}^{-1}$  with differences between the three periods reduced to few tens of meters with the first and second cyclonic image pairs with higher values if compared to the period 8<sup>th</sup> -18<sup>th</sup> August.

Along B2 and B3 the ice velocities underwent a sharp decline within 8 km and 5 km from the front going from  $6000 \text{ m yr}^{-1}$  to respectively  $750 \text{ m yr}^{-1}$  and  $2000 \text{ m yr}^{-1}$  with values of few tens of km higher during the two cyclone image periods within 4 km from the calving front if compared to pre-cyclonic image period. Subsequently the decrease became more gently until the end of the flowline where ice velocities reached values between  $230$  and  $400 \text{ m yr}^{-1}$  and overlapped during the three periods considered. In contrast to B1, B2 and B3, at B4, ice velocities followed an increase trend from  $100\text{-}180 \text{ m yr}^{-1}$  to  $180\text{-}240 \text{ m yr}^{-1}$  within 14 km from the front, with the highest values during the second cyclonic image period followed by the first cyclonic image period and then the pre-cyclonic image period. A gradual downward trend followed, from  $240 \text{ m yr}^{-1}$  to  $200 \text{ m yr}^{-1}$  during the period

Late Summer/Early Autumn Cyclonic Rainfall and Ice flow of the GRS

30<sup>th</sup> August-9<sup>th</sup> September till 22 km where data end and from 210-180  $m\ yr^{-1}$  to 110  $m\ yr^{-1}$  during the other two periods.

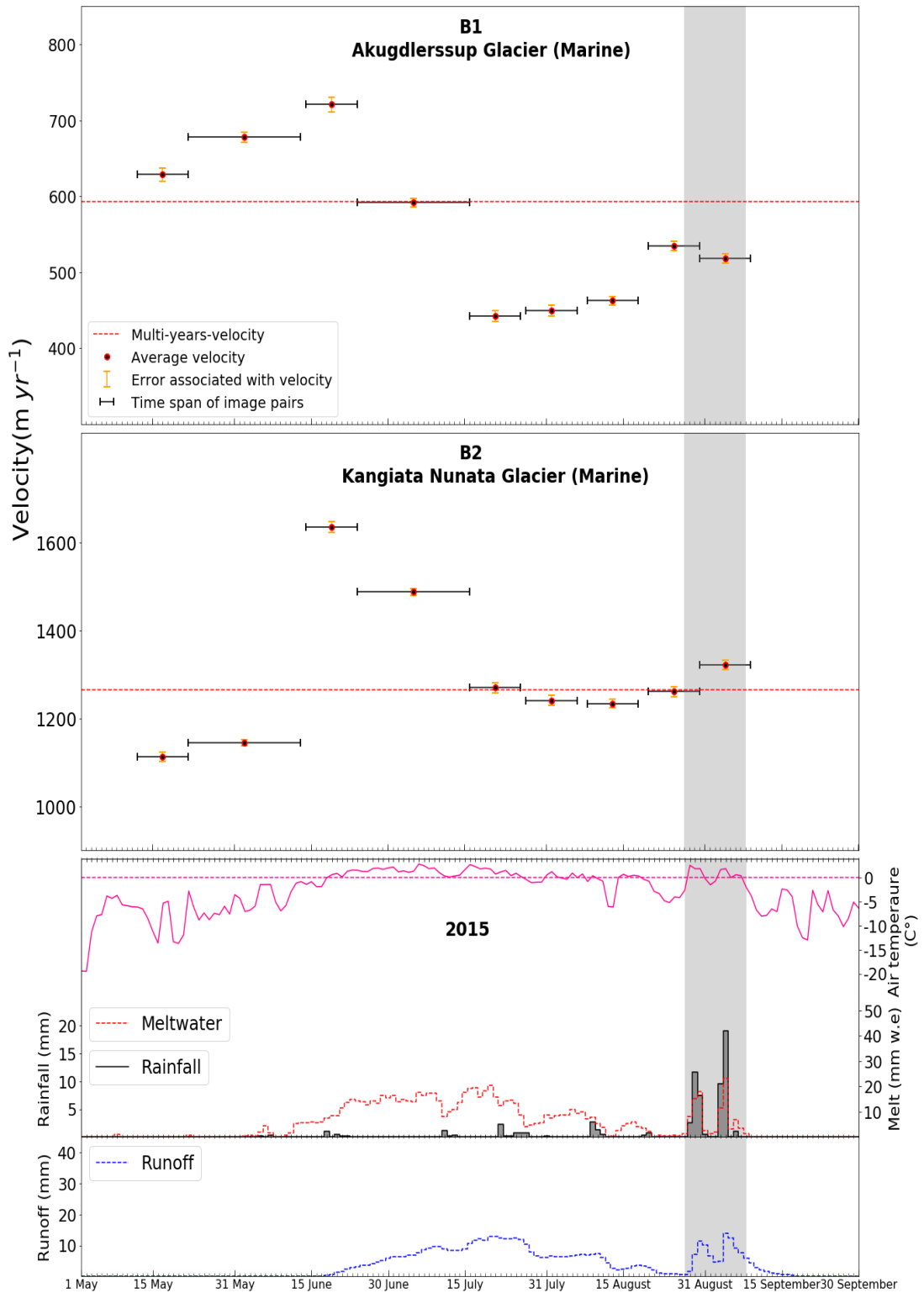


**Figure 5.17.** Same as Fig 5.15 but for site B, flowlines B1 and B2

Late Summer/Early Autumn Cyclonic Rainfall and Ice flow of the GrIS

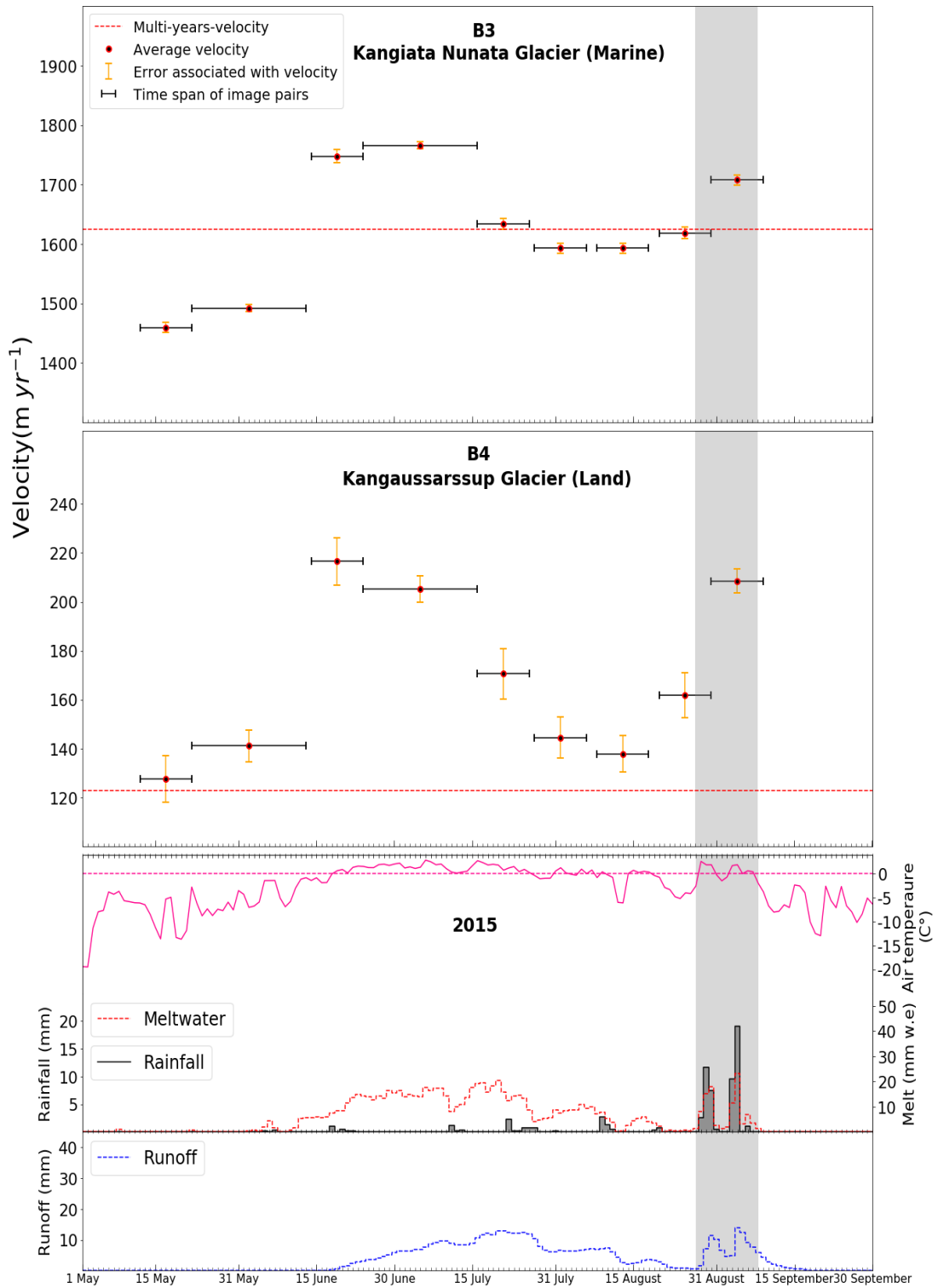
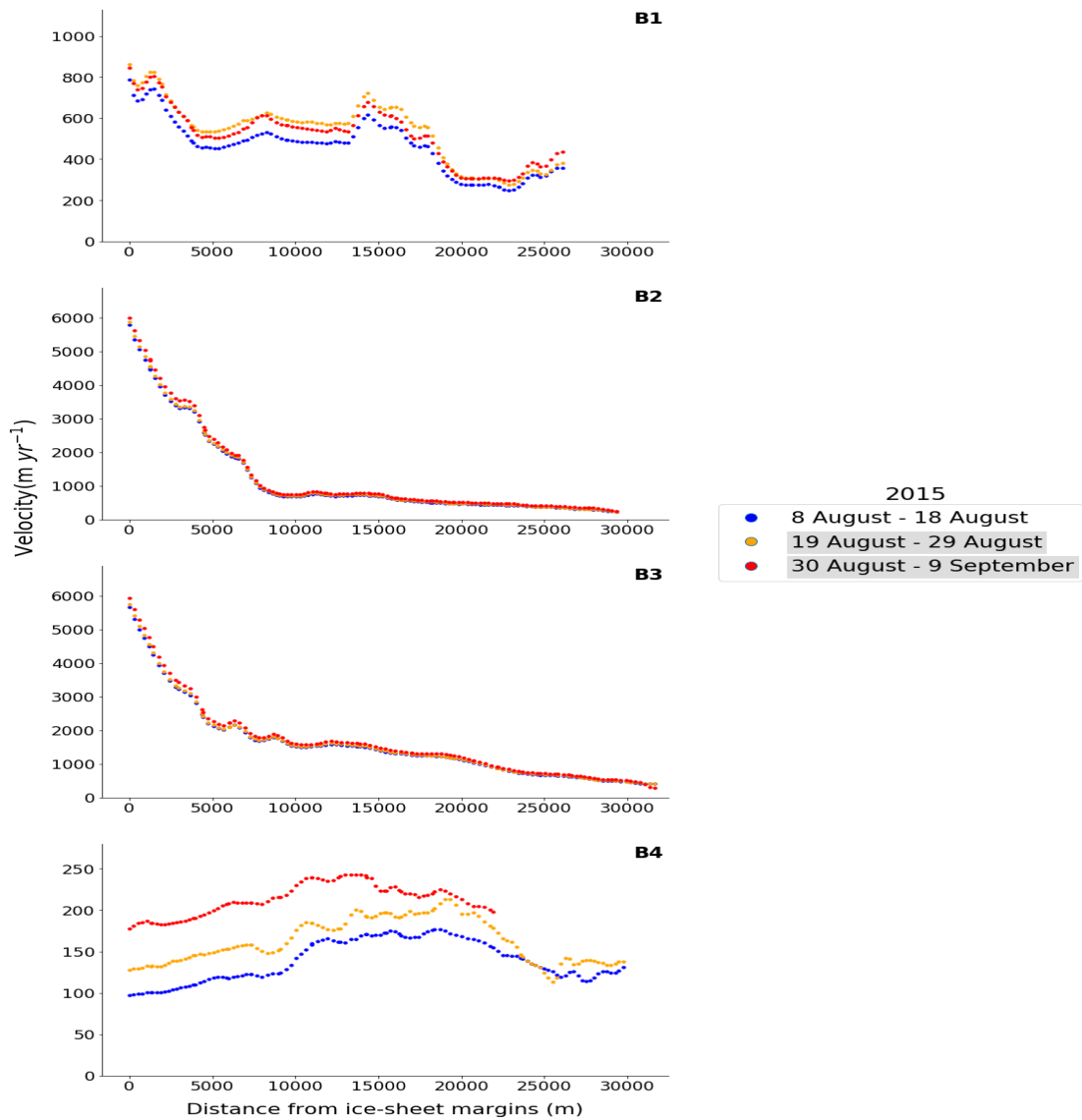


Figure 5.18. Same as Fig 5.15 but for site B, flowlines B3 and B4.



**Figure 5.19.** Same as Fig 5.16 along flowlines B1, B2, B3 and B4. Here, two image pairs cover the cyclonic period and are shaded in grey in the legend.

### 5.3.3.5 Site C, 2015

During the month of May, there were some small intermittent episodes of melt but no runoff (Figure 5.20, Figure 5.21). The period 12<sup>th</sup> to 27<sup>th</sup> May was covered by the velocity image pair available for this month and average ice velocities along C1, C2 C3 and C4 were 161  $m yr^{-1}$ , 34  $m yr^{-1}$ , 28  $m yr^{-1}$  and 678  $m yr^{-1}$  above the MEASUREs multi-year velocities (respectively 269  $m yr^{-1}$ , 120  $m yr^{-1}$ , 121  $m yr^{-1}$  and 1735  $m yr^{-1}$ ). Image pair 4<sup>th</sup>-19<sup>th</sup> June showed a reduction in ice velocity of 10  $m yr^{-1}$  at C1 while an increase of 71  $m yr^{-1}$  is detected at C2, when compared to velocities of the previous image pair. Missing data along C3 and C4 for 4-19<sup>th</sup> June

made comparison for these flowlines in the image period impossible. During this period, a small peak up to 6 mm and 2 mm in melt and runoff between 4<sup>th</sup> to 7<sup>th</sup> June, precedes an increase of 13 mm of meltwater and 3 mm in runoff occurred in conjunction with temperatures well above zero between 15<sup>th</sup> to 19<sup>th</sup> June. A subsequent image pair covered the period 29<sup>th</sup> June - 14<sup>th</sup> July where average ice velocity along C1, C2 and C3 reached the highest values of the image pair periods ( $462 \text{ m yr}^{-1}$ ,  $403 \text{ m yr}^{-1}$  and  $339 \text{ m yr}^{-1}$  respectively) while along C4 the second highest value was reached of  $2680 \text{ m yr}^{-1}$ . This period was characterised by a gradual increase in meltwater and runoff favoured by temperatures well above zero, reaching values up to 35 mm and 26 mm. This increase is interrupted by a slight drop between 11<sup>th</sup> and 14<sup>th</sup> July with a decrease in meltwater and runoff to values around 18 mm and 17 mm. The 15<sup>th</sup> - 30<sup>th</sup> July image period showed ice velocity along all flowlines underwent a sharp decline around  $200/250 \text{ m yr}^{-1}$ . Despite meltwater and runoff reaching the highest values of the entire melt season around 40 mm and 30 mm between 15<sup>th</sup> and 18<sup>th</sup> July, there then followed a sharp decline to around 7 mm and 9 mm in conjunction with decreasing temperatures. In the subsequent image pair 31<sup>st</sup> July – 15<sup>th</sup> August, the velocity started to rise again with an order of magnitude around  $100\text{-}200 \text{ m yr}^{-1}$  along all flowlines with an increase in ice velocity between +8 % and +85 % if compared to the preceding period, accompanied by a reduction of -68 % in runoff 1(see Table 5.6). This period was characterised by a peak in meltwater and runoff around 13 mm and 12 mm which occurred between 3<sup>rd</sup> and 6<sup>th</sup> August followed by a decrease until 14<sup>th</sup> August where meltwater and runoff were around 0 mm and temperature below freezing. The next image pair, 23<sup>rd</sup> August - 7<sup>th</sup> September, included the passage of a cyclone between 28<sup>th</sup> August to 2<sup>nd</sup> September which led to a momentary increase in meltwater from 0 mm up to 16 mm along with cyclonic rainfall around 3 mm feeding an increase in runoff from 0 mm up to 8 mm. There was then a drop in temperature below freezing with runoff and meltwater around zero for the rest of the season. The image pair included 100 % of the cyclonic event, although it represented only 37% of the total days in the image period (see Table 5.7). A decrease in ice velocity of -8 % and -32 % is observed along C1 and C2 opposite to +2 % and +9 % along C3 and C4 accompanied by a reduction in runoff 4 (-

Late Summer/Early Autumn Cyclonic Rainfall and Ice flow of the GrIS

59 %) and runoff 3 (-28 %) but not runoff 2 (+198). The last image pair covered the period 8<sup>th</sup> -23<sup>rd</sup> September and is characterised by a velocity decline from -1 to -40 % along all the flowlines if compared to velocity of the previous image pair, more marked along C3 and C4 with a reduction in velocity of 74  $m\ yr^{-1}$  and 322  $m\ yr^{-1}$  respectively.

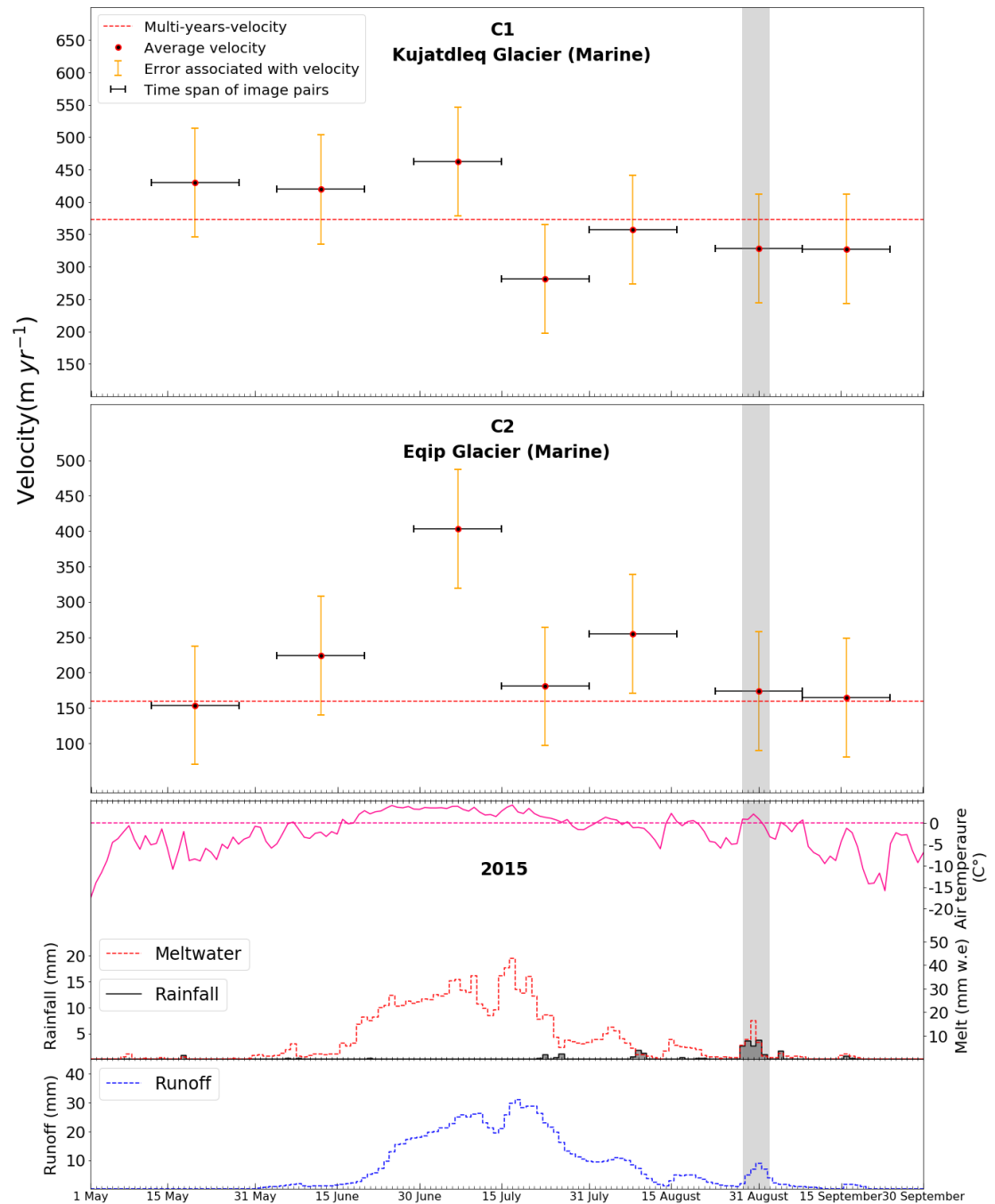
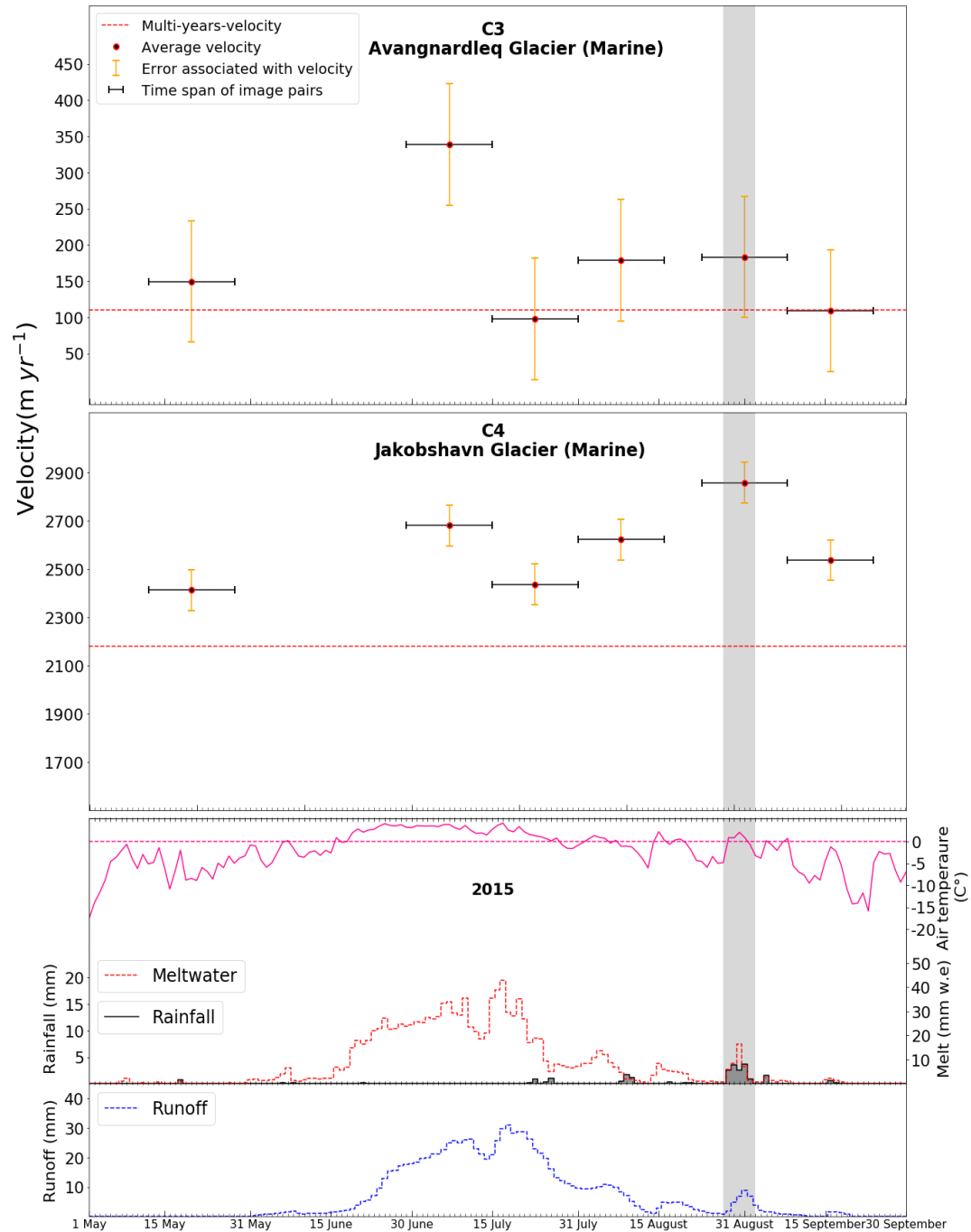


Figure 5.20. Same as Fig 5.15 but for site C, flowlines C1 and C2.



**Figure 5.21.** Same as Fig 5.15 but for site C, flowlines C3 and C4.

The velocity analysis along the entire flowlines before, during and after the cyclone event (Figure 5.22), gave further information. Within 10 km from the front along C1 values of ice velocity of the three periods were of the same magnitude and followed a decline from  $1250 \text{ m yr}^{-1}$  to  $350 \text{ m yr}^{-1}$ . Along C1, from 10 km to 39 km there was a general trend of decreasing ice velocities with large fluctuation ranging between  $500 - 350 \text{ m yr}^{-1}$  to values below  $200 \text{ m yr}^{-1}$  for the cyclone image period,

between  $1100 \text{ m yr}^{-1}$  to  $100 \text{ m yr}^{-1}$  for the pre-event period and from  $500 \text{ m yr}^{-1}$  to  $150 \text{ m yr}^{-1}$  for the post event period, although data resulted fragmented due to missing values in the image pairs. Ice velocity along this portion of the flowline during the period 31<sup>st</sup> July – 15<sup>th</sup> August were generally below the values of 8<sup>th</sup>-23<sup>rd</sup> September. In turn, ice velocity during 8<sup>th</sup>-23<sup>rd</sup> September was 150 to  $200 \text{ m yr}^{-1}$  below the period 23<sup>rd</sup> August-7<sup>th</sup> September apart from 9 to 18 km from the calving front where they often overlapped or inverted. From 39 km onward, ice velocity during the period 23<sup>rd</sup> August-7<sup>th</sup> September remained around values between  $20 \text{ m yr}^{-1}$  and  $200 \text{ m yr}^{-1}$  while ice velocity during the period 8<sup>th</sup>-23<sup>rd</sup> September remained between 180 and  $230 \text{ m yr}^{-1}$  and a gradual increase was observed from values around  $300 \text{ m yr}^{-1}$  to  $400 \text{ m yr}^{-1}$  for the period 31<sup>st</sup> July to 15<sup>th</sup> August.

The ice velocity along C2 went from  $380 \text{ m yr}^{-1}$  at the calving front to values below around  $200 \text{ m yr}^{-1}$  at 10 km from the calving front during the period 31<sup>st</sup> July to 15<sup>th</sup> August whereas from  $450 \text{ m yr}^{-1}$  to values below  $100 \text{ m yr}^{-1}$  during the other two periods. From 10 km to 52 km from the calving front, missing values in the image pairs, results in only a fragmented picture of velocity for this section. Here, during the period 23<sup>rd</sup> August-7<sup>th</sup> September, values from  $200 \text{ m yr}^{-1}$  underwent a general decrease from 30 km onwards till the 57<sup>th</sup> km where data ended. Ice velocity values during the period 8<sup>th</sup>- 23<sup>rd</sup> September after being below  $100 \text{ m yr}^{-1}$  rose to a value around a value of  $180 \text{ m yr}^{-1}$ , remaining stable from the 30 km onwards. During the period 15<sup>th</sup> July - 15<sup>th</sup> August ice velocity fluctuated between values of  $20 \text{ m yr}^{-1}$  and  $580 \text{ m yr}^{-1}$  till 58 km from the calving front where a gradual increase in ice velocity is observed during this period from values around  $200 \text{ m yr}^{-1}$  to values around  $450 \text{ m yr}^{-1}$  above the values of the period 23<sup>rd</sup> August-7<sup>th</sup> September.

At C3 within 13 km from the front, ice velocity values during the three periods remained between 0 and  $200 \text{ m yr}^{-1}$ . A gradual ice velocity increase during the period 8<sup>th</sup>-23<sup>rd</sup> September was observed from 13 km onwards with values that went from 20 -  $30 \text{ m yr}^{-1}$  to  $200 \text{ m yr}^{-1}$ . From 13 km to 62 km, ice velocities during the other two periods were characterised by a fluctuating “seesaw” pattern with values of the two periods higher or lower between them depending on the portion of the flowline analysed ranging from  $200 \text{ m yr}^{-1}$  to  $550 \text{ m yr}^{-1}$ . From 62 km from the

front onwards, ice velocity during the period 23<sup>rd</sup> August-7<sup>th</sup> September remained stable between 0 and 100  $m\ yr^{-1}$  till the end of the flowline. Conversely, ice velocity during the period 31<sup>st</sup> July to 15<sup>th</sup> August followed a gradual increase from 180  $m\ yr^{-1}$  to 300  $m\ yr^{-1}$ .

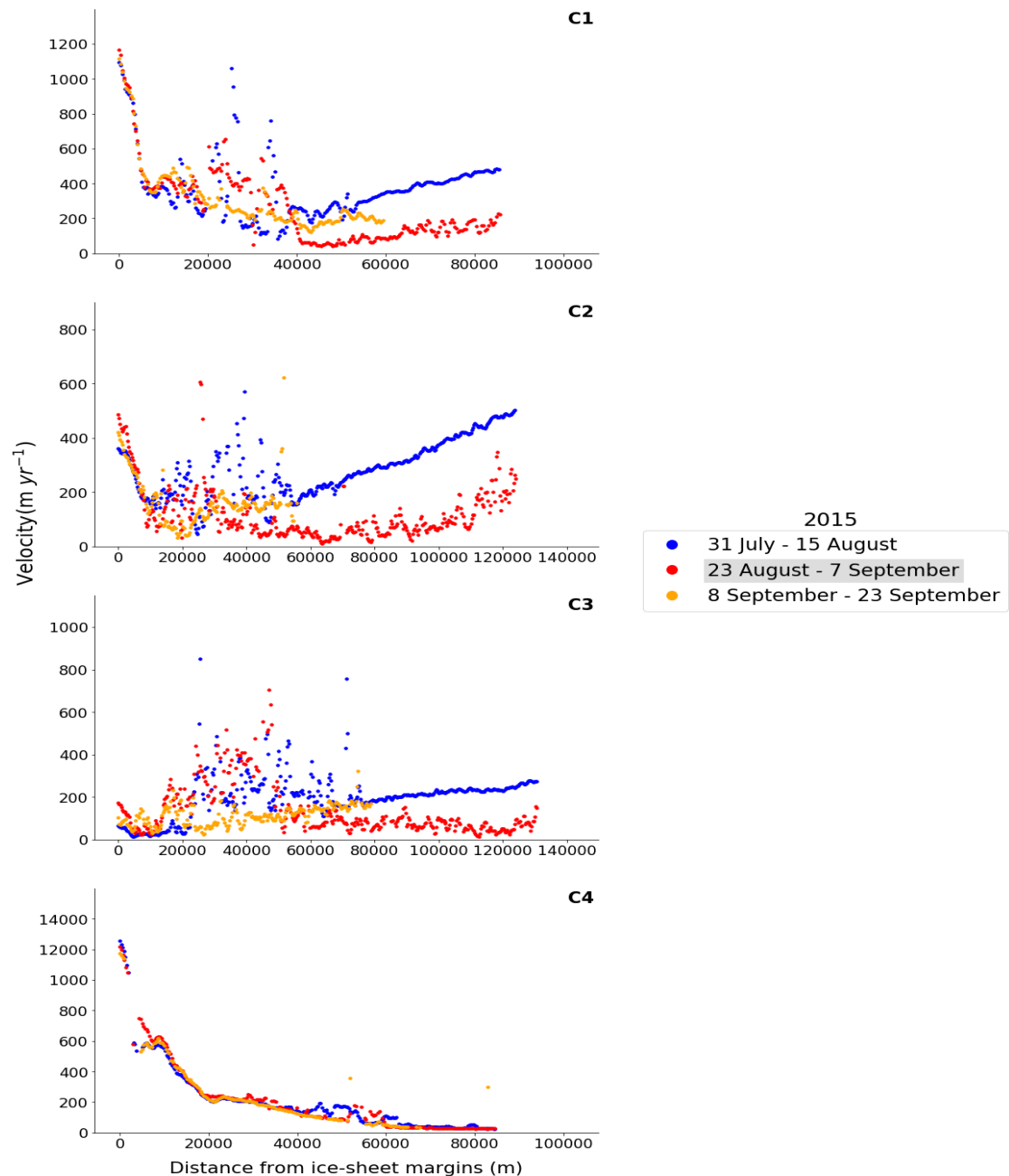


**Figure 5.22.** Same as Fig 5.16 along flowlines C1, C2, C3 and C4.

The velocity along C4, unlike the other flowlines, followed a negative exponential trend during all three periods (excluding between 2 and 3 km from the calving front where data are not available), from values around 12,500  $m\ yr^{-1}$  at the

calving front to values close to  $50 \text{ m yr}^{-1}$  from 65 km onwards. Despite the velocities from the image appear quite similar, however within 40 km from the front, there was a predominance of higher values during the period 23<sup>rd</sup> August-7<sup>th</sup> September, followed by the period 8<sup>th</sup>-23<sup>rd</sup> September. Conversely, from 40 km onwards, there was a predominance of higher values during the period 31<sup>st</sup> July to 15<sup>th</sup> August if compared to the others.

#### 5.3.3.6. Site D, 2015

Temperature below freezing characterised the month of May. In the periods 7<sup>th</sup>-17<sup>th</sup> May and 18<sup>th</sup>-28<sup>th</sup> May average ice velocities at D1 were around  $25 \text{ m yr}^{-1}$  below the value of  $2731 \text{ m yr}^{-1}$  of the MEASUREs multi-year reference for D1 (Figure 5.23) and around  $140 \text{ m yr}^{-1}$  above the multi-year reference value of  $1130 \text{ m yr}^{-1}$  at D2. The subsequent ice velocity data available cover a period of 33 days from the 29<sup>th</sup> May to 30<sup>th</sup> June and these data indicate an opposite behaviour at the two sites: 1) at D1 the lowest value of our data record ( $2568 \text{ m yr}^{-1}$ ) was reached 2) the highest values ( $1370 \text{ m yr}^{-1}$ ) was reached at D2. From 29<sup>th</sup> May to 20<sup>th</sup> June, temperatures were below or around freezing with little meltwater (less than 2 mm) and no runoff. Conversely, starting from the 21<sup>st</sup> June an abrupt increase in temperatures favoured high amounts of meltwater up to 14 mm production followed a few days later by runoff onsets that by the 30<sup>th</sup> June reached a value of 4 mm. In the subsequent image pairs, 1<sup>st</sup>-11<sup>th</sup> July, there was a gradual increase in meltwater and runoff up to 21 mm and 10 mm, an abrupt increase was detected, if compared to the preceding image pair, along the flow line D1 ( $+246 \text{ m yr}^{-1}$ ) opposite to a decrease along D2 ( $-108 \text{ m yr}^{-1}$ ). In the next period, 11<sup>th</sup> July- 2<sup>nd</sup> August (covered by two 11 days image pairs), there was an overall decrease in ice velocity detected at both flowlines. At D1 the average ice velocity went from  $2814 \text{ m yr}^{-1}$  on 11<sup>th</sup> July to  $2705 \text{ m yr}^{-1}$  on 2<sup>nd</sup> August while at D2 from  $1262 \text{ m yr}^{-1}$  to  $1128 \text{ m yr}^{-1}$ . During this period an overall decrease in melt and runoff was observed reaching values of 2 mm and 3 mm between 31<sup>st</sup> July-2<sup>nd</sup> August accompanied by a drop in temperature below zero. For image 2<sup>nd</sup> to 13<sup>th</sup> August there is a slight increase (decrease) of about  $10 \text{ m yr}^{-1}$  at D1 (D2). Here, an increase of a few mm in meltwater for the first three days was

followed by values near zero due to temperature well below zero while runoff continued its descent towards values close to zero without any peak. An acceleration of +2 and +7 % at D1 and D2 if compared to the previous period occurred in the

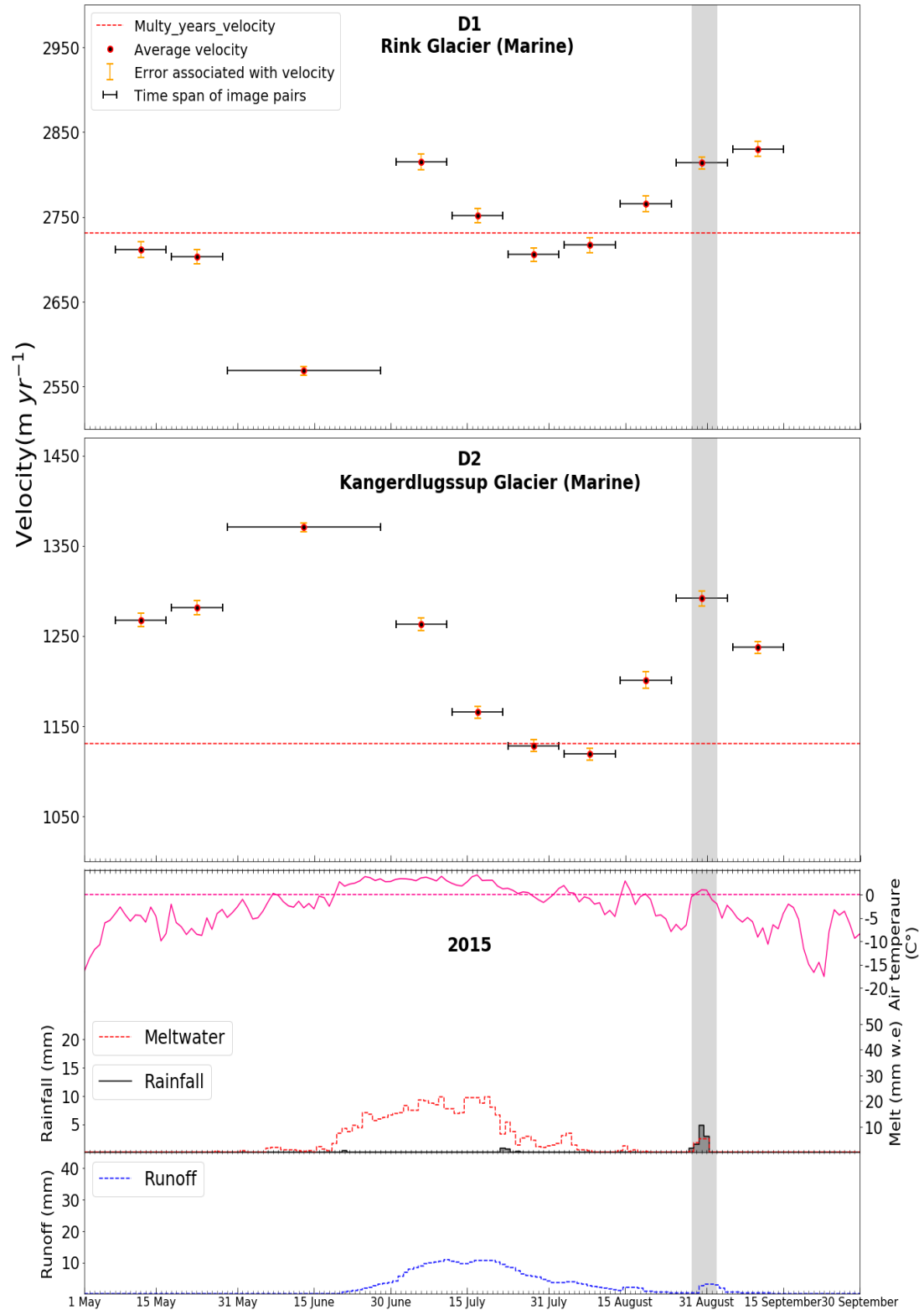
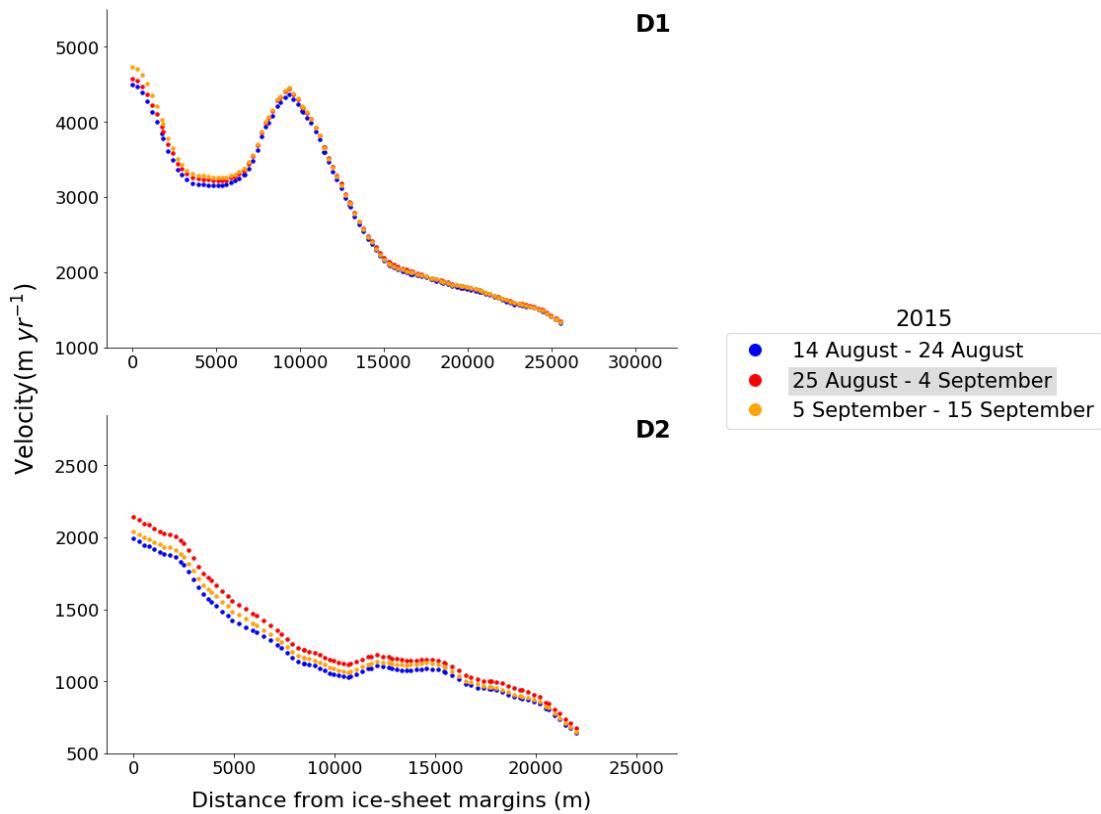


Figure 5.23. Same as Fig 5.15 but for site D, flowlines D1 and D2.

image pair covering the period from 14<sup>th</sup> to 24<sup>th</sup> August with a value of -69 % in runoff 1 (See Table 5.6) despite a brief (few days) and small peak of a few mm in runoff was detectable from 15<sup>th</sup> to 18<sup>th</sup> August. The acceleration continued with values of + 2 % and +7 % (+48  $m\ yr^{-1}$  +90  $m\ yr^{-1}$  at D1 and D2) in the subsequent image pairs velocity period, 25<sup>th</sup> August-4<sup>th</sup> September. This period covered 100 % of the cyclone event but the event only represented 55 % of total days in the period (See Table 5.7). From 20<sup>th</sup> August onwards, temperatures remained well below freezing not favouring melt and runoff. However, a passage of a cyclone between 28<sup>th</sup> August-2<sup>nd</sup> September induced a momentary increase of temperatures which caused a small peak in meltwater and rain of 5 mm and 4 mm which fed runoff of around 3 mm giving a value of +56 % in runoff 2 and values of -16 % and -18 % in runoff 3 and 4. After the event, image pair period 5<sup>th</sup>-15<sup>th</sup> September, an increase of +1 % (+17  $m\ yr^{-1}$ ) in ice velocity along D1 was opposite to a deceleration along D2 of -4 % (- 54  $m\ yr^{-1}$ ) and no runoff and meltwater were detected.

The analysis along the entire flowlines of the two glaciers (Figure 5.24) showed a gradual decline along the entire path of D2 with ice velocity from values at the front in a range between 1990 to 2120  $m\ yr^{-1}$  to values at the end around 670  $m\ yr^{-1}$ . Here, ice velocity during the cyclonic period remained well above the other two periods with the largest difference of the order of 50-100  $m\ yr^{-1}$  within 7 km from the front and then reduced to a few dozen of  $m\ yr^{-1}$  in the rest of the flowline. Along D1 a decrease in ice velocity from values around 4500  $m\ yr^{-1}$  at the front to values around 3200  $m\ yr^{-1}$  is followed by an increase from 5 to 9 km up to 4400  $m\ yr^{-1}$ . From here on, a gradual decreasing trend is observed till the end of the flowline, more marked between 9 and 15 km. Within 15 km are higher velocity values during the period 5<sup>th</sup> -15<sup>th</sup> September followed by the period 25<sup>th</sup> August - 4<sup>th</sup> September and then 14<sup>th</sup>-24<sup>th</sup> August. From 15 km onwards the differences between the values in the three periods reduce and even overlap.



**Figure 5.24.** Same as Fig 5.16 along flowlines D1, D2.

### 5.3.3.7. Site E, 2013

Two image pairs covered the period from 4<sup>th</sup> to 25<sup>th</sup> May (Figure 5.25, Figure 5.26) where the temperature remained below freezing and neither meltwater nor runoff were detected. From 4<sup>th</sup> to 14<sup>th</sup> May the average ice velocity remained around the MEASUREs multi-year value of 88, 160, 82, 73 and 95  $m\ yr^{-1}$  at E1, E2, E3, E4 and E5 with a slight decrease during 15<sup>th</sup> to 25<sup>th</sup> May. The image pair period 26<sup>th</sup> May to 5<sup>th</sup> June included the melt and runoff onsets and reveal a slight increase in ice velocity of + 16, + 19, + 19 and + 12  $m\ yr^{-1}$  at E1, E2, E3 and E4 but not at E5 where a decrease of 5  $m\ yr^{-1}$  was observed. The next image pair, 6<sup>th</sup> to 16<sup>th</sup> June, showed a strong meltwater and runoff increase up to values around 23 mm and 10 mm. During this period an acceleration around + 100 % occurred at E1 and E2 and around +50 % at E3, E4 and E5. The subsequent image pair period, 17<sup>th</sup> to 27<sup>th</sup> June, showed a decrease in velocity along E1 and E2 of -12 and -53  $m\ yr^{-1}$  and a further increase at E3, E4 and E5 of + 23, +50 and +58  $m\ yr^{-1}$ . During this period a momentary decrease in meltwater and runoff of few mm was followed by another peak with the same values

of the previous one. In the first half of the period 28<sup>th</sup> June to 8<sup>th</sup> July, data revealed a drop in meltwater and runoff, driven by temperatures below freezing, to values around 3 mm and 6 mm which started to rise again due to an increase in temperatures in the second part of this period to values up to 15 mm and 11 mm on 8<sup>th</sup> of July. The image pair covering this period revealed a decrease in ice velocity along all flowlines of an order between  $-40$  and  $-70 \text{ m yr}^{-1}$  if compared to the previous image pair covered period. The subsequent image pair, 9<sup>th</sup> - 30<sup>th</sup> July, where meltwater and runoff gradually increased, reaching the highest values of the entire melt season on 22<sup>nd</sup> (34 mm) and on 26<sup>th</sup> (30 mm) July. An increase in ice velocity along all flowlines was detected during this period if compared to the period before at E1 and E2 (+12 %, +11 %) and more marked along land terminating glacier (+24 %, +26 % and +20 % at E3, E4 and E5). Subsequently a decline in temperature was observed in August with values of meltwater and runoff gradually decreasing to values close to zero from 20<sup>th</sup> August onwards. The decrease of these variables coincided with a trend of decline in ice velocity values along all the flowlines obtained from the two image pairs which cover the period from 31<sup>st</sup> July to 21<sup>st</sup> August. The reduction in ice velocity was around  $-60 \text{ m yr}^{-1}$  for marine terminating glaciers and  $-90 \text{ m yr}^{-1}$  for land terminating glacier. The ice velocity continued its downwards trend along all flowlines in the subsequent image pair period, 22<sup>nd</sup> August-2<sup>nd</sup> September, ranging from -9 % to -41 % with a concomitant decrease in runoff 1 of -95 % (see Table 5.6 and Table 5.8). Values in the subsequent image pair covering the entire cyclonic event which represented 64 % of the days in the image pair period (see Table 5.7 and Table 5.9), showed acceleration ranging from +46 % to +72 % and was accompanied by a large increase in runoff 4 (+71 %), runoff 3 (+102 %) and runoff 2 (+292 %). This increase in runoff was due a cyclonic event of six days from 5<sup>th</sup> to 11<sup>th</sup> September which interrupted a trend of meteorological and glaciological values in transition to winter mode and led episodes of rainfall (between 0.5 and 3 mm) accompanied by two small peaks in meltwater (between 2 and 11 mm) that fed runoff (around 4 mm) for 6 days. Finally, during the period after the cyclonic event, image pair period 13<sup>th</sup> to 22<sup>nd</sup> September, a drop in ice velocity between -28 % and -38 %

Late Summer/Early Autumn Cyclonic Rainfall and Ice flow of the GrIS

was detected along all the flowlines accompanied by values of meltwater and runoff around zero.

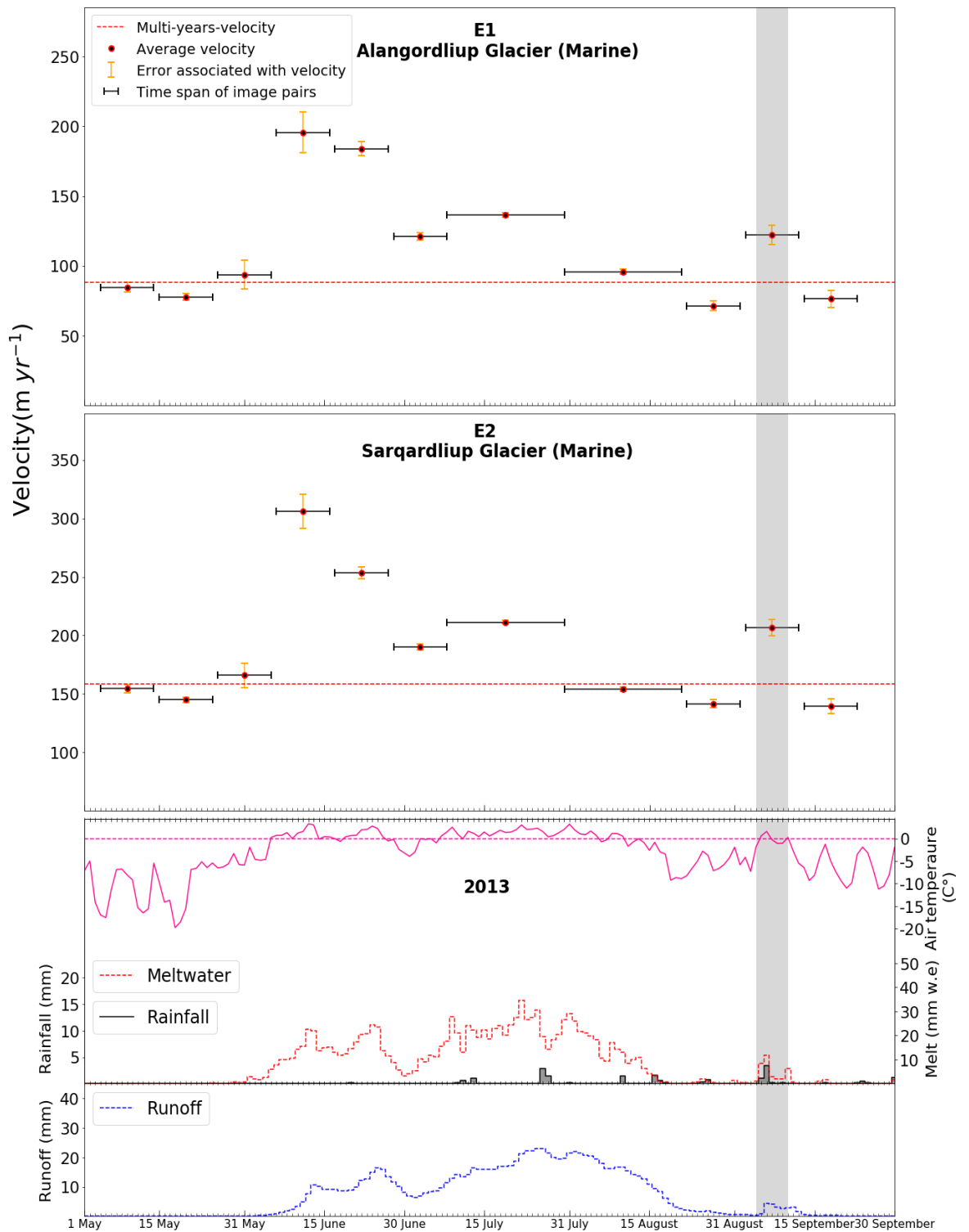


**Figure 5.25.** Same as Fig 5.15 but for the cyclonic event 2013, site E. Flowlines E1, E2.

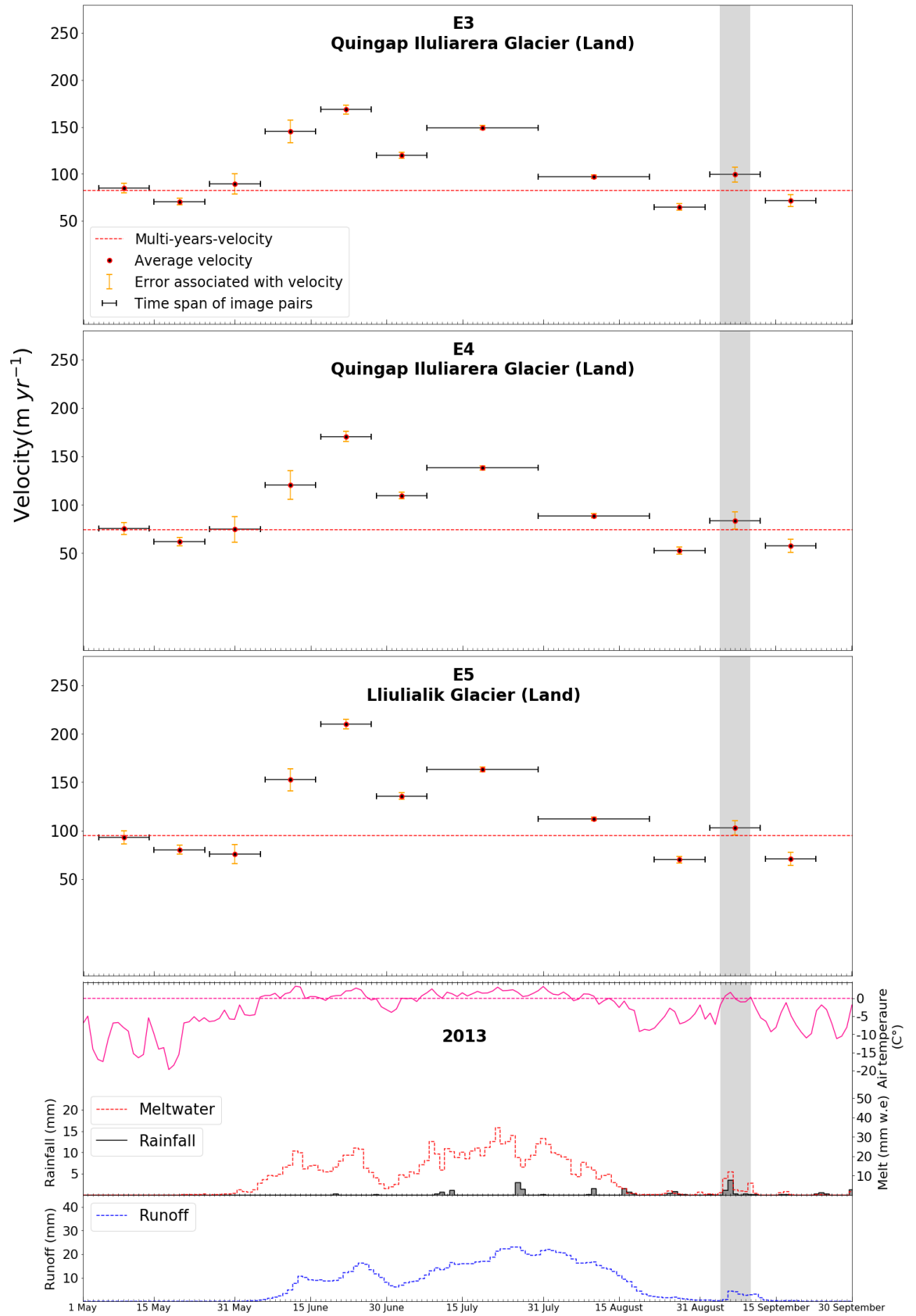


**Figure 5.26.** Same as Fig 5.15 but for the cyclonic event 2013, site E. Flowlines E3, E4, E5.

Focusing on ice velocity along the flowlines (Figure 5.27), the values extracted from the image pair covering the cyclone event, remained above those during the previous and subsequent period along the entire path of all the flowlines, apart within 1 km from the front. E1 was the only exception, where within 8 km the front, ice velocity during the period 22<sup>nd</sup> August- 2<sup>nd</sup> September was above the other two. Along E1, ice velocity during the period that included the cyclonic event remained within a range between  $100 \text{ m yr}^{-1}$  and  $150 \text{ m yr}^{-1}$  with no significant trend. During the previous period, after reaching a peak around  $175 \text{ m yr}^{-1}$  at 7 km, ice velocity followed a decreasing trend up to 15 km from the front to a value around  $60 \text{ m yr}^{-1}$ , and then stabilizes between  $50 \text{ m yr}^{-1}$  and  $80 \text{ m yr}^{-1}$ . During the period 13<sup>th</sup>- 23<sup>rd</sup> September, velocity followed an increasing trend, going from  $48 \text{ m yr}^{-1}$  at the calving front to  $115 \text{ m yr}^{-1}$  around 23 km from the front. At E2 the ice velocities decreased as the distance from the front increases, with a decrease in velocity between the two extremes of about 75 % and with the highest difference of around  $100 \text{ m yr}^{-1}$  between ice velocity during the cyclonic period and other two periods within 20 km from the front. Along E3, ice velocities in the first 5 km remained in a range between  $100 \text{ m yr}^{-1}$  and  $170 \text{ m yr}^{-1}$  with the difference being between the highest velocity values during the period 2<sup>nd</sup>-12<sup>th</sup> September and the other two periods. It follows a decline from 5 km till 13 km from the front and subsequent slightly rise in the following 3 km towards values that after 16 km from the front remains between  $40 \text{ m yr}^{-1}$  and  $100 \text{ m yr}^{-1}$ . Along E4 ice velocity calculated during the period 2<sup>nd</sup>-12<sup>th</sup> September, after reaching a peak of  $125 \text{ m yr}^{-1}$  around 5 km from the front, underwent a slight decline interspersed by smaller peaks till the end of the flowline where velocity was around  $70 \text{ m yr}^{-1}$ . During the others two periods, ice velocity remains between  $50 \text{ m yr}^{-1}$  and  $100 \text{ m yr}^{-1}$  within 10 km from the front and then underwent a decline to values below  $50 \text{ m yr}^{-1}$  from 10 km onwards during the period 22<sup>nd</sup> August - 2<sup>nd</sup> September. During the period 13<sup>th</sup>-23<sup>rd</sup> September values started to rise again from 15 km onwards, reaching values around  $70 \text{ m yr}^{-1}$  in the last 20 km of the flowline. At E5, ice velocities during the period 2<sup>nd</sup>-12<sup>th</sup> September, after an increase within the first km from 60 to  $140 \text{ m yr}^{-1}$ , decreased to 15 km to values below  $100 \text{ m yr}^{-1}$ , interrupted by a momentary peak around 7

Late Summer/Early Autumn Cyclonic Rainfall and Ice flow of the GRIS

km of  $130 \text{ m yr}^{-1}$ . From 15 km onwards, after a slightly rising of  $20 \text{ m yr}^{-1}$ , values remained stable between  $60 \text{ m yr}^{-1}$  and  $125 \text{ m yr}^{-1}$ . Ice velocities during the other two periods followed the same behaviour although with a velocity difference from -30 to  $-40 \text{ m yr}^{-1}$ .

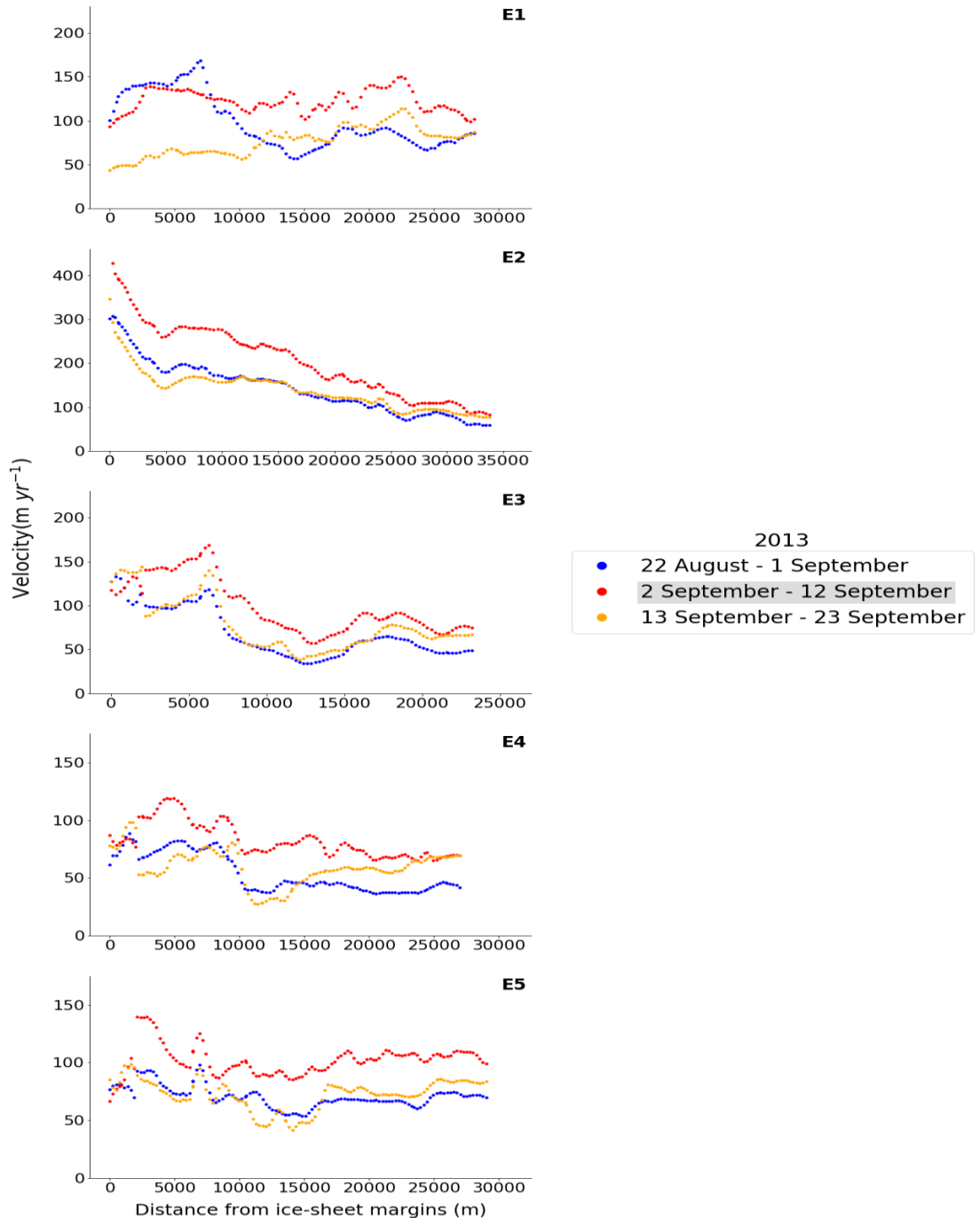


**Figure 5.27.** Same as Fig 5.16 but for cyclonic event 2013. Flowlines E1, E2, E3, E4 and E5.

**5.3.3.8. Site E, 2012**

The first image pair covered 11 days from 17<sup>th</sup> to 27<sup>th</sup> May (Figure 5.28, Figure 5.29) where meltwater up to 2 mm was detected with no runoff. The average velocity during this period was around  $8 \text{ m yr}^{-1}$  above the MEaSURES multi-years value of  $88.25 \text{ m yr}^{-1}$  at E1 and  $10 \text{ m yr}^{-1}$ ,  $17 \text{ m yr}^{-1}$ ,  $12 \text{ m yr}^{-1}$  and  $20 \text{ m yr}^{-1}$  below the MEaSURES multi-years values at sites E2, E3, E4 and E5, that were respectively  $160 \text{ m yr}^{-1}$ ,  $82 \text{ m yr}^{-1}$ ,  $73 \text{ m yr}^{-1}$  and  $95 \text{ m yr}^{-1}$ , being the lowest in our study data in the last three flowlines. Data covering the period 28<sup>th</sup> May to 7<sup>th</sup> June showed an acceleration along each flowline with the highest values of the series of  $194 \text{ m yr}^{-1}$  and  $241 \text{ m yr}^{-1}$  at E1 and E2. This period was characterised by a sudden increase in meltwater and runoff onset which reached values respectively of 23 mm and 13 mm. At E3, E4 and E5 the acceleration continued during the two subsequent periods of the image pairs (8<sup>th</sup> -18<sup>th</sup> June and 19<sup>th</sup> June -10<sup>th</sup> July), reaching the highest values of  $162 \text{ m yr}^{-1}$ ,  $154 \text{ m yr}^{-1}$  and  $191 \text{ m yr}^{-1}$  but not at marine terminating glaciers E1 and E2 where a decrease to values around  $150 \text{ m yr}^{-1}$  and  $206 \text{ m yr}^{-1}$  was detected. The period 8<sup>th</sup> June - 10<sup>th</sup> July was characterised by temperature well above zero and a gradual increase in meltwater and runoff reaching the highest values of 49 mm and 36 mm on 10<sup>th</sup> July despite a temporary drop occurring between 29<sup>th</sup> June to 7<sup>th</sup> July. A deceleration of  $28 \text{ m yr}^{-1}$  at E1 and  $48 \text{ m yr}^{-1}$  along the other flowlines continued in the following period 11<sup>th</sup>- 21<sup>st</sup> July during which a decline in meltwater production and runoff from 36 and 40 mm on 12<sup>th</sup> of July to 18 mm and 28 mm on 21<sup>st</sup> July occurred. In the subsequent image pair period, 22<sup>nd</sup> July – 1<sup>st</sup> August, an increase in ice velocity around  $70 \text{ m yr}^{-1}$  at E1 and E2 and  $30 \text{ m yr}^{-1}$  at land terminating glaciers was detected. It concurrently occurred with a peak in meltwater and runoff reaching values of 47 mm and 25 mm on 28<sup>th</sup> July driven by an increase in temperature and fed by rainfall. In the subsequent image pair period, 2<sup>nd</sup> to 12<sup>th</sup> August, after another peak on 5<sup>th</sup> August, values underwent an important decrease, with runoff at lowest level within the last two months. During this period a decrease in average ice motion was widely observed along all flowlines with an order of  $-70 \text{ m yr}^{-1}$  along E1 and E2 and  $-50 \text{ m yr}^{-1}$  along E3, E4 and E5. The next image pair,

13<sup>th</sup> and 23<sup>rd</sup> August, covered a period where a slightly small new peak in meltwater and runoff occurred, where a slight acceleration was detected at E1 and E2 but not along land terminating glaciers flowlines. During image pair 24<sup>th</sup> August- 3<sup>rd</sup> September, all the flowlines at site E underwent a decrease in ice velocity between

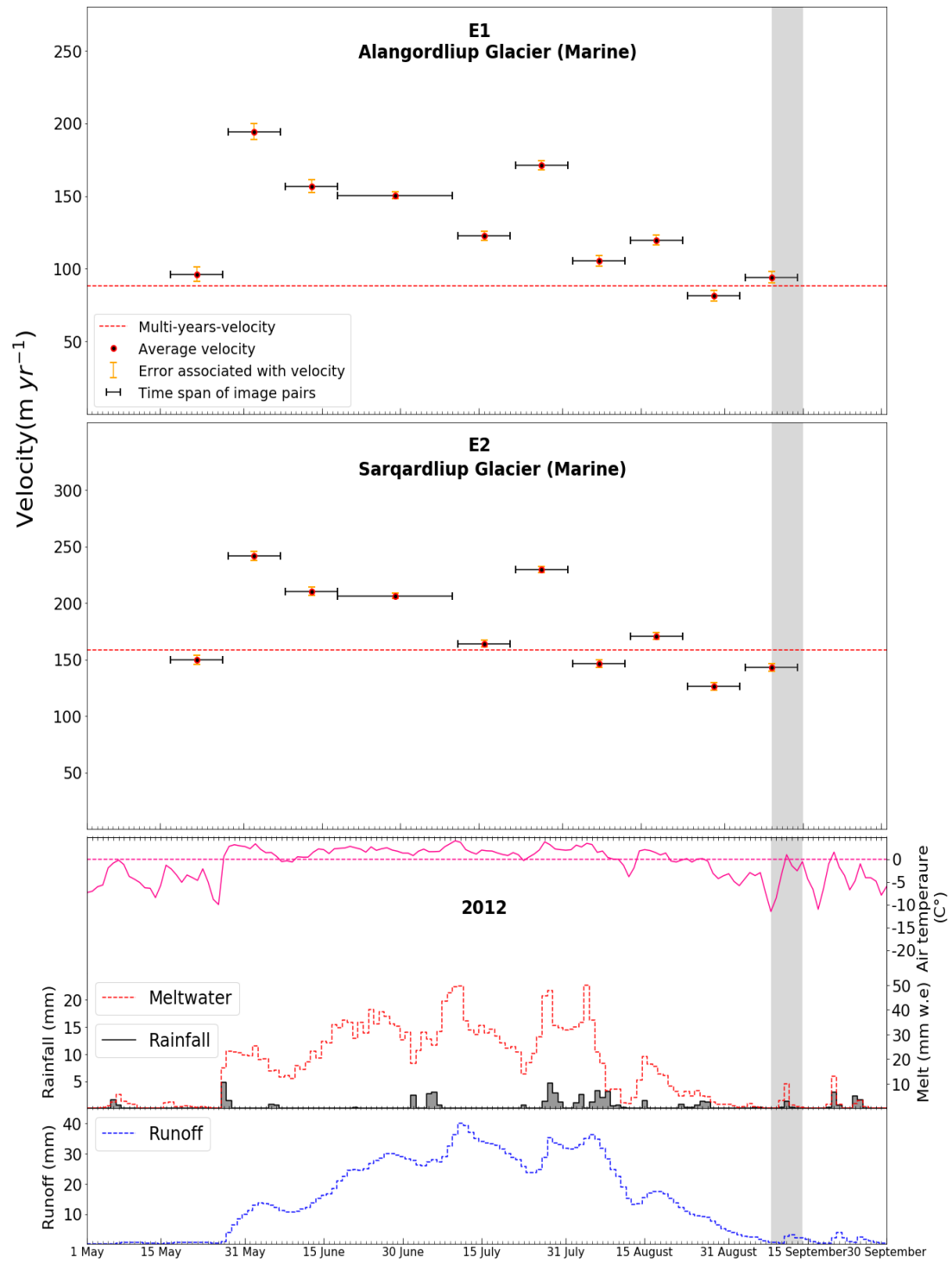


**Figure 5.28.** Same as Fig 5.15 but for the cyclonic event 2012, site E. Flowlines E1, E2.

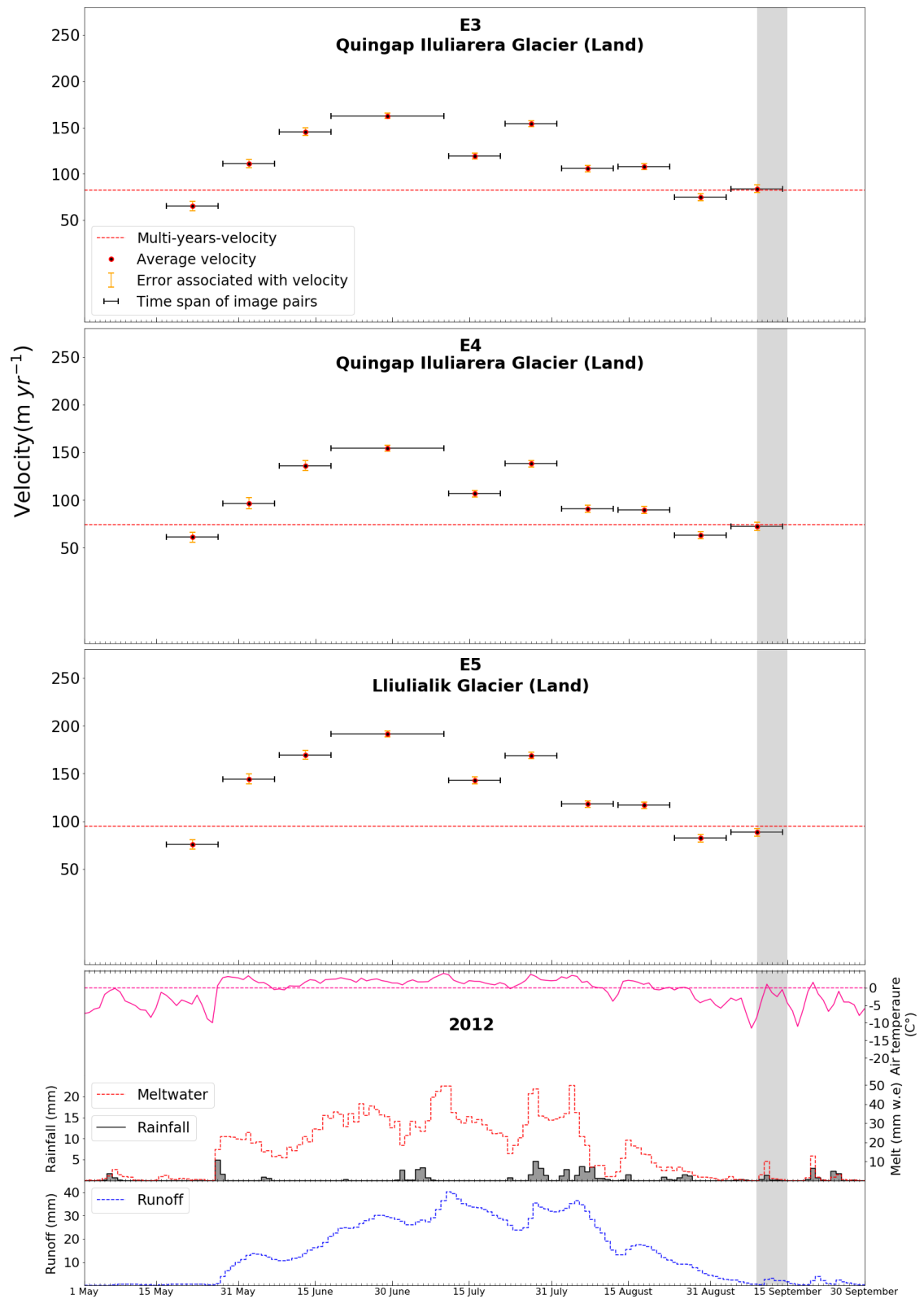


**Figure 5.29.** Same as Fig 5.15 but for the cyclonic event 2012, site E. Flowlines E3, E4, E5.

-26 % and -32 % (see Table 5.6 and Table 5.8) ) if compared to velocity of the image pair before, reaching the lowest values of the entire series at E1 and E2 (81 and 126  $m yr^{-1}$ ) and the second lowest values at E3, E4 and E5 (74, 73 and 82  $m yr^{-1}$ ) and accompanied by a decrease of -57 % in runoff 1 and reduction in meltwater around 2-3 mm. The decrease in ice velocity was interrupted in the subsequent image pair period from 4<sup>th</sup> to 14<sup>th</sup> September by a slight acceleration from +8 % to +16 % if compared to the period before along all the flowlines in conjunction to an increase of + 43 % in runoff 2 but not in runoff 3 (-64 %) and runoff 4 (-74 %). The image pair entirely covered a cyclonic event between 10<sup>th</sup> and 14<sup>th</sup> September representing 45 % of the days in this period (see Table 5.7 and Table 5.9), which generated a modest amount of rainfall and meltwater favoured by temperatures above zero.

Ice velocity along the paths of the entire flowlines (Figure 5.30) were analysed during the period before the cyclonic event, and that which include it. The velocity during the period that includes the cyclonic event from 4<sup>th</sup>-14<sup>th</sup> September was generally higher than the previous period going from 24<sup>th</sup> August to 3<sup>rd</sup> September along E2, and E3, although in some places the reverse occurred, or they overlapped. At E1, E4 and E5 ice velocity of one period is greater, less or overlapped the other depending on the portion of the flowline considered. At E1 ice velocity followed an increasing trend from the front till 20 km going from 65  $m yr^{-1}$  to 115  $m yr^{-1}$ , to then decrease till 80  $m yr^{-1}$  in its terminal part. A completely opposite behaviour of ice velocity emerged at E2 where a declining trend from 360  $m yr^{-1}$  to 70  $m yr^{-1}$  was observed along the entire flowline from the calving front onwards, gentler after 5 km onwards. Regarding E3, the peak in ice velocity was reached around 6 km from the front. It then declined towards the lowest values, detected around 13 km followed by a slight increase and then remained stationary till the end of the line path between values ranging from 50  $m yr^{-1}$  to 90  $m yr^{-1}$ . At E4, after values between 65  $m yr^{-1}$  and 95  $m yr^{-1}$ , the velocity decreased around 10 km and remained between 50  $m yr^{-1}$  and 80  $m yr^{-1}$  along the rest of the flowline. At E5, ice velocity of the two periods generated two "sea-saws" of values almost stationary between 60 and 105  $m yr^{-1}$  between 2 and 17 km. A general ice velocity increase trend from 17

Late Summer/Early Autumn Cyclonic Rainfall and Ice flow of the GrIS

km onwards was observed from values around  $80 \text{ m yr}^{-1}$  to values around  $120 \text{ m yr}^{-1}$  at the end of the flowline.

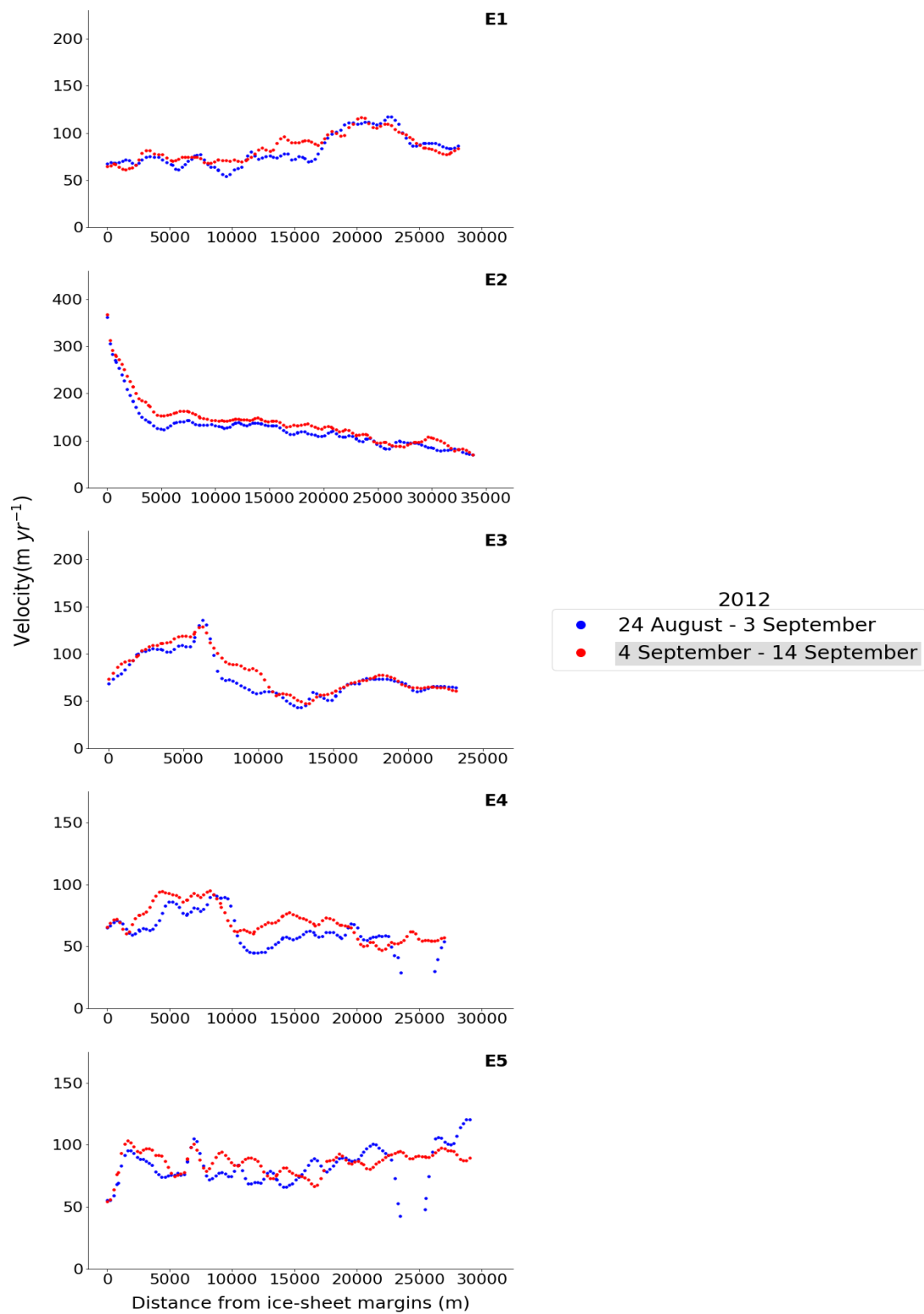


**Figure 5.30.** Same as Fig 5.16 but for the cyclonic event 2012. Flowlines E1, E2, E3, E4 and E5.

### **5.3.3.9. Summary of ice velocity and runoff around the cyclone events**

Overall, in land terminating glaciers and most of marine terminating a general decrease in ice velocity during late summer was interrupted by an acceleration concurrently with a cyclonic rainfall event, although many with negative percentage in runoff 3 and/or 4, opposite to positive percentage of runoff 2. At site A and E, a deceleration was supported by negative values in runoff 1 but not at site B and D where an increase in velocity is observed along some flowlines. At site A, B, D and E the acceleration during the cyclonic event and deceleration or values around zero in the subsequent period (for site D and E) was detected. All acceleration during the cyclonic period were accompanied by positive values of runoff 2, and lower values in runoff 3 and 4 often negative. At site C, an intense acceleration before the cyclonic event is accompanied by a decrease in runoff 1. This acceleration continued even during the image pairs which include the cyclonic period along C3 and C4 but not at C1 and C2 with positive values of runoff 2 opposite to negative values of runoff 3 and 4. It followed a decrease in velocity along each flowline. Overall, considering only the marine glaciers, 12 out of 14 flowlines underwent an acceleration during the cyclonic periods and the binomial analysis explained in the methods section applied on these values, revealed that the number of accelerations observed are statistically significant at the 95% level and not due to chance alone.

## **5.4. Discussion**

### **5.4.1. Land Terminating Glaciers**

The general pattern of the summer ice velocity behaviour in the ablation zone of the GrIS land margins, during the ablation season is consistent with expectations (Bartholomew et al., 2010; Hoffman et al., 2011; Bartholomew et al., 2012; Hoffman & Price, 2014; Doyle et al., 2015; Davison et al., 2019). Ice velocity increase during the melt onset is followed by a decline throughout summer, interrupted only by accelerations due to runoff pulses equal to or greater than the previous days (Bartholomew et al., 2011; Cowton et al., 2013). A reduction in meltwater and runoff in transition towards a winter mode, along with a decrease in ice velocity, prior the cyclonic events, was favoured at all sites by temperature below freezing. It was more

marked at site E (2012 and 2013) than at site B where the lower deceleration could be explained by two small peaks in runoff, that may have partially hindered the slowdown of the glacier image pair velocity period before the cyclonic event.

The deceleration trend was interrupted by a period of temperature above freezing due to cyclonic rainfall events as shown by the meteorological analysis. During these rainfall episodes, an acceleration was detected at all land-terminating glaciers also at those at site E (2012) which had the highest decrease in runoff 3 and 4 of -64 % and -74 % and where the lowest accelerations were observed. These runoff decreases, in contrast with those of site E (2013) could be explained by 1) runoff during the cyclonic period 2012 does not present an anomaly with respect to the climatic mean 1986-2015 indicating a cyclonic event of modest intensity, 2) days with previous temperatures below freezing and melt/runoff around zero in the satellite data period which cover the event, in contrast to site E (2013), account for a larger percentage at the expenses of cyclonic days. In this context, the negative values of runoff 3 and 4 at E (2012) could suggest overshadowing of the small and brief cyclonic peak in runoff if compared to the week before.

Conversely at site B, where the two image pairs velocity period covering the cyclonic event also included ten previous days with temperatures below or around freezing and runoff values around zero, a +18 % in runoff 4 was detected. This, along with high values of runoff 2 and 3 that better capture the magnitude difference in runoff during and before the cyclonic event, demonstrated the exceptional nature of the event at this site as confirmed by the high positive anomalies of rainfall, melt and runoff compared to the climatic average.

Overall, a positive value of runoff 2 across all sites, which came from the comparison between the amount of runoff during cyclonic days and the week before supports the hypothesis that the week before the event with temperature below freezing could have favoured a transition of the subglacial drainage system to a less efficient mode before the events. (Bartholomew et al., 2010; Bartholomew et al., 2011; Hoffman et al., 2011; Bartholomew et al., 2012; Andrews et al., 2014) This was then overwhelmed by the modest runoff not buffered by snow cover in this period of the year (Tedesco & Fettweis, 2020), that underwent a fast routing through

channels and moulins developed during the summer season, inducing an acceleration due to basal sliding.

#### **5.4.2. Marine Terminating Glaciers**

The ice velocity behaviour during the melt season of marine terminating glaciers follows the land terminating counterpart, although it appears more complex and uneven around the cyclonic event. This is not surprising since for this type of glacier as the influence of the sea currents, fjord bathymetry and geometry could play a key role in determining the ice velocity (Straneo et al., 2013; Benn et al., 2017; Van den Broeke et al., 2017).

The values of the percentage increase in ice velocity around zero at site A and B and positive at site D before the cyclonic event support the hypothesis advanced to explain the behaviour of land terminating glacier B4 where small momentary peaks in runoff may have contributed to a reduced slowdown/slight acceleration although negative values in runoff 1. The forementioned hypothesis behind the ice acceleration during the cyclonic event along land terminating glacier of site B can explain the increase in ice motion along the marine terminating glaciers of this site although with lesser magnitude. At site A and D acceleration is concurrent with a high positive runoff 2 but negative values of runoff 3 and 4, apart runoff 3 at site A. As for land terminating glaciers at site E 2012 we attribute the negative values to the imprecise nature of the image pairs to cover and separately isolate the runoff during around and before the cyclonic event. In fact, the image pair before the cyclonic event at site A included a period of sustained runoff and didn't cover the four days of low runoff preceding the event. Conversely at site D, the image pair, apart from entirely cover the weak cyclonic event in terms of runoff, also covered three days before and two days after with runoff at the lows since the beginning of the melt season preceded by the slightly higher peak covered by the image pair before.

Site C deserves particular attention. Here, an increase from 8% to 85% of ice velocity affected all the flowlines in the image pair velocity period before the cyclonic event in conjunction to a decrease in runoff 1 of -68%. This image pair preceded the image pair velocity period during the cyclonic event with a gap of 7 days being the

earliest period of the melt season of the entire study. During this period a decrease trend in runoff was interrupted by two peaks, less high than values earlier in the season in runoff but higher than all those detected during the cyclonic event. The image included these two peaks in runoff and consequent acceleration, although their values were less than runoff detected by the preceding image pair with consequent negative runoff 1. The velocity values from the image pair velocity period which includes the cyclonic event, unlike all the other sites, underwent a deceleration along two flowlines, opposite to a slight acceleration of the other two, with a decrease of -28% and -59 % in runoff 3 and runoff 4. Analysing the available data, emerged that the image pair covering the cyclonic period included five previous days and five following days with temperature below or around freezing and runoff at the minimum from the beginning of the melt season. This explain the negative values of runoff 3 and 4 while if it considered only the cyclonic event and the previous week, once again runoff 2 is positive. A suggested hypothesis is that the acceleration during the event occurred along all flowlines, but along two flowlines was less intense than the preceding period resulting in a % velocity decrease.

Overall, the results lead us to conclude that different ice velocities behaviour detected around the cyclonic events were influenced by poor temporal cover and gaps issues of velocity data than the marine terminating environment. In this direction, ice velocity and runoff interrogation in relation to the daily values of temperatures, melt, runoff and rainfall have provided plausible explanations of the apparent inconsistent response between velocity, cyclonic event and changes in runoff values during image pairs velocity period. What emerged was that the peaks in runoff within a decreasing trend, induced a response in terms of acceleration along all the glaciers studied both marine and land terminating.

### **5.4.3. Rainfall Trend and self-regulation in the ablation zone**

In a global warming scenario, the behaviour of the ablation and accumulation zone in term of annual ice velocity under the impact of an ever-increasing predicted number of cyclonic rain events in late summer/early autumn (McCrystall et al., 2021) already underway (Niwano et al., 2021) remains unknown. Our analysis detected a

general increase of the rainfall fraction in the ablation zone of the sites studied during the period 15<sup>th</sup> August-15<sup>th</sup> October from 1986 to 2015 (Figure 5.31). In the southwestern sites (A and B) there was a significant increase trend from 1985 onwards in the fraction of rain with a peak around 30-35 % within the five-year window 2001-2005 followed by a slight decrease in the following two periods. The northernmost (D) was the site with the lowest fraction of rain during the decade from 1986 to 1995 while C and E had similar values of A and B around 15 %. At sites C and D, a peak in the rainfall fraction was observed during the period 1996-2000, followed by a decrease in subsequent five years, more marked at D. An increase was detected at these sites between the period 2006-2010 when the peak of the entire series at site E was reached. It follows a value of rainfall fractions around 20 % among all sites during 2011-2015. Trend lines indicate an increase among all sites during the period considered although not statistically significant, due to the short series and only six velocity data for each site.

Overall, three important aspects emerged:

- The south-western sites were those where the rainfall fraction reached higher values and is on average higher than the western sites during the period 1985-2010.
- A general higher values of rainfall fraction in the second half of the 1986-2015 period at all sites if compared to the first half
- A quite homogeneous rainfall fraction around 22 % at all sites during 2011-2015 with no difference related to the latitude that can be explained as a faster warming of the northern part of the GrIS due to an increase in downward longwave heat flux (Orsi et al., 2017).

These results are supported by the analysis in section 3.4.1 and corroborated by a recent study carried by Oltmanns et al. (2019) which detected between 1979 and 2012 an increase of cyclonic rainfall over the GrIS in this period of the year, although statistically significant during the period September-April.

A recent review by Davison et al. (2019) suggests that in a warmer climate, an increase in the drainage system efficiency and surface thinning led to annual to decadal widespread deceleration of the land terminating ablation zone of the GrIS

Late Summer/Early Autumn Cyclonic Rainfall and Ice flow of the GrIS

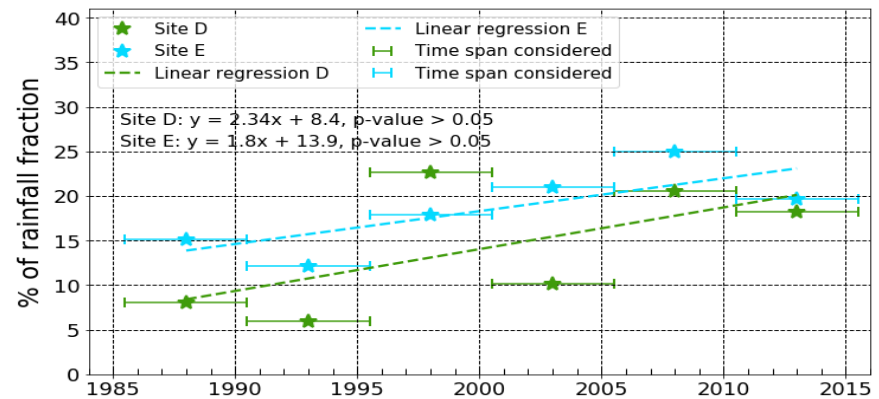
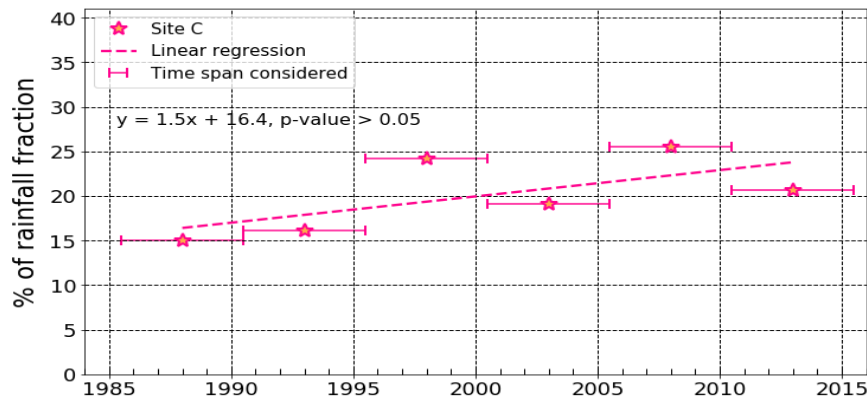
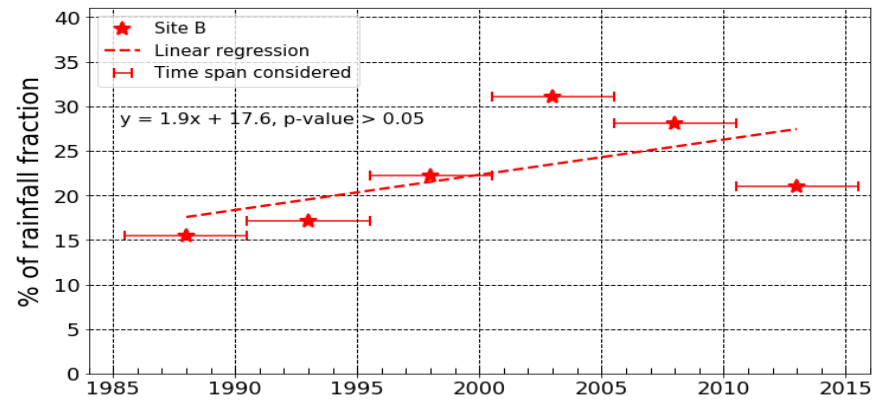
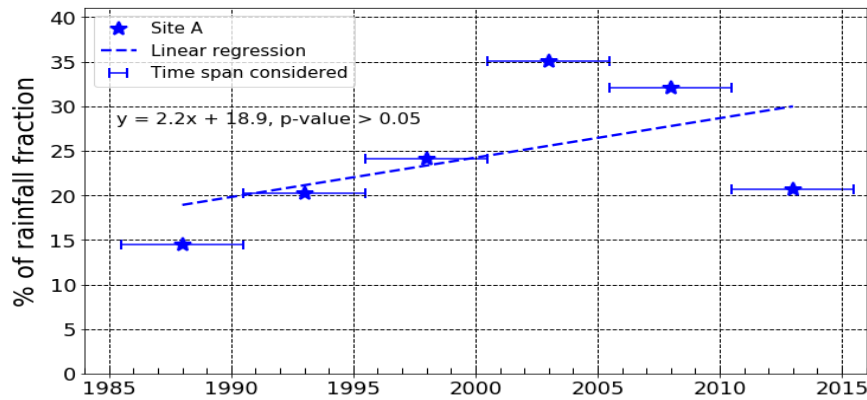


**Figure 5.31.** Rainfall fraction compared to the total precipitation between 15<sup>th</sup> August-15<sup>th</sup> October at each site below the ELA, calculated every five years and covering the climatological reference period 1986-2015 along with the trend their equation and statistical significance (p-value) are shown at site A (top right), B (top left), C (bottom left), D and E (bottom right).

through a mechanism called “self-regulation”. Regarding the lower accumulation zone, they claim that ice flow self-regulation at higher altitude of the GrIS was not currently observed and an ice velocity increase was detected during warmer summer (Doyle et al., 2014). However, our analysis supports the hypothesis that in a warming and wetter climate, the self-regulation mechanism in the ablation zone may not hold with more frequent and intense rainfall cyclonic episodes hitting the GrIS in a period where it is in transition to winter mode. Moreover, results indicate that meltwater and rainfall have expanded well above the ELA during the cyclonic event, also affecting the lower accumulation zone. At site C, the only one where ice velocity data of this zone were available, it appeared to be insensitive to cyclonic meltwater and rainfall pulses. Nevertheless, the impact may have been shadowed by the previous higher runoff peak associated with higher values in velocity in the accumulation zone at C1 and C2 in the image pair velocity period before the cyclonic event. In fact, the peak in runoff in late July may have overwhelmed the subglacial drainage system at these higher altitudes, causing the acceleration in the accumulation zone prior to the cyclonic event (ice velocity in the image pair 31<sup>st</sup> July – 15<sup>th</sup> August if compared to the previous one) as shown in Figure 5.32, producing a more efficient drainage system capable of accommodating the modest meltwater and rainfall pulses driven by the cyclonic event at these altitudes.

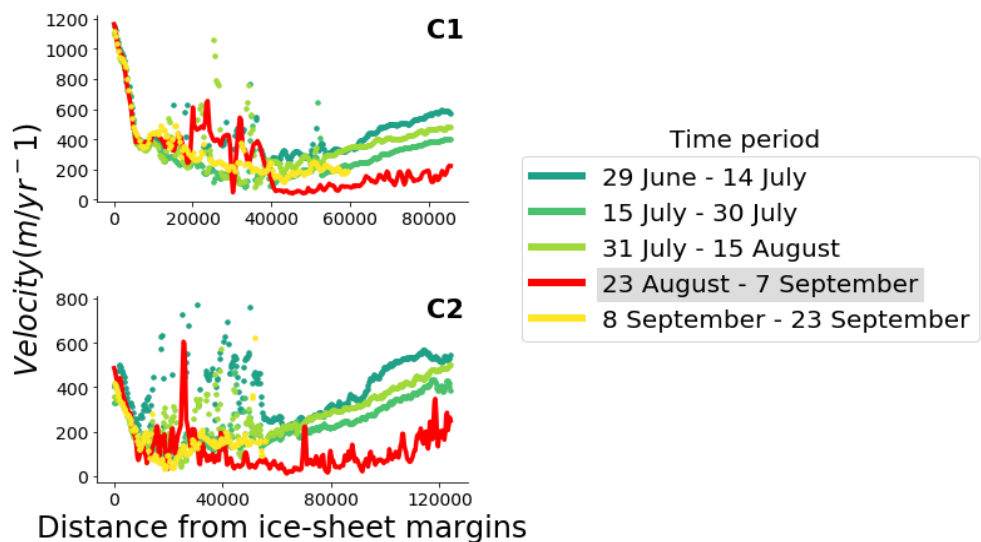


**Figure 5.32.** Ice velocities along flowline C1 and C2 during selected image pairs periods. Ice velocity of image pair which covers most of the cyclonic event is in red and shaded in grey in the legend.

## 5.5. Conclusion

By combining ice velocity data from different remote sensing techniques together with reanalysis data and the MAR outputs, this chapter has shown that cyclonic rainfall events can increase the ice flow of the ablation region in the south-west and west of the GrIS during late summer/early autumn when a general decrease in velocity is normally observed. Through the advection of heat and moisture driven by a low pressure centred south of Baffin Bay/ North-East Canada, the cyclonic events lead to an increase in cloud cover, amplified turbulent heat fluxes, and enhanced downward long-wave radiation. This favours temperatures above freezing with production of abundant quantities of meltwater and rainfall feeding runoff. In turn this can overwhelm the subglacial drainage system, which is in transition to a less efficient mode during this period of the year, and results in ice flow acceleration along the majority glaciers in this study, both marine and land terminating.

As mentioned in the discussion section, the recent increase in temperatures, which is expected to further increase in the coming decades, already favours more frequent and intense events of rainfall and meltwater production in all seasons which replaces snowfall at higher altitudes. In this context, it is urgent an increase in the quantity and quality of ice velocity satellite data. These along with more in situ studies would shed light on the impact in term of annual ice motion and hence dynamic thinning in a predicted warmer and wetter climate, with consequences on the average sea level to be evaluated

## **6. *Synthesis and Discussion***

---

### **6.1. Introduction**

In this work two specific aims were proposed:

- a) Improve understanding of how extratropical cyclones influence the energy and mass balance of the GrIS;
- b) Identify how GrIS ice motion and hence, dynamic thinning, responds to influx of water related to cyclonic events.

These aims were pursued through consideration of the following research objectives, which:

- 1) computed climatologies of mass/energy balance for regions of the GrIS when under the influence of extratropical cyclones;
- 2) investigated the GrIS response in terms of ice motion during selected cyclonic events along the western margins of the GrIS.

The aim of the first part of this chapter is to summarise and discuss results obtained in answering the above research objectives and how they fit in with published literature. In the second part, limitations of this study are evaluated, and future research and methodological developments are explored which would extend the research undertaken in this study. Finally, the chapter ends with a section on concluding remarks.

### **6.2. Summary of the Research and Limitations**

#### **6.2.1 Objective 1: Extratropical Cyclones and their Impact on the GrIS SMB and SEB**

Extratropical cyclones are known to be a key weather system responsible for precipitation on the GrIS and to date, research has concentrated on their spatial behaviour around Greenland and related precipitation pattern over the GrIS (Chen et al., 1997; Rogers et al., 2004). A recent study underlined this important relationship demonstrating the key role of extratropical cyclones in driving the inter-annual

variance of the SMB through their control on snow accumulation patterns (Chen et al., 2016). The analysis in this thesis (Chapter 4) confirms the previous findings and emphasised an overall positive contribution of cyclones to the GrIS SMB via snowfall both in winter and summer.

In winter, cyclones affected the surface energy balance by increasing air temperature and long-wave downward radiation, consistent with the advection of maritime North Atlantic air masses over most of the GrIS. This was in line with previous findings (Sorteberg & Walsh, 2008; Rinke et al., 2017; Valkonen et al., 2021) which underlined the key role of extratropical cyclones in transporting a significant amount of moisture and heat into the Arctic. The increase in snow surface temperatures (as inferred from the upward flux of longwave radiation) is consistent with Van Tricht et al. (2016) who found an increase in runoff over the GrIS related to heating of the snowpack due to enhanced long-wave radiation forced by cloud cover. This may be the reason of an overall negative anomaly of sensible heat flux over almost the entire GrIS coming from the reduced temperature difference between the surface and the air above. These positive anomalies were linked to a modest cyclonic activity along Baffin Bay but not over the GrIS. This could be attributed to the impact of the GrIS plateau described by Chen et al. (1997) impeding cyclones moving from west to east. It was suggested that this flow configuration favoured warm advection from the south and south-west. This could also explain the slightly positive anomalies of the sensible heat flux and reduced cloud cover north-east of the highest altitudes of the central region of the GrIS. It was attributed to descending winds (Foehn) coming from the higher areas of the GrIS, driven by the warm advection from the south-west with low pressure centred over Baffin Bay. This interpretation is supported by the literature which underlined how cyclonicity in the Baffin Bay produces high values of meltwater at the margins and high precipitation along the west GrIS associated with south-westerly onshore flow (Mote, 1997; Schuenemann et al., 2009).

The results also highlight that the positive anomalies of temperature, humidity, long-wave upward and downward radiation followed a decreasing trend from the north-west towards the south-east until values reach around zero in the

extreme south-east. This decrease was firstly attributed to the high cyclonic frequency off the coast in a region stretched from the north end of the Atlantic Ocean along the Irminger up to the Denmark Strait. Secondly, it was suggested that cyclones in their movement from the southern tips of Greenland towards the Denmark Strait, firstly delivered moist and warm air from the south-west and subsequently dry north-westerly flow onshore when moving towards the north-east/east. This area was studied by previous work (Chen et al., 1997; Berdahl et al., 2018) and was recognised as the region with a semi-permanent centre of low atmospheric pressure, after which the name of the Icelandic Low was given due to its proximity to Iceland (Serreze, 1995; Serreze et al., 1997). What emerged from these studies is in line with the results of the thesis. When the Icelandic Low is in a more westerly position, storm tracks are pushed nearer to the SE coast of Greenland delivering high amount of moisture and heat along the coast. Conversely, when the Icelandic Low is further east, cyclones track farther east into the North Atlantic Ocean driving dry cold air from north-east with no significant precipitation along the eastern/south-eastern flank of the GrIS. This result underlines the importance of considering changes of cyclones' tracks in the future projections, since they are source of uncertainties as shown by Ulbrich et al. (2009) and Priestley and Catto (2022) and they could translate into substantial impacts for the SMB of the GrIS.

In summer, the impact of cyclones on SEB variable appears more spatially homogeneous if compared to the winter north-west/west south-east gradient. This was attributed to a concomitant decrease of cyclonic activity of the Icelandic Low detected in section 3.4.3, in agreement with previous studies which detected a weakening of the Icelandic Low in the warm season (Chen et al., 1997; Serreze et al., 1997; Schuenemann et al., 2009; Akperov et al., 2018). Positive anomalies of long-wave downward and negative short-wave downward anomalies over the entire GrIS were attributed to the advection of maritime air masses from the North Atlantic. This produced an increase in temperature and meltwater over the higher altitudes of the GrIS where the short-wave downward play a minor role due to high albedo as shown in Chapter 3 and in agreement with previous studies (Van den Broeke et al., 2008; Box et al., 2012; Stroeve et al., 2013; Noël et al., 2015). Conversely, at lower altitude,

it was inferred that the increase of long-wave downward was offset by a decrease in short-wave downward driven by clouds which at the same time can increase surface albedo through delivering fresh snowfall and hence reduce melt through the snow-albedo-melt feedback (cf. Noël et al. (2015)).

Thus, the proximity of extratropical cyclones during the cold season drives a high level of solid precipitation whereas, in summer, snowfall and cold air advection increases the albedo in the ablation zone and suppresses meltwater production. In winter, more intense cyclones provided more solid precipitation and were not associated with a significant rise in temperature if compared to cyclones of lower intensity. In summer higher cyclonic intensity was associated with lower temperatures and melt in the ablation zone along with an increase over the entire GrIS of snowfall. These results lead the conclusion that, along with changes in cyclones' frequency and track, changes in intensity should also be considered as a key parameter that may influence future GrIS surface mass balance.

The interpretations provided above are, however, subject to some important caveats. The coarse resolution of the cyclone' dataset translates to uncertainties in their position of the order of hundreds of kilometres. Moreover, although a threshold distance from the centre of 750 km was used to identify cyclone influence, their radius is in reality, variable. For example, ranging from 300-400 km over the western and northern part of the GrIS in summer, to more than 900 km off of its south-eastern coast (Rudeva & Gulev, 2007). This may have made it possible to consider areas under the cyclonic impact that were not or viceversa, since the 750 km values is only an average assumed in this work. It can therefore be argued that the lower positive impact on SMB recorded by including cyclones with lower intensity in the analysis could not only be due to this parameter. It can also be attributed to the fact that the less intense cyclones also have a smaller radius and hence, their passage over a portion of the GrIS has been assumed and the values of variables have been extracted, yet in reality, the GrIS portion was not under their influence, as emerged from manually checked approach on a small sub-sample of cases. Finally, the mismatch in temporal frequency between the MAR and cyclone dataset means that even if a cyclone had also impacted a certain area of the GrIS for only 6 hours, the

recorded anomalies from the MAR covered the whole day. This introduced further uncertainties regarding the accuracy of the results obtained beyond the limitations mentioned before.

In summarising the major findings of Chapter 4, it is important to stress how this work showed for the first time the profound differences of meteorological and SEB variables on different areas of the GrIS under the cyclonic influence. Such information is relevant for future research and should be considered in future studies regarding the impact of this weather type on the GrIS. Their recent reduced activity in the Greenlandic region in summer in favour of an intensification of strong anticyclonic events along with their key role as precursor cyclones were related to long dry periods with high temperatures and clear sky and consequent widespread surface GrIS melting (Fettweis et al., 2010; Franco et al., 2013; Hanna et al., 2014; McLeod & Mote, 2015, 2016; Tedesco & Fettweis, 2020). This underlined the positive impact of extratropical cyclones related to their ability to deliver fresh snow on the GrIS as shown by many studies (Chen et al., 1997; Schuenemann et al., 2009; Chen et al., 2016) but without answering the question, addressed in this work, through which SEB and precipitation pathways.

However, the results obtained also raise some questions about the future impact of cyclones on the GrIS in a future warming scenario. The warm cyclonic advections in winter are likely to become more frequent and extended while in summer the cooling effect in the peripheral areas of the GrIS is likely to decrease (Oltmanns et al., 2019). A warming scenario is likely to favour the replacement of snow by rain at higher altitudes and especially in the ablation zone, where the ice is darker than elsewhere, further increasing meltwater production. This suggests that the positive impact of cyclones on the surface mass balance is likely to decrease in a warmer climate (Rae et al., 2012; McCrystall et al., 2021) and lead us to hypothesize larger and faster changes in the GrIS-related hydrological cycle which could further contribute to the projected sea level rise with profound, ecosystem and socio-economic impacts.

For future research and follow-up work, it is suggested to apply the methodology presented in in this work also on spring and autumn in order to have a

complete overview regarding the impact of cyclones on the GrIS during a glaciological year. Moreover, it is proposed to establish different radii threshold based on their different intensity, since this work has shown how a decreasing cyclonic intensity is often correlated with a smaller cyclonic diameter.

### **6.2.2 Aim 2: Cyclonic rainfall and their Impact on GrIS Ice Motion**

The meteorological analysis emphasised the moist and warm advection carried by the three cyclonic episodes studied over the GrIS, with temperature anomalies up to 4°C at sites studied and overcast skies. This favoured high values of long-wave downward radiation, and turbulent heat fluxes which favoured peaks in the amounts of meltwater and rainfall with anomalies up to 250 % if compared to the 1986-2015 climatological mean which fed runoff. The highest peaks in runoff were observed in the wettest southernmost sites (Schuenemann et al., 2009; Cappelen et al., 2014) where the daily rainfall rate reached peaks around 28 mm/24 h and meltwater around 20 mm/24 h while the lowest values at the northernmost and driest site D (Cappelen et al., 2014). Positive anomalies of total runoff with respect to the climatological mean during cyclonic periods were observed at site A and B, C and E (2013) but not at site D and site E (2012). The lower values in meltwater, rainfall and runoff and the calculation of the meltwater altitude limit during the event, in the northernmost sites if compared to the southernmost, show the different intensity with which the cyclonic events hit the study sites.

All land terminating glaciers studied underwent an acceleration during the cyclonic events which interrupted a slowdown trend typical of the transition period towards a winter mode (Tedstone et al., 2013; Tedstone et al., 2015). The image pairs from which these ice velocities were extracted had a temporal coverage of eleven days, and they have no overlapping periods. This did not allow the acquisition of ice velocity data limited to the cyclonic event alone because some images only partially covered the cyclonic event while others included the whole event plus some non-event surrounding days. This was a limitation of this study since it is well known how the short-term variability in ice motion is restricted within a few days of the

temporary peaks in meltwater drainage and its discharge (Bartholomew et al., 2011; Bartholomew et al., 2012; Tedstone et al., 2013) as confirmed by analysis of Doyle et al. (2015) regarding ice flow acceleration due to a late summer cyclonic event. The runoff calculation of our data confirms this limitation. Its calculation during the period of the image pairs including the cyclonic event is influenced by many surrounding days with values close to zero, producing in many cases lower values if compared to runoff of the image pairs before the event which included periods with much higher runoff.

However, the analysis shows that the more circumscribed the calculation of runoff values is during the cyclonic days, the more the percentage increase in runoff was high if compared to the period covered by the image pair before and became positive at all sites if compared to the week before the event. This reconciles the negative runoff anomalies obtained considering the periods covered by image pairs, apparently in contrast with acceleration along flowlines. This suggests that the accelerations during the cyclonic periods studied, if linked to runoff, could be greater than those detected from the image pairs periods. This is supported by the greatest acceleration and the highest positive runoff anomalies being detected among the land and marine terminating glaciers at site E (2013). It is suggested that it was due to the two image pairs velocity periods enabling the separation of the cyclonic event of 2013 with few surrounding days and the preceding period with temperatures below zero and runoff at its minimum.

Focusing on marine terminating glaciers, they exhibited more erratic behaviour. Along seven out of fourteen flowlines an acceleration in the period preceding the cyclonic event was detected with values up to +85% at site C. At the same site two flowlines showed a slowdown during the cyclonic period unlike the other 12 where ice velocity increases were up to 72% at site E (2013). A general decrease in ice motion was detected after the cyclonic period along 7 out of 8 flowlines for which velocity data were available.

These results show a predominant positive impact of cyclonic rainfall in term of ice motion on marine terminating glaciers and at the same time support the recent literature where it was argued that the termini of some fast marine-terminating

glaciers could be less sensitive in terms of ice motion to meltwater pulses reaching and perturbing the subglacial drainage system (Joughin et al., 2008; Catania et al., 2020) during the melt season. However, the analysis of the poor temporal spacing and coverage of ice velocity data, along with analysis on daily runoff values proposed in this study, led us to conclude that the inconsistent ice velocity response found along these glaciers may be influenced more by the poor velocity data coverage of the events than the fact that they were marine terminating.

At site C, the image pairs covering the cyclonic event and the period before, had a temporal coverage of sixteen days. Between them there was the largest temporal gap in the velocity data in the study with seven days having no data coverage which did not make it possible to study ice motion in response to runoff inputs the week before the image pair covering the cyclonic event. The image pair before the event also covered the earliest period (31 July-15 August) of the melt season of the five study sites. Analysing the daily data of meltwater and runoff it emerged that the image pair before the event included a momentary peak in runoff sustained by high meltwater production typical of this period, higher than the peak in runoff occurred during the cyclonic period studied.

From the literature is well known that pulses equal to or greater than the previous period in the melt season could overwhelm the subglacial drainage system (Bartholomew et al., 2011; Cowton et al., 2013) resulting in acceleration. It was then suggested that a momentary peak in runoff sustained by high meltwater production (albeit decreasing) in early August could have produced enough runoff to perturb the basal hydrologic system not able to drain it. This could have caused the acceleration detected in the image pair before the event, so vigorous due to high runoff values, to overshadow the impact in terms of acceleration and runoff of the cyclonic event covered by the subsequent image pair which also included the five days before and five days the event with runoff around zero.

Finally, the ice velocity change and runoff results obtained for sites B and D confirm the limitations of this study due to the temporal coverage of the ice velocity images. It was suggested that detected peaks in runoff induced an acceleration in the image period before and during the cyclonic event at these two sites. However, these

peaks were within a decreasing trend or surrounded by daily values around zero leading to negative runoff percentages if compared to the values calculated during the period of the image pair before. Conversely, the comparison of runoff calculated only during the cyclonic event to runoff of the previous week was positive, reconciling the apparent contrast between runoff data and ice velocity response calculated during the image pair periods.

Overall, results suggested that cyclones of any intensity in terms of meltwater and rainfall production in the late summer/early autumn could induce an acceleration of the ice sheet at its margins towards lower elevations, enhancing the dynamic thinning of both land and marine terminating glaciers. It has been observed that two factors play a key role in ice acceleration: 1) the intensity of the runoff peak during the cyclonic period, 2) a period of temperatures around or below zero preceding the cyclonic event. It is suggested that temperatures below zero before the event, favoured the transition of subglacial drainage system towards a winter mode, perturbed by a sudden increase in cyclonic drainage that was able to enhance the decoupling between the bed and then inducing the response in terms of surface acceleration, related to its magnitude (Cowton et al., 2013). This mechanism is not different to what is observed during the runoff onset (Bartholomew et al., 2010; Hoffman et al., 2011; Chu, 2013; Cowton et al., 2013; Andrews et al., 2014) and corroborated by values of temperature, proglacial discharge and borehole water pressure before and around the cyclonic event studied by Doyle et al. (2015) in the same period of the year.

In summarising the major findings on ice velocity, it is important again to stress the limit of this study due to scarcity of satellite data along with poor temporal resolution. The ice velocity data used had a temporal resolution ranging from 11 to 33 days with some temporal gaps between them. This limited the ability to have image pairs that included specific chosen periods before, during and after the cyclonic events but rather to have data that partially includes them or where they are totally included, they only represented a maximum of 73 % of the total days covered. However, the analysis of daily data of temperature, meltwater production and comparison of runoff values during selected periods, allowed an understanding of

the difference between the ice velocity response and runoff anomalies calculated during the image pairs velocity period.

Findings in this chapter are very relevant for research which seeks to predict the future ice dynamic behaviour of the GrIS margins in a future warming scenario. Previous studies have shown that the lower annual ice velocity during warmer summers is related to a self-regulation mechanism (Sundal et al., 2011; Sole et al., 2013; Tedstone et al., 2013; Tedstone et al., 2015; Nienow et al., 2017; Williams et al., 2020). However, the data presented here invite the hypothesis that the delicate balance of self-regulation mechanism in the ablation zone doesn't hold under a predicted increase in frequency and intensity of cyclonic rainfall (McCrystall et al., 2021), already underway, especially in September (Niwano et al., 2021). Secondly, doubts remain regarding the lower accumulation area response in terms of ice velocity to ever greater impulses of rainfall and meltwater driven by cyclones. In situ and modelling studies suggest a further increase in the future of the ice flow at this altitude is most likely with an impact on SMB still unexplored (Dow et al., 2014; Doyle et al., 2014; Dow et al., 2015). This is due to a shallower morphology of the bed and less intense surface meltwater pulses in these locations avoiding the development of a mature subglacial drainage system able to drain water quickly (Doyle et al., 2014). Finally, it is hypothesised that a higher frequency of cyclonic rain events in spring should not have the same impact, since in this period of the year, most of meltwater and rainfall can be retained in the firn without feed runoff and penetration of water into the subglacial drainage system.

In this context an increase in cyclonic rainfall reveals two new future scenarios on the GrIS dynamics. The first is a future acceleration of the GrIS margins in the key period of late summer/early autumn that would be able to counterbalance the ice velocity decrease in winter induced by warmer summer. This would exacerbate the GrIS decline and could expose through accelerations, an ever-greater portion of GrIS towards lower altitudes, further enhancing ice motion meltwater production and hence contribute to sea level rise. Conversely, the second scenario contemplates the hypothesis that an increase in velocity induced by cyclonic rainfall in late summer/early autumn could reorganise the subglacial drainage system, able to

further decrease ice motion in winter with an overall decrease in annual ice motion. This mechanism could reduce and slow down the decline of the GrIS and its contribution to the sea level rise.

### **6.3. Prospects for Future Research**

#### **6.3.1 Impact of Extratropical Cyclones on the GrIS SMB and SEB**

The Serreze (2016) cyclone dataset used in this study was obtained by applying an algorithm on NCEP-NCARv1 reanalysis of  $2.5^\circ \times 2.5^\circ$  if compared to the resolution of 20 km of the MAR. The coarse resolution of this dataset already mentioned in section 6.2.1 allowed the study of positioning of the cyclones with uncertainties of an order of hundreds of kilometres. Furthermore, due to detection and tracking algorithm of this dataset applied on sea level pressure fields, it presented critical issues during the warm season as underlined in section 3.3.2, identifying spurious system over the GrIS, some of which remained even after the filtering operations carried out in this study. A detection and tracking algorithm based on the calculation of relative vorticity at 850 hPa, applied on reanalysis with a higher resolution, as done by Chen et al. (2016), could overcome the aforementioned problems. This would reduce the errors related to the positioning of the cyclones allowing to estimate with more precision when the GrIS is really under the cyclonic influence or not. At the same time, the geopotential height of 850 hPa would be a better field to detect synoptic system avoiding the problems related to the higher interior of the GrIS due to its influence in summer on sea level pressure.

Another limitation of this study derived from the fact that while the cyclone dataset had a temporal resolution of 6 hours, the variables extracted from the MAR had a daily resolution. This means that even if a cyclone has also impacted a certain area of the GrIS for only six hours, however, the recorded value covers the whole day. A solution to overcome this problem is to apply the same procedure developed in Chapter 4 with the MAR forced at its lateral boundaries by the same NCEP-NCARv1 reanalysis every 6 hours as done by Tedesco and Fettweis (2020)

Another possible development of this research concerns the choice of the amplitude of the cyclonic coverage. In this work, the distance of 750 km distance was chosen, as underlined in section 3.3.2, because it is the distance that includes the upper limit of the range of coverage of most cyclones affecting Greenland and therefore as mentioned in section 3.3.2, that can have a direct impact on GrIS. However, cyclones radius may vary due to different factors, for example season, minimum sea level pressure, deepening rate and life time, with radius ranging from 300/400 km over the western and northern part of the GrIS in summer, to more than 900 km off its south-east coast (Rudeva & Gulev, 2007). It is considered that an interesting development of the research would be to adopt a methodology that considers this heterogeneity, establishing different radii thresholds according to the season and different areas around the GrIS to investigate the impact of this on the results.

In addition to the different radius thresholds, another important improvement would consist of detecting and quantifying separately the impact of the warm and cold air advection which follow the warm and cold front of a cyclone. This would allow more precise predictions of the impact of cyclones on the GrIS surface mass balance due to their position and change in their trajectories in a climate warming scenario, since the warm and cold advection on one area of the GrIS depend on their location and path followed. A simple approach to reach this aim, could be a development of an algorithm able to automatically classify which portion of the GrIS is under the cold or warm advection based on two key parameters that affect the air mass advection: 1) the position of the cyclone centre and 2) the time elapsed since its formation.

It is also suggested to expand this study to include seasons not analysed in this study, such as spring and autumn, where air temperatures may be close to the rain/snow threshold. This would enable a clearer overview regarding the impact of cyclones in different areas of the GrIS in terms of temperature, radiation and precipitation pathways, underlining which part of the margins will be more likely affected by cyclonic episodes of rainfall at the expense of snow, which is predicted to

increase sooner (later) in Spring (Autumn)(Franco et al., 2013; McCrystall et al., 2021) and already underway in September (Niwano et al., 2021)

Finally, it is underlined that results were obtained using the MAR, one of the best regional climate models in modelling the GrIS behaviour and interaction with the atmosphere (Fettweis et al., 2017). It was widely validated with in situ and satellite measurements and used for past simulations and future projections of the GrIS surface mass balance (Tedesco & Fettweis, 2012; Franco et al., 2013; Vernon et al., 2013; Fettweis et al., 2017; Goelzer et al., 2020). However, the model still presents some limitations in modelling the objective parameters of this study, especially in the ablation area which is also the one of greatest interest due to its sensitivity in terms of mass balance to climate change (Fettweis et al., 2017). It was shown that the MAR is less confident than elsewhere in the ablation zone in predicting temperature because here the resolution doesn't capture the processes that occur at a lower scale with high confidence (Vernon et al., 2013). The errors in estimates in this area between in situ and modelled values derive from the difficulties in modelling the physical properties of the snowpack, its change in extension, the presence or not of bare ice along with its parameterization in terms of albedo. In turn these uncertainties influence the ability of the model to parameterize meltwater refreezing (Fettweis et al., 2017; Goelzer et al., 2020). For these reasons, further research may therefore be valuable following the procedure developed in this work but with different regional climatic models. This would allow an intercomparison between model' outputs, especially useful for understanding which parameter estimates are affected by the greatest uncertainty and inter-model spread, especially in the ablation zone. This would expand the knowledge, already advanced in this work, regarding which parameters future research needs to focus on to better estimate the impact of cyclones on the GrIS.

Apart from the research perspective aforementioned, it is important to stress the suitability of the methodology presented in Chapter 4 to be applied to future climatic projections. It is suggested that it can also be applied to the outputs of the GCMs regarding the future projections of cyclones around Greenland. This, along

with and RCMs forced by the same GCMs will permit to study the future impact of cyclones on SMB and SEB of the GrIS in a warmer and wetter climate.

### **6.3.2 Impact of Cyclonic Rainfall on the GrIS Ice Motion**

An easily reproducible and replicable methodology was presented to extract glacier ice velocity from the different satellite data sets. Since it can be applied to any ice velocity data, it allows considerable perspective for future research. However, the major limitations of the research were the poor temporal spacing and temporal coverage of satellite data. This did not allow us to accurately study the ice velocity changes due to a change in meltwater and rainfall drainage, as it occurs on a shorter time scale than the period covered by the image pairs which often only partially cover the cyclonic event. Another limit was the absence of in situ data of the borehole water pressure and the proglacial discharge which give key information in interpreting ice velocity change at daily resolution. It is then suggested that future work could involve a combination of approaches and data (satellite and in situ) to understand the mechanisms at play in ice velocity change detected by satellite images. This would have the advantage of combining the widescale/multiple glacier data over many years that satellite data can provide with the detail that can be gained from in-situ studies of individual glaciers. Satellite velocity data could be combined with ice velocity data from GPS along selected transects of glaciers involved along with in situ analysis such as dye tracing experiments in the subglacial drainage system or proglacial discharge (Cowton et al., 2013; Doyle et al., 2015). This combination of data from multiple techniques would enable resolution of the close link between surface melt, englacial water storage, proglacial discharge, and ice velocity change on different time scales.

Current studies with GPS do not go beyond 140 km from the margins up to 1500 m.a.s.l along the K-transect of some land terminating glaciers along the west margins of the GrIS (Bartholomew et al., 2011; Tedstone et al., 2013). Thus, the satellite images represent an enormous potential for the exploration of the ice velocity of the internal areas of the GrIS. These, together with modelling of melt, rainfall and runoff will allow research into ice motion of portions of the GrIS

increasingly affected by summer ablation and cyclonic rainfall events in a warmer and wetter climate but where in situ measurements are difficult to conduct.

The future importance of the use of satellite images is reinforced by their ever-increasing availability demonstrated by the continuous updating with new images coming from the datasets utilised in this study (Scambos et al., 2016; Joughin et al., 2020) or coming from other projects whose images were not suitable for this study. For example, the programme for monitoring of the GrIS (PROMICE) has recently published a timeseries of the GrIS velocity mosaics based on ESA Sentinel-1 SAR covering the period from September 2016 onwards (Solgaard et al., 2021) (not useful since our data ended in 2016). Other ice velocity datasets which were not useful for our study are those produced by Dresden University (Rosenau et al., 2015) and the ESA Climate Change Initiative project (CCI) which ice velocity data of specific glaciers for selected periods covering the time span 1972 - to present.

Apart from the future research perspective aforementioned, it is important to stress again the suitability of the methodology presented in Chapter 5 in extracting ice velocity data of selected glaciers. The methodology, along with an output of regional climate model, proved to be a particularly useful approach to study and interpret ice velocity behaviour during the melt season and the cyclonic events, that can be extended and applied to future data, with great savings in terms of resources and equipment.

#### **6.4. Concluding Remarks**

The GrIS is of the utmost societal importance since it represents the recent major single contributor to global sea level rise and whose future contribution is critical to the socio-economic impacts of sea-level rise yet to come. Extratropical cyclones exert a primary role in determining the surface mass budget and dynamics of the GrIS. However, determining mechanisms of energy exchange and precipitation pathways has received little research, and this thesis contributes to knowledge in this regard.

The first aim of the thesis was to investigate the impact of extratropical cyclones on the GrIS surface mass and energy balance through a methodology that involved a regional climate model and a dataset of cyclone positions. The method

proved particularly suitable for showing the spatial footprint on the GrIS surface of the main physical processes involved during the passage of the cyclones not yet performed in other works up to date. Their overall positive contribution to surface mass balance via snowfall, conceals numerous regional differences in their impact on the GrIS, between the ablation and accumulation zone. Some limitations due to the spatial and temporal resolution of the tools used, together with some simplifications in the choices regarding cyclonic parameters, suggest that exploring and refining these techniques further offers opportunities for further detailed research which would increase the precision of outputs.

The second aim of the study was to investigate the impact of cyclonic rain in the key hydrological period between late summer and early autumn on the western margins of the GrIS. This study, the largest in terms of glaciers and cyclonic events studied so far, showed a widespread acceleration of marine and land terminating glaciers in five different sites of the GrIS affected by three cyclonic events. The GIS methodology developed to extract ice velocity from satellite data, provides a simple and reproducible tool that can be utilised in future studies involving satellite ice velocity images.

Overall, our findings show the positive contribution of extratropical cyclones on the GrIS surface mass balance via snowfall and their ability to dampen meltwater production, especially in the ablation zone via solid precipitation and reduction of positive surface energy balance in summer. However, replacement of rain at the expense of snow would limit the positive impact of extratropical cyclones upon the GrIS mass balance. In this context, we have shown how episodes of rainfall in the period of transition between summer and autumn are able to perturb the dynamics of the GrIS, inducing acceleration at its margin and introducing a negative impact on the GrIS mass balance. This impact could be amplified in a wetter and warmer climate.

Despite the results obtained, our findings highlight some necessary research priorities. Firstly, it was underlined the importance to improve research regarding the future trajectories, frequency and intensity of cyclones around Greenland which have been shown having a profound impact in regulating the surface mass balance and

## Synthesis and Discussion

surface energy balance on different regions of the GrIS. Secondly, although cyclonic rainfall has been shown to induce the GrIS margins acceleration, however further studies in this direction are needed to corroborate our findings and show if cyclonic rainfall will be able to induce an acceleration at annual scale.

## References Cited

---

- Abadie, L. M., Jackson, L. P., Sainz de Murieta, E., Jevrejeva, S., & Galarraga, I. (2020). Comparing urban coastal flood risk in 136 cities under two alternative sea-level projections: RCP 8.5 and an expert opinion-based high-end scenario. *Ocean & Coastal Management, 193*, 105249-105260.
- Akperov, M., Rinke, A., Mokhov, I. I., Matthes, H., Semenov, V. A., Adakudlu, M., Cassano, J., Christensen, J. H., Dembitskaya, M. A., Dethloff, K., Fettweis, X., Glisan, J., Gutjahr, O., Heinemann, G., Koenigk, T., Koldunov, N. V., Laprise, R., Mottram, R., Nikiéma, O., Scinocca, J. F., Sein, D., Sobolowski, S., Winger, K., & Zhang, W. (2018). Cyclone Activity in the Arctic From an Ensemble of Regional Climate Models (Arctic CORDEX). *Journal of Geophysical Research: Atmospheres, 123*(5), 2537-2554.
- Akperov, M. G., & Mokhov, I. I. (2013). Estimates of the sensitivity of cyclonic activity in the troposphere of extratropical latitudes to changes in the temperature regime. [journal article]. *Izvestiya, Atmospheric and Oceanic Physics, 49*(2), 113-120.
- Andrews, L. C., Catania, G. A., Hoffman, M. J., Gulley, J. D., Luthi, M. P., Ryser, C., Hawley, R. L., & Neumann, T. A. (2014). Direct observations of evolving subglacial drainage beneath the Greenland Ice Sheet. *Nature, 514*(7520), 80-83.
- Appenzeller, C., Schwander, J., Sommer, S., & Stocker, T. F. (1998). The North Atlantic Oscillation and its imprint on precipitation and ice accumulation in Greenland. *Geophysical Research Letters, 25*(11), 1939-1942.
- Archer, C. L., & Caldeira, K. (2008). Historical trends in the jet streams. *Geophysical Research Letters, 35*(8), L08803.
- Bakker, P., Schmittner, A., Lenaerts, J. T. M., Abe-Ouchi, A., Bi, D., van den Broeke, M. R., Chan, W. L., Hu, A., Beadling, R. L., Marsland, S. J., Mernild, S. H., Saenko, O. A., Swingedouw, D., Sullivan, A., & Yin, J. (2016). Fate of the Atlantic Meridional Overturning Circulation: Strong decline under continued warming and Greenland melting. *Geophysical Research Letters, 43*(23), 12,252-212,260.
- Bamber, J. L., Ekholm, S., & Krabill, W. B. (2001). A new, high-resolution digital elevation model of Greenland fully validated with airborne laser altimeter data. *Journal of Geophysical Research: Solid Earth, 106*(B4), 6733-6745.
- Bamber, J. L., Griggs, J. A., Hurkmans, R. T. W. L., Dowdeswell, J. A., Gogineni, S. P., Howat, I., Mouginot, J., Paden, J., Palmer, S., Rignot, E., & Steinhage, D. (2013). A new bed elevation dataset for Greenland. *The Cryosphere, 7*(2), 499-510.

## References Cited

- Barnes, E. A., Dunn-Sigouin, E., Masato, G., & Woollings, T. (2014). Exploring recent trends in Northern Hemisphere blocking. *Geophysical Research Letters*, *41*(2), 638-644.
- Barnes, E. A., & Screen, J. A. (2015). The impact of Arctic warming on the midlatitude jet-stream: Can it? Has it? Will it? *Wiley Interdisciplinary Reviews: Climate Change*, *6*(3), 277-286.
- Bartholomaeus, T. C., Stearns, L. A., Sutherland, D. A., Shroyer, E. L., Nash, J. D., Walker, R. T., Catania, G., Felikson, D., Carroll, D., Fried, M. J., Noël, B. P. Y., & Van Den Broeke, M. R. (2016). Contrasts in the response of adjacent fjords and glaciers to ice-sheet surface melt in West Greenland. *Annals of Glaciology*, *57*(73), 25-38.
- Bartholomew, I., Nienow, P., Mair, D., Hubbard, A., King, M. A., & Sole, A. (2010). Seasonal evolution of subglacial drainage and acceleration in a Greenland outlet glacier. *Nature Geoscience*, *3*(6), 408-411.
- Bartholomew, I., Nienow, P., Sole, A., Mair, D., Cowton, T., & King, M. A. (2012). Short-term variability in Greenland Ice Sheet motion forced by time-varying meltwater drainage: Implications for the relationship between subglacial drainage system behavior and ice velocity. *Journal of Geophysical Research: Earth Surface*, *117*(F3), F03002.
- Bartholomew, I. D., Nienow, P., Sole, A., Mair, D., Cowton, T., King, M. A., & Palmer, S. (2011). Seasonal variations in Greenland Ice Sheet motion: Inland extent and behaviour at higher elevations. *Earth and Planetary Science Letters*, *307*(3-4), 271-278.
- Belleflamme, A., Fettweis, X., Lang, C., & Ericum, M. (2012). Current and future atmospheric circulation at 500 hPa over Greenland simulated by the CMIP3 and CMIP5 global models. *Climate Dynamics*, *41*(7-8), 2061-2080.
- Bender, G. (1984). The distribution of snow accumulation on the Greenland Ice Sheet. M.S. thesis, Geophysical Institute, University of Alaska. [Available from Geophysical Institute, University of Alaska, P.O. Box 7555780, Fairbanks, AK 99775- 5780.], 110 pp.
- Bengtsson, L., Hodges, K. I., & Roeckner, E. (2005). Storm Tracks and Climate Change. *Journal of Climate*, *19*, 3518-3542.
- Benn, D. I., Cowton, T., Todd, J., & Luckman, A. (2017). Glacier Calving in Greenland. *Current Climate Change Reports*, *3*(4), 282-290.
- Bennartz, R., Shupe, M. D., Turner, D. D., Walden, V. P., Steffen, K., Cox, C. J., Kulie, M. S., Miller, N. B., & Pettersen, C. (2013). July 2012 Greenland melt extent enhanced by low-level liquid clouds. *Nature*, *496*(7443), 83-86.

## References Cited

- Berdahl, M., Rennermalm, A., Hammann, A., Mioduszewski, J., Hameed, S., Tedesco, M., Stroeve, J., Mote, T., Koyama, T., & McConnell, J. R. (2018). Southeast Greenland Winter Precipitation Strongly Linked to the Icelandic Low Position. *Journal of Climate*, *31*(11), 4483-4500.
- Blackport, R., & Screen, J. A. (2020a). Insignificant effect of Arctic amplification on the amplitude of midlatitude atmospheric waves. *Nature Climate Change*, *2019*, 1-2.
- Blackport, R., & Screen, J. A. (2020b). Weakened evidence for mid-latitude impacts of Arctic warming. *Nature Climate Change*, *10.12*, 1065-1066.
- Boisvert, L. N., Petty, A. A., & Stroeve, J. C. (2016). The Impact of the Extreme Winter 2015/16 Arctic Cyclone on the Barents–Kara Seas. *Monthly Weather Review*, *144*(11), 4279-4287.
- Box, J. E. (2013). Greenland Ice Sheet Mass Balance Reconstruction. Part II: Surface Mass Balance (1840–2010)\*. *Journal of Climate*, *26*(18), 6974-6989.
- Box, J. E., Bromwich, D. H., & Bai, L. S. (2004). Greenland ice sheet surface mass balance 1991–2000: Application of Polar MM5 mesoscale model and in situ data. *Journal of Geophysical Research: Atmospheres*, *109*(D16), 1-21.
- Box, J. E., & Colgan, W. (2013). Greenland Ice Sheet Mass Balance Reconstruction. Part III: Marine Ice Loss and Total Mass Balance (1840–2010). *Journal of Climate*, *26*(18), 6990-7002.
- Box, J. E., Cressie, N., Bromwich, D. H., Jung, J.-H., van den Broeke, M., van Angelen, J. H., Forster, R. R., Miège, C., Mosley-Thompson, E., Vinther, B., & McConnell, J. R. (2013). Greenland Ice Sheet Mass Balance Reconstruction. Part I: Net Snow Accumulation (1600–2009). *Journal of Climate*, *26*(11), 3919-3934.
- Box, J. E., Fettweis, X., Stroeve, J. C., Tedesco, M., Hall, D. K., & Steffen, K. (2012). Greenland ice sheet albedo feedback: thermodynamics and atmospheric drivers. *The Cryosphere*, *6*(4), 821-839.
- Braun, M., Saurer, H., Vogt, S., Simoes, J. C., & Gossman, H. (2001). The influence of large-scale atmospheric circulation on the surface energy balance of the King George Island ice cap. *International Journal of Climatology*, *21*(1), 21-36.
- Bromwich, D. H., Chen, Q.-s., Li, Y., & Cullather, R. I. (1999). Precipitation over Greenland and its relation to the North Atlantic Oscillation. *Journal of Geophysical Research: Atmospheres*, *104*(D18), 22103-22115.

## References Cited

- Bromwich, D. H., Cullather, R. I., Chen, Q.-s., & Csathó, B. M. (1998). Evaluation of recent precipitation studies for Greenland Ice Sheet. *Journal of Geophysical Research: Atmospheres*, *103*(D20), 26007-26024.
- Brun, E., David, P., Sudul, M., & Brunot, G. (1992). A numerical model to simulate snow-cover stratigraphy for operational avalanche forecasting. *Journal of Glaciology*, *38*(128), 13-22.
- Brunt, D. (2011). *Physical and dynamical meteorology*: Cambridge University Press.
- Buckley, M. W., & Marshall, J. (2016). Observations, inferences, and mechanisms of the Atlantic Meridional Overturning Circulation: A review. *Reviews of Geophysics*, *54*(1), 5-63.
- Cappelen, J., Jorgensen, B. V., Laursen, E. V., Stannius, L. S., & Thomsen, R. S. (2001). The observed climate of Greenland 1959-99 with climatological standard normals 1961-1990. *Technical Report*.
- Cappelen, J., Kern-Hansen, C., Laursen, E. V., & Jorgensen, P. V. (2014). Greenland - DMI Historical Climate Data Collection 1784-2013- Technical Report. *Danish Meteorological Insitute*.
- Catania, G. A., Stearns, L. A., Moon, T. A., Enderlin, E. M., & Jackson, R. H. (2020). Future Evolution of Greenland's Marine-Terminating Outlet Glaciers. *Journal of Geophysical Research: Earth Surface*, *125*(2), e2018JF004873.
- Chang, E. K. M., Ma, C.-G., Zheng, C., & Yau, A. M. W. (2016). Observed and projected decrease in Northern Hemisphere extratropical cyclone activity in summer and its impacts on maximum temperature. *Geophysical Research Letters*, *43*(5), 2200-2208.
- Chen, J., Qin, X., Kang, S., Du, W., Sun, W., & Liu, Y. (2018). Effects of clouds on surface melting of Laohugou glacier No. 12, western Qilian Mountains, China. *Journal of Glaciology*, *64*(243), 89-99.
- Chen, L., Fettweis, X., Knudsen, E. M., & Johannessen, O. M. (2016). Impact of cyclonic and anticyclonic activity on Greenland ice sheet surface mass balance variation during 1980-2013. *International Journal of Climatology*, *36*(10), 3423-3433.
- Chen, Q. S., Bromwich, D. H., & Bay, L. (1997). Precipitation over Greenland retrieved by a dynamic method and its relation to cyclonic activity. *Journal of Climate*, *10*.5, 839-870.
- Chu, V. W. (2013). Greenland ice sheet hydrology. *Progress in Physical Geography*, *38*(1), 19-54.

## References Cited

- Cline, D. W. (1997). Snow surface energy exchanges and snowmelt at a continental, midlatitude Alpine site. *Water Resources Research*, 33(4), 689-701.
- Colgan, W., Rajaram, H., Abdalati, W., McCutchan, C., Mottram, R., Moussavi, M. S., & Grigsby, S. (2016). Glacier crevasses: Observations, models, and mass balance implications. *Reviews of Geophysics*, 54(1), 119-161.
- Colgan, W., Rajaram, H., Anderson, R., Steffen, K., Phillips, T., Joughin, I., Zwally, H. J., & Abdalati, W. (2011). The annual glaciohydrology cycle in the ablation zone of the greenland ice sheet part 1 hydrology model. *Journal of Glaciology*, 57(204), 697-709.
- Conway, J. P., & Cullen, N. J. (2016). Cloud effects on surface energy and mass balance in the ablation area of Brewster Glacier, New Zealand. *The Cryosphere*, 10(1), 313-328.
- Cowton, T., Nienow, P., Sole, A., Wadham, J., Lis, G., Bartholomew, I., Mair, D., & Chandler, D. (2013). Evolution of drainage system morphology at a land-terminating Greenlandic outlet glacier. *Journal of Geophysical Research: Earth Surface*, 118(1), 29-41.
- Cowton, T. R., Sole, A. J., Nienow, P. W., Slater, D. A., & Christoffersen, P. (2018). Linear response of east Greenland's tidewater glaciers to ocean/atmosphere warming. *Proc Natl Acad Sci U S A*, 115(31), 7907-7912.
- Creyts, T. T., & Schoof, C. G. (2009). Drainage through subglacial water sheets. *Journal of Geophysical Research*, 114(F4), F04008.
- Cuffey, K. M., & Paterson, W. S. B. (2010). The physics of glaciers, 4th edition. *Academic Press*.
- Cullen, N. J., & Conway, J. P. (2017). A 22 month record of surface meteorology and energy balance from the ablation zone of Brewster Glacier, New Zealand. *Journal of Glaciology*, 61(229), 931-946.
- Cullen, N. J., Gibson, P. B., Mölg, T., Conway, J. P., Sirguey, P., & Kingston, D. G. (2019). The Influence of Weather Systems in Controlling Mass Balance in the Southern Alps of New Zealand. *Journal of Geophysical Research: Atmospheres*, 124(8), 4514-4529.
- Czaja, A., & Marshall, J. (2005). The Partitioning of Poleward Heat Transport between the Atmosphere and Ocean. *Journal of the atmospheric sciences*, 63(5), 1498-1511.
- Davison, B. J., Sole, A. J., Livingstone, S. J., Cowton, T. R., & Nienow, P. W. (2019). The Influence of Hydrology on the Dynamics of Land-Terminating Sectors of the Greenland Ice Sheet. *Frontiers in Earth Science*, 7(10).

## References Cited

- Delhasse, A., Hanna, E., Kittel, C., & Fettweis, X. (2021). Brief communication: CMIP6 does not suggest any atmospheric blocking increase in summer over Greenland by 2100. *International Journal of Climatology*, *41*(4), 2589-2596.
- Diolaiuti, G., Smiraglia, C., Vassena, G., & Motta, M. (2004). Dry calving processes at the ice cliff of Strandline Glacier northern Victoria Land, Antarctica. *Annals of Glaciology*, *39*, 201-208.
- Dow, C., Kulesa, B., Rutt, I., Doyle, S. H., & Hubbard, A. (2014). Upper bounds on subglacial channel development for interior regions of the Greenland ice sheet. *Journal of Glaciology*, *60*(224), 1044-1052.
- Dow, C. F., Kulesa, B., Rutt, I., Tsai, V., Pimentel, S., Doyle, S., Van As, D., Lindbäck, K., Pettersson, R., & Jones, G. (2015). Modeling of subglacial hydrological development following rapid supraglacial lake drainage. *Journal of Geophysical Research: Earth Surface*, *120*(6), 1127-1147.
- Doyle, S. H., Hubbard, A., Fitzpatrick, A. A. W., van As, D., Mikkelsen, A. B., Pettersson, R., & Hubbard, B. (2014). Persistent flow acceleration within the interior of the Greenland ice sheet. *Geophysical Research Letters*, *41*(3), 899-905.
- Doyle, S. H., Hubbard, A., van de Wal, R. S. W., Box, J. E., van As, D., Scharrer, K., Meierbachtol, T. W., Smeets, P. C. J. P., Harper, J. T., Johansson, E., Mottram, R. H., Mikkelsen, A. B., Wilhelms, F., Patton, H., Christoffersen, P., & Hubbard, B. (2015). Amplified melt and flow of the Greenland ice sheet driven by late-summer cyclonic rainfall. *Nature Geoscience*, *8*(8), 647-653.
- Dunn-Sigouin, E., & Son, S. W. (2013). Northern Hemisphere blocking frequency and duration in the CMIP5 models. *Journal of Geophysical Research: Atmospheres*, *118*(3), 1179-1188.
- Enderlin, E. M., Howat, I. M., Jeong, S., Noh, M.-J., van Angelen, J. H., & van den Broeke, M. R. (2014). An improved mass budget for the Greenland ice sheet. *Geophysical Research Letters*, *41*(3), 866-872.
- Ettema, J., van den Broeke, M. R., van Meijgaard, E., van de Berg, W. J., Bamber, J. L., Box, J. E., & Bales, R. C. (2009). Higher surface mass balance of the Greenland ice sheet revealed by high-resolution climate modeling. *Geophysical Research Letters*, *36*(12).
- Fealy, R., & Sweeney, J. (2007). Identification of frequency changes in synoptic circulation types and consequences for glacier mass balance in Norway. *Norsk Geografisk Tidsskrift - Norwegian Journal of Geography*, *61*(2), 76-91.

## References Cited

- Fettweis, X. (2007). Reconstruction of the 1979-2006 Greenland ice sheet surface mass balance using the regional climate model MAR. *The Cryosphere Discussions*, 1(1), 123-168.
- Fettweis, X., Box, J. E., Agosta, C., Amory, C., Kittel, C., Lang, C., van As, D., Machguth, H., & Gallée, H. (2017). Reconstructions of the 1900–2015 Greenland ice sheet surface mass balance using the regional climate MAR model. *The Cryosphere*, 11(2), 1015-1033.
- Fettweis, X., Franco, B., Tedesco, M., Van Angelen, J., Lenaerts, J. T., van den Broeke, M. R., & Gallée, H. (2013a). Estimating the Greenland ice sheet surface mass balance contribution to future sea level rise using the regional atmospheric climate model MAR. *The Cryosphere*, 7(2), 469-489.
- Fettweis, X., Franco, B., Tedesco, M., van Angelen, J. H., Lenaerts, J. T. M., van den Broeke, M. R., & Gallée, H. (2012). Estimating Greenland ice sheet surface mass balance contribution to future sea level rise using the regional atmospheric climate model MAR. *The Cryosphere Discussions*, 6(4), 3101-3147.
- Fettweis, X., Hanna, E., Lang, C., Belleflamme, A., Ericum, M., & Gallée, H. (2013b). Important role of the mid-tropospheric atmospheric circulation in the recent surface melt increase over the Greenland ice sheet. *The Cryosphere*, 7(1), 241-248.
- Fettweis, X., Mabilie, G., Ericum, M., Nicolay, S., & den Broeke, M. V. (2010). The 1958–2009 Greenland ice sheet surface melt and the mid-tropospheric atmospheric circulation. *Climate Dynamics*, 36(1-2), 139-159.
- Fitzharris, B. B., Hay, J. E., & Jones, P. D. (1992). Behaviour of New Zealand glaciers and atmospheric circulation changes over the past 130 years. *the Holocene*, 2(2), 97-106.
- Fitzharris, B. B., J., C. T., & Lamont, G. N. (1997). Glacier balance fluctuations and atmospheric circulation patterns over the Southern Alps, New Zealand. *International Journal of Climatology*, 17(7), 745-763.
- Fountain, A. G., & Walder, J. S. (1998). Water flow through temperate glaciers. *Reviews of Geophysics*, 36(3), 299-328.
- Franco, B., Fettweis, X., & Ericum, M. (2013). Future projections of the Greenland ice sheet energy balance driving the surface melt. *The Cryosphere*, 7(1), 1-18.
- Gallée, H. (1995). Simulation of the Mesocyclonic Activity in the Ross Sea, Antarctica. *Monthly Weather Review*, 123(7), 2051-2069.

## References Cited

- Gallée, H., Guyomarc'h, G., & Brun, E. (2001). Impact of snow drift on the Antarctic ice sheet surface mass balance: possible sensitivity to snow-surface properties. *Boundary Layer Meteorology*, *99*(1), 1-19.
- Gallée, H., & Schayes, G. (1994). Development of a three-dimensional meso- $\gamma$  primitive equation model: katabatic winds simulation in the area of Terra Nova Bay, Antarctica. *Monthly Weather Review*, *122*(4), 671-685.
- Giuliaci, M., Giuliaci, A., & Corazzon, P. (2010). *Manuale di meteorologia: Alpha Test*.
- Goelzer, H., Nowicki, S., Payne, A., Larour, E., Seroussi, H., Lipscomb, W. H., Gregory, J., Abe-Ouchi, A., Shepherd, A., Simon, E., Agosta, C., Alexander, P., Aschwanden, A., Barthel, A., Calov, R., Chambers, C., Choi, Y., Cuzzone, J., Dumas, C., Edwards, T., Felikson, D., Fettweis, X., Golledge, N. R., Greve, R., et al. (2020). The future sea-level contribution of the Greenland ice sheet: a multi-model ensemble study of ISMIP6. *The Cryosphere*, *14*(9), 3071-3096.
- Gourieroux, C., Holly, A., & Monfort, A. (1982). Likelihood ratio test, Wald test, and Kuhn-Tucker test in linear models with inequality constraints on the regression parameters. *Econometrica: journal of the Econometric Society*, *50*(1), 63-80.
- GRASS\_Development\_Team. (2020). Geographic Resources Analysis Support System (GRASS GIS) Software, Version 7.8.3. Open Source Geospatial Foundation.
- Griggs, J. A., Bamber, J. L., L., H. R. T. W., Dowdeswell, J. A., Gogineni, S. P., Howat, I., Mouginot, J., Paden, J., Palmer, S., Rignot, E., & Steinhage, D. (2012). A new bed elevation dataset for Greenland. *The Cryosphere Discussions*, *6*(6), 4829-4860.
- Gulev, S. K., Zolina, O., & Grigoriev, S. (2001). Extratropical cyclone variability in the Northern Hemisphere winter from the NCEP-NCAR reanalysis data. *Climate Dynamics*, *17*, 795-809.
- Haerberli, W., & Whiteman, C. (2015). Snow and ice-related hazards, risks, and disasters: a general framework *Snow and Ice-Related Hazards, Risks and Disasters* (pp. 1-34): Elsevier.
- Hanna, E. (2003). Recent cooling in coastal southern Greenland and relation with the North Atlantic Oscillation. *Geophysical Research Letters*, *30*(3), 32.31-32.33.
- Hanna, E., Cropper, T. E., Hall, R. J., & Cappelen, J. (2016). Greenland Blocking Index 1851-2015: a regional climate change signal. *International Journal of Climatology*, *36*(15), 4847-4861.

## References Cited

- Hanna, E., Cropper, T. E., Jones, P. D., Scaife, A. A., & Allan, R. (2015). Recent seasonal asymmetric changes in the NAO (a marked summer decline and increased winter variability) and associated changes in the AO and Greenland Blocking Index. *International Journal of Climatology*, 35(9), 2540-2554.
- Hanna, E., Fettweis, X., Mernild, S. H., Cappelen, J., Ribergaard, M. H., Shuman, C. A., Steffen, K., Wood, L., & Mote, T. L. (2014). Atmospheric and oceanic climate forcing of the exceptional Greenland ice sheet surface melt in summer 2012. *International Journal of Climatology*, 34(4), 1022-1037.
- Hanna, E., Huybrechts, P., Cappelen, J., Steffen, K., Bales, R. C., Burgess, E., McConnell, J. R., Peder Steffensen, J., Van den Broeke, M., Wake, L., Bigg, G., Griffiths, M., & Savas, D. (2011). Greenland Ice Sheet surface mass balance 1870 to 2010 based on Twentieth Century Reanalysis, and links with global climate forcing. *Journal of Geophysical Research: Atmospheres*, 116(D24), D24121.
- Hanna, E., Jones, J. M., Cappelen, J., Mernild, S. H., Wood, L., Steffen, K., & Huybrechts, P. (2013). The influence of North Atlantic atmospheric and oceanic forcing effects on 1900-2010 Greenland summer climate and ice melt/runoff. *International Journal of Climatology*, 33(4), 862-880.
- Hanna, E., McConnell, J., Das, S., Cappelen, J., & Stephens, A. (2006). Observed and modeled Greenland ice sheet snow accumulation, 1958-2003 and links with regional climate forcing. *Journal of Climate*, 19.3, 344-358.
- Hanna, E., Mernild, S. H., Cappelen, J., & Steffen, K. (2012). Recent warming in Greenland in a long-term instrumental (1881–2012) climatic context: I. Evaluation of surface air temperature records. *Environmental Research Letters*, 7(4), 045404.
- Hanna, E., Pattyn, F., Navarro, F., Favier, V., Goelzer, H., van den Broeke, M. R., Vizcaino, M., Whitehouse, P. L., Ritz, C., & Bulthuis, K. (2020). Mass balance of the ice sheets and glaciers—Progress since AR5 and challenges. *Earth-Science Reviews*, 201, 102976.
- Hannah, D. M., & McGregor, G. R. (1997). Evaluating the impact of climate on snow and icemelt dynamics in the Taillon basin French Pyrenees. *Journal of Glaciology*, 43(145), 563-568.
- Harvey, B. J., Shaffrey, L. C., & Woollings, T. J. (2013). Equator-to-pole temperature differences and the extra-tropical storm track responses of the CMIP5 climate models. *Climate Dynamics*, 43(5-6), 1171-1182.
- Heid, T., & Käab, A. (2012). Repeat optical satellite images reveal widespread and long term decrease in land-terminating glacier speeds. *The Cryosphere*, 6(2), 467-478.

## References Cited

- Hofer, S., Tedstone, A. J., Fettweis, X., & Bamber, J. L. (2017). Decreasing cloud cover drives the recent mass loss on the Greenland Ice Sheet. *Science Advances*, 3(6), e1700584.
- Hofer, S., Tedstone, A. J., Fettweis, X., & Bamber, J. L. (2019). Cloud microphysics and circulation anomalies control differences in future Greenland melt. *Nature Climate Change*, 9(7), 523-528.
- Hoffman, M., & Price, S. (2014). Feedbacks between coupled subglacial hydrology and glacier dynamics. *Journal of Geophysical Research: Earth Surface*, 119(3), 414-436.
- Hoffman, M. J., Catania, G. A., Neumann, T. A., Andrews, L. C., & Rumrill, J. A. (2011). Links between acceleration, melting, and supraglacial lake drainage of the western Greenland Ice Sheet. *Journal of Geophysical Research*, 116(F4), F04035.
- Hoinkes, H. C. (1968). Glacier variation and weather. *Journal of Glaciology*, 7(49), 3-18.
- Holland, D. M., Thomas, R. H., De Young, B., Ribergaard, M. H., & Lyberth, B. (2008). Acceleration of Jakobshavn Isbrae triggered by warm subsurface ocean waters. *Nature geoscience*, 1(10), 659-664.
- Hoskins, B., & Hodges, K. I. (2002). New Perspectives on the Northern Hemisphere Winter Storm Tracks. *Journal of the Atmospheric Sciences*, 59(6), 1041-1061.
- Howat, I., Negrete, A., & Smith, B. (2017). MEaSURES Greenland Ice Mapping Project (GIMP) Digital Elevation Model from GeoEye and WorldView Imagery, Version 1. Boulder, Colorado USA. NASA National Snow and Ice Data Center Distributed Active Archive Center.
- Howat, I. M., Box, J. E., Ahn, Y., Herrington, A., & McFADDEN, E. M. (2010). Seasonal variability in the dynamics of marine-terminating outlet glaciers in Greenland. *Journal of Glaciology*, 56(198), 601-613.
- Howat, I. M., Joughin, I., & Scambos, T. A. (2007). Rapid changes in ice discharge from Greenland outlet glaciers. *Science*, 315(5818), 1559-1561.
- Howat, I. M., Negrete, A., & Smith, B. E. (2014). The Greenland Ice Mapping Project (GIMP) land classification and surface elevation data sets. *The Cryosphere*, 8(4), 1509-1518.
- Hu, Y., & Fu, Q. (2007). Observed poleward expansion of the Hadley circulation since 1979. *Atmospheric Chemistry and Physics*, 7, 5229-5236.
- Hu, Y., Tao, L., & Liu, J. (2013). Poleward expansion of the hadley circulation in CMIP5 simulations. *Advances in Atmospheric Sciences*, 30(3), 790-795.

## References Cited

- Huang, J., & McElroy, M. B. (2014). Contributions of the Hadley and Ferrel Circulations to the Energetics of the Atmosphere over the Past 32 Years. *Journal of Climate*, 27(7), 2656-2666.
- Hugonnet, R., McNabb, R., Berthier, E., Menounos, B., Nuth, C., Girod, L., Farinotti, D., Huss, M., Dussaillant, I., Brun, F., & Käab, A. (2021). Accelerated global glacier mass loss in the early twenty-first century. *Nature*, 592(7856), 726-731.
- Hurrell, J. W. (1995). Decadal Trends in the North Atlantic Oscillation Regional Temperatures and Precipitation. *Science*, 269(5224), 676-679.
- Hurrell, J. W., & Deser, C. (2010). North Atlantic climate variability: The role of the North Atlantic Oscillation. *Journal of Marine Systems*, 79(3-4), 231-244.
- Hurrell, J. W., Kushnir, Y., Ottersen, G., & Visbeck, M. (2003). The North Atlantic Oscillation: Climate Significance and Environmental Impact. *Geophysical monograph series*, 134, 134-279.
- Hutterli, M. A., Raible, C. C., & Stocker, T. F. (2005). Reconstructing climate variability from Greenland ice sheet accumulation: An ERA40 study. *Geophysical Research Letters*, 32(23), L23712.
- Iken, A., Bindshadler, R. A., Cuffey, K. M., & Paden, J. (1986). Combined measurements of subglacial water pressure and surface velocity of Findelengletscher, Switzerland: conclusions about drainage system and sliding mechanism. *Journal of Glaciology*, 32(110), 101-119.
- IPCC. (2013). The Physical Science Basis. Contribution of Working Group I to the Fifth Assessment Report of the Intergovernmental Panel on Climate Change. 2013. *There is no corresponding record for this reference.*[Google Scholar], 33-118.
- Jenkins, A. (2011). Convection-driven melting near the grounding lines of ice shelves and tidewater glaciers. *Journal of Physical Oceanography*, 41(12), 2279-2294.
- Joughin, I. (2002). Ice-sheet-velocity-mapping-a-combined-interferometric-and-speckle-tracking-approach. *Annals of Glaciology*, 34, 195-201.
- Joughin, I., Alley, R. B., & Holland, D. M. (2012). Ice-Sheet Response to Oceanic Forcing. *Science*, 338(6111), 1172-1176.
- Joughin, I., Das, S., King, M. A., Smith, B. E., Howat, I., & Moon, T. (2008). Seasonal Speedup Along the Western Flank of the Greenland Ice Sheet. *Science*, 320(5877), 781-783.

## References Cited

- Joughin, I., Howat, I., Smith, B., & Scambos, T. (2020). MEaSURES Greenland Ice Velocity: Selected Glacier Site Velocity Maps from InSAR, Version 3 [March 2008 to January 2016]. *Boulder, Colorado USA. NASA National Snow and Ice Data Center Distributed Active Archive Center* [Accessed October 18, 2020.].
- Joughin, I., Smith, B., Howat, I., & Scambos, T. (2016). MEaSURES Multi-year Greenland Ice Sheet Velocity Mosaic, Version 1. *Boulder, Colorado USA. NASA National Snow and Ice Data Center Distributed Active Archive Center* [Accessed October 18, 2020.].
- Joughin, I., Smith, B. E., & Howat, I. (2018a). Greenland Ice Mapping Project: Ice Flow Velocity Variation at sub-monthly to decadal time scales. *Cryosphere*, *12*(7), 2211-2227.
- Joughin, I., Smith, B. E., & Howat, I. M. (2018b). A Complete Map of Greenland Ice Velocity Derived from Satellite Data Collected over 20 Years. *J Glaciol*, *64*(243), 1-11.
- Kalnay, E., Kanamitsu, M., Kistler, R., Collins, W., Deaven, D., Gandin, L., Iredel, M., Saha, S., White, G., Woollen, J., Zhu, Y., Chelliah, M., Ebisuzaky, W., Higgins, W., Janowiak, J., Mo, K. C., Ropelewsky, C., Wang, J., Leetmaa, A., Reynolds, R., Jenne, R., & Joseph, D. (1996). The NCEPNCAR 40-year Reanalysis project. *Bulletin of the American meteorological Society*, 437-472.
- Khan, S. A., Bjork, A. A., Bamber, J. L., Morlighem, M., Bevis, M., Kjaer, K. H., Mouginot, J., Lokkegaard, A., Holland, D. M., Aschwanden, A., Zhang, B., Helm, V., Korsgaard, N. J., Colgan, W., Larsen, N. K., Liu, L., Hansen, K., Barletta, V., Dahl-Jensen, T. S., Sondergaard, A. S., Csatho, B. M., Sasgen, I., Box, J., & Schenk, T. (2020). Centennial response of Greenland's three largest outlet glaciers. *Nat Commun*, *11*(1), 5718.
- Kim, B.-M., Hong, J.-Y., Jun, S.-Y., Zhang, X., Kwon, H., Kim, S.-J., Kim, J.-H., Kim, S.-W., & Kim, H.-K. (2017). Major cause of unprecedented Arctic warming in January 2016: Critical role of an Atlantic windstorm. [Article]. *Scientific Reports*, *7*, 40051.
- King, M. D., Howat, I. M., Candela, S. G., Noh, M. J., Jeong, S., Noël, B. P. Y., van den Broeke, M. R., Wouters, B., & Negrete, A. (2020). Dynamic ice loss from the Greenland Ice Sheet driven by sustained glacier retreat. *Communications Earth & Environment*, *1*(1), 1-7.
- Knight, J., Folland, C. K., Linderholm, H. W., Fereday, D., Ineson, S., & Hurrell, J. W. (2009). The Summer North Atlantic Oscillation: Past, Present, and Future. *Journal of Climate*, *22*(5), 1082-1103.
- Koyama, T., Stroeve, J., Cassano, J., & Crawford, A. (2017). Sea ice loss and Arctic cyclone activity from 1979 to 2014. *Journal of Climate*, *30*(12), 4735-4754.

## References Cited

- Leclercq, P., Pitte, P., Giesen, R., Masiokas, M. H., & Oerlemans, J. (2012). Modelling and climatic interpretation of the length fluctuations of Glaciar Frías (north Patagonian Andes, Argentina) 1639–2009 AD. *Climate of the Past*, 8(5), 1385-1402.
- Lehmann, J., Coumou, D., Frieler, K., Eliseev, A. V., & Levermann, A. (2014). Future changes in extratropical storm tracks and baroclinicity under climate change. *Environmental Research Letters*, 9(8), 084002.
- Lenaerts, J. T. M., Le Bars, D., van Kampenhout, L., Vizcaino, M., Enderlin, E. M., & van den Broeke, M. R. (2015). Representing Greenland ice sheet freshwater fluxes in climate models. *Geophysical Research Letters*, 42(15), 6373-6381.
- Li, H., Ng, F., Li, Z., Qin, D., & Cheng, G. (2012). An extended “perfect-plasticity” method for estimating ice thickness along the flow line of mountain glaciers. *Journal of Geophysical Research: Earth Surface*, 117(F1), F01020.
- Linsbauer, A., Paul, F., & Haeberli, W. (2012). Modeling glacier thickness distribution and bed topography over entire mountain ranges with GlabTop: Application of a fast and robust approach. *Journal of Geophysical Research: Earth Surface*, 117(F3), F03007.
- MacCabe, G. J., Clark, M. P., & Serreze, M. C. (2001). Trends in Northern Hemisphere Surface Cyclone Frequency and Intensity. *Journal of Climate*, 14(12), 2763-2768.
- Mankoff, K. D., Solgaard, A., Colgan, W., Ahlstrøm, A. P., Khan, S. A., & Fausto, R. S. (2020). Greenland Ice Sheet solid ice discharge from 1986 through March 2020. *Earth System Science Data*, 12(2), 1367-1383.
- Masson-Delmotte, V., Zhai, B., Pirani, S. L., Connors, C., Péan, S., Berger, N., Caud, Y., Chen, L., Goldfarb, M. I., Gomis, M., Huang, K., Leitzell, E., Lonnoy, J. B. R., Matthews, T. K., Maycock, T., Waterfield, O., Yelekci, R., Zhou, Y., & Zhou, B. (2021). IPCC, 2021: Climate Change 2021: The Physical Science Basis. Contribution of Working Group I to the Sixth Assessment Report of the Intergovernmental Panel on Climate Change. *Cambridge University Press*.
- Matthews, T., Hodgkins, R., Guðmundsson, S., Pálsson, F., & Björnsson, H. (2015). Inter-decadal variability in potential glacier surface melt energy at Vestari Hagafellsjökull (Langjökull, Iceland) and the role of synoptic circulation. *International Journal of Climatology*, 35(10), 3041-3057.
- McCrystall, M. R., Stroeve, J., Serreze, M., Forbes, B. C., & Screen, J. A. (2021). New climate models reveal faster and larger increases in Arctic precipitation than previously projected. *Nat Commun*, 12(1), 1-12.

## References Cited

- McDonagh, E. L., Allen, J., Bacon, S., & Holliday, N. P. (2009). Circulation and Transport in the Western Boundary Currents at Cape Farewell, Greenland. *Journal of Physical Oceanography*, 39(8), 1854-1870.
- McLeod, J. T., & Mote, T. L. (2015). Assessing the role of precursor cyclones on the formation of extreme Greenland blocking episodes and their impact on summer melting across the Greenland ice sheet. *Journal of Geophysical Research: Atmospheres*, 120(24), 12357-12377.
- McLeod, J. T., & Mote, T. L. (2016). Linking interannual variability in extreme Greenland blocking episodes to the recent increase in summer melting across the Greenland ice sheet. *International Journal of Climatology*, 36(3), 1484-1499.
- McMillan, M., Leeson, A., Shepherd, A., Briggs, K., Armitage, T. W. K., Hogg, A., Kuipers Munneke, P., van den Broeke, M., Noël, B., van de Berg, W. J., Ligtenberg, S., Horwath, M., Groh, A., Muir, A., & Gilbert, L. (2016). A high-resolution record of Greenland mass balance. *Geophysical Research Letters*, 43(13), 7002-7010.
- Meleshko, V. P., Johannessen, O. M., Baidin, A. V., Pavlova, T. V., & Govorkova, V. A. (2016). Arctic amplification: does it impact the polar jet stream? *Tellus A: Dynamic Meteorology and Oceanography*, 68(1), 32330-32342.
- Melkonian, A. K., Willis, M. J., & Pritchard, M. E. (2014). Satellite-derived volume loss rates and glacier speeds for the Juneau Icefield, Alaska. *Journal of Glaciology*, 60(222), 743-760.
- Mesquita, M. D. S., Gunnar Kvamstø, N., Sorteberg, A., & Atkinson, D. E. (2008). Climatological properties of summertime extra-tropical storm tracks in the Northern Hemisphere. *Tellus A*, 60(3), 557-569.
- Mitasova, H., Hofierka, J., Zlocha, M., & Iverson, L. R. (1996). Modelling topographic potential for erosion and deposition using GIS. *International journal of geographical information systems*, 10(5), 629-641.
- Mohajerani, Y. (2019). *Understanding Regional Ice Sheet Mass Balance: Remote Sensing, Regional Climate Models, and Deep Learning*. UC Irvine.
- Mohr, S., Wandel, J., Lenggenhager, S., & Martius, O. (2019). Relationship between atmospheric blocking and warm-season thunderstorms over western and central Europe. *Quarterly Journal of the Royal Meteorological Society*, 145(724), 3040-3056.
- Mosley-Thompson, E., Readinger, C. R., Craigmile, P., Thompson, L. G., & Calder, C. A. (2005). Regional sensitivity of Greenland precipitation to NAO variability. *Geophysical Research Letters*, 32(24), L24707. 24701-L24707. 24704.

## References Cited

- Mote, T. L. (1997). Mid-tropospheric circulation and surface melt on the Greenland ice sheet. Part II synoptic climatology. *International Journal of Climatology*, 18(2), 111-129.
- Mottram, R., Boberg, F., Langen, P., Yang, S., Rodehacke, C., Christensen, J. H., & Madsen, M. S. (2017). Surface mass balance of the Greenland ice sheet in the regional climate model HIRHAM5: Present state and future prospects. *低温科学= Low Temperature Science*, 75, 105-115.
- Motyka, R. J., Cassotto, R., Truffer, M., Kjeldsen, K. K., Van As, D., Korsgaard, N. J., Fahnestock, M., Howat, I. A. N., Langen, P. L., Mortensen, J., Lennert, K., & Rysgaard, S. (2017). Asynchronous behavior of outlet glaciers feeding Godthåbsfjord (Nuup Kangerlua) and the triggering of Narsap Sermia's retreat in SW Greenland. *Journal of Glaciology*, 63(238), 288-308.
- Mouginot, J., & Rignot, E. (2019). Glacier catchments/basins for the Greenland Ice Sheet. *UC Irvine Dash: Irvine, CA, USA*.
- Mouginot, J., Rignot, E., Bjork, A. A., van den Broeke, M., Millan, R., Morlighem, M., Noel, B., Scheuchl, B., & Wood, M. (2019). Forty-six years of Greenland Ice Sheet mass balance from 1972 to 2018. *Proc Natl Acad Sci U S A*, 116(19), 9239-9244.
- Nick, F. M., Vieli, A., Andersen, M. L., Joughin, I., Payne, A., Edwards, T. L., Pattyn, F., & van de Wal, R. S. (2013). Future sea-level rise from Greenland's main outlet glaciers in a warming climate. *Nature*, 497(7448), 235-238.
- Nielsen, J. W., & Randall, M. D. (1991). A survey of Extratropical Cyclone Characteristics during GALE. *Monthly Weather Review*, 120, 1156-1166.
- Nienow, P. W., Sole, A. J., Slater, D. A., & Cowton, T. R. (2017). Recent Advances in Our Understanding of the Role of Meltwater in the Greenland Ice Sheet System. *Current Climate Change Reports*, 3(4), 330-344.
- Niwano, M., Box, J. E., Wehrlé, A., Vandecrux, B., Colgan, W. T., & Cappelen, J. (2021). Rainfall on the Greenland Ice Sheet: Present-Day Climatology From a High-Resolution Non-Hydrostatic Polar Regional Climate Model. *Geophysical Research Letters*, 48(15), e2021GL092942.
- Noël, B., van de Berg, W. J., van Meijgaard, E., Kuipers Munneke, P., van de Wal, R. S. W., & van den Broeke, M. R. (2015). Evaluation of the updated regional climate model RACMO2.3: summer snowfall impact on the Greenland Ice Sheet. *The Cryosphere*, 9(5), 1831-1844.

## References Cited

- Nuth, C., Kohler, J., König, M., Deschwanden, A. v., Hagen, J., Kääb, A., Moholdt, G., & Pettersson, R. (2013). Decadal changes from a multi-temporal glacier inventory of Svalbard. *The Cryosphere*, 7(5), 1603-1621.
- Oerlemans, J. (1997). A flowline model for Nigardsbreen, Norway: projection of future glacier length based on dynamic calibration with the historic record. *Annals of Glaciology*, 24, 382-389.
- Ohmura, A. (1999). Precipitation, accumulation and mass balance of the Greenland Ice Sheet. *Zeitschrift für Gletscherkunde und Glazialgeologie*, 35, 1-20.
- Oltmanns, M., Straneo, F., & Tedesco, M. (2019). Increased Greenland melt triggered by large-scale, year-round cyclonic moisture intrusions. *The Cryosphere*, 13(3), 815-825.
- Orsi, A. J., Kawamura, K., Masson-Delmotte, V., Fettweis, X., Box, J. E., Dahl-Jensen, D., Clow, G. D., Landais, A., & Severinghaus, J. P. (2017). The recent warming trend in North Greenland. *Geophysical Research Letters*, 44(12), 6235-6243.
- Overland, J. E., Francis, J. A., Hanna, E., & Wang, M. (2012). The recent shift in early summer Arctic atmospheric circulation. *Geophysical Research Letters*, 39(19), L19804-L19810.
- Pauluis, O., Czaja, A., & Korty, R. (2008). The global atmospheric circulation on moist isentropes. *Science*, 321(5892), 1075-1078.
- Pauluis, O., Czaja, A., & Korty, R. (2010). The global atmospheric circulation in moist isentropic coordinates. *Journal of climate*, 23(11), 3077-3093.
- Pena-Ortiz, C., Gallego, D., Ribera, P., Ordonez, P., & Alvarez-Castro, M. D. C. (2013). Observed trends in the global jet stream characteristics during the second half of the 20th century. *Journal of Geophysical Research: Atmospheres*, 118(7), 2702-2713.
- Placidi, L., Hutter, K., & Faria, S. H. (2006). A Critical Review of the Mechanics of Polycrystalline Polar Ice. *GAMM-Mitteilungen*, 29(1), 80-117.
- Pohjola, V. A., & Rogers, J. C. (1997). Coupling between the atmospheric circulation and extremes of the mass balance of Storglaciären northern Scandinavia. *Annals of Glaciology*, 24, 229-233.
- Polar\_Portal. (2021). Polar\_Portal season 2020 report.
- Price, S. F., Payne, A. J., Howat, I. M., & Smith, B. E. (2011). Committed sea-level rise for the next century from Greenland ice sheet dynamics during the past decade. *Proc Natl Acad Sci U S A*, 108(22), 8978-8983.

## References Cited

- Priestley, M. D., & Catto, J. L. (2022). Future changes in the extratropical storm tracks and cyclone intensity, wind speed, and structure. *Weather and Climate Dynamics*, 3(1), 337-360.
- Pritchard, H. D., Arthern, R. J., Vaughan, D. G., & Edwards, L. A. (2009). Extensive dynamic thinning on the margins of the Greenland and Antarctic ice sheets. *Nature*, 461(7266), 971-975.
- Rae, J. G. L., Aðalgeirsdóttir, G., Edwards, T. L., Fettweis, X., Gregory, J. M., Hewitt, H. T., Lowe, J. A., Lucas-Picher, P., Mottram, R. H., Payne, A. J., Ridley, J. K., Shannon, S. R., van de Berg, W. J., van de Wal, R. S. W., & van den Broeke, M. R. (2012). Greenland ice sheet surface mass balance: evaluating simulations and making projections with regional climate models. *The Cryosphere*, 6(6), 1275-1294.
- Rahmstorf, S. (2003). Thermohaline circulation: The current climate. *Nature*, 421(6924), 699-699.
- Raible, C. C., Yoshimori, M., Stocker, T. F., & Casty, C. (2007). Extreme midlatitude cyclones and their implications for precipitation and wind speed extremes in simulations of the Maunder Minimum versus present day conditions. [journal article]. *Climate Dynamics*, 28(4), 409-423.
- Rao, Y. S. (2011). Synthetic Aperture Radar (SAR) Interferometry for Glacier Movement Studies. In V. P. Singh, P. Singh & U. K. Haritashya (Eds.), *Encyclopedia of Snow, Ice and Glaciers* (pp. 1133-1142). Dordrecht: Springer Netherlands.
- Reijmer, C. H., van den Broeke, M. R., Fettweis, X., Ettema, J., & Stap, L. B. (2012). Refreezing on the Greenland ice sheet: a comparison of parameterizations. *The Cryosphere*, 6(4), 743-762.
- Rennermalm, A. K., Smith, L. C., Stroeve, J. C., & Chu, V. W. (2009). Does sea ice influence Greenland ice sheet surface-melt? *Environmental Research Letters*, 4(2), 024011.
- Rignot, E., & Kanagaratnam, P. (2006). Changes in the Velocity Structure of the Greenland Ice Sheet. *Science*, 311(5763), 986-990.
- Rinke, A., Dethloff, K., Dorn, W., Handorf, D., & Moore, J. C. (2013). Simulated Arctic atmospheric feedbacks associated with late summer sea ice anomalies. *Journal of Geophysical Research: Atmospheres*, 118(14), 7698-7714.
- Rinke, A., Maturilli, M., Graham, R. M., Matthes, H., Handorf, D., Cohen, L., Hudson, S. R., & Moore, J. C. (2017). Extreme cyclone events in the Arctic: Wintertime variability and trends. *Environmental Research Letters*, 12(9), 094006.

## References Cited

- Rogers, J. C., Bathke, D. J., Mosley-Thompson, E., & Wang, S.-H. (2004). Atmospheric circulation and cyclone frequency variations linked to the primary modes of Greenland snow accumulation. *Geophysical Research Letters*, *31*(23), L23208.
- Rosenau, R., Scheinert, M., & Dietrich, R. (2015). A processing system to monitor Greenland outlet glacier velocity variations at decadal and seasonal time scales utilizing the Landsat imagery. *Remote Sensing of Environment*, *169*, 1-19.
- Rudeva, I., & Gulev, S. K. (2007). Climatology of Cyclone Size Characteristics and Their Changes during the Cyclone Life Cycle. *Monthly Weather Review*, *135*(7), 2568-2587.
- Russo, S., Dosio, A., Graversen, R. G., Sillmann, J., Carrao, H., Dunbar, M. B., Singleton, A., Montagna, P., Barbola, P., & Vogt, J. V. (2014). Magnitude of extreme heat waves in present climate and their projection in a warming world. *Journal of Geophysical Research: Atmospheres*, *119*(22), 12,500-512,512.
- Sasgen, I., van den Broeke, M., Bamber, J. L., Rignot, E., Sørensen, L. S., Wouters, B., Martinec, Z., Velicogna, I., & Simonsen, S. B. (2012). Timing and origin of recent regional ice-mass loss in Greenland. *Earth and Planetary Science Letters*, *333*, 293-303.
- Scambos, T., Fahnestock, M., Moon, T., Gardner, A., & Klinger, M. (2016). Global Land Ice Velocity Extraction from Landsat 8 (GoLIVE), Version 1[May 2013 to January 2016]. Boulder, Colorado USA. NSIDC: National Snow and Ice Data Center [Accessed October 18, 2020.].
- Schneider, T., O'Gorman, P. A., & Levine, X. J. (2010). Water Vapor and the Dynamics of Climate Changes. *Reviews of Geophysics*, *48*(3), RG3001.
- Schneiderreit, A., Blender, R., Fraedrich, K., & Lunkeit, F. (2007). Icelandic climate and North Atlantic cyclones in ERA-40 reanalyses. *Meteorologische Zeitschrift*, *16*, 17-23.
- Schoof, C. (2010). Ice-sheet acceleration driven by melt supply variability. *Nature*, *468*(7325), 803-806.
- Schuenemann, K. C., & Cassano, J. J. (2010). Changes in synoptic weather patterns and Greenland precipitation in the 20th and 21st centuries: 2. Analysis of 21st century atmospheric changes using self-organizing maps. *Journal of Geophysical Research*, *115*(D5), D05108.
- Schuenemann, K. C., Cassano, J. J., & Finniss, J. (2009). Synoptic Forcing of Precipitation over Greenland: Climatology for 1961–99. *Journal of Hydrometeorology*, *10*(1), 60-78.

## References Cited

- Seale, A., Christoffersen, P., Mugford, R. I., & O'Leary, M. (2011). Ocean forcing of the Greenland Ice Sheet: Calving fronts and patterns of retreat identified by automatic satellite monitoring of eastern outlet glaciers. *Journal of Geophysical Research: Earth Surface*, *116*(F3), F03013.
- Sepp, M., & Jaagus, J. (2011). Changes in the activity and tracks of Arctic cyclones. [journal article]. *Climatic Change*, *105*(3), 577-595.
- Serreze, M. C. (1995). Climatological aspects of cyclone development and decay in the Arctic. *Atmosphere-Ocean*, *33*(1), 1-23.
- Serreze, M. C. (2016). Northern Hemisphere Cyclone Locations and Characteristics from NCEP/NCAR Reanalysis Data. In M. C. Serreze (Ed.). Digital Media, Natl. Snow and Ice Data Cent, Boulder, Colorado.
- Serreze, M. C., & Barrett, A. P. (2008). The Summer Cyclone Maximum over the Central Arctic Ocean. *Journal of Climate*, *21*(5), 1048-1065.
- Serreze, M. C., Carse, F., Barry, R. G., & Rogers, J. C. (1997). Icelandic low cyclone activity: Climatological features, linkages with the NAO, and relationships with recent changes in the Northern Hemisphere circulation. *Journal of Climate*, *American Meteorological Society*, *10*(3), 453-464.
- Simmonds, I., & Keay, K. (2001). Surface fluxes of momentum and mechanical energy over the North Pacific and North Atlantic Oceans. *Meteorology and Atmospheric Physics*, *80*, 1-18.
- Slater, D. A., Goldberg, D. N., Nienow, P. W., & Cowton, T. R. (2016). Scalings for submarine melting at tidewater glaciers from buoyant plume theory. *Journal of Physical Oceanography*, *46*(6), 1839-1855.
- Slater, D. A., Straneo, F., Das, S. B., Richards, C. G., Wagner, T. J. W., & Nienow, P. W. (2018). Localized Plumes Drive Front-Wide Ocean Melting of A Greenlandic Tidewater Glacier. *Geophysical Research Letters*, *45*(22), 12,350-312,358.
- Slater, T., Lawrence, I. R., Otosaka, I. N., Shepherd, A., Gourmelen, N., Jakob, L., Tepes, P., Gilbert, L., & Nienow, P. (2021). Review article: Earth's ice imbalance. *The Cryosphere*, *15*(1), 233-246.
- Sodemann, H., Schwierz, C., & Wernli, H. (2008). Interannual variability of Greenland winter precipitation sources: Lagrangian moisture diagnostic and North Atlantic Oscillation influence. *Journal of Geophysical Research*, *113*(D3), D03107.

## References Cited

- Sole, A., Nienow, P., Bartholomew, I., Mair, D., Cowton, T., Tedstone, A., & King, M. A. (2013). Winter motion mediates dynamic response of the Greenland Ice Sheet to warmer summers. *Geophysical Research Letters*, *40*(15), 3940-3944.
- Solgaard, A., Kusk, A., Merryman Boncori, J. P., Dall, J., Mankoff, K. D., Ahlstrøm, A. P., Andersen, S. B., Citterio, M., Karlsson, N. B., & Kjeldsen, K. K. (2021). Greenland ice velocity maps from the PROMICE project. *Earth System Science Data*, *13*(7), 3491-3512.
- Sorteberg, A., & Walsh, J. E. (2008). Seasonal cyclone variability at 70°N and its impact on moisture transport into the Arctic. *Tellus A*, *60*(3), 570-586.
- Spinoni, J., Vogt, J. V., Naumann, G., Barbosa, P., & Dosio, A. (2018). Will drought events become more frequent and severe in Europe? *International Journal of Climatology*, *38*(4), 1718-1736.
- Stachnik, J. P., & Schumacher, C. (2011). A comparison of the Hadley circulation in modern reanalyses. *Journal of Geophysical Research: Atmospheres*, *116*(D22).
- Stendel, M. (2019). Polar Portal *Danish Meteorological Insitute*, Available from: <http://polarportal.dk/en/greenland/surface-conditions/>
- Straneo, F., Heimbach, P., Sergienko, O., Hamilton, G., Catania, G., Griffies, S., Hallberg, R., Jenkins, A., Joughin, I., Motyka, R., Pfeffer, W. T., Price, S. F., Rignot, E., Scambos, T., Truffer, M., & Vieli, A. (2013). Challenges to Understanding the Dynamic Response of Greenland's Marine Terminating Glaciers to Oceanic and Atmospheric Forcing. *Bulletin of the American Meteorological Society*, *94*(8), 1131-1144.
- Strigaro, D., Moretti, M., Mattavelli, M., Frigerio, I., Amicis, M. D., & Maggi, V. (2016). A GRASS GIS module to obtain an estimation of glacier behavior under climate change: A pilot study on Italian glacier. *Computers & Geosciences*, *94*, 68-76.
- Stroeve, J., Box, J. E., Wang, Z., Schaaf, C., & Barrett, A. (2013). Re-evaluation of MODIS MCD43 Greenland albedo accuracy and trends. *Remote Sensing of Environment*, *138*, 199-214.
- Sundal, A. V., Shepherd, A., Nienow, P., Hanna, E., Palmer, S., & Huybrechts, P. (2011). Melt-induced speed-up of Greenland ice sheet offset by efficient subglacial drainage. *Nature*, *469*(7331), 521-524.
- Tao, L., Hu, Y., & Liu, J. (2015). Anthropogenic forcing on the Hadley circulation in CMIP5 simulations. *Climate Dynamics*, *46*(9-10), 3337-3350.

## References Cited

- Tedesco, M., Box, J., Cappelen, J., Fausto, R., Fettweis, X., Hansen, K., Mote, T., Smeets, C., van As, D., & van de Wal, R. (2015). Arctic Report Card Greenland Ice Sheet. *Tech. Rep. 1, Update for 2015*.
- Tedesco, M., & Fettweis, X. (2012). 21st century projections of surface mass balance changes for major drainage systems of the Greenland ice sheet. *Environmental Research Letters*, 7(4), 045405.
- Tedesco, M., & Fettweis, X. (2020). Unprecedented atmospheric conditions (1948-;2019) drive the 2019 exceptional melting season over the Greenland ice sheet. *The Cryosphere*, 14(4), 1209-1223.
- Tedstone, A. J., Nienow, P. W., Gourmelen, N., Dehecq, A., Goldberg, D., & Hanna, E. (2015). Decadal slowdown of a land-terminating sector of the Greenland Ice Sheet despite warming. *Nature*, 526(7575), 692-695.
- Tedstone, A. J., Nienow, P. W., Sole, A. J., Mair, D. W., Cowton, T. R., Bartholomew, I. D., & King, M. A. (2013). Greenland ice sheet motion insensitive to exceptional meltwater forcing. *Proc Natl Acad Sci U S A*, 110(49), 19719-19724.
- Toyokuni, G., Takenaka, H., Takagi, R., Kanao, M., Tsuboi, S., Tono, Y., Childs, D., & Zhao, D. (2018). Changes in Greenland ice bed conditions inferred from seismology. *Physics of the Earth and Planetary Interiors*, 277, 81-98.
- Trenberth, K. E., & Caron, J. M. (2001). Estimates of Meridional Atmosphere and Ocean Heat Transports. *Journal of Climate*, 14(16), 3433-3443.
- Truffer, M., & Motyka, R. J. (2016). Where glaciers meet water: Subaqueous melt and its relevance to glaciers in various settings. *Reviews of Geophysics*, 54(1), 220-239.
- Trüssel, B. L., Motyka, R. J., Truffer, M., & Larsen, C. F. (2013). Rapid thinning of lake-calving Yakutat Glacier and the collapse of the Yakutat Icefield, southeast Alaska, USA. *Journal of Glaciology*, 59(213), 149-161.
- Ulbrich, U., Leckebusch, G. C., & Pinto, J. G. (2009). Extra-tropical cyclones in the present and future climate: a review. *Theoretical and Applied Climatology*, 96(1-2), 117-131.
- Valkonen, E., Cassano, J., & Cassano, E. (2021). Arctic Cyclones and Their Interactions With the Declining Sea Ice: A Recent Climatology. *Journal of Geophysical Research: Atmospheres*, 126(12).
- Van den Broeke, M., Box, J., Fettweis, X., Hanna, E., Noël, B., Tedesco, M., van As, D., van de Berg, W. J., & van Kampenhout, L. (2017). Greenland Ice Sheet Surface Mass Loss:

## References Cited

- Recent Developments in Observation and Modeling. *Current Climate Change Reports*, 3(4), 345-356.
- Van den Broeke, M., Smeets, P., & Ettema, J. (2009). Surface layer climate and turbulent exchange in the ablation zone of the west Greenland ice sheet. *International Journal of Climatology*, 29(15), 2309-2323.
- Van den Broeke, M., Smeets, P., Ettema, J., & Munneke, P. K. (2008). Surface radiation balance in the ablation zone of the west Greenland ice sheet. *Journal of Geophysical Research*, 113(D13), D13105.
- Van den Broeke, M. R., Enderlin, E. M., Howat, I. M., Kuipers Munneke, P., Noël, B. P. Y., van de Berg, W. J., van Meijgaard, E., & Wouters, B. (2016). On the recent contribution of the Greenland ice sheet to sea level change. *The Cryosphere*, 10(5), 1933-1946.
- van den Broeke, M. R., Smeets, C. J. P. P., & van de Wal, R. S. W. (2011). The seasonal cycle and interannual variability of surface energy balance and melt in the ablation zone of the west Greenland ice sheet. *The Cryosphere*, 5(2), 377-390.
- Van Tricht, K., Lhermitte, S., Lenaerts, J. T. M., Gorodetskaya, I. V., L'Ecuyer, T. S., Noël, B., van den Broeke, M. R., Turner, D. D., & van Lipzig, N. P. M. (2016). Clouds enhance Greenland ice sheet meltwater runoff. *Nature Communications*, 7(1), 1-9.
- Vernon, C. L., Bamber, J. L., Box, J. E., van den Broeke, M. R., Fettweis, X., Hanna, E., & Huybrechts, P. (2013). Surface mass balance model intercomparison for the Greenland ice sheet. *The Cryosphere*, 7(2), 599-614.
- Visbeck, M., Hurrell, J. W., Polvani, L., & Cullen, H. M. (2001). The North Atlantic Oscillation Past, present, and future. *Proceedings of the National Academy of Sciences*, 98(23), 12876-12877.
- Wallace, J. M., Lim, G.-H., & Blackmon, M. L. (1988). Relationship between cyclone tracks, anticyclone tracks and baroclinic waveguides. *Journal of the atmospheric sciences*, 45(3), 439-462.
- Walsh, J. E., Ballinger, T. J., Euskirchen, E. S., Hanna, E., Mård, J., Overland, J. E., Tangen, H., & Vihma, T. (2020). Extreme weather and climate events in northern areas: A review. *Earth-Science Reviews*, 103324.
- Walsh, J. E., Chapman, W. L., & Fetterer, F. (2015). Gridded Monthly Sea Ice Extent and Concentration, 1850 Onward, Version 1, Boulder, Colorado USA. NSIDC: National Snow and Ice Data Center. doi: <https://doi.org/10.7265/N5833PZ5>.

## References Cited

- Wang, X. L., Swail, V. R., & Zwiers, F. W. (2006). Climatology and Changes of Extratropical Cyclone Activity Comparison of ERA-40 with NCEP–NCAR Reanalysis for 1958–2001. *Journal of Climate*, *19*(13), 3145–3166.
- Wanner, H., Bronnimann, S., Casty, C., Gyalistras, D., Luterbacher, J., Schmutz, C., Stephenson, D. B., & Xoplaki, E. (2001). North Atlantic Oscillation – Concepts and Studies. *Survey in geophysics*, *22*(4), 321–381.
- Weertman, J. (1973). Can a water-filled crevasse reach the bottom surface of a glacier. *IASH publ*, *95*, 139–145.
- Werder, M. A., Hewitt, I. J., Schoof, C. G., & Flowers, G. E. (2013). Modeling channelized and distributed subglacial drainage in two dimensions. *Journal of Geophysical Research: Earth Surface*, *118*(4), 2140–2158.
- Williams, J. J., Gourmelen, N., & Nienow, P. (2020). Dynamic response of the Greenland ice sheet to recent cooling. *Sci Rep*, *10*(1), 1647.
- Woollings, T., Franzke, C., Hodson, D. L. R., Dong, B., Barnes, E. A., Raible, C. C., & Pinto, J. G. (2014). Contrasting interannual and multidecadal NAO variability. *Climate Dynamics*, *45*(1–2), 539–556.
- Xu, M., Yang, Q., Hu, X., Liang, K., & Vihma, T. (2022). Record-breaking rain falls at Greenland summit controlled by warm moist-air intrusion. *Environmental Research Letters*, *17*(4), 044061.
- Yarnal, B. (1984). Relationships between synoptic-scale atmospheric circulation and glacier mass balance in southwestern Canada during the international hydrological decade 1965–74. *Journal of Glaciology*, *30*(105), 188–198.
- Yin, J. H. (2005). A consistent poleward shift of the storm tracks in simulations of 21st century climate. *Geophysical Research Letters*, *32*(18), L18701.
- Zappa, G., Shaffrey, L. C., Hodges, K. I., Sansom, P. G., & Stephenson, D. B. (2013). A Multimodel Assessment of Future Projections of North Atlantic and European Extratropical Cyclones in the CMIP5 Climate Models. *Journal of Climate*, *26*(16), 5846–5862.
- Zhang, D., Yao, X., Duan, H., Liu, S., Guo, W., Sun, M., & Li, D. (2020). A new automatic approach for extracting glacier centerlines. *The Cryosphere Discussions*, *15*(4), 1–29.
- Zhang, X., Walsh, J. E., Zhang, J., Bhatt, U. S., & Ikeda, M. (2004). Climatology and Interannual Variability of Arctic Cyclone Activity 1948–2002. *Journal of Climate*, *17*(12), 2300–2317.

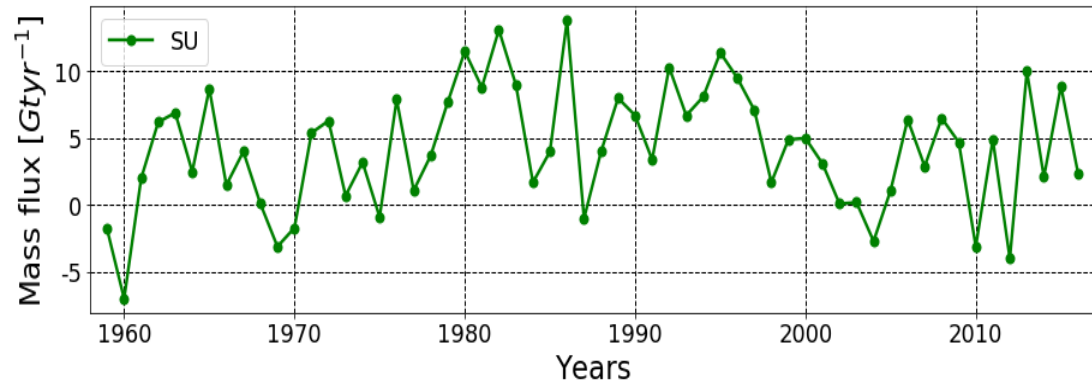
## References Cited

Zwally, H. J., Abdalati, W., Herring, T., Larson, K., Saba, J., & Steffen, K. (2002). Surface Melt-Induced Acceleration of Greenland Ice-Sheet Flow. *Science*, 297, 218-222.

## Appendix A

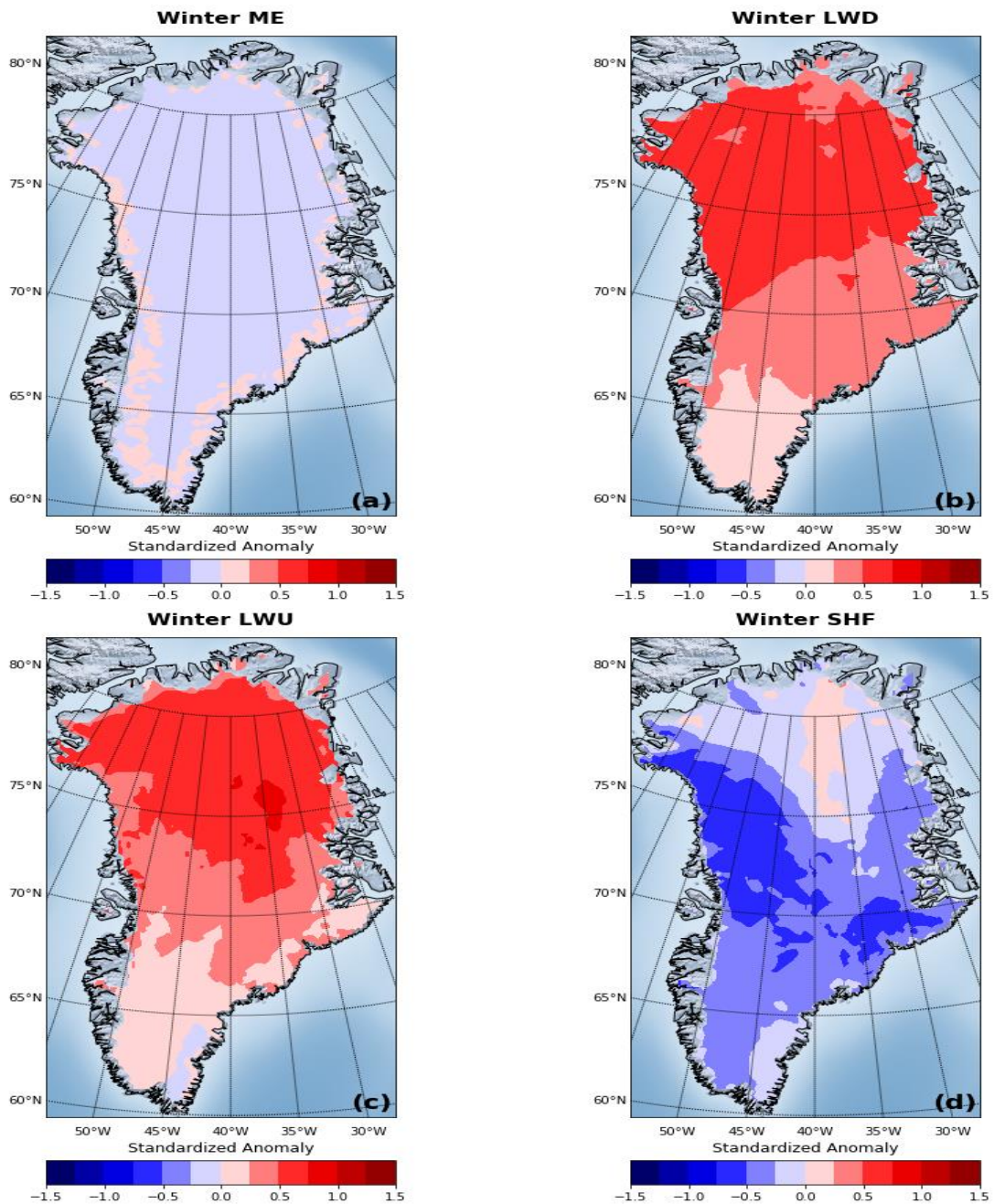
---

Annual values of the Sublimation (SU) integrated over the entire GrIS during glaciological years.

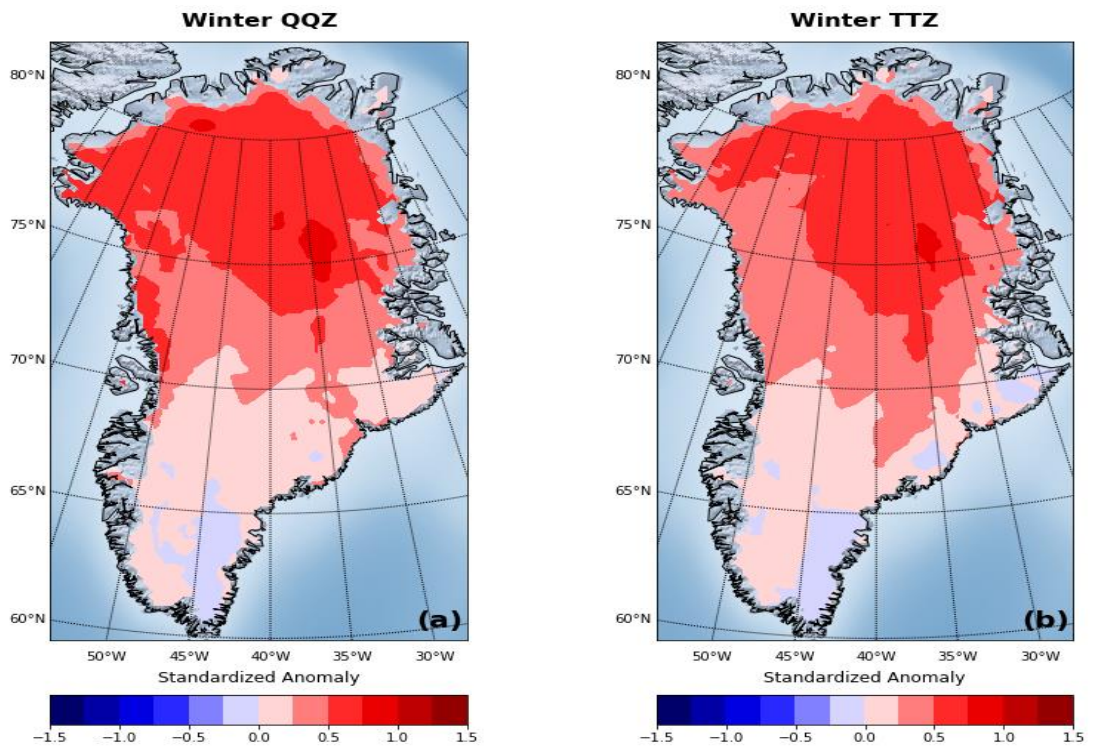


## Appendix B

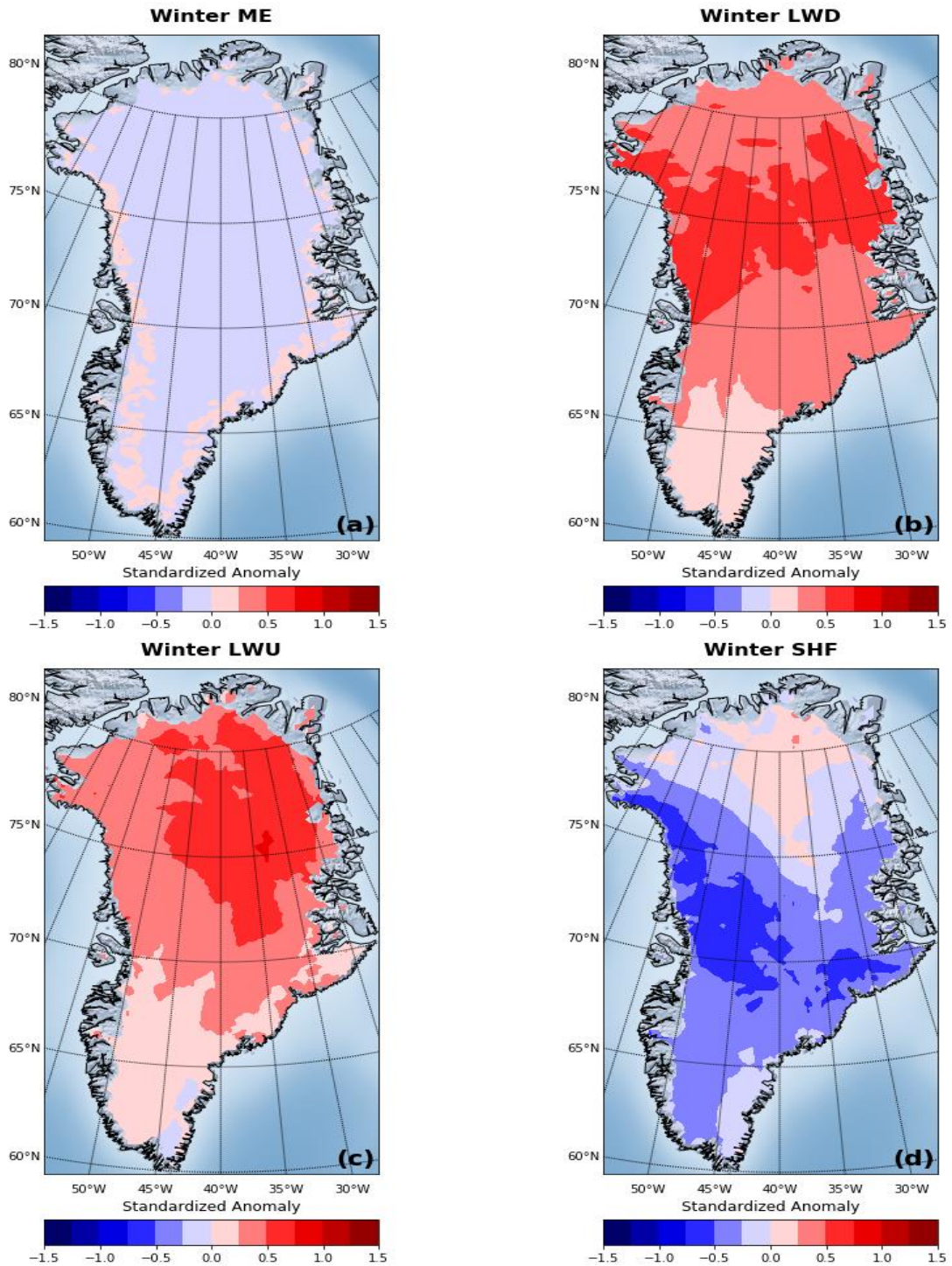
Spatial representation of the standardized anomalies over the entire GrIS of ME (a), LWD (b), LWU (c) and SHF (d). Value of each pixel is calculated by averaging all values in the form of standardized anomaly obtained whenever a cyclone of the 40 % most intense during the period 1958-2016 was within 750 km from that pixel in winter.



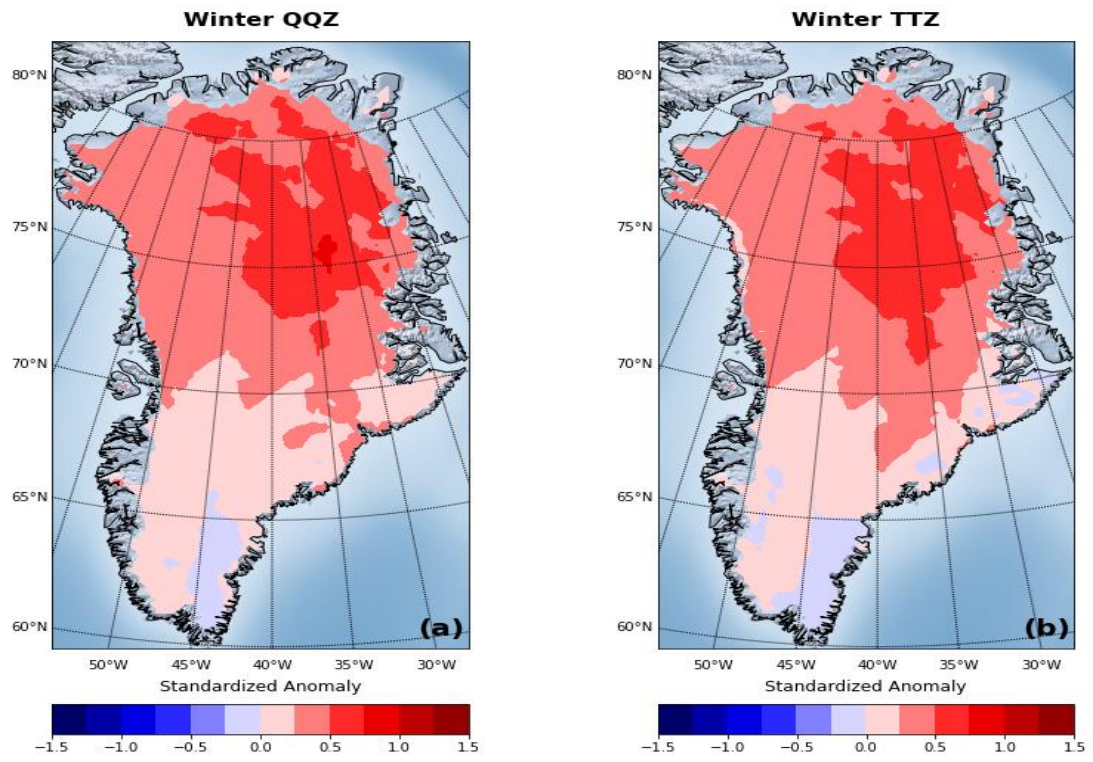
Same as above but for QQZ and TTZ



Spatial representation of the standardized anomalies over the entire GrIS of ME (a), LWD (b), LWU (c) and SHF (d). Value of each pixel is calculated by averaging all values in the form of standardized anomaly obtained whenever a cyclone of the 60 % most intense during the period 1958-2016 was within 750 km from that pixel in winter.

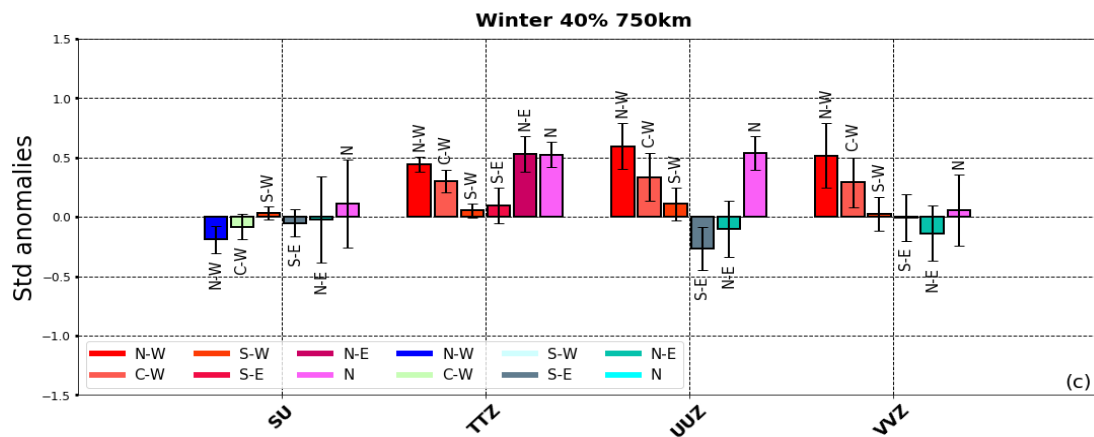
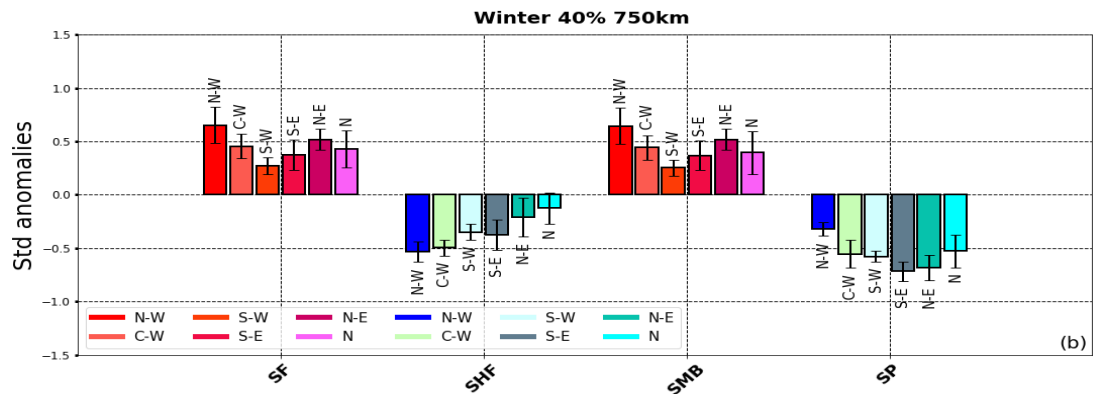
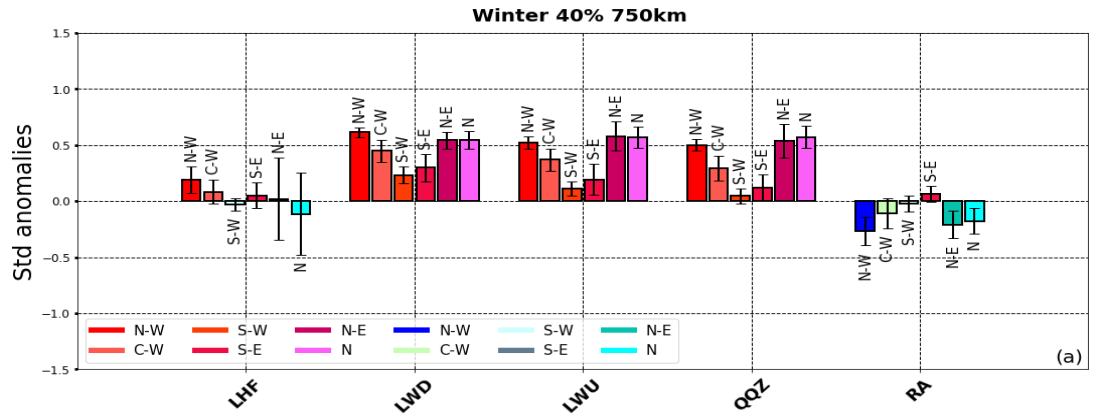


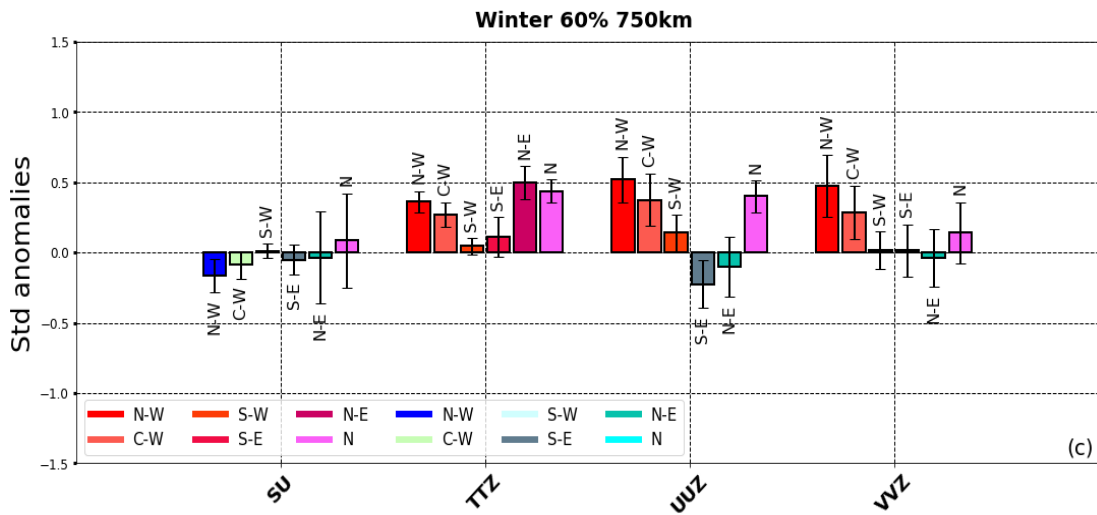
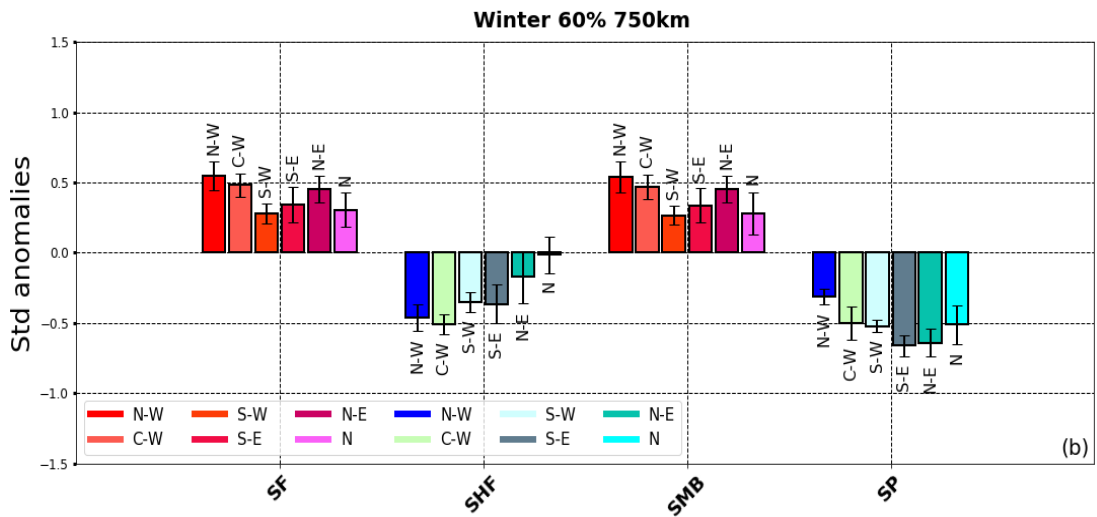
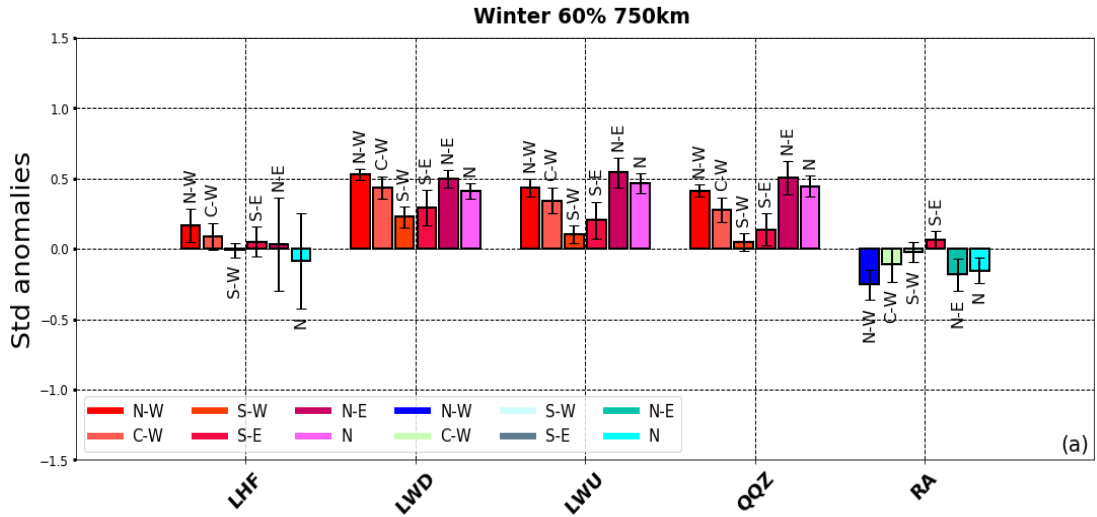
Same as above but for QQZ and TTZ



# Appendix C

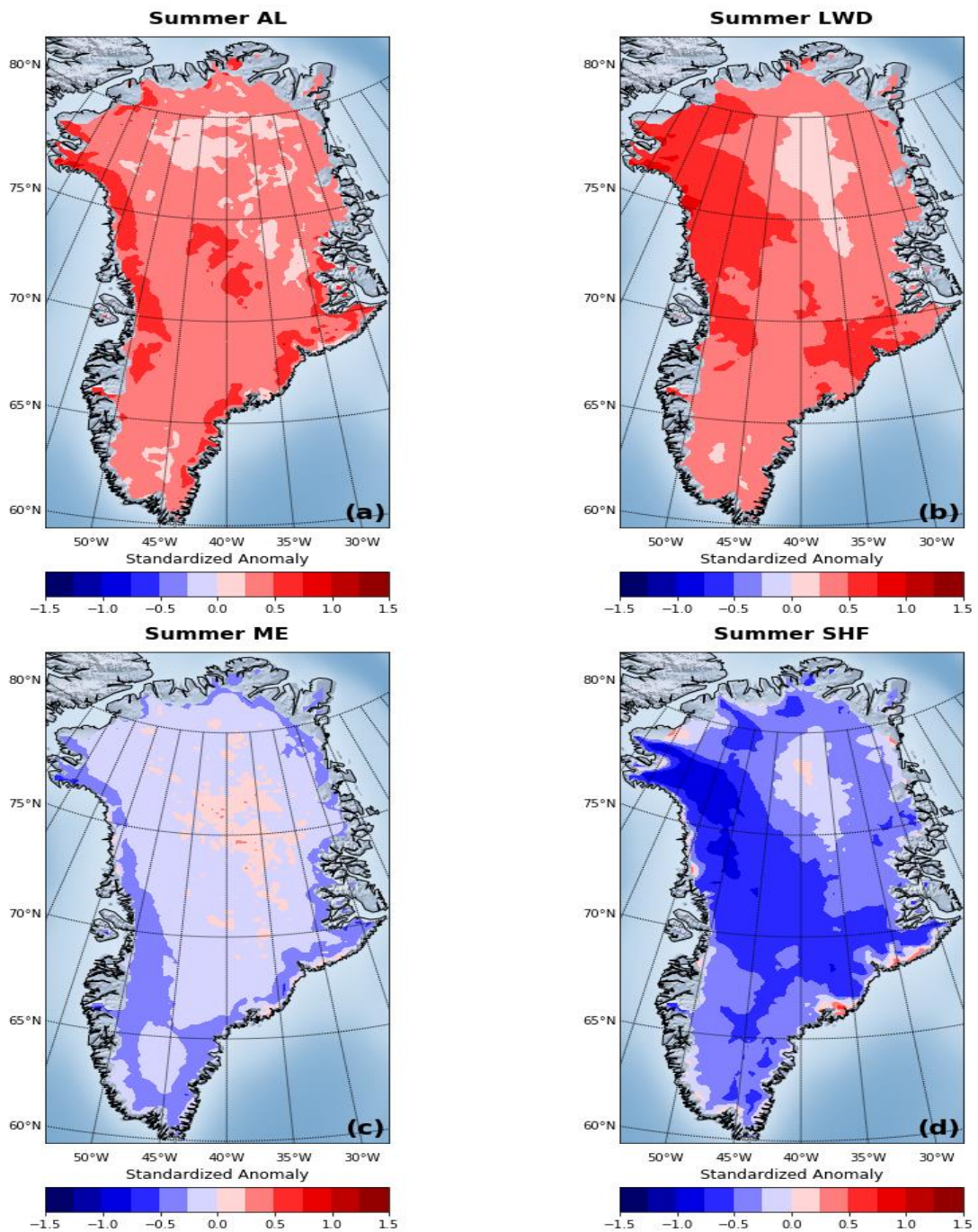
Standardized anomalies of SMB and SEB variables averaged over the six entire drainage basins. Value of each pixel is calculated by averaging all values in the form of standardized anomaly obtained whenever a cyclone of the 40 % and 60 % most intense during the period 1958-2016 was within 750 km from that pixel in winter.



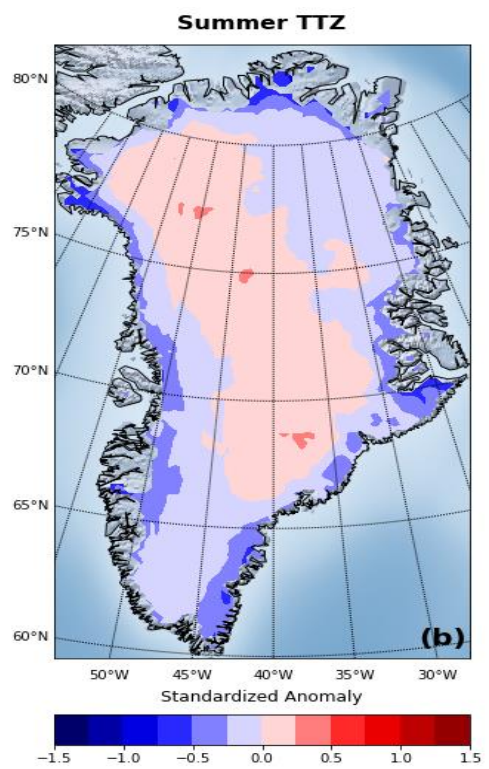
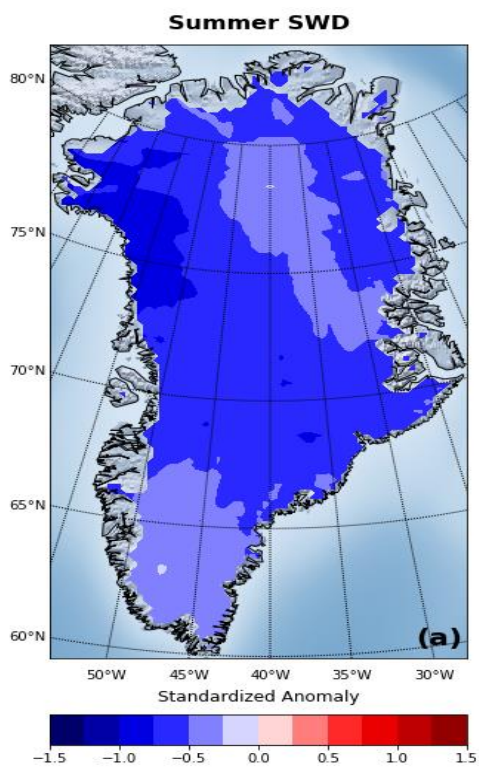


## Appendix D

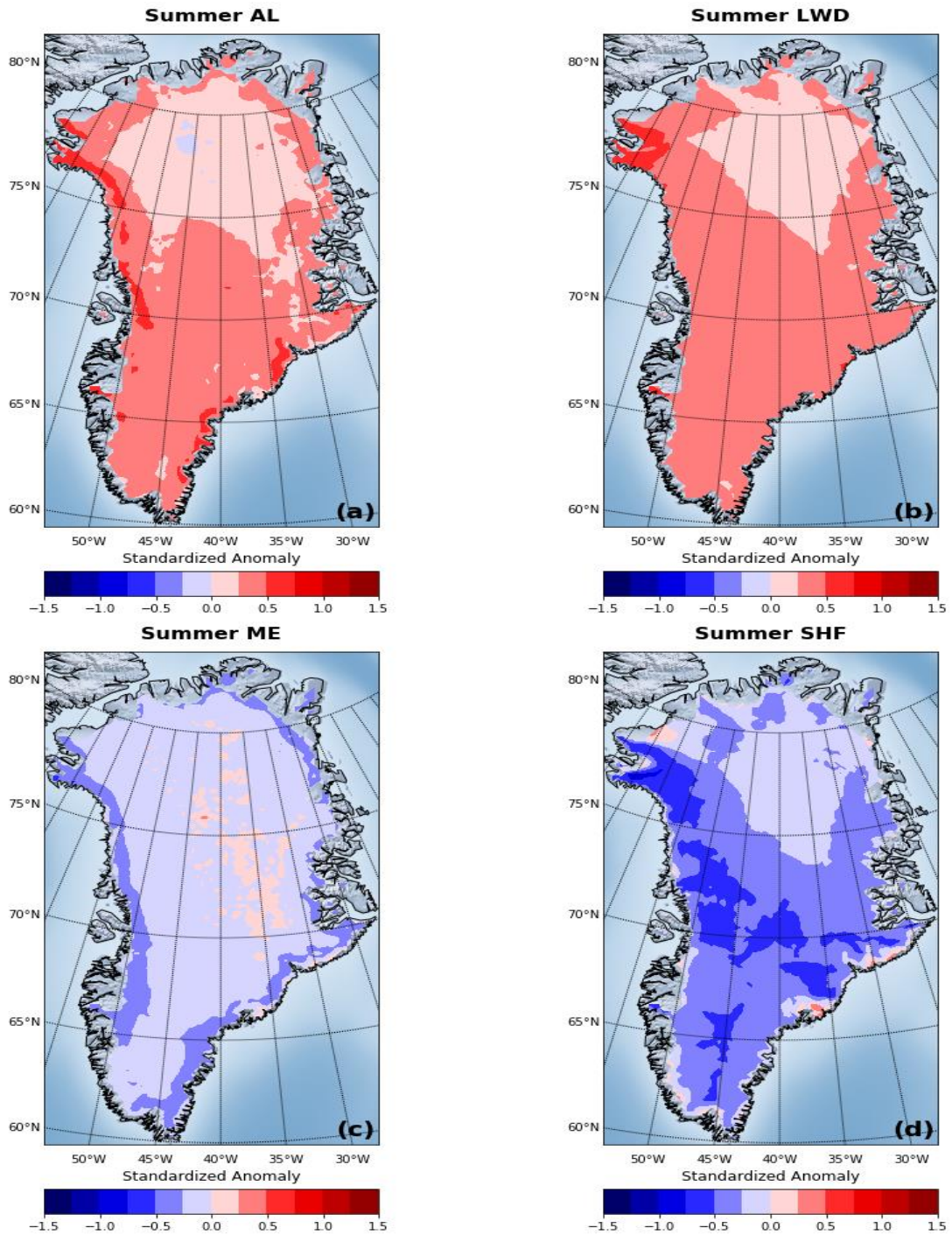
Spatial representation of the standardized anomalies over the entire GrIS of AL (a), LWD (b), ME (c) and SHF(d). Value of each pixel is calculated by averaging all values in the form of standardized anomaly obtained whenever a cyclone of the 40 % most intense during the period 1958-2016 was within 750 km from that pixel in summer.



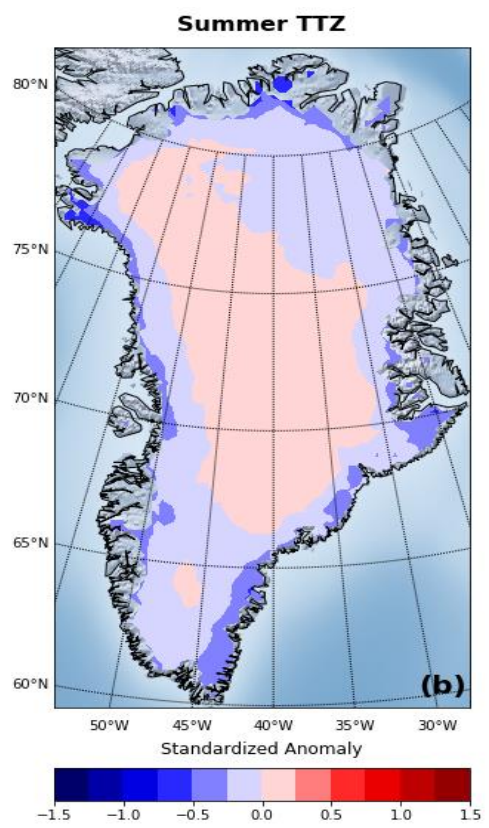
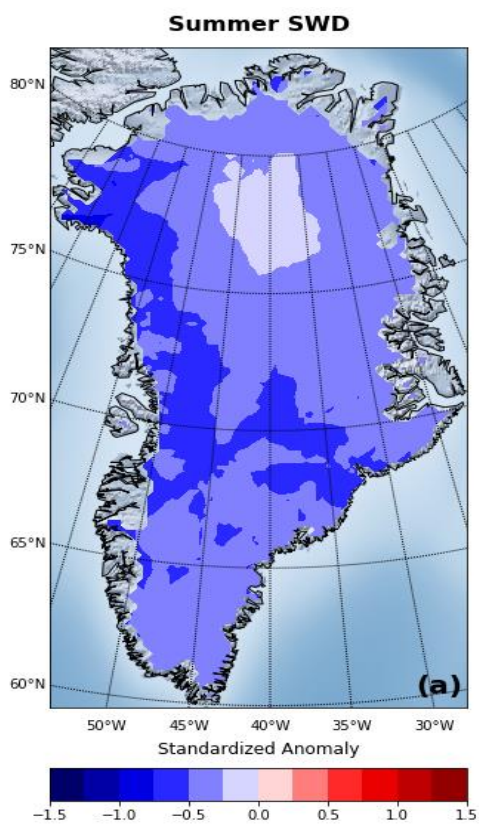
Same as above but for QQZ and TTZ



Spatial representation of the standardized anomalies over the entire GrIS of AL (a), LWD (b), ME (c) and SHF(d). Value of each pixel is calculated by averaging all values in the form of standardized anomaly obtained whenever a cyclone of the 60 % most intense during the period 1958-2016 was within 750 km from that pixel in summer.

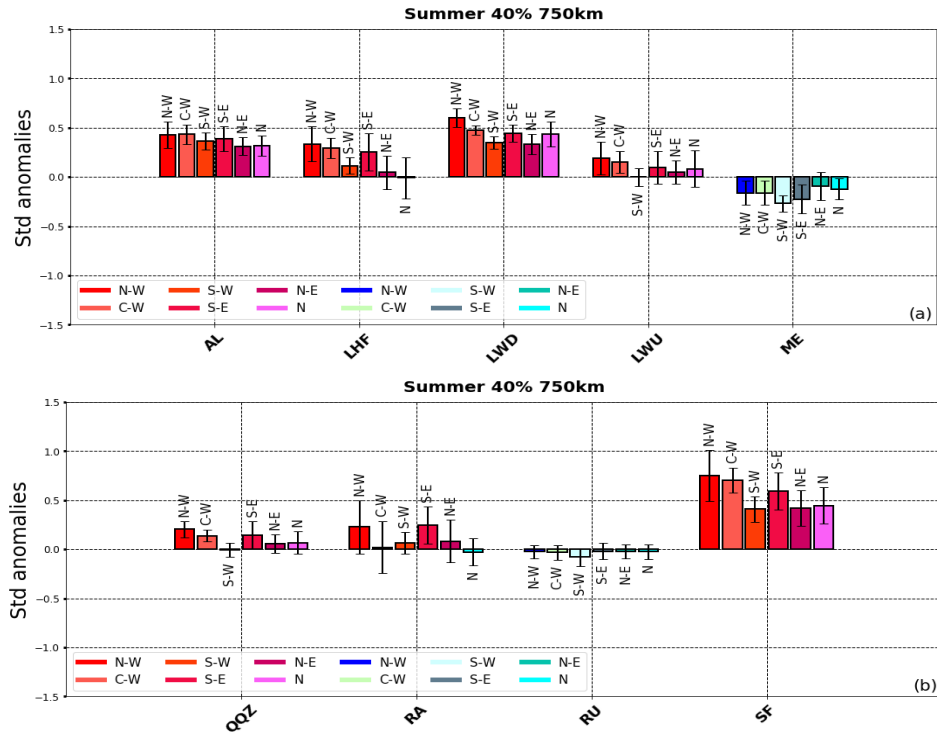


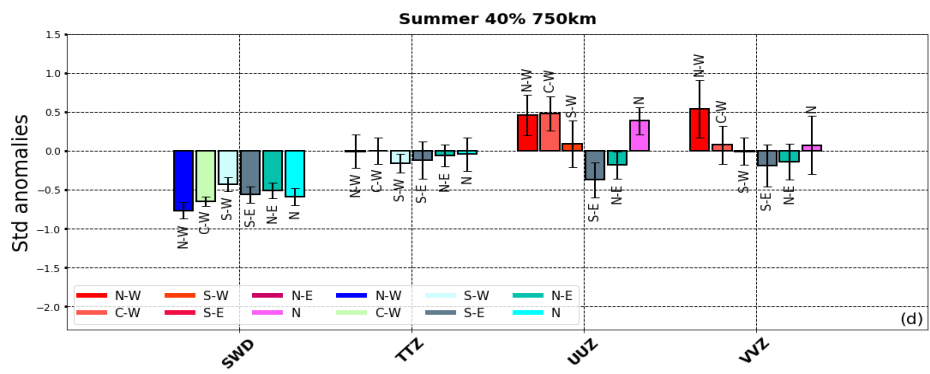
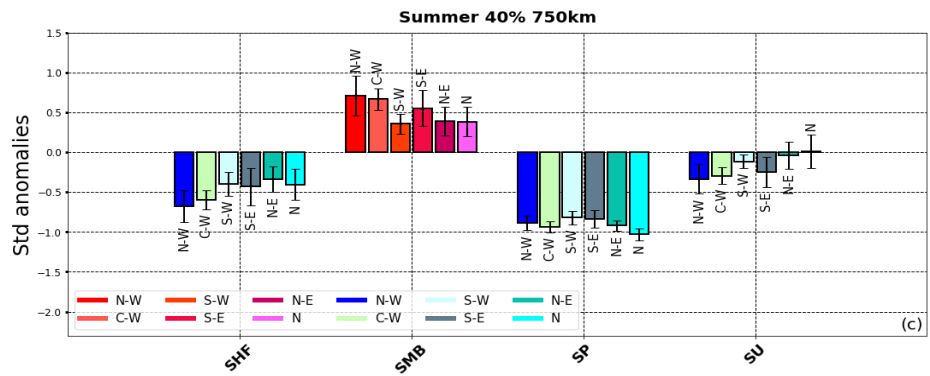
Same as above but for QQZ and TTZ

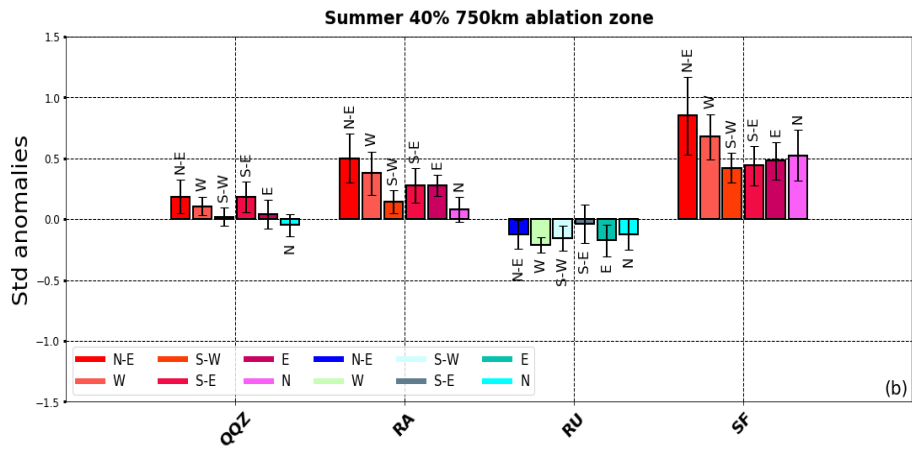
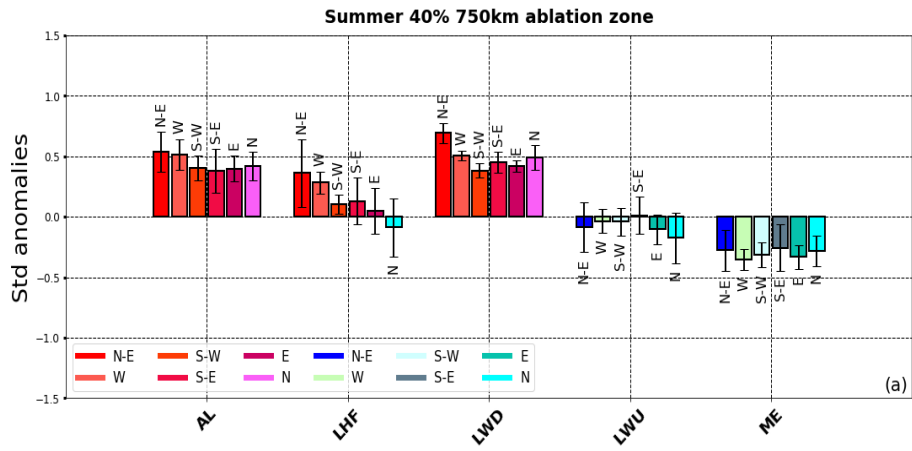


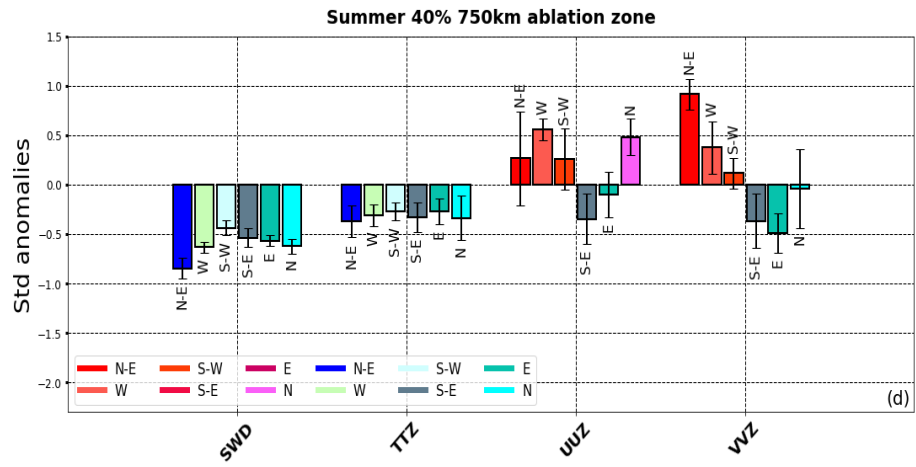
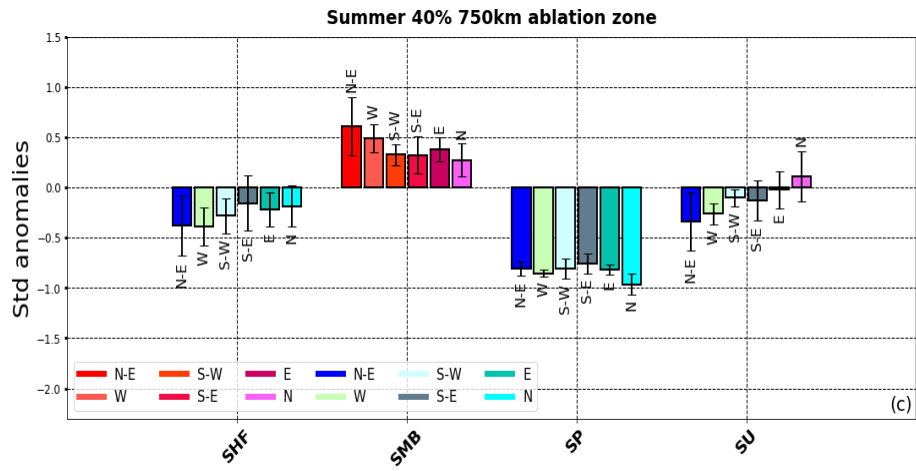
# Appendix E

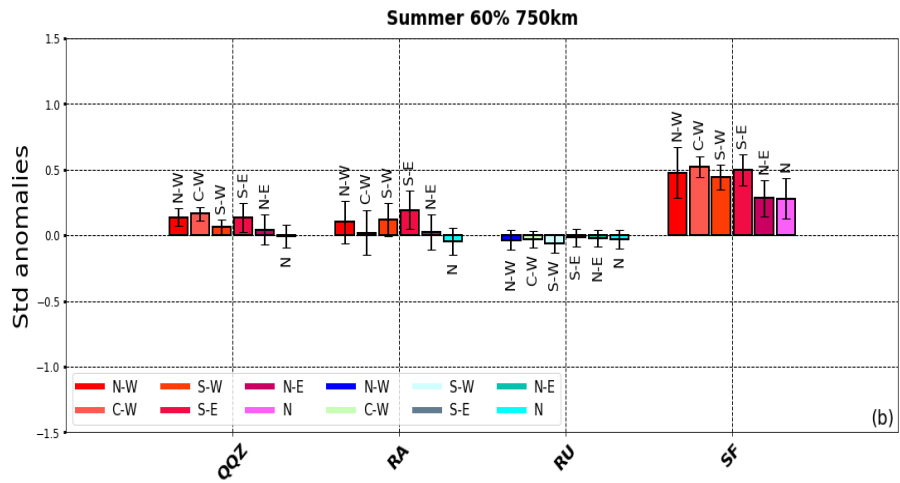
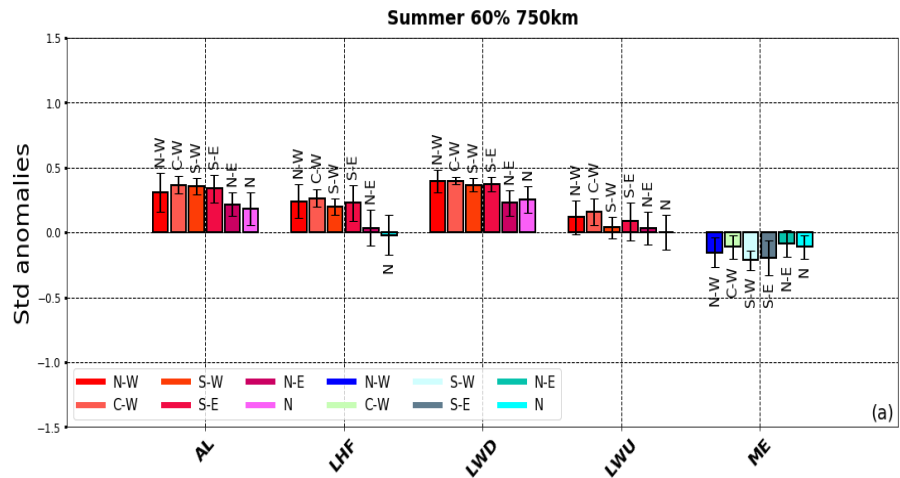
Standardized anomalies of SMB and SEB variables averaged over the six entire drainage basins or only their ablation zone. Value of each pixel is calculated by averaging all values in the form of standardized anomaly obtained whenever a cyclone of the 40 % and 60 % most intense during the period 1958-2016 was within 750 km from that pixel in summer.

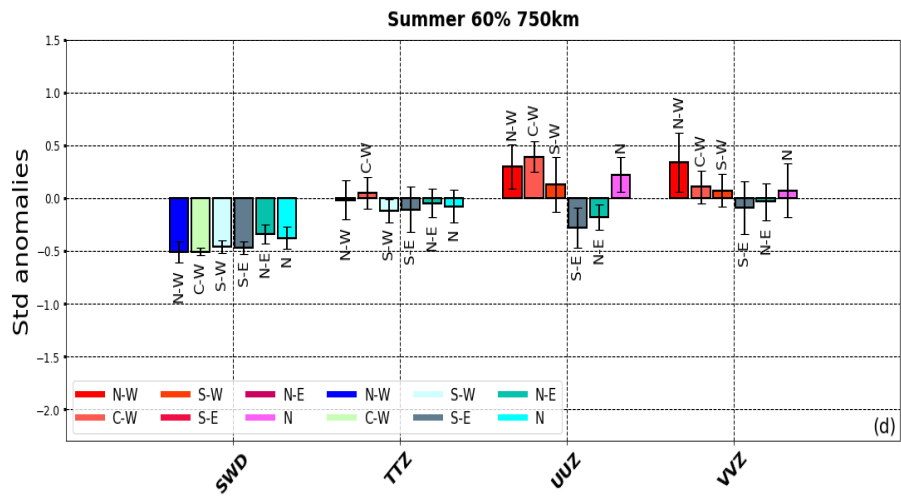
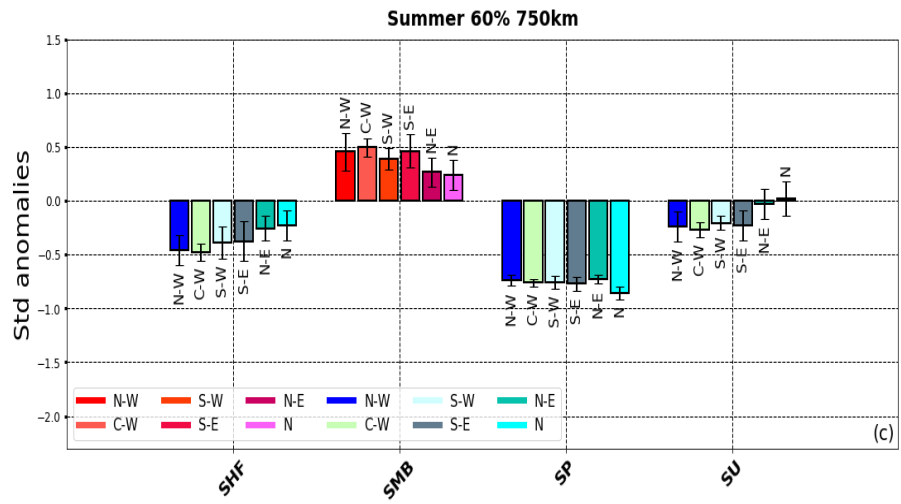


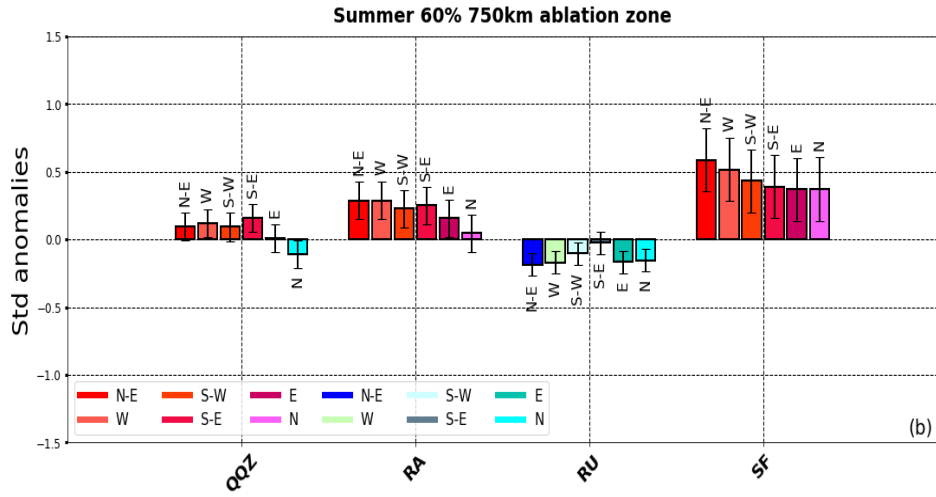
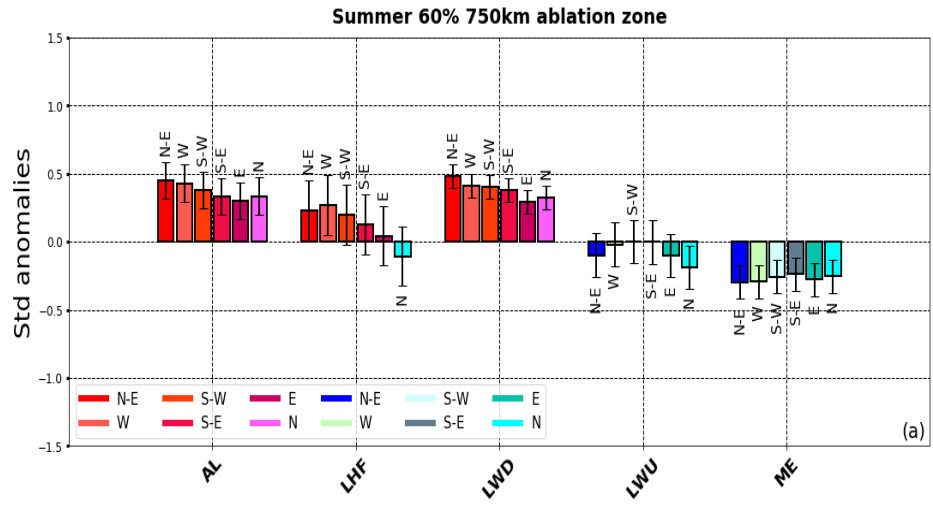


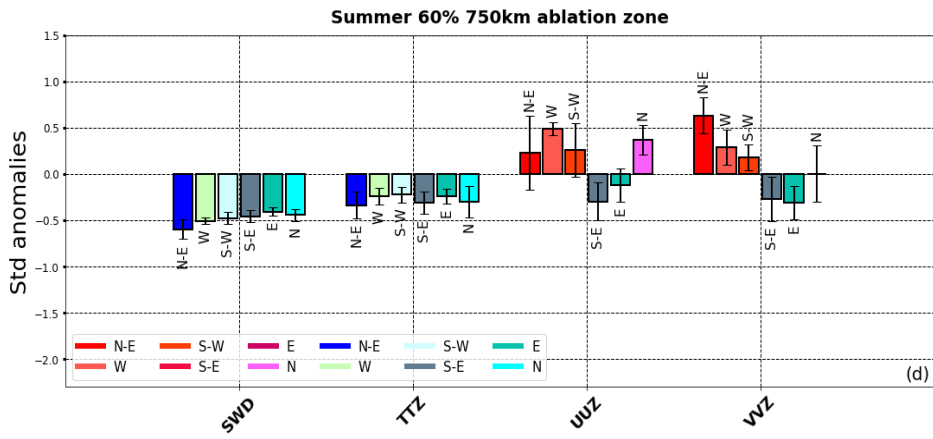
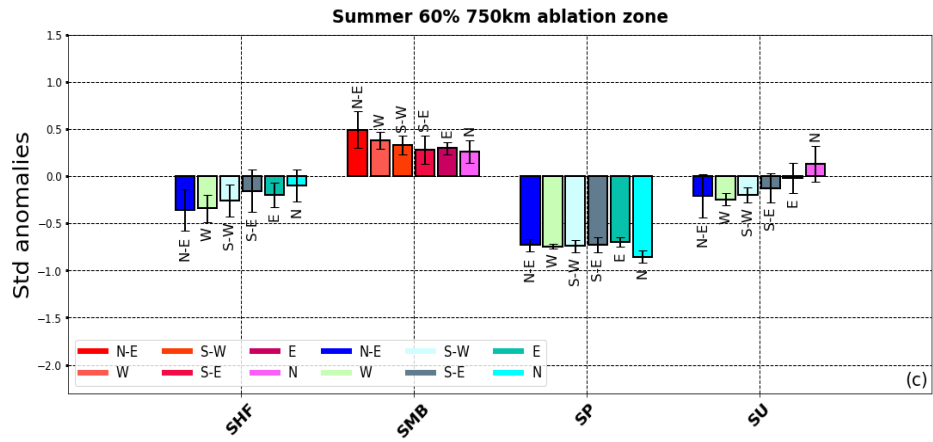






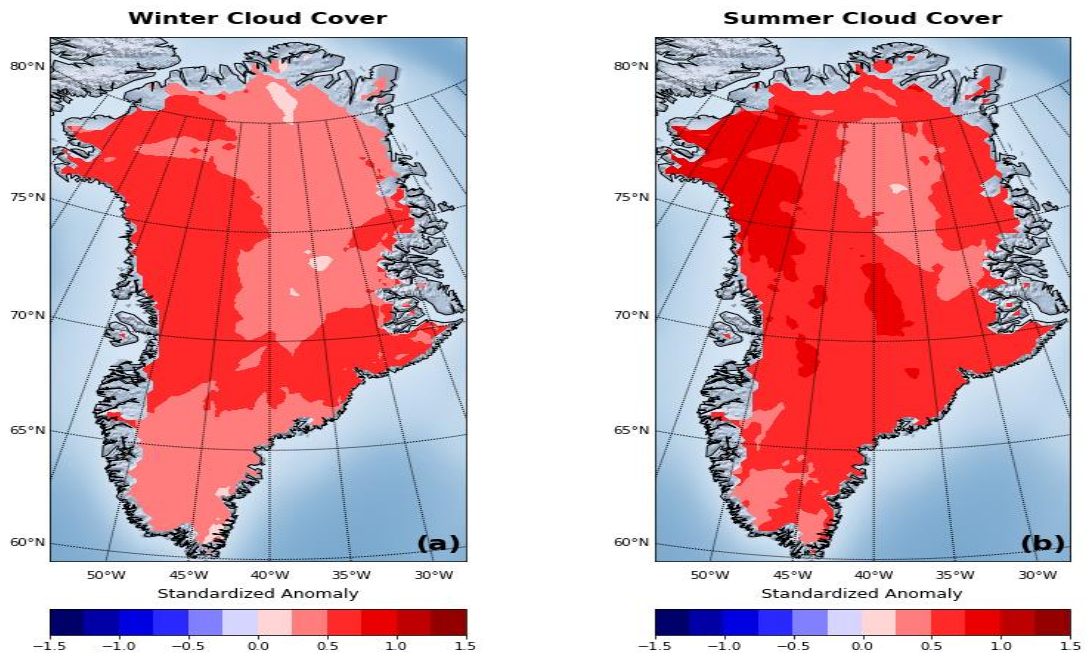






## Appendix F

Spatial representation of the standardized anomalies over the entire GrIS of cloud cover. Value of each pixel is calculated by averaging all values in the form of standardized anomaly obtained whenever a cyclone of the 40 % most intense during the period 1958-2016 was within 750 km from that pixel in winter and summer.



Same as above but for the 60% of the most intense cyclones

